Preparation and Characterisation of Mixed CeO_2-Nb_2O_5-Bi_2O_3 Nanoparticles

Katharine Louise Moore
Murray Edwards College
University of Cambridge

This dissertation is submitted for the degree of Doctor of Philosophy
February 2015

Declarations

The work described in this dissertation was carried out in the Department of Chemistry between October 2011 and February 2015. The work is the author's own original research and not the result of any collaboration. Discussion of any research not carried out by the author is clearly referenced. This work has not previously been submitted for a degree or other qualification at the University of Cambridge or any other University. The length of this thesis does not exceed the word limit of 60,000 words as instructed by the Degree Committee for the Faculty of Chemistry and Physics.

Katharine Moore
February 2015

Acknowledgements

I would like to express my sincere appreciation to all of those who have helped and supported me during my time as a PhD student.

Firstly, I am immensely grateful to my supervisor Dr David Jefferson for all of his advice and patience over the last three years. It has been invaluable being able to draw upon his knowledge of microscopy and crystallography throughout my time as a PhD student. It has been a pleasure working in the solid state chemistry group and having the chance to study these nanomaterials. I would also like to thank the following people who have been a part of the research group during my time in Cambridge and made the chemistry department such an enjoyable place to be: Alex Jones, Dee Shen, Lewis Owen and Lorna Radford. I am extremely grateful to them for helping to discuss my results and further my research project, as well as providing cake on a regular basis.

I would like to thank the EPSRC for funding, thereby allowing me to carry out this work. I would also like to thank NEXUS at the University of Newcastle for carrying out XPS analysis and their help with processing the information. Thank you to the girls of Murray Edwards who made College a wonderful place to be. Thank you to the many friends I've made in the chemistry department over the last three years for chemical discussions and lots of tea breaks!

I also want to thank my parents and sister for their constant support and reassurance for the duration of my time at Cambridge. Finally, I would like to thank John Dunn for all of his encouragement and support.

Abstract

Preparation and characterisation of mixed CeO_2-Nb_2O_5-Bi_2O_3 nanoparticles

By

Katharine Moore

Mixed metal oxides are ionic compounds containing at least two metal ions within an oxide structure. The literature contains a plethora of examples of mixed metal oxides on the bulk scale, which have been well characterised, however, mixed metal oxides on the nanoscale are far less well understood. The work presented here investigates the Bi_2O_3-CeO_2-Nb_2O_5 mixed oxide system and characterises the resulting nanoparticles and crystal structures. Although the parent oxides are well known and much work has previously been done in analysing their crystal structures, combinations of these oxides have not been well characterised, especially on the nanoscale. Using high resolution electron microscopy (HRTEM), powder X-ray diffraction (PXRD), electron dispersive X-ray spectroscopy (EDS) and X-ray photoelectron spectroscopy (XPS) as analytical tools, the structures of the nanoparticles in this system have been explored.

As each of the parent oxides possess useful properties, which have been utilised in industrial applications such as electrolyte components in solid oxide fuel cells and as catalysts in a range of chemical reactions, it was hypothesised that if all three metal ions could be contained in one particle they could show novel and interesting characteristics. It was proposed that due to the more relaxed crystal structure in nanoparticles, the solid solubility of the metal ions should be increased, and a solid solution of ions would form.

This work presents results showing the synthesis of binary and ternary oxides in the nano-form within the Bi_2O_3-CeO_2-Nb_2O_5 system, including quantitative analysis of these particles. Secondly, and most importantly, it presents the first successful synthesis of quaternary oxide nanoparticles containing bismuth, cerium and niobium using the low temperature resin-gel method. Finally, the work attempts to explain how and why the ions are ordered in a given arrangement, with bismuth showing a preference for surface site occupation, as shown by XPS data, and describes some preliminary computational results which corroborate the experimental data.

Table of Contents

List of abbreviations

Å	ångström
Δr_c	radius of the disc of least confusion
2θ	scattering angle
a.u	arbitrary units
AFM	atomic force microscope
C_s	coefficient of spherical aberration
d	interplanar distance in a crystal lattice
EDS	energy-dispersive X-ray spectroscopy
ESCA	electron spectroscopy for chemical analysis
fcc	face-centred cubic
FEG	field emission gun
FT	Fourier transform
g	grams
hcp	hexagonal close-packed
hkl	Miller indices
HRTEM	high resolution transmission electron microscope
HSA	hemispherical analyser
k	shape factor
M	magnification of the lens
nm	nanometer
P(S)	power spectrum
PCTF	phase contrast transfer function
PEG	polyethylene glycol
PXRD	powder X-ray diffraction
$\phi\underline{r}$	electrical potential in HRTEM specimen
SEM	scanning electron microscope
SOFC	solid oxide fuel cell
STEM	scanning transmission electron microscope
STM	scanning tunnelling microscope
TEM	transmission electron microscope
XPS	X-ray photoelectron spectroscopy
YSZ	yttrium stabilised zirconia
α	scattering angle
η	absorption coefficient
λ	wavelength
μm	micrometer

1. Introduction

1.1 General overview

The research presented in this dissertation explores the crystal structures formed when CeO_2, Nb_2O_5 and Bi_2O_5 are combined to form mixed metal oxide nanoparticles of varying compositions. Each of the parent oxide structures has been thoroughly investigated in the past, and their crystal structures and polymorphs are well documented. However, there is plenty of scope for investigation in this area, as although a considerable amount is known about the atomic arrangement and lattice structure of the parent oxides, surprisingly little is known of the unit cell arrangements of combinations of the oxides, particularly in the nano-form. As seen previously in numerous studies, [1-3] doping of one oxide with another can enhance the useful properties of the material, such as conductivity and catalytic activity, as the crystal structure is forced to adapt. It is a method commonly used to tune one favourable property of a material. It would be hugely advantageous to be able to understand how and why mixed metal oxide particles form with a given arrangement, as being able to manipulate these factors could be beneficial for industrial application. This is because, as will be explained further in this chapter, the oxides in question have a large number of attractive properties.

In describing the mixed oxide systems in this thesis the terms binary, ternary and quaternary oxides are used. The naming convention can be explained in two ways with both being used concurrently in the literature. The first system takes the total number of elements present in the compound into account. Therefore, CeO_2 is described as a binary oxide as it is composed of two elements (including oxygen). Likewise, $CeNbO_4$ is described as a ternary oxide as it is composed of three elements in total. The second system counts only the metal atoms in the prefix. Therefore, according to this system $CeNbO_4$ would be a binary oxide. Only the first naming system will be used in this dissertation.

A mixed metal oxide is usually defined as a solid ionic compound containing two or more metal ions, irrespective of the material being in a crystalline or amorphous state. However, more information about the structure and lattice arrangement can be gained by HRTEM and PXRD if the material is crystalline, therefore, this was the preferred synthetic result. Due to the inherent nature of the nanoparticle lattice tending to relax due to the decreased pressure within the material in comparison with the bulk, a solid solution of ions in the material becomes the most energetically favourable arrangement in terms of free energy. A solid solution is defined as a homogeneous mixture of two or more types of atom in the solid state. In the early part of the 20th century, William Hume-Rothery set out four rules outlining the conditions required for a solid solution in metals to be formed [4]. The main factors, which he found to determine whether a solid solution can form are: ionic radii, lattice type, valency of the metal ions and the chemical affinity factors. For complete solid-solid solubility, the ionic radii of the metals should be similar (a difference of less than 15%) and have the same structure type, for example fcc or hcp. It is also important that the metals have a low chemical affinity for each other so that it is preferable to form a solid solution rather than a specific compound. CeO_2 has been studied extensively and has been found to have high solid solubility with other oxides, particularly with other rare earth metals [5-7]. Bismuth oxide also readily forms solid solutions with rare earth metals, as demonstrated by Cahen *et al.*, [8] and these may retain their high ionic conductivity. It was found that solid solutions were present in a variety of Bi_2O_3 systems containing rare earth metals, for example La_2O_3 and Er_2O_3. In general, the solid solutions formed defect fluorite phases, based on δ-Bi_2O_3. There are also several examples of Nb_2O_5 forming solid solutions with a range of metals including bismuth [9-11]. It was, therefore, hoped that solid solutions would be found across the range of compositions for the CeO_2, Nb_2O_5 and Bi_2O_5 nanoparticles.

The remainder of this chapter explains the importance of studying nanoparticles for industrial applications, as well as why they are interesting in respect of their novel properties. In addition, the crystal structures and polymorphs of the parent oxides investigated in this thesis are presented in more detail, with a literature survey detailing the previous research carried out in this area.

1.2 An introduction to nanoparticles

The terms nanoparticle, nanoscience and nanotechnology are now commonplace in countless scientific journals, research laboratories, and even the mainstream media. However, the field of nanoscience is still relatively recent having only gained mass interest in the 1950's after Richard Feynman's pioneering lecture entitled 'There's plenty of room at the bottom' [12, 13]. This is often credited as the inspiration for the first research into the field of nanotechnology. Feynman, described as the father of nanotechnology, accurately predicted that the next big advances in science and technology would occur by discovering more about molecules on the nanoscale and being able to manipulate them. As this field is so well publicised, not only by the scientific community but by many other industries worldwide, it is important to define the key terms which open this subchapter. Nanoscience has come to mean research into any area involving particles or components on the nanoscale, while nanotechnology is the use of these components in industry and products in everyday life. A nanoparticle is conventionally defined as a particle with a diameter of < 100 nm. It is at this size that the properties of a material begin to change radically from those in the bulk, and why it is an important area to study, as the laws of quantum mechanics begin to influence the properties of the material rather than classical mechanics.

The first published scientific reference to nanoparticles was in 1857 by Michael Faraday. He noted that the properties of nanometer sized particles of gold leaf changed with heating; the metallic film was destroyed and white light could be freely transmitted leading to an increase in resistance [14]. Despite the fact that novel properties of nanoparticles were known in the 19th century, the extensive research into the field of nanoscience only evolved after Feynman's speech in the 1950s. The reason for research in this area accelerating rapidly is the progress of modern technology and miniaturisation in the appropriate industries. The phenomenon of nanoscale research has been commonly described as a 'bottom up' approach to research (in contrast to the 'top down' approach). This phrase 'bottom up' involves assembling larger molecules from the atomic level upwards, rather than breaking down much larger molecules into their component parts to study them.

As already stated, nanoparticulate systems have been of much interest in research due to their unusual properties in comparison with bulk materials. This is because, as nanoparticles by definition have a diameter of less than 100 nm, they have a significant increase in surface area compared with the bulk material, which can alter their reactivity. In the bulk, the proportion of atoms at the surface is negligible to the number in the structure, whereas in nanoparticle form the proportion of atoms at the surface is far higher. The increase in surface area is one property that can prove incredibly useful in areas such as heterogeneous catalysis. If a catalytic material has a higher surface area, it will be a more effective catalyst and potentially more economically viable. Another important difference between a bulk material and the corresponding nanoparticulate material is that the crystal lattice of a nanoparticle may be more relaxed, therefore, there is less inherent strain than in the bulk structure. This can be utilized in designing new structures, as the lattice can be manipulated by changing the stoichiometry of the material much more easily, thereby altering the properties. Furthermore, due to the size of nanoparticles, there are quantum effects to be considered. As a material decreases in size, from a bulk solid towards the size of an atom, its behavior moves away from the laws of classical physics and towards quantum mechanics. This is one of the most important reasons why materials on the nanoscale are interesting to study, as their behaviour is in between these two well understood extremes. The electronic properties of a material are governed by these laws, which explains why conductivity can change in a material as the particle size decreases. Band theory is used to explain conduction properties. It states that electrons are confined to a band structure with electrons in different bands only free to move to higher levels when the band gap is small enough to permit this and enough energy is given to the material to promote an electron into the conduction band, Figure 1.1. Usually in the bulk the electronic structure is seen as a continuous band, as the band gap is so small due to lots of overlapping orbitals from many atoms or molecules, in which the electrons are free to move. This is not the case in the nanoparticle form because as particle size decreases, the gap between the valance band and the conduction band may increase as the number of atoms in a nanoparticle is finite. The change in conductivity as particle size decreases can be used to 'tune' the conducting properties of nanoparticles.

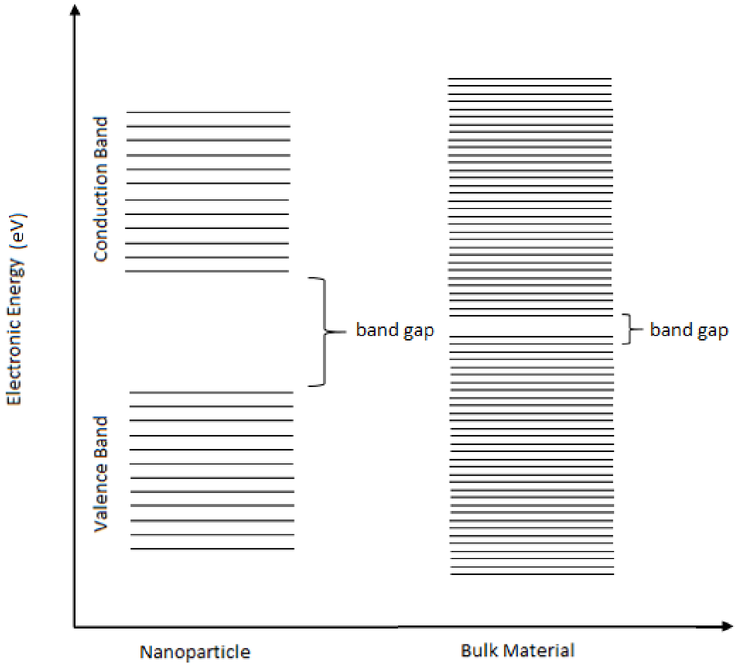

Figure 1.1 Plot illustrating the different band gap energies for a nanoparticle and a bulk material.

In so far as chemical properties are concerned, those of any solid compound are, to a considerable extent, determined by its crystal structure. In simplistic terms, although any chemical bonds in a structure are determined by the electronic structure of the atoms concerned, the exact position within the potential well of a bond is generally dependent on the overall crystal structure. If any atom is substituted by a different one, the crystal structure will be perturbed, and in an infinite 3-dimensional crystal the extent of this perturbation will of necessity be limited, as strain will be set up in adjacent parts of the crystal lattice where atoms will normally be in their idealised positions. This is what gives rise to the Hume-Rothery rules. If a nanoparticle is now considered, however, if can no longer be regarded as infinite. In this case, the conventional model of the structure as composed of a 3-dimensional repeat of identical unit cells no longer applies, and in considering the energy of the system we must consider the particles as a single entity. In such a system, therefore, there is no reason why the perturbation set up by atomic substitution cannot be taken up by alternative adjustments in atomic position elsewhere in the particle, providing that these do not produce unacceptable bond energies. Therefore, it is expected that the Hume-Rothery rules will be somewhat relaxed in nanoparticulate species and solid solubility will be increased.

Experimentally, scientists have investigated the morphology of nanoparticles, synthesising a variety of forms such as nanorods, nanofibres, nanowires, and nanotubes, all of which have high shape anisotropy (examples seen in Figure 1.2). All of these structures have different potential applications.

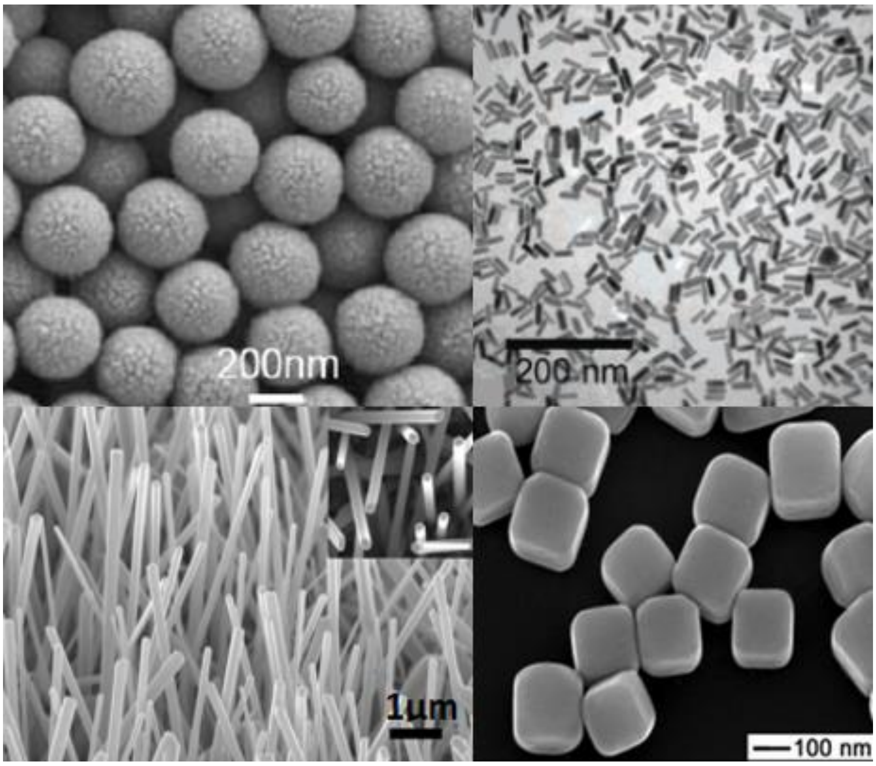

Figure 1.2. Examples of nanospheres (top left), nanorods (top right), nanowires (bottom left) and nanocubes (bottom right). [15-18]

As research into nanoscience has grown in popularity, it has encompassed many overlapping areas in science and engineering. During the 1960's and 1970's much research was carried out in trying to form nanoparticles for use as vaccines to treat infections such as tetanus and diphtheria. Nanoparticles have the potential to revolutionise the vaccination process against these illnesses as currently multiple injections are needed, but with nanoparticles providing a sustained release of drug, only one injection would be necessary [19]. As well as vaccination, there is currently medical research into using nanoparticles for fighting cancer by selectively killing cancer cells. Nanoparticles are particularly well suited to drug delivery and medical applications due to their high stability and ability to be manipulated to contain both hydrophobic and hydrophilic areas making it possible for them to pass through the body [20]. In order to create a particle suitable for use in the body, there has been much work done on coating nanoparticles with polar materials so they can be easily absorbed in the body.

Another potential medical use of nanoparticles is in bio-imaging, as maximum resolution could be attained due to the fact that most biochemical processes are on the nanoscale. Having functional particles at the nanoscale creates limitless possibilities in medical research. Magnetic nanoparticles such as iron oxide are creating much interest in the scientific community currently for use as contrast agents in MRI and for labelling within the cell. There are two mechanisms by which the magnetic nanoparticles can operate. The first is to use polymer coated nanoparticles, which are not recognised by a specific bio-receptor. Polymer coatings commonly include dextran, dextran sulphate and silane [21, 22]. The second group of iron oxide nanoparticles constitute molecular targeted nanoparticles. These particles are able to bind to a specific group on a biomolecule, for example a peptide group [23]. In addition, much current research focusses on gold nanoparticles, which have been shown to be very effective in cancer treatments. These nanoparticles interfere with the DNA in the cancer cells causing a mutation, which leads to apoptosis of the cell [24].

Due to their size, nanoparticles have inevitably become of interest in the field of electronics. The smaller size of the particles makes it possible to pack more transistors onto a chip. Transition metal oxides such as ZnO have been studied in detail to improve their properties, which would be useful as the semiconductor component in a transistor. Research in ZnO has looked at both nanoparticles forms and bulk forms of the material [25]. A variety of metal oxide nanoparticles have been examined in detail for applications in energy storage, due to their high ion conductivity and variable oxidation states. This makes them suitable for electrolytes in solid oxide fuel cells (SOFC) and as catalysts. Some of these structures will be looked at in detail in this project (see Bi_2O_3 and CeO_2).

Progress in nanotechnology has been greatly facilitated by the invention and development of characterization tools such as the scanning tunnelling microscope (STM), atomic force microscope (AFM), scanning electron microscope (SEM) and the transmission electron microscope (TEM). An important leap forward in analysis of materials on the nanoscale came with the development of the scanning tunnelling microscope (STM) in 1981. It enabled the surface of a material to be imaged with a resolution of 0.1 nm. This allowed materials to be manipulated on the atomic scale and gave a far more in depth knowledge of how these molecules were structured. Other microscopy techniques have also proved exceptionally useful in analysing the composition and structure of nanoparticles. The SEM allows the surface of the material to be seen in addition to the shape and size of the particles formed. The TEM has a higher resolution than the SEM, which permits the atomic structure of crystalline nanoparticles to be observed directly and the different phases determined. Often coupled with the TEM is energy dispersive X-ray spectroscopy (EDS) which enables the composition of the specimen to be established. These techniques will be discussed in detail in the following chapter.

As methods for studying materials on the nanoscale improve, so does our understanding of how molecules and structures interact on this level. Nanoparticles continue to fascinate scientists as they bridge the gap between the bulk system and atoms and frequently display surprising properties. It is likely that there is much more to learn about with regard to the reactivity and structure of nanoparticles. Coupled with this is the progression of technology by utilising this surge in research for miniaturisation which could make technology more efficient and cost effective.

1.3 Crystal structures investigated

1.3.1 Introduction to metal oxide compounds

The uses of metal oxides are numerous, such as in fuel cells [26], catalysts [27] and in fabrication of microelectronic circuits [28]. Due to their diverse structures and conductivity properties they are not only useful but also interesting to study. Usually the crystal structures of metal oxides are characterized as having metal cations surrounded by oxygen anions forming an infinite array of atoms arranged in a repeating three dimensional pattern. The unit cell of a structure is the basic repeating unit from which the whole lattice can be formed. It is a convenient concept as it simplifies the structure to see how the atoms are related to each other by symmetry.

Most known metal oxide structures have been investigated and their crystal structures identified, usually using X-ray or neutron diffraction to locate the positions of the ions in the structure. For any one metal oxide, it is not uncommon to observe different phases depending on the temperature or pressure. Examples of this will be seen in more detail in later sections when discussing the polymorphs of various compounds. Metal oxides can possess a range of properties including superconductivity as in the lanthanum barium copper oxide structure [29], semiconductivity and magnetism, for example in iron oxide [30]. Therefore, being able to synthesise these materials on the nanoscale could facilitate the modification of existing properties, making them more suitable for use in industry, or introduce novel properties which could also be exploited for new industrial applications.

Many studies in the area of metal oxide synthesis in nanoparticulate form have been carried out, in order to combine the valuable properties of the metal oxide with the unusual properties of nanoparticles. For example the ability of the lattice to relax as particle size is reduced has been proven by Tsunekawa *et al.* [31] where they demonstrated, with evidence from X-ray photoelectron spectroscopy (XPS), that the crystal lattice expands in CeO_2. It was suggested this was due to reduction of some Ce atoms from +4 to +3. Further studies by Zhou and Huebner confirmed these results by XRD analysis [32].

As the crystal lattice relaxes, it becomes more able to accommodate the presence of a second metal ion, which is not usually possible due to the extra strain on the lattice. Therefore, incorporation of a second metal can be more readily achieved and a solid solution can be formed.

1.3.2 Bismuth oxide

Although bismuth sesquioxide (Bi_2O_3) has been of scientific interest since the beginning of the 20th century, due to increased awareness of its application in the electronics field, it was not until the early 1960's that the first detailed review of Bi_2O_3 was carried out, by Levin and Roth [33]. They were able to distinguish four distinct polymorphs of Bi_2O_3 and determine the relationship between these phases. Up until this time it was known that a low temperature and high temperature phase of Bi_2O_3 existed, but there was debate as to the crystal structures of the metastable phases. Levin and Roth's work concluded that there were four crystalline polymorphs of Bi_2O_3, described in the original paper as the monoclinic form, the tetragonal form, the bcc form and the cubic form. These are now conventionally known as the α, β, γ and δ phases respectively. A schematic diagram showing all four structures can be seen in Figure 1.3.

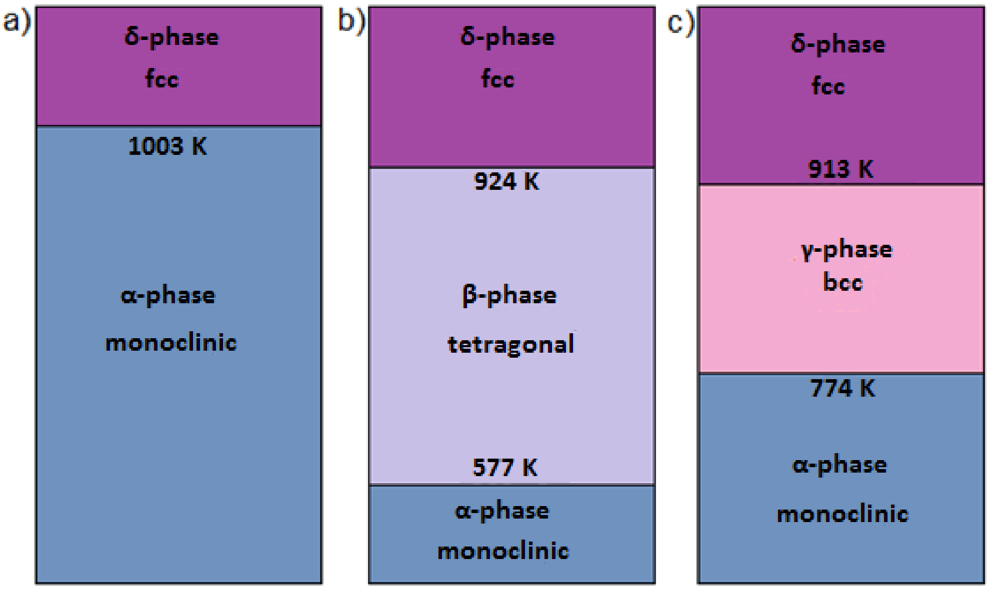

Figure 1.3. Schematic diagram illustrating the four polymorphs of Bi_2O_3. a) shows the two stable phases observed when heating, b) and c) show the additional phases seen upon cooling the sample.

The crystal structure of the low temperature form of bismuth oxide, the α-Bi_2O_3 polymorph, was first solved by Sillen in 1937, who determined that the structure had a monoclinic unit cell with a cell volume of 326.92 Å^3 [34]. He was able to identify the positions of the bismuth atoms using Patterson methods, and from this knowledge, derive approximate oxygen positions. However, as X-ray crystallographic techniques evolved, more accurate data regarding the oxygen positions could be calculated using single crystal X-ray analysis [35]. The crystal structure of α-Bi_2O_3 can be seen in Figure 1.4. The structure is made up of layers of bismuth atoms, which lie parallel to the {100} plane with sheets of oxygen atoms present in between the layers of bismuth atoms.

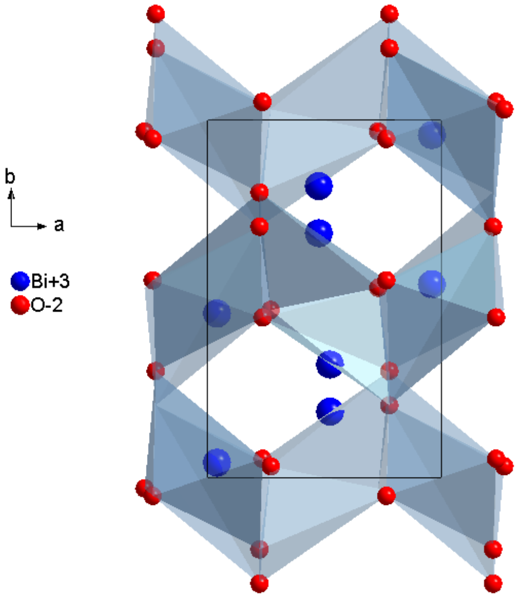

Figure 1.4. The crystal structure of α-Bi_2O_3 *viewed along the c axis. [36]*

When α-Bi_2O_3 is heated to 1003 K, a phase transition occurs to form the δ-Bi_2O_3 structure which remains stable until the melting point at 1098 K [37]. This cubic phase, discovered by Sillen [38] using X-ray diffraction methods, is similar to the fluorite structure type with the only difference being the oxygen deficient sub-lattice. The crystal structure of δ-Bi_2O_3 can be seen in Figure 1.5. It has generated much interest in industry for use in solid oxide fuel cells as it is an excellent oxygen ion conductor. Although δ-Bi_2O_3 is known as the high temperature polymorph of bismuth oxide, it forms at a relatively low temperature in comparison with other oxygen electrolytes making it a more economically viable material for use commercially.

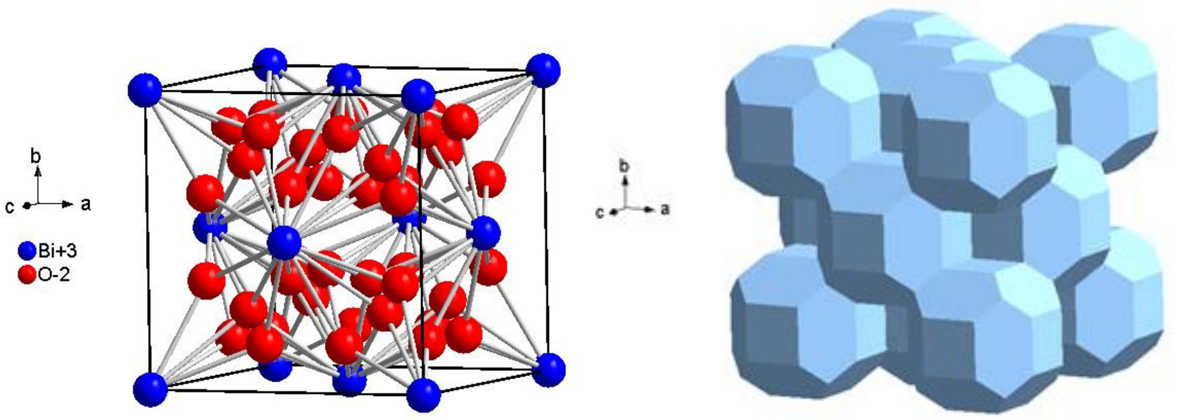

Figure 1.5. The crystal structure of fcc δ-Bi_2O_3 viewed between the a and c axes (left) and polyhedral representation viewed between the a and c axes (right). [39]

There has been considerable debate previously as to whether the oxygen-defective sub-lattice is ordered. Sillen [38] concluded that the sub-lattice was ordered from powder X-ray diffraction data. However, Gattow and Schroder [40] disagreed with this description and preferred to describe the structure as having 75% of the sub-lattice sites filled by oxygen ions. In other words, the six oxygen ions are randomly distributed over the eight oxygen sites. These two descriptions are illustrated in Figure 1.6.

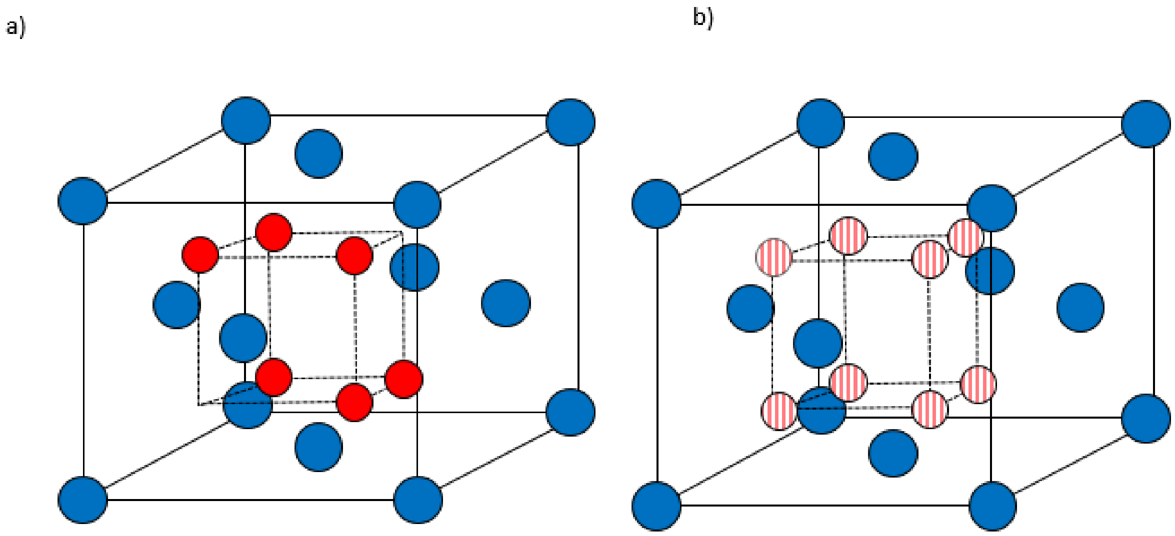

Figure 1.6. The Sillen model (a), shows the oxygen vacancies ordered along the <111> plane. The Gattow model (b) suggests that the oxygen vacancies in the sub-lattice are randomly distributed. Therefore, as there are 8 oxygen sites and only 6 oxygen atoms per unit cell, each site has 75% occupancy.

It is well known that δ-Bi_2O_3 has a very high ionic conductivity and disorder in the sub-lattice would account for this as the ions could freely move through the structure. Therefore, Gattow's model containing a disordered sub-lattice is currently the accepted theory amongst researchers. Willis [41] investigated the CaF_2 structure via neutron diffraction and concluded that the structure was not an ideal ‘fluorite’ structure as the fluoride ions were displaced towards the centres of the interstices between the fluoride tetrahedra. Sammes *et al.* [42] suggested that this theory could also apply to the δ-Bi_2O_3 structure as this disorder would again account for the high ionic conductivity of the material. The Battle model [39], presented in Figure 1.5 and seen again below in Figure 1.7, indicates all possible oxygen positions in the structure showing that they could occupy a site exactly in the centre of the tetrahedra formed by bismuth, or be displaced towards a vertex of this tetrahedron.

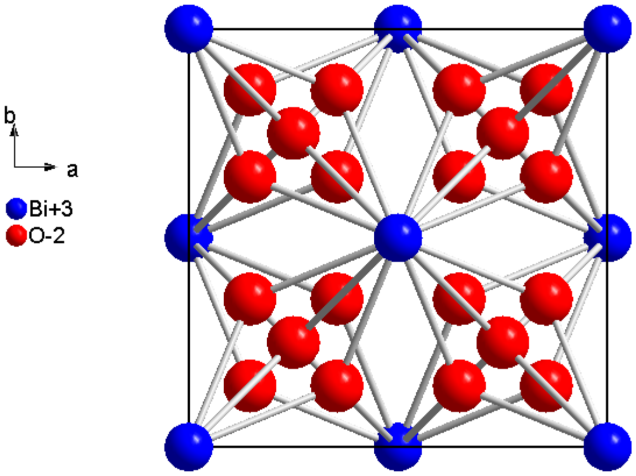

Figure 1.7. The δ-Bi_2O_3 structure, viewed along the c-axis, as described by Battle et al., with variable oxygen positions. [39]

There is still ongoing debate as to the ‘real’ structure of δ-Bi_2O_3 with many conflicting opinions as to how the oxygen sub lattice is arranged. Computer simulations using electrostatic factors and also density functional theory have suggested that the lowest energy structure could have the oxygen vacancies paired along the <111>, the <100> or the <110> axes [43-47].

In all likelihood, the energy barriers between these different oxygen conformations are very small, meaning that in any crystal of δ-Bi_2O_3 there will be a combination of all the arrangements, making the average arrangement of oxygen vacancies random. With new ways of probing the structure, the δ-Bi_2O_3 structure theory continues develop and adapt to the new information acquired.

The β- and γ- forms of Bi_2O_3 are observable upon cooling of the δ-Bi_2O_3 phase. These are metastable phases and are therefore more difficult to study. β-Bi_2O_3 is obtained by quenching the melt of the δ-phase and forms a tetragonal structure with a volume of 343 $Å^3$ at 924 K. Upon cooling, the oxygen vacancies become more ordered in the {001} direction. Unlike γ-Bi_2O_3, the β-phase has never been stabilised at room temperature and decomposes into the α-phase at 577 K [42]. The crystal structure of β-Bi_2O_3 can be seen in Figure 1.8.

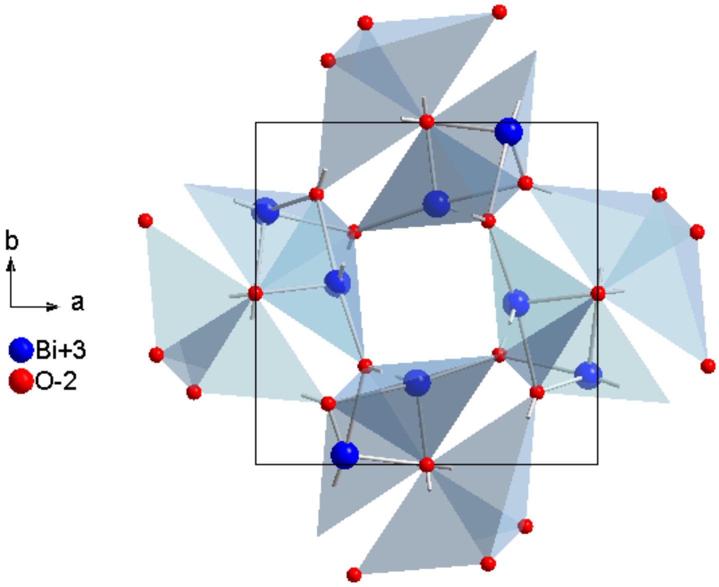

Figure 1.8. The crystal structure of β-Bi_2O_3 viewed along the c axis. [36]

γ-Bi_2O_3 is formed by cooling δ-Bi_2O_3 to 913 K and can still be seen down to room temperature if the rate of cooling is sufficiently slow. If the rate of cooling is too fast, a phase transition to the α-form will occur. The crystal structure of γ-Bi_2O_3 consists of a body centred cubic unit cell with a cell volume of 1077 Å^3 and can be seen in Figure 1.9.

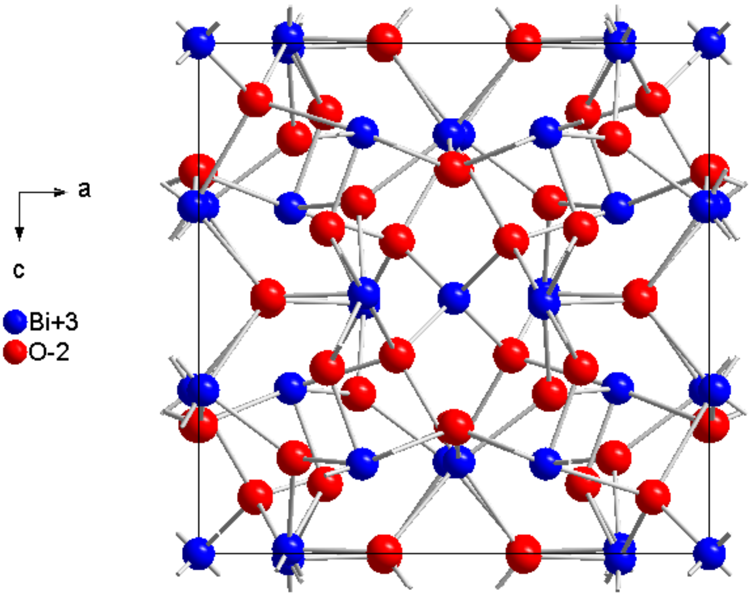

Figure 1.9. The crystal structure of γ-Bi_2O_3 viewed along the b axis. [48]

Harwig and Gerards [49] described the conductivity in the δ, β and γ phases as ionic, with the oxide ions carrying the charge. It has been demonstrated [50] that conductivity in the α-phase increases with the partial pressure of oxygen whereas in δ-Bi_2O_3 the conductivity is unaffected by variation in the oxygen partial pressure (down to 10^{-3} Pa). This data indicates that in the α-phase the charge is carried through the oxygen vacancies, as it is a very ordered phase with structured oxygen vacancies along the c-axis, whereas in the δ-phase, the fluorite structure is less rigid with only short range order meaning the oxygen vacancies are more random. The conductivity of the δ-phase is almost three times as high as the β and γ-phases, which is has been of great interest to researchers looking to use it as an electrolyte in solid oxide fuel cells (SOFCs). The electrolyte is the membrane component in an electrochemical cell which separates the two electrodes and conducts ions between them. Currently yttrium stabilised zirconia (YSZ) is the most popular choice as an electrolytic material, however, δ-Bi_2O_3 has a conductivity of twice the magnitude of YSZ at comparable temperatures. It is hoped in the future a more effective electrolyte could be fabricated from δ-Bi_2O_3 in electrochemical devices, using lower temperatures and consequently lasting longer than devices using YSZ. At 1024 K the conductivity of δ-Bi_2O_3 is approximately 1 Scm^{-1}, which is over three times higher than α-Bi_2O_3 [51, 52]. The reason for its high ionic conductivity is usually explained by the high degree of disorder in the sub-lattice, with Mairesse [53] summarising the reasons for the disorder more formally as:

- The oxygen sub-lattice is only 75% occupied.
- The Bi^{3+} ion has a lone pair of 6s electrons which gives rise to a highly polarizable cation lattice. This in turn leads to more mobile anions
- The fact that Bi^{3+} is able to tolerate a highly disordered environment.

Although δ-Bi_2O_3 is a very good ionic conductor, the high temperatures required for a stable structure severely limit its applications as a conductor.

Research involving bismuth oxide has also revolved around its potential application in catalysis, either on a support or in granulated form. The reactions studied using bismuth oxide as a catalyst are numerous, including oxidative coupling of hydrocarbons [54], oxidative dehydrogenation [55] and CO oxidation [56]. However, more interest has been shown in mixed metal oxides involving bismuth for use in catalysis. Doping the Bi_2O_3 structure with other ions can alter its properties slightly. This occurs because bismuth is able adopt a range of oxidation states making the structure easily distorted by incorporating other elements. Commonly seen is the bismuth-molybdenum system for use in selective oxidation reactions of hydrocarbons [57-59]. Being able to oxidize small chain hydrocarbons to aldehydes is incredibly useful in industry as they are used extensively in the manufacture of commercial products. It is thought that when bismuth oxide is doped with an element such as molybdenum, the activation energy for the oxidation reaction is decreased as although the first activation step of the C-H activation occurs on the bismuth atom; the subsequent oxidation stage occurs on the molybdenum atoms [60].

As already mentioned, Bi_2O_3 has attracted interest for application in SOFCs due to its high oxide ion conductivity. Solid oxide fuel cells are being explored as a viable way to generate electricity by directly converting the reactants, such as methanol, methane or hydrogen, into electricity via oxidation reactions. They are particularly of interest as they offer a cheap and efficient way to produce electricity with the fuel cells remaining stable over a relatively long period of time [61]. Bismuth oxide has been evaluated as the electrolyte component in these cells. Bi_2O_3 has also been noted for its application in gas sensors. It is able to detect NO gas, which given the widespread interest in ‘green chemistry’ and in environmental chemistry could be extremely useful in monitoring NO emissions from car exhausts. It is highly sensitive at detecting NO gas in preference to NO_2, which is very desirable as it has been difficult to find a material which is as sensitive and selective as Bi_2O_3 [62]. Bismuth doped TiO_2 has been shown to have photocatalytic properties by enhancing the photocatalytic rate of the decomposition of phenol when compared to pure TiO_2 without changing the crystal lattice. When the material is illuminated, electron-hole pairs are generated which enables a reaction to occur on its surface [63].

The polymorphism of Bi_2O_3 has fascinated scientists for over a hundred years, not simply for the crystal structures exhibited, but also for potential applications as a result of the high ionic mobility in δ-Bi_2O_3. Being able to tune or enhance the properties of bismuth oxide by combining it with other metal oxides provides many more opportunities for research and discovery.

1.3.3 Niobium pentoxide

Niobium pentoxide (Nb_2O_5) is a complicated structure to study due to its extensive polymorphism. The basic structure is made up principally from NbO_6 octahedra, which are coordinated by corner and edge sharing linkages. It is the variety of ways that the octahedra can link together which gives rise to such a large range of polymorphs. Brauer [64] discovered the first three polymorphs of Nb_2O_5 in 1941. They were defined as the T-, M- and H- temperature forms (from the German for low, medium and high) and have been investigated in detail over the years. The low temperature form of Nb_2O_5 is known as T-Nb_2O_5 and is seen from 773 K up to 1103 K. Its crystal structure can be seen in Figure 1.10. This poorly crystalline structure has an orthorhombic unit cell with a volume of 708 Å^3 [65]. The niobium atoms are coordinated to the oxygen atoms via both distorted octahedral and pentagonal bipyramidal linkages. Within each unit cell, eight niobium ions are present in distorted octahedra while eight additional niobium ions occupy pentagonal bipyramids. The remaining 0.8 niobium ion per unit cell is present in an interstitial nine coordinate site. Kodama *et al*. [66] implied that T-Nb_2O_5 is the kinetic product at 874 K as this was the majority product observed in the decomposition of Nb_3O_7Cl, despite further results showing H-Nb_2O_5 is the most thermodynamically stable form. After further heating (to 1034 K) and transitions through several metastable phases, H-Nb_2O_5 was formed.

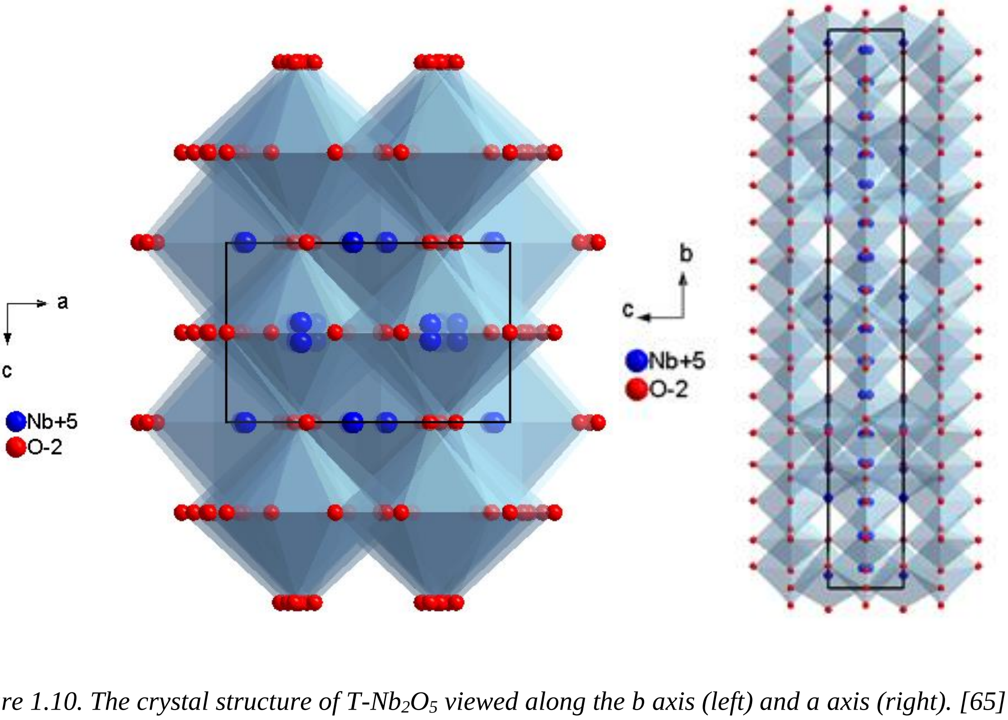

Figure 1.10. The crystal structure of T-Nb_2O_5 viewed along the b axis (left) and a axis (right). [65]

A TT-Nb_2O_5 phase is seen at temperatures below 1073 K and is closely related to the T-structure but has a hexagonal unit cell. The TT form shows even less crystallinity than the T-form and is often stabilised by impurity ions such as OH^- [67]. The most stable phase of Nb_2O_5 is the H-form, which emerges at temperatures above 1173 K shown. The crystal structure of the H-form is presented in Figure 1.11, where it can be seen that the octahedra of NbO_6 are arranged in blocks of 3x4 and 3x5. It has a monoclinic unit cell with a volume of 1358.40 Å^3. Within the structure, the octahedra assemble themselves so that they share corners with octahedra in their own block but share edges with octahedra in other blocks.

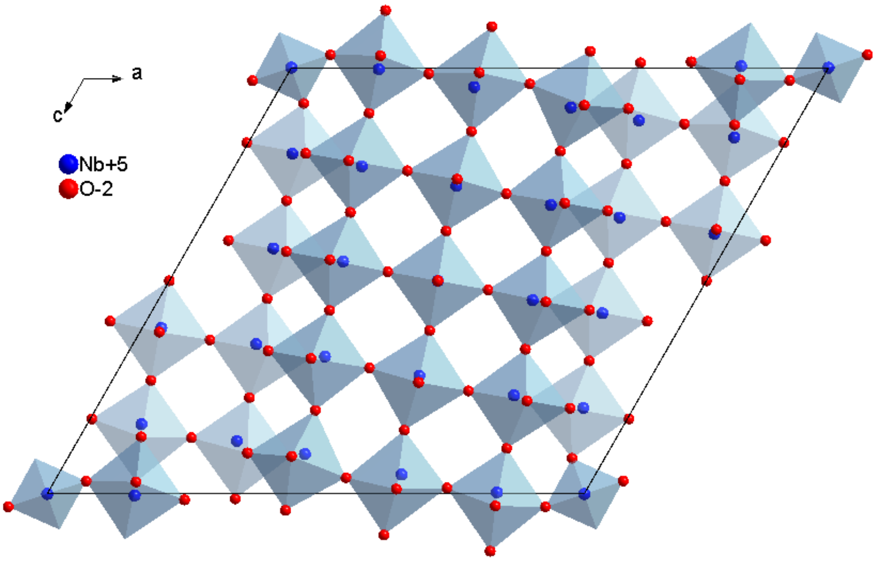

Figure 1.11. The crystal structure of H-Nb_2O_5 viewed along the b axis. [68]

The intermediate structure between the T-type and H-type Nb_2O_5 is the M-form, which has a tetragonal unit cell and cell volume of 1600.99 Å^3, seen in Figure 1.12. The transition from the T-form to the M-form occurs at 1103 K, with the speed of crystallisation increasing with temperature. As the temperature is increased further to 1273 K, complete conversion of T- to M-Nb_2O_5 occurs [64]. The M-Nb_2O_5 structure is made of blocks of 3x4 and 3x5 corner sharing octahedra, with adjacent blocks sharing edges as with the H-form. Studies have shown that the temperature at which the structures are converted to different polymorphs is variable and also irreversible [69]. The M- and H-form are very similar with some studies suggesting they are essentially the same structure, however, Mertin *et al.* [70] were able to show that they are two distinctive forms. Anderson *et al.* [71] also studied these polymorphs by analysing the structure defects in the H-form through high-resolution transmission electron microscopy and looked at what influence temperature had on the structure.

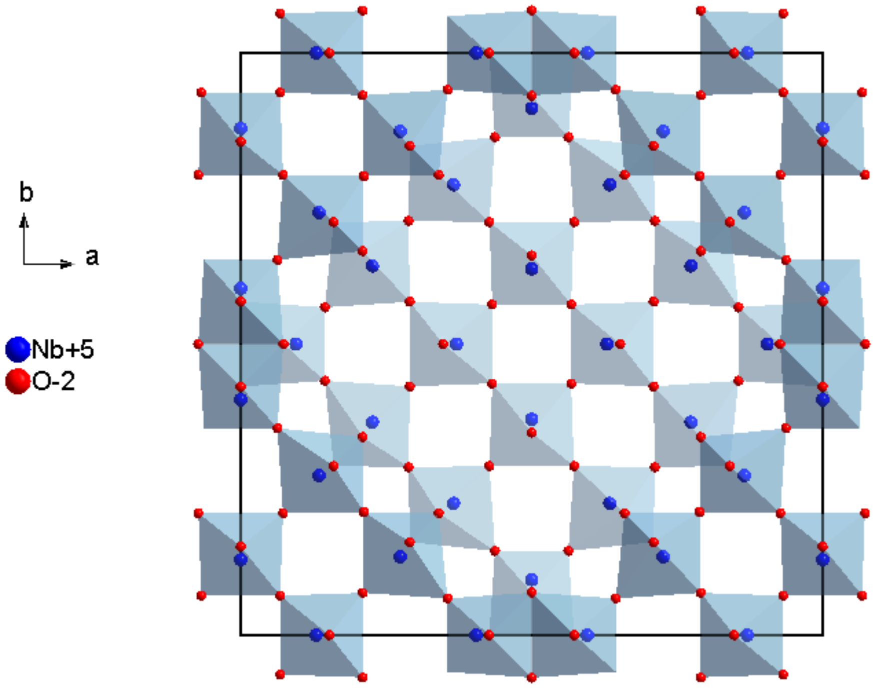

Figure 1.12. The crystal structure of M-type Nb_2O_5 as viewed along the c axis. [70]

In 1964 Schäfer *et al*. [72] discovered three new polymorphs of Nb_2O_5, B- (monoclinic), N- (monoclinic), and P- (tetragonal) forms. N-Nb_2O_5, seen in Figure 1.13, is similar to the M-form as it is based upon NbO_6 octahedra which are corner linked to form square blocks, however, the dimensions of the blocks are 4x4.

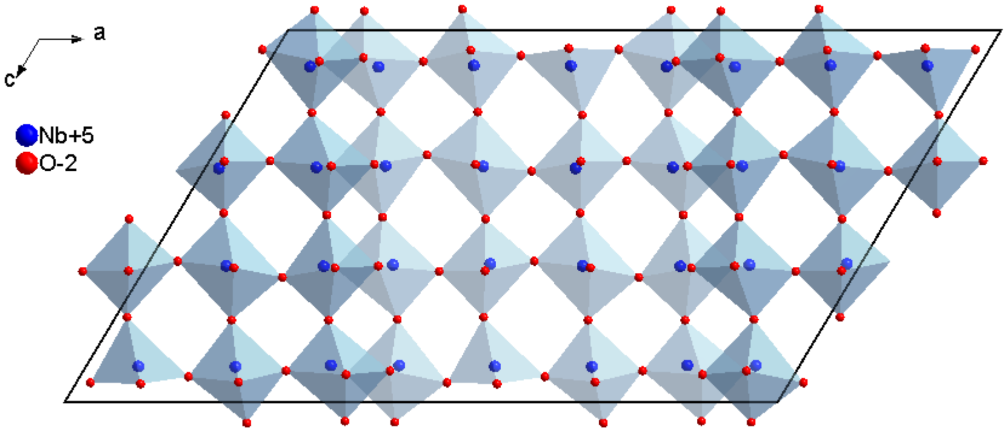

Figure 1.13. The crystal structure of N-type Nb_2O_5 as viewed along the b axis. [73]

Further structures have also been reported, such as the monoclinic R-form discovered by Gruehn [74], however, these structures are much more difficult to study as their thermodynamic stability is uncertain.

The R-form has been seen to change to the N-form upon rapid heating and P-form upon slow heating [75]. It seems to be accepted that the polymorphs of Nb_2O_5 can be grouped into high and low temperature categories with the higher temperature structures being more ordered. A summary of the polymorphs of Nb_2O_5 can be seen in Figure 1.14.

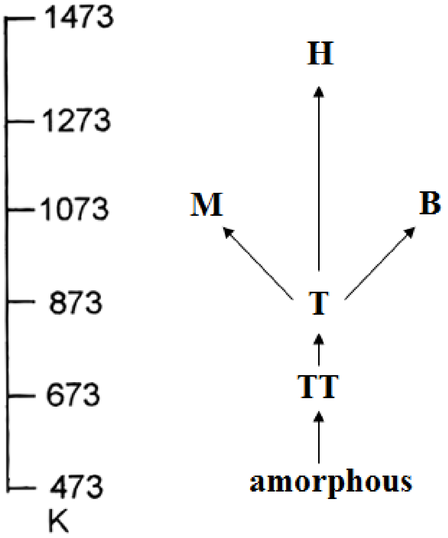

Figure 1.14. Polymorphism of Nb_2O_5.

It should be noted that another range of niobium oxide compounds exist, which are formed by reducing Nb_2O_5 with hydrogen at high temperatures (1073-1573 K). These compounds, such as NbO and NbO_2, have interesting magnetic properties and have found uses in industry such as in capacitors and in producing niobium metal [76, 77]. However, due to the high temperatures and reducing conditions required to form them, they are not relevant to the research presented in this thesis and will not be expanded upon.

Nb_2O_5 has been looked at in detail for its application in catalysis. For example, redox properties of niobia have been seen to enhance the oxidation properties of other metal oxides, such as chromium and vanadium. This has been successful in methanol oxidation when vanadium oxide has been deposited on the niobia support to form an effective catalyst [78]. Niobium oxide has also been used as a catalyst for the dehydration of alcohols, for example 2-propanol, 2-butanol and cyclopentanol [79-81]. These reactions are possible due to niobia's ability to act as a strong Brønsted acid. The method usually used to observe Brønsted acid behaviour involves impregnating an alumina, silica or zirconium support with the niobium oxide catalyst at 373 K. A probe molecule, such as pyridine, is then added to the catalyst and will coordinate to any exposed Nb^{5+} consequently inducing proton generation from the pyridine. Niobium oxide has also been used to catalyse several other reactions. For example, isomerisation, NO reduction and alkylation, all of which are extremely important in industry [81, 82]. There has also been evidence that layered, perovskite type, niobium oxide compounds can be used as photocatalysts for evolving H_2 from various alcohols [83]. These are encouraging results for energy production through niobium oxide catalysed reactions. Furthermore, in the electronics industry, niobia has been used as a cathode material for the 2-V lithium battery. The tetragonal form of Nb_2O_5 (M-Nb_2O_5) was found to exhibit the best properties, by Kodama *et al*. [84], with a discharge capacity of 190 mAh (g oxide)$^{-1}$. It was found that during an electrochemical reaction the niobium cycles between Nb^{5+} to Nb^{4+} as the lithium is intercalated into the structure. It was concluded that the tetragonal form performed the best, as its structure was most flexible in regard to allowing the intercalation because of its layered structure.

1.3.4 Cerium oxide

Cerium (IV) oxide (CeO_2) has been widely investigated in recent years, as it is a suitable material for application in SOFCs, due to its high oxygen ion conductivity. CeO_2 has a cubic unit cell structure of the fluorite type, seen in Figure 1.15, where the oxygen atoms are all in the same plane as one another. Depending on the number of oxygen vacancies, this means that oxygen can be rapidly transported through the crystal structure. The necessity for oxygen vacancies demands some of the ceria to be reduced from Ce^{4+} to Ce^{3+}. The electronic conductivity of the material is increased and this makes it a better electrolyte for use in SOFCs. The function of the electrolyte in the SOFCs is to separate the air and fuel compartments of the cell, but allow reactions to occur across the membrane by the transfer of ions. The requirements for an effective electrolyte are a good oxygen ion conductor, low conventional electrical conductivity as well as a material which is stable in both oxidising and reducing conditions. Generally SOFCs are operated between 500 °C and 1000 °C, therefore as CeO_2 displays its highest ionic conductivity between 500 °C and 650 °C, it is in the ideal range for use in SOFCs. In fact, as it would operate in the lower temperature range, the cost of running CeO_2 SOFCs would be reduced significantly from the current YSZ electrolytes which operate at 1000 °C.

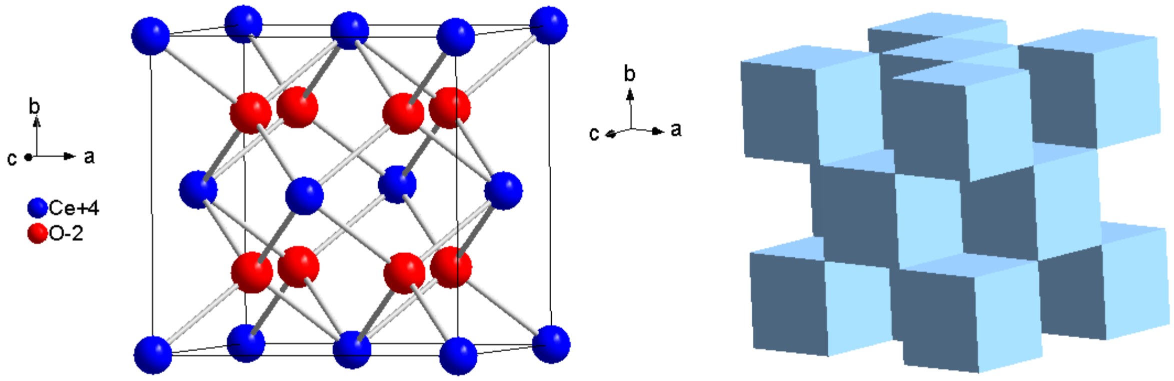

Figure 1.15. Crystal structure of CeO_2 as viewed in between the a and c axes (left) and polyhedral representation (right). [85]

Another important application of CeO_2 is in catalysis, as the oxygen vacancies imply that molecules adsorbed on the surface of the material can be oxidised or reduced. Its oxygen storage capacity was first proposed in 1976 when Gandhi *et al.* [86] described how CeO_2 is able to take up oxygen when there is excess in the gas phase, and then give it back to metal particles when the amount of oxygen is greatly reduced. It has been used heavily as a catalyst in a vast number of different chemical reactions. For example, it has exhibited high catalytic properties for the dehydration of alcohols to give an alkene [83, 87, 88]. Also, many examples of hydrogenation reactions have been studied as the cerium atoms can easily interchange between Ce^{4+} and Ce^{3+} under varying conditions to allow electron donation to other molecules. Other reactions where CeO_2 has been shown to exhibit catalytic properties are hydrogen transfer reactions [89], aldol condensation [90], synthesis of carbonates [91], substitution reactions [92] and also for the treatment of exhaust gases [93]. It has also been shown that in association with other catalysts, such as Pt, CeO_2 is able to convert CO to the far less toxic CO_2 species, which can be used in automotive applications as part of a catalytic converter [94]. In addition to CO oxidation, CeO_2 catalysts can also be used to reduce NO_x emissions in the exhaust stream from engines [95]. All of these reactions are useful in industry so it is, therefore, not surprising that cerium oxide chemistry is currently so popular.

CeO_2 is the most stable structure of cerium oxide at room temperature, however, Ce_2O_3 also exists and is used in the CeO_2/Ce_2O_3 cycle. This process is used for water splitting which produces hydrogen with the amount of hydrogen produced increasing as temperature is increased. It is potentially very useful but there is one problem with the reaction: CeO_2 is partially vaporized during the reduction step at pressures of 0.1-0.2 bar and temperatures of 2,000 °C, which reduces the amount of H_2 evolved in the process [96]. Studies carried out by Abanades *et al.* [97] have sought to carry out the process at lower temperatures in order to increases the yield of H_2 produced. This could be a viable way of producing clean energy, which given the global environmental and fuel problems we face today is of utmost importance. The crystal structure of Ce_2O_3 is shown in Figure 1.16. It has a hexagonal unit cell where the oxygen atoms are packed in a cubic structure and the cerium atoms sit in the octahedral holes.

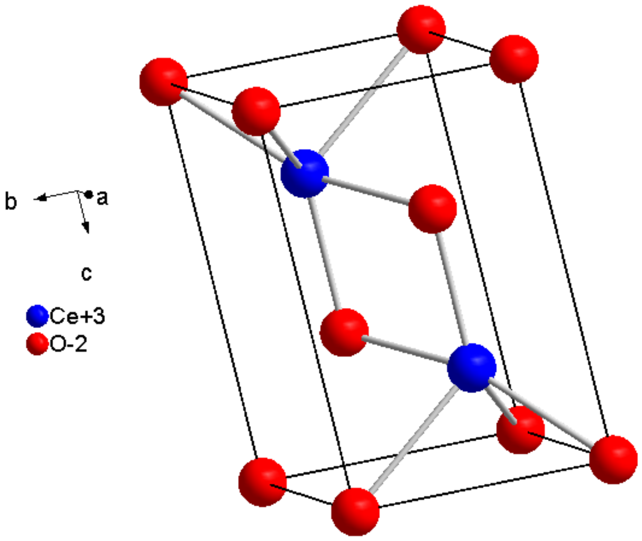

Figure 1.16. The crystal structure of Ce_2O_3 as viewed in-between the a and b axes. [98]

Many other elements are often doped into CeO_2 to take advantage of its oxygen storing properties and combine it with useful properties of other metals. For example, Gregori *et al.* [1] have observed that adding a small amount of boron to nanocrystalline CeO_2 can improve its electrical conductivity properties by one order of magnitude. This is due to the boron ions sitting at the grain boundaries of the CeO_2 crystals and facilitating the movement of charge. Dziembaj *et al.* [99] have looked at using copper as a dopant and how that affects the catalytic properties of CeO_2. They found that the Ce-Cu crystals did exhibit catalytic behaviour for methanol and ethanol oxidation but the efficiency of the catalyst was dependant on the loading of copper in the structure. The copper ions were found to distort the fluorite structure of CeO_2 and depending on the amount of dopant it could improve or inhibit the catalytic properties of the material. Gadolinium doped CeO_2 has been investigated by Endler-Schuck *et al.* [100] to see how its properties are altered for use in solid oxide fuel cells. It was discovered that by doping the ceria with Gd, the resistivity of the material is increased due to defects in the lattice. There are many more examples of doped ceria materials with useful properties in the literature.

1.3.5 Mixed metal oxides

This purpose of this project is to investigate mixed metal oxides of bismuth, niobium and cerium. Several combinations of these metal oxides have previously been synthesised, although it is still a relatively unexplored area.

Over the past 60 years, several studies have been carried out in the Bi_2O_3-Nb_2O_5 system. This is because the δ-Bi_2O_3 structure can be stabilised by doping with niobium ions, yielding a solid solution. The solid solutions have high ionic conductivity due to oxygen vacancies in the fluorite structures. The β-$BiNbO_4$ structure is the most studied form of mixed bismuth-niobium compositions. It was first synthesised by Aurivillius [101] in 1951 and then subsequently in the 1960's by Roth and Waring. The β-$BiNbO_4$ structure that Aurivillius examined was the high temperature phase, which appears at 1373K. Later investigations by Roth and Waring [102] found that in addition to the triclinic form of $BiNbO_4$, there was a low temperature orthorhombic structure. Further studies [103] on the Bi_2O_3-Nb_2O_5 binary system found that the structure consisted of sheets of NbO_6 octahedra separated by bismuth ions. The octahedra are linked via four vertices leaving two free. This is an unusual structure as the sheets are furrowed. The crystal structure can be seen in Figure 1.17.

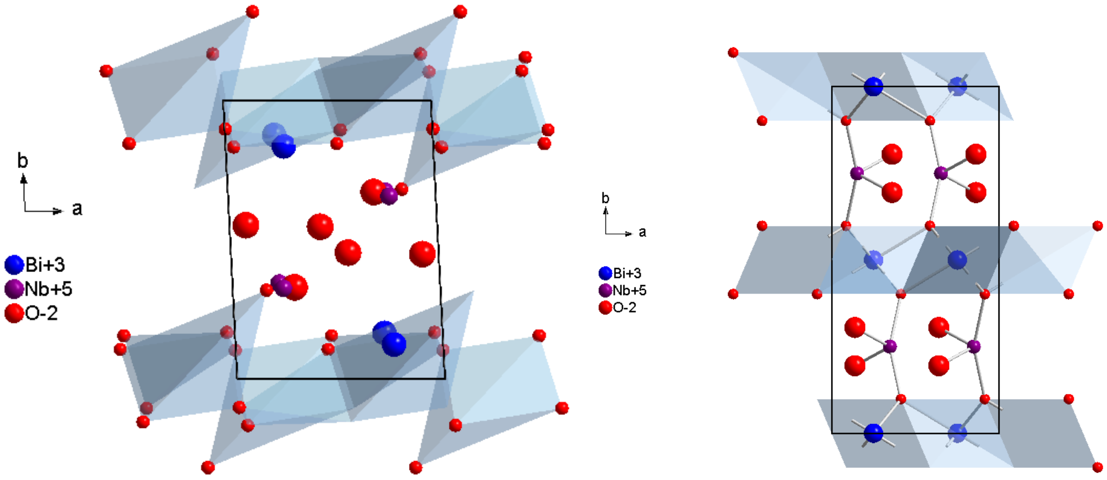

Figure 1.17. Crystal structures of $BiNbO_4$ as viewed along the c axis. The triclinic form of $BiNbO_4$ is seen on the left. [104, 105]

The theory of a continuous solid solution system across the range of Bi_2O_3-Nb_2O_5 compositions was later modified by Zhou *et al.* [106] in the 1980's, who found four distinct structure types within the system using high-resolution transmission electron microscopy (HRTEM). The four structure types were fully analysed to see how the δ-Bi_2O_3 structure adapted to cope with the increasing niobium ion concentration. The most prevalent phase found in this system was the so-called type II phase based on a pyrochlore structure arrangement of the niobium atoms with the bismuth atoms in a defect fluorite environment. The ratio of Bi:Nb in this structure was found to be 4:1. The pyrochlore structure is derived from the fluorite structure by the removal of oxygen atoms and has the general formula $A_2B_2O_7$ or $A_2B_2O_6$ where A and B are cations. The type III phase was also studied in detail and was found to be a composite phase of perovskite, pyrochlore and fluorite units, with a general formula of $7Bi_2O_3.3Nb_2O_5$. The perovskite structure is body centred cubic with the general formula of ABO_3. The crystal structures for both pyrochlore and perovskite can be seen in Figure 1.18.

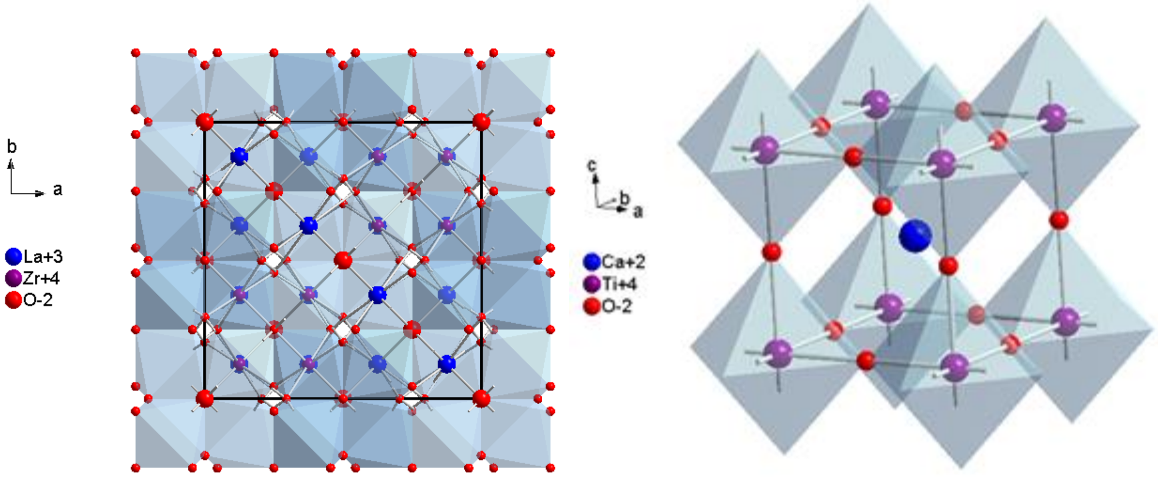

Figure 1.18. Crystal structure of pyrochlore (left) and perovskite (right). [107, 108]

There have also been two other distinct structure types found within the Bi_2O_3-Nb_2O_5 system, Bi_3NbO_7 and $Bi_5Nb_3O_{15}$. The first of these, Bi_3NbO_7, can exist in two phases, as a distorted fluorite structure (type II) or as a tetragonal (type III) phase (see Figures 1.19 and 1.20 for crystal structures). The fluorite type structure has disordered oxygen vacancies, making it a potential ionic conductor.

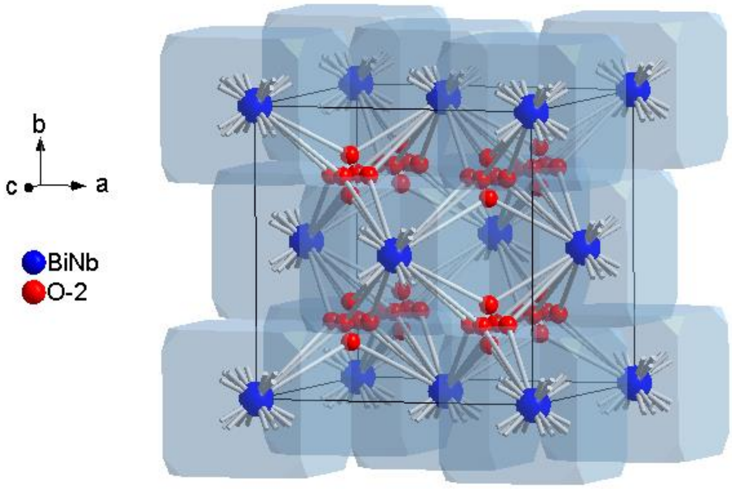

Figure 1.19. Crystal structure of the distorted fluorite structure (type II) Bi_3NbO_7 phase as viewed between the a and c axes. [109]

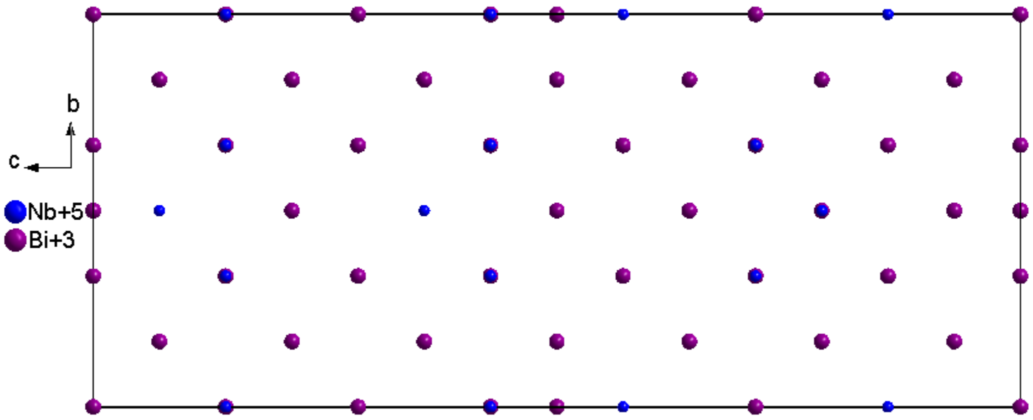

Figure 1.20. Crystal structure of the tetragonal (type III) Bi_3NbO_7 phase as viewed down the a axis. [110]

Bi_2O_3-Nb_2O_5 materials have been of particular interest in research as they have shown photocatalytic properties. Wang *et al.* [111] have reported a low temperature synthesis of Bi_3NbO_7 in nanoparticulate form with the particles being able to evolve H_2 from water using visible light. They also demonstrated how the Bi_2O_3-Nb_2O_5 catalyst could be used for the degradation of organic contaminants. Both of these reactions could prove very useful in industry.

There has been less research into the $Bi_5Nb_3O_{15}$ structure as it is more difficult to synthesise. Its crystal structure can be seen in Figure 1.21. This phase was originally thought to have an Aurivillius-type layered structure [112], however, results from Gurunathan and Maruthamuthu [113] have shown it to have a distorted pyrochlore structure from XRD results. These authors have conducted further studies on $Bi_5Nb_3O_{15}$ and obtained promising results in using it as a photocatalyst for the production of hydrogen in the presence of methyl viologen.

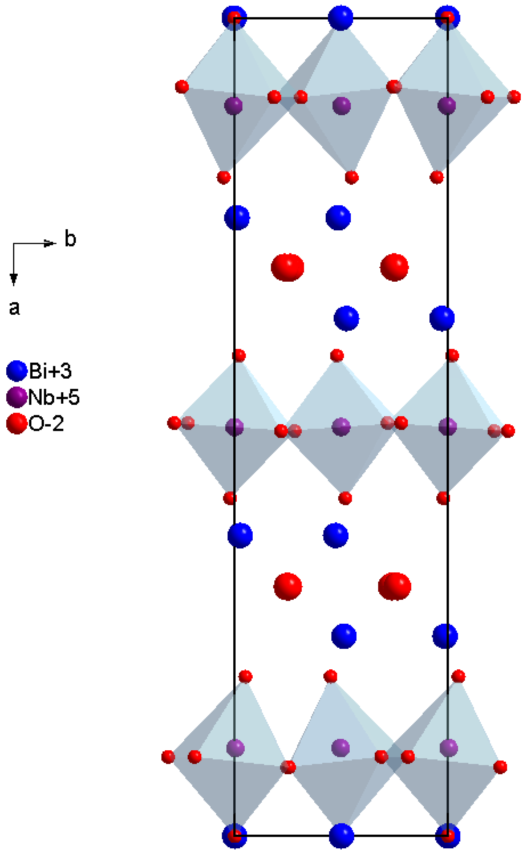

Figure 1.21. Crystal structure of the orthorhombic $Bi_5Nb_3O_{15}$ structure as viewed along the c axis. [114]

In the CeO_2-Nb_2O_5 system there has been one reported stable structure, that of $CeNbO_4$. This structure was explored in detail in the 1970s by several research groups including Negas *et al.*, Roth *et al.*, Cava *et al.* and Santoro *et al.* [115-118].

It was found, using neutron diffraction methods, that the cerium ions form two interpenetrant tetrahedra bonding a total of 8 oxygen atoms. The niobium ions also form a distorted tetrahedron by binding four oxygen ions with all of the Nb-O bonds having the same length. The 8 Ce-O bonds have two distinct bond lengths. Santoro described this monoclinic distorted Scheelite structure as an intermediate between the Scheelite and fluorite structures. The Santoro crystal structure of $CeNbO_4$ can be seen in Figure 1.22.

Skinner *et al.* [119] investigated this structure in 2003, in order to observe how the structure changed at high temperatures if the oxygen stoichiometry remained constant. It was hypothesised in the 1970s that the structure would oxidise above 847 K with a concomitant structural transition. The interest in this research was again mainly due to the potential application of $CeNbO_4$ in solid electrolytes for SOFCs if oxygen interstitials were apparent in the high temperature structure. However, the evidence suggested that the high temperature polymorph was stoichiometric and no oxygen interstitials were observed.

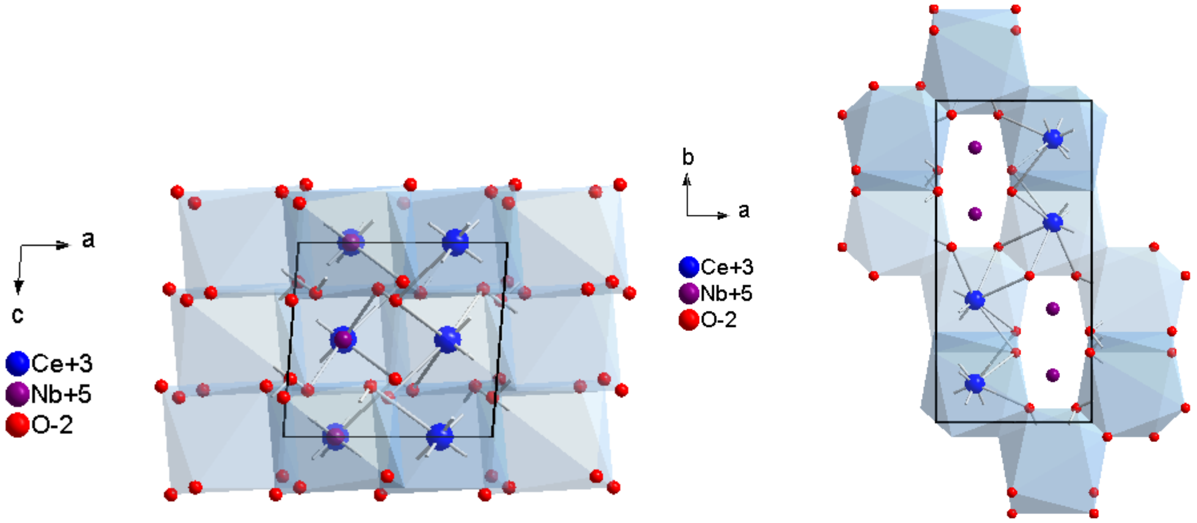

Figure 1.22. Crystal structure of $CeNbO_4$ as viewed along the b and c axes. [118]

$CeNbO_4$ is of particular interest in research due to its variety of oxygen stoichiometries. Cerium niobate can exist as $CeNbO_{4+\delta}$ where δ can equal: 0, 0.08, 0.25 and 0.33 [117, 119-120]. This range of oxygen vacancies has generated interest for application as components in solid oxide fuel cells. The charges in the lattice are balanced by a change in the oxidation state of some cerium atoms from +4 to +3. The extra oxygen atoms must be accommodated in interstitial sites. Stošić *et al*. [121] have looked into the CeO_2-Nb_2O_5 system as a whole in order to identify any new materials with catalytic properties, looking towards uses in green-catalysis. To deduce the catalytic abilities of the newly synthesised materials, they were tested as catalysts in the fructose dehydration reaction. They found that all compositions of the CeO_2-Nb_2O_5 samples were catalytically active, with the more niobium rich samples giving the best results. They also established that the surfaces of the sample were niobia rich, which would have strongly contributed to the catalytic properties.

Within the Bi_2O_3-CeO_2 system, there has only been one reported stable structure, Ce_2BiO_2, which was first discovered by Benz in 1971 [122]. He found that the Ce_2BiO_2 adopted a body centered tetragonal structure. The crystal structure can be seen in Figure 1.23. This pnictide compound was thought to be stabilized by the presence of both Ce^{+3} and Ce^{+4}, with the bismuth in the –3 state. However, more recent studies have shown that the cerium exists exclusively in the +3 state in this compound and more generally the rare earth metal in other metal pnictides is always in the +3 state [123].

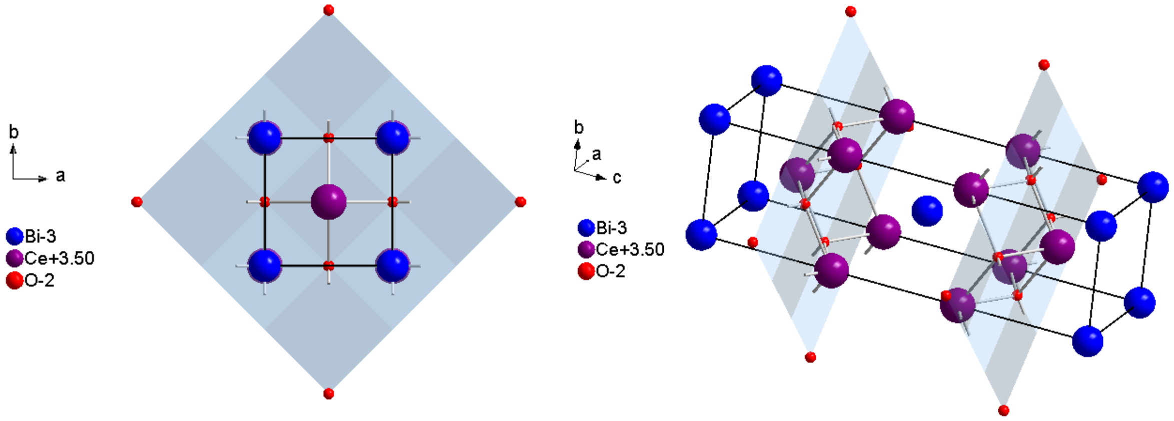

Figure 1.23. Crystal structure of Ce_2BiO_2 *as viewed along the c axis (left) and in-between the a and c axes (right). [122]*

In addition to studying the crystal structure of Ce_2BiO_2, much work has been carried out on bismuth doped ceria. There is interest in this area, as doping the ceria structure with bismuth, introduces oxygen vacancies to balance the charges, as well as introducing structural distortion due to the preference of Bi^{3+} to have unsymmetrical coordination. These factors encourage oxide ion migration, which is advantageous for use in SOFCs. Recently, Beckers *et al*. [124] have found that doping ceria with 10% bismuth results in a highly efficient catalyst for hydrogen combustion. Chen *at al*. [125] carried out extensive studies in the Bi_2O_3-CeO_2 system and found that across their wide compositional range, CeO_2 was present in all samples indicating that a solid solution was not formed. Although several studies into the Bi_2O_3-CeO_2 system have been carried out, complete structural investigations have not been undertaken.

At this present moment, there have been no studies carried out on the quaternary Ce-Nb-Bi oxide system. This research hopes to investigate the possible structures and phases existing within the system.

1.4 Objectives

The objectives for this project are outlined below:

1. To synthesise a variety of compositions of oxide nanoparticles containing Ce, Nb and Bi. In particular to attempt to synthesise quaternary oxides with nanoparticles containing all three metal ions.
2. To analyse these nanoparticles, both structurally and compositionally, using HRTEM, PXRD, EDS and XPS.
3. To investigate what crystalline (or non-crystalline) phases were present in the resulting nanoparticles and, hence, to form deductions about the atomic arrangements present.
4. To construct model particles and then to run computational simulations of these nanoparticles to compare with the experimental results.

2. Characterisation techniques

The purpose of this chapter is to discuss the background theory of the analytical techniques used in the characterisation of the samples prepared for this thesis. As is described subsequently in Chapter 3, the preparation of mixed oxide nanoparticles is almost certainly not a procedure which occurs at chemical equilibrium. Consequently, the products of these syntheses are rarely homogeneous. Structural and chemical characterisation of the products is therefore difficult, and as the particles produced are sub-100 nm dimensions, this requires techniques having relatively high spatial resolution. For this reason, the majority of the structural analysis was carried out using high resolution transmission electron microscopy (HRTEM), and the compositional data was obtained via microanalysis using energy dispersive X-ray spectroscopy (EDS). Although very effective, both of these techniques suffer from the disadvantage that they do not necessarily give an average view of the sample as a whole. This is due to the analysis of several specific particles within a sample of hundreds of thousands of individual particles. For this reason, all specimens were examined also using powder X-ray diffraction (PXRD). In order to ascertain whether the surface composition of the particles was the same as their bulk, X-ray photoelectron spectroscopy was also performed on selected specimens. For experimental reasons this procedure cannot be performed on a micro-analytical scale: consequently XPS results could only be compared with average bulk compositions taken over a large number of particles.

This chapter also includes discussion of data collection on each of the instruments used and how this data was subsequently analysed. Whilst effort has been made to present an in depth assessment of the techniques, it is impossible to discuss every aspect of the background theory and operation of the instruments. Therefore, the chapter may be limited in some areas. For a more complete understanding of transmission electron microscopy, energy dispersive X-ray spectroscopy, powder X-ray diffraction and X-ray photoelectron spectroscopy, please see the following texts respectively: ‘Transmission Electron Microscopy: A Textbook for Materials Science’ by D.B. Williams and C.B. Carter [126], ‘Quantitative Electron-Probe Microanalysis’ by V.D. Scott and G. Love [127], ‘Fundamentals of Powder Diffraction and Structural Characterization of Materials’ by V. Pecharsky and P. Zavalij [128], and ‘Practical Surface Analysis: Auger and X-ray photoelectron spectroscopy’ by D. Briggs and M.P. Seah [129]. The transmission electron microscopy and EDS discussion is based heavily on lectures notes and personal communication with Dr. D.A. Jefferson.

2.1 High-resolution electron microscopy (HRTEM)

2.1.1 Theory

Transmission electron microscopy is a powerful technique, allowing the imaging of materials on an atomic scale due to the small de Broglie wavelength of the electron beam. As electrons are described in quantum-mechanics as having wave-particle duality, they can be diffracted in the same manner as light. The following relationship determined by de Broglie relates the wavelength of an electron to its momentum:

$$\lambda = \frac{h}{\rho} \tag{2.1}$$

Where λ is the wavelength, h is Planck's constant and ρ is the momentum of the object. The larger the momentum of the electron, the shorter its wavelength. In the HRTEM, the electrons are accelerated through a high voltage meaning they attain a large momentum and therefore, an extremely small wavelength. This makes the wavelength of the electrons comparable to the size of an atom meaning materials can be imaged at this scale. The use of electrons for diffraction of a specimen allows the resolution limit to be increased from 0.2 μm, the maximum resolution of a light microscope, to 0.05 nm in a HRTEM.

Imaging in the HRTEM is achieved by the interaction of the high energy electron beam with a thin specimen. As electrons are charged, their path can be manipulated by a magnetic field. Hence electrons can be focussed to form an image. As the beam passes through the specimen, the electrons interact with the sample and are scattered by the crystal planes. An image is formed from the interference of these interactions and is focussed by electromagnetic lenses on a fluorescent screen. It is only the elastically scattered electrons that contribute towards the final image, not the electrons which lose energy. A schematic diagram of a standard transmission electron microscope is seen in Figure 2.1.

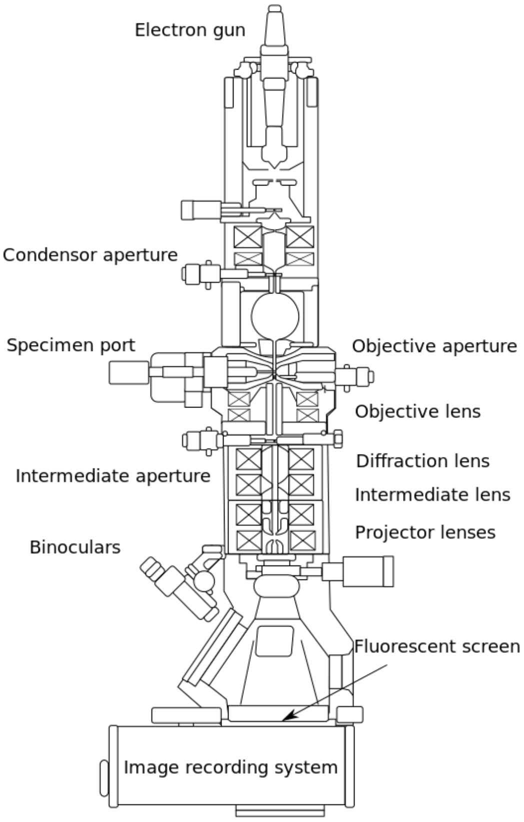

Figure 2.1. Schematic diagram of a transmission electron microscope.

The electron gun is the source of electrons used to pass through the column and specimen. Two types of electron gun are used in modern HRTEMs. These are thermionic emission guns and field emission guns (FEG). The thermionic emission gun is composed of a material which, when a current is applied and the material heats up sufficiently, will release electrons by thermionic emission. Common materials used as a filament in the electron gun are tungsten or a crystal of LaB_6. Both of these emission sources were used for collection of data included in this thesis. The FEG is composed of a very thin sharply pointed material such as a tungsten crystal or a single carbon nanotube. Electrons are emitted from the material due to the potential gradient between the filament and nearby electrode. Once the electrons are emitted by the filament, they are collected and focussed by the Wehnelt cap which focusses the electrons into the column, see Figure 2.2. The column is under high vacuum (1×10^{-3} to 1×10^{-9} Torr) at all times to prevent electron collisions with air molecules.

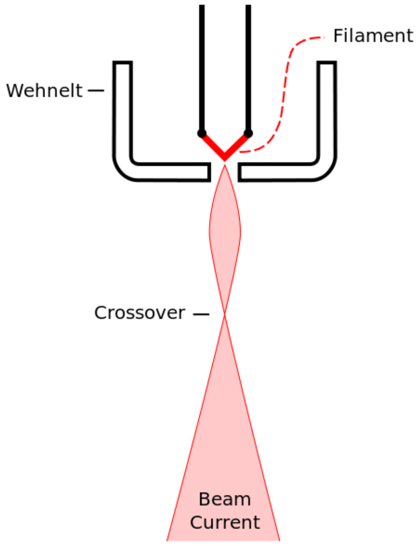

Figure 2.2. Schematic diagram of the electron gun and Wehnelt cap directing the electron beam.

The ultimate resolution of any electron microscope is determined by the wavelength of the radiation used, and if the Rayleigh criterion is used this gives a figure of:

$$\mathrm{d}_{min} \approx \frac{\lambda}{2} \qquad (2.2)$$

In practice, however, this is only true if the radiation is completely monochromatic and for an electron gun this can never be so, as there is inevitably an energy spread arising from the Fermi-Dirac distribution of electron energies, which causes a blurring of the image. As the energy spread is a function of the emitter temperature, then the FEG, which can operate at much lower temperatures, is intrinsically capable of higher resolution.

The electron beam is then directed through various electromagnetic lenses, as well as the specimen, before an image is formed. There are three types of lenses in a HRTEM: the condensor lens, the objective lens and the projector lens. The condensor lens forms the primary electron beam after the electrons are emitted from the gun. The objective lens focusses the beam after it has penetrated the specimen and the projector lens expands the beam to form a magnified image.

As the electron beam can be described mathematically as a wave, after it has passed through the specimen its wave amplitude can be written as follows:

$$\Psi_0\left(\underline{r}\right) = \exp[i\sigma\phi\left(\underline{r}\right) \exp\left[-\eta\left(\underline{r}\right)\right] \qquad (2.3)$$

In this expression, the first exponential term corresponds to the phase contrast, which is the elastic scattering and phase retardation, while the second exponential term refers to the amplitude contrast where electrons lose energy and are hence removed from the elastic image. Therefore, the specimen can be described as a phase/amplitude grating. The interaction parameter σ depends on the electron wavelength and (ϕ) is the electrical potential in the specimen. The absorption coefficient η $(\underline{r})$ depends on the local structure. Heavier atoms produce stronger diffracted beams and contribute more to the amplitude contrast so tend to show up more clearly. If a very thin specimen is being analysed, the above expression can be expanded to neglect all terms higher than the first one. This is the weak phase/amplitude approximation and can be written as follows:

$$\Psi_0\ (r) \approx 1 + i\sigma\phi(r) - \eta(r) \tag{2.4}$$

It follows that the amplitude in the diffraction plane is given by the Fourier transform of Ψ_0 (r), leading to the following expression:

$$\Psi_{\mathrm{D}}(S) = \mathrm{FT}\ [\Psi_0\ (r)] = \ \delta(0) + i\sigma V(S) - \ \Omega\ (S) \tag{2.5}$$

Where $\delta(0)$ is a delta-function of unit weight at the origin, $V(S)$ is the Fourier transform of $\phi(r)$ and $\Omega\ (S)$ is the transform of $\eta(r)$. In the case of a perfect lens, the image is then recorded at the Gaussian focus. However, the main problem with the HRTEM is spherical aberration in a real lens. This means that the lens is not perfect and off-axis electrons are bent more sharply towards the Gaussian image plane than in a perfect lens. This occurs because the electrons are temporarily accelerated by the magnetic field in the electromagnetic lens and because the lens must have a hole at its centre to allow the electrons to pass through, the maximum field strength is slightly to one side of the optic axis of the lens. When the electrons reach the image plane, therefore, they have undergone an additional phase change, which consequently gives a ‘disc of least confusion’, rather than a single point, which is the case in the perfect lens. The radius of the disc is given by the following expression:

$$\Delta r_c = MC_s\alpha^3 \tag{2.6}$$

Where M is the magnification of the lens, C_s is the coefficient of spherical aberration and α is the scattering angle of the off-axis ray. A diagram illustrating spherical aberration can be seen in Figure 2.3. The complete phase shift introduced from both spherical aberration and defocus, which is where the focal length is increased and causes a non-axial ray to be brought to the optic axis further away from the specimen, can be described by Scherzer’s formula, which is as follows:

$$\chi(\alpha) = \frac{2\pi}{\lambda}\left(\frac{1}{2}\,\Delta F\alpha^2 - \frac{1}{4}C_s\alpha^4\right) \tag{2.7}$$

ΔF is the distance between the focal length of the lens and the Gaussian image plane. If S is defined so that:

$$|S| = \frac{2\sin\theta}{\lambda} \approx \frac{\alpha}{\lambda} \tag{2.8}$$

The when α is small, the following expression is valid:

$$\chi(S) = \frac{2\pi}{\lambda}\left(\frac{1}{2}\;\Delta F\lambda^2\,|S|^2 - \frac{1}{4}C_s\lambda^4|S|^4\right) \tag{2.9}$$

By multiplying the diffracted amplitude by a phase factor, $\exp\big(i\chi(S)\big)$, the effect of the phase shift can be represented as follows:

$$\Psi'_{\mathrm{D}}(S) = \delta(0) + [i\sigma\mathrm{V}\,(S) - \Omega(S)]\exp\big(i\chi(S)\big) \tag{2.10}$$

The Phase Contrast Transfer Function (PCTF) for a real lens is represented as $\chi(S)$. The new image intensity can then be calculated from this by expanding $\exp(i\chi(S))$ as real and imaginary parts. This gives the image intensity as:

$$I_I(r) = 1 - 2\sigma\phi\,(r) * \mathrm{FT}[sin\,\chi\,(S)] - 2\eta(r) * \mathrm{FT}[\cos\chi\,(S)] \tag{2.11}$$

This is the so-called ‘Weak Phase/Amplitude’ approximation.

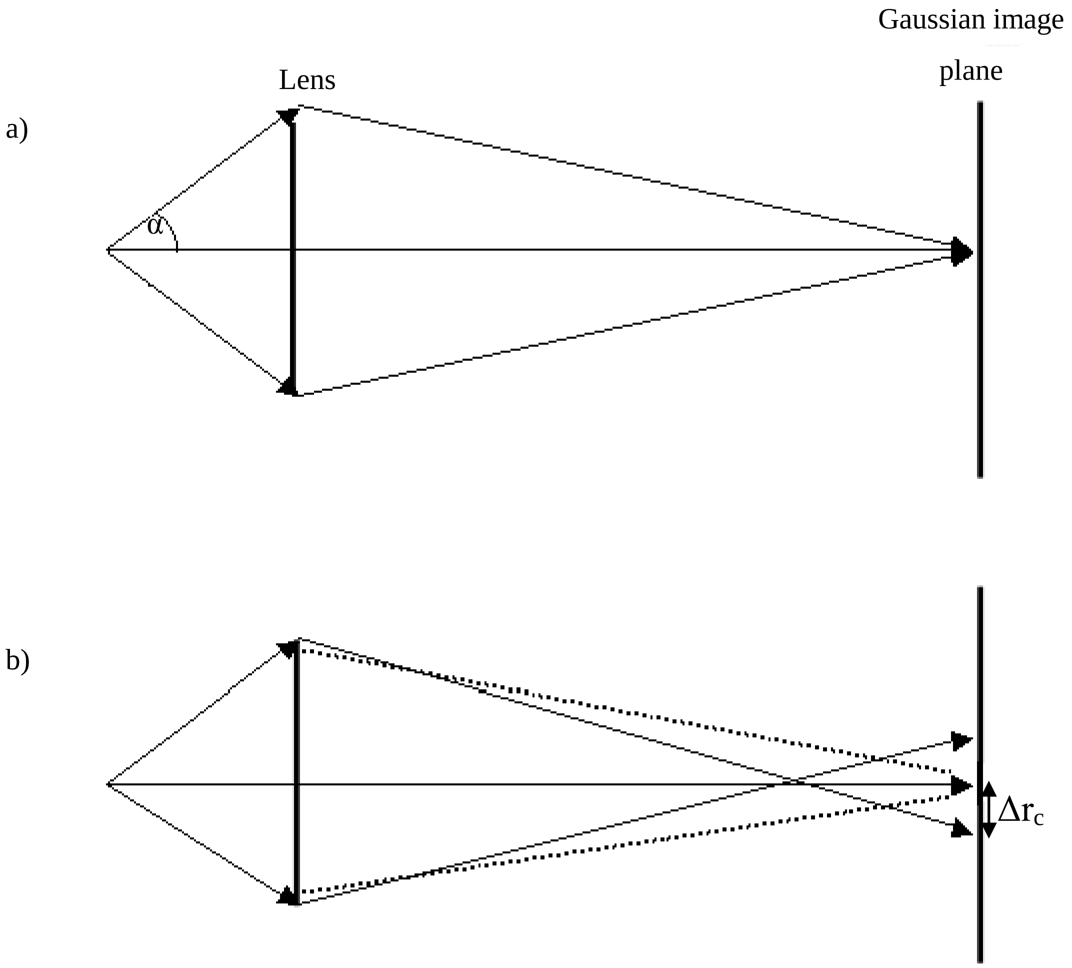

Figure 2.3. Diagram showing the off-axis rays in a perfect lens (a) and a real lens suffering from spherical aberration (b). [Adapted from DAJ lecture notes]

To analyse the effects of spherical aberration and defocus on the image intensity, the power spectrum can be used. This is the Fourier transform of the image contrast. The expression representing the power spectrum is as follows:

$$P(S) = \mathrm{FT}[I_I(r)] = \delta(0) - 2\sigma V(S)\sin\big(\chi(S)\big)\sum \delta\,(S) \qquad (2.12)$$

Where $\sum \delta\,(S)$ is an array of delta functions with weight $|2\sigma V(S)\sin(\chi\,(S))|$. It contains only the electron beams that contributed to the image. The image contrast is maximised at a defocus of 400 Å, where a positive plateau occurs in sin χ (S). Within the plateau the effects of spherical aberration and defocus practically cancel leaving a large number of diffracted electron beams with their correct relative phase shifts contributing to the contrast. This optimum focus position is known as the Scherzer focus [130].

2.1.2 Experimental details and analysis of HRTEM data

High Resolution Transmission Electron Microscopy (HRTEM). Analysis was carried out on a JEOL JEM-3011 electron microscope operated at 300 kV. This machine was fitted with a high-resolution pole-piece (Cs = 0.6 mm, Cc = 1.2 mm) giving an interpretable point resolution of ca. 1.64 Å. Samples were prepared for analysis by grinding under acetone to produce a fine powder before forming a suspension of each sample in acetone and sonicating for 10 minutes to ensure a disperse sample. Several drops of this suspension were then pipetted onto a carbon coated copper grid (Agar Scientific, 300 mesh) and left to dry before inserting the grid into the microscope.

A Gatan charge-coupled device (CCD) camera system was used for recording images in the microscope. The programme Digital Micrograph was then used to analyse the data and gain more information from the image. The fast Fourier transform (FFT) of the image, also referred to as the Power Spectrum, could be used for fringe spacing analysis as the distance between principle maxima in the FFT directly corresponds to the reciprocal of the lattice d-spacings. Fringes appear as thin white and dark bands in the image, cause by the diffraction of electrons through the specimen. They corresponds to the atomic arrangement in the structure. Crossed lattice fringes are seen when the crystal is orientated close to a zone axis, so that two or more lattice planes intersect. Errors in d-spacing measurements could be calculated from the standard deviation of values indicating the same lattice plane in a number of different particles. From the calculated d-spacings, crystallographic information about the samples could be deduced by comparison to known crystal structures. This is because d-spacings are characteristic of each phase as they depend on the scattering from the lattice planes of the crystal structure. Calculating fringe spacings allows phase identification as they are dependent on the unique arrangement of atoms in a unit cell.

The FFT shows a region of reciprocal space. A crystalline region will show sharp spots in the FFT corresponding to the d-spacings in reciprocal space. These measurements can then be converted back to give lattice spacings in real space. An amorphous region will only show diffuse rings in the power spectrum due to the lack of order in the structure.

2.2 Energy dispersive X-ray spectroscopy (EDS)

2.2.1 Theory

This technique is often used in combination with the HRTEM, as is seen in this dissertation, as it allows the elemental composition of a sample to be seen on a micro-scale. The principle of EDS is that a high-energy beam of electrons, when focussed onto a sample, will eject a core electron from an atom leaving a hole. An electron in an outer, higher energy shell will drop down in energy to fill the hole. The difference in energy between the core electron and outer shell electron is emitted in the form of an X-ray and detected. The energy of the X-ray is indicative of the type of atom it came from due to the quantised energy levels in atoms. Therefore, the elemental composition of a sample is revealed. The electrons in the atoms of the sample are located in different shells, which can be seen in Figure 2.4. The shells are termed K, L, M, N etc., moving away from the nucleus. Each orbital within the shells can hold two electrons.

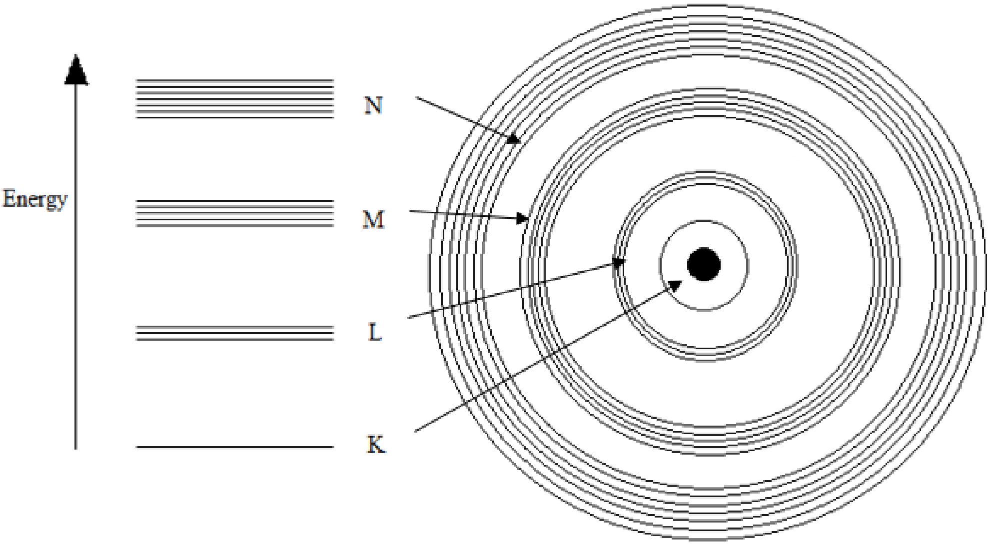

Figure 2.4. The structure of atomic orbitals around a nucleus.

The labels for the radiation given out by the atom follow the form:

- Transitions between the L and K levels = Kα radiation
- Transitions between the M and K levels = Kβ radiation
- Transitions between the M and L levels = Lα radiation
- Transitions between the N and L levels = Lβ radiation

A difference of one level is described as α radiation, two levels is β radiation and a difference of three levels is γ radiation etc.

Although EDS is useful for determining which elements are present in each sample, extra steps are required to make the results quantitative. It cannot be assumed that the integrals of the peaks correspond directly to the elemental composition, therefore, usually the lines in the spectra are compared to those of a standard. Three main factors affecting the peak intensities must be considered when carrying out EDS analysis. The first problem is the Z effect; this is associated with the fact that the electron beam is attenuated more rapidly as the atomic mass increases. Therefore, if a sample of $Mg_xCa_ySi_zO$ is compared with a standard sample of $CaSiO_3$, the sample containing Mg will have a lower average Z value and hence a greater volume will be irradiated in the sample. This means the Ca Kα peak in the sample will be artificially enhanced in comparison with the standard and when calculating the concentration of calcium in the sample, an incorrect value will be obtained. The second common effect is absorption in the sample. This is caused by X-rays emitted by the sample being absorbed by other areas of the specimen on their way to the detector. The degree of absorption is dependent on the energy of the X-rays, and is most pronounced with emission from atoms of low Z, but it also depends on the average Z of the absorbing material. This will also affect the apparent concentration of each element in the specimen. In order to verify if results are being subjected to large amounts of absorption, the intensity ratio between two lines of one element can be calculated, for example the intensity of the M and Lα. This value should be constant. Any analyses with an $I_M/I_{L\alpha}$ ratio lower than the average should be discarded. The third factor found influencing EDS data is the fluorescence effect. This is where X-rays emitted from one atom can subsequently produce X-rays from a different element with a lower Z, whilst the X-ray is absorbed by the second element in the process. This will give the impression in the spectrum that there is more of the second element present and less of the first element. All three effects can significantly affect the results. Due to these factors, as well as the detector's varying sensitivities for each element, it would be incorrect to say that the integral for each elemental peak directly correlates to the elemental composition. Consequently, several steps need to be taken to make the results from EDS analysis quantitative.

In order to account for the detector's variation in sensitivity to different X-ray wavelengths, standard samples of known composition need to be synthesised. From the standard samples, the relative intensities of two emission lines can be calculated. It cannot be said to be the actual composition, as the thickness of the sample is not accurately known. However, as the specimen is normally sufficiently thin (<10 nm) the values of the Z and fluorescence corrections are negligible. Absorption effects still need to be taken into account and analyses that have suffered evident absorption must be discounted.

However, assuming negligible absorption it can be said that for a sample containing magnesium and calcium:

$$\frac{C_{Mg(specimen)}}{C_{Ca(specimen)}} = K_{Mg:Ca} \frac{I_{Mg\ K(specimen)}}{I_{Ca\ K\alpha(specimen)}} \tag{2.13}$$

Where C is concentration and I is the intensity of the comparable X-ray emission lines. $K_{Mg:Ca}$ is a constant, which depends both on the detector sensitivity and on the relative generation efficiency of Mg and Ca X-ray photons. It can be derived from the two standard samples in the following way:

$$K_{Mg:Si} = \frac{2I_{Si\ K(std)}}{2I_{Mg\ K(std)}} \tag{2.14}$$

$$K_{Ca:Si} = \frac{I_{Si\ K\ (std)}}{I_{Ca\ K\alpha(std)}} \tag{2.15}$$

Hence,

$$K_{Mg:Ca} = \frac{K_{Mg:Si}}{K_{Ca:Si}} \tag{2.16}$$

for the standard samples of Mg_2SiO_4 and $CaSiO_3$.

The relative elemental ratios for the specimen can then be calculated. For errors in these calculations to be minimised, analysis of many particles must be carried out. Therefore, approximately 30 particles were analysed for each specimen.

2.2.2 Experimental details and analysis of EDS data

Elemental analysis was carried out using energy dispersive X-ray analysis (EDS). The analysis was performed using the electron beam generated in the high resolution JEOL- 3011 HRTEM with the electron beam probe diameters in the range 500 - 100 Å. A PGT thin-window Si/Li detector with a resolution of 138 eV was employed and the program PGT eXcalibur was used to gather and analyse the EDS data. Integrated intensities of the Bi Lα, Ce Lα and Nb Kα emission lines were calculated for each particle studied and Nb Lα/Nb Kα, Bi Lα/Bi Lβ and Ce Lα/ Ce Lβ ratios were used to monitor effects of differential absorption within the particles. Significant peaks were seen for Cu Kα and Cu Kβ radiation, which were generated from scattered electrons impinging on the copper grid bars as well as from the specimen holder. For collection of the EDS spectrum the specimen holder was tilted 15 ° towards the detector to enhance the 'take-off' angle of the X-rays that are emitted. The X-rays were detected by a solid-state lithium doped silicon detector. Due to the time-lapse for the collection of data, there is a so-called 'dead-time' where X-rays have been emitted from an atom and reached the detector, but have not been recorded. The dead-time is expressed as a percentage of all events which occur. In order to ensure that the data collected is as reliable as possible, the dead-time was kept below 10% at all times (usually less than 5%). This means that very few emitted X-rays from the sample went unrecorded.

To see if the tilt angle affect absorption in the specimen, results were collected for the $Bi_{0.6}Nb_{0.4}$ oxide sample at a tilt angle of 15 ° and a tilt angle 25 °. It was found that the Bi $L\alpha_1$:Bi $L\beta_1$ ratio and the Nb $K\alpha_1$:Nb $L\alpha_1$ ratio was constant with less than a 1% difference in absorption between the two tilt angles.

For each EDS spectrum a background subtraction was performed by PGT eXcalibur before the integrated intensities of the emission lines for the two elements of interest were plotted against each other. The background calculated in PGT eXcalibur was done by performing an artificial intelligence routine, as described by the manufacturers. The process of measuring EDS intensities and creating a plot of the data was repeated for all the EDS spectra recorded for each sample. Fitting a line to this plot then gave some idea of the homogeneity of the specimen, and if the plot could only be fitted to two or more lines, the compositions of the various phases present could be assessed.

In order to assess the reliability of the automatic background correction performed in PGT eXcalibur, a manual background subtraction was carried out on one of the standard bulk samples, with the results of the two methods then being compared.

The $CeNbO_4$ bulk sample was chosen for the analysis comparison due to significant differences in energy of the Ce $L\alpha_1$ and Nb $K\alpha_1$ lines, therefore, an incorrectly fitted background would have a more noticeable effect on the subsequent relative integrated peak areas. A plot of EDS intensities recorded from 30 separate crystals in the bulk sample were plotted, after the PGT eXcalibur background routine had been performed, with the line of best fit giving a gradient of 0.698 and a standard deviation of 5%. The plot can be seen in Figure 2.5. The value of the gradient corresponds directly to the Nb $K\alpha_1$: Ce $L\alpha_1$ ratio. The Nb $L\alpha_1$:Nb $K\alpha_1$ ratio was monitored to check for absorption; values lower than average were discarded.

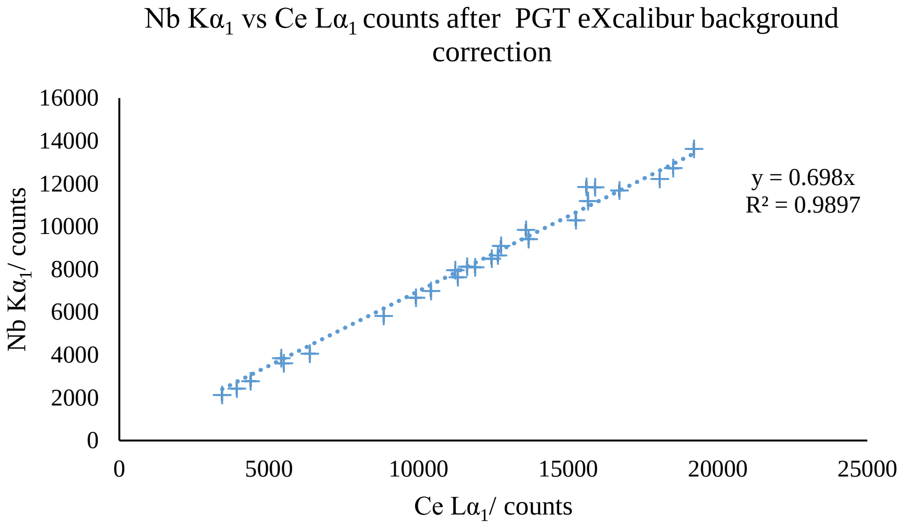

Figure 2.5. A plot of Nb Kα_1 vs Ce Lα_1 counts from EDS data of the CeNbO$_4$ bulk sample. Data points plotted after a PGT eXcalibur automatic background correction.

A manual background estimation and subsequent subtraction was then performed on the data. This was done by firstly using a quadratic smoothing on all spectra to reduce the noise. The spectra were then added together, giving more weight to more intense peaks, and then taking the average. The average plot was then used to fit a background between peaks. A fifth order polynomial was used to get a good fit to the designated background points with an R-value of 0.9118 results, Figure 2.6.

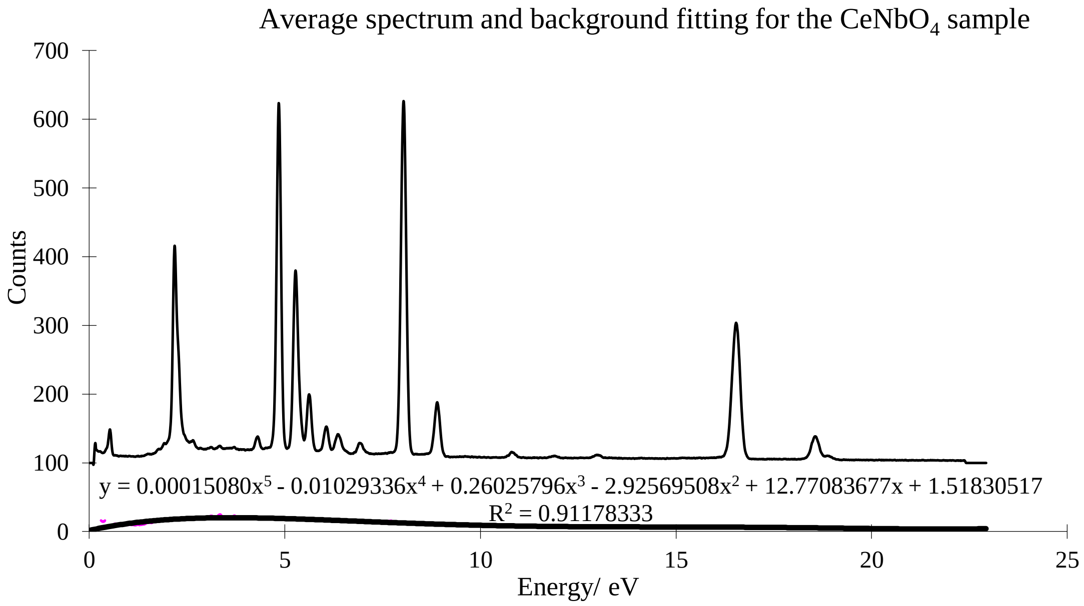

Figure 2.6. Average spectrum for the CeNbO$_4$ sample with a background fitted from a 5th order polynomial.

The calculated polynomial was then subtracted from the average spectrum to give a final plot with the background subtracted, Figure 2.7. From this the final Nb Kα_1: Ce Lα_1 ratio could be calculated by addition of all the channels within the Ce Lα_1 and Nb Kα_1 peaks, and accepted as the average Nb Kα_1:Ce Lα_1 ratio for the data set. This was found to be 0.728, which is in good agreement with the ratio found from the PGT eXcalibur background subtraction data (ca. 1% error).

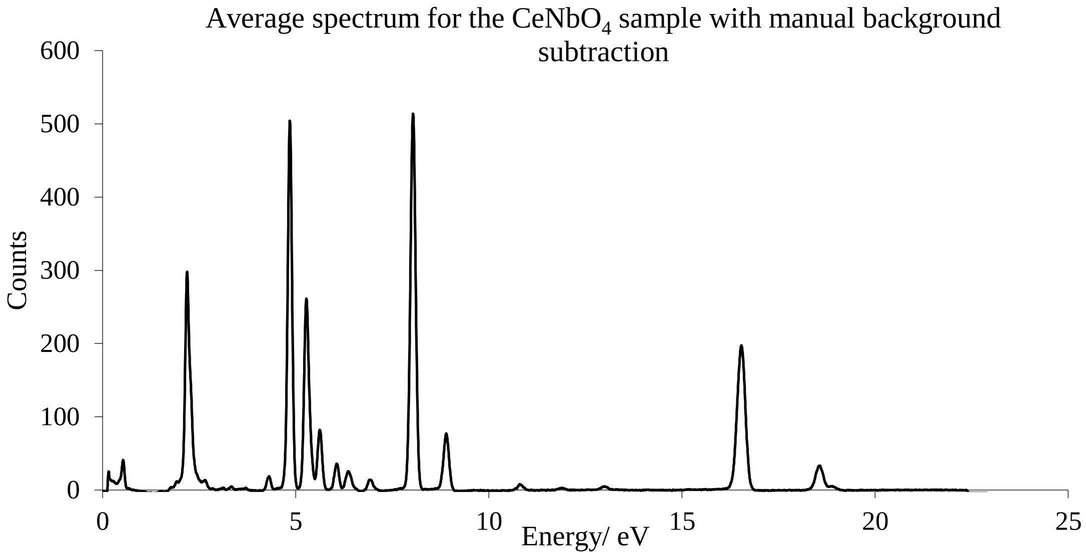

Figure 2.7. Averaged EDS spectrum of $CeNbO_4$ with background subtraction.

Therefore, it was assumed that the PGT eXcalibur background was suitable to use for analysis of EDS data of all samples prepared for this thesis to give reliable results.

2.3 Powder X-ray diffraction (PXRD)

2.3.1 Theory

PXRD is a technique in which a polycrystalline sample is irradiated with X-rays in order to gain information about the phases present in the sample. It is a very useful technique as powder patterns can be produced quickly, giving information about the structure of the sample. The technique works because theoretically every possible orientation of the crystals is present in the specimen. Therefore, the reciprocal lattice will consist of a series of concentric spheres centred on the origin of reciprocal space. Each cone represents each reciprocal lattice point. The angle between the cone and the beam is known as the scattering angle, which is denoted as 2θ. By measuring the diffraction intensity as a factor of 2θ

a diffraction pattern can be built up by rotating the detector through 90 °C. The relationship between 2θ and the d-spacing of the lattice is given by the Bragg equation:

$$\lambda = 2d_{(hkl)} \sin(\theta) \tag{2.17}$$

The pattern produced is specific for each different compound and can show if a sample has a mixture of phases or if only one phase is present. The peaks are then indexed, usually by comparison to known pure phases. However, the main problem with PXRD is the fact that because a three-dimensional reciprocal space is being recorded onto a one-dimensional powder pattern, which then becomes very complicated. There can often be many overlapping lines, which are difficult to resolve. Therefore, assigning the peaks of the powder pattern can be difficult and time consuming.

PXRD is useful for being able to calculate the mean crystallite size of the sample using the Scherrer equation (2.18) for particles < 0.1 µm.

$$\Delta(2\theta) = \frac{k\lambda}{(L \cos\theta)} \tag{2.18}$$

Where $\Delta(2\theta)$ is the full width of a peak at half its maximum height, λ= 1.540498 Å for the PANalytical Empyrean series 2 diffractometer, L is the crystallite size, θ is the Bragg angle and (k) is the shape factor which has a value of 0.88. The errors introduced into the Scherrer equation can be large, as line broadening can also occur as a result of disorder in the crystals and lattice strain.

2.3.2 Experimental details and analysis of XRD data

A PANalytical Empyrean series 2 diffractometer was used to record all PXRD data. Cu Kα radiation (λ = 1.542 Å) was used in all cases. Samples were loaded into the diffractometer in alumina sample holders with sunken circular centers packed with sample. The diffractometer was equipped with an automatic sample changer. Samples were run using 20 minute scans from 5°-80° values of 2θ, with resulting scans being compared to known phases. These were found in the literature and the database provided in the programme X'pert HighScore Plus. For more complicated patterns which contained two or more known phases, Rietveld refinements were carried out using the Full Prof suite. This enabled percentages of each phase in the sample to be calculated as well as lattice parameters and particle sizes.

2.4 X-ray photoelectron spectroscopy (XPS)

2.4.1 Theory

X-ray photoelectron spectroscopy (XPS) alternatively known as electron spectroscopy for chemical analysis (ESCA), is a non-destructive analytical technique used to investigate the surface composition of a material. A complete description of XPS analysis and its applications can be found in Briggs and Seah (1990) [129].

The principle of XPS analysis involves soft X-rays impinging on a sample surface, with the effect of ejecting core electrons from the surface atoms (top 1-10 nm of material). The energy of the X-ray photons is enough to excite core electrons to an extent where they are emitted from the atom. These photoelectrons are energy filtered by a hemispherical analyser (HSA) before the kinetic energies and number of electrons are recorded. The hemispherical analyser is composed of two concentric hemispherical electrodes. The voltage between the two electrodes is calculated as follows, where R_1 and R_2 are the radii of the two hemispheres:

$$V_2 - V_1 = V_0 \frac{R_2}{R_1} - \frac{R_1}{R_2} \tag{2.19}$$

A voltage is applied between the two electrodes, (negative on the outer) and swept to obtain the selected 'pass energies':

$$E_0 = |e|V_0 \tag{2.20}$$

Only electrons with the required energy, E_0, will pass through the exit slit of the HSA and reach the detector. The electrons are dispersed as they travel through the HSA, depending on their kinetic energy. The ejected electrons travel through the HSA to a detector and are recorded based on their kinetic energies. As electrons in an atom are quantised, the recorded electron energies correspond to a specific quantum shell of a particular element. The spectra produced, therefore, show electronic binding energies against counts per second (CPS). From the CPS, an overall surface composition for a sample can be calculated based on the integrated area of the peaks in the spectrum. Although the X-ray beam penetrates the material far deeper than 10 nm, the electrons ejected from a deeper depth are absorbed by surrounding atoms, and therefore, lose energy and only contribute to the background signal rather than well-defined photoelectric peaks. The binding energy is calculated as follows:

$$E_{binding} = E_{photon} - E_{kinetic} + \phi \tag{2.21}$$

Where E_{photon} = the energy of the X-ray photons being used.

$E_{binding}$ = the energy of the core electrons being ejected.

$E_{kinetic}$ = the kinetic energy of the ejected electron measured by the instrument.

ϕ = the work function of the spectrometer.

Typically kinetic energies are measured from 20 eV to 20000 eV. The XPS spectrum produced is a plot of electron counts per second (y-axis) versus the electron binding energy (x-axis), which corresponds to the electron configuration of the atom i.e. if the electron is from the 1s, 2p, 3d orbital etc. For each element, a specific set of photoelectric peaks will be produced to identify that element based on its binding energies. The electron counts for each peak correspond directly to the proportion of that element on the surface of the material. An example of an XPS survey spectrum with quantification regions is seen in Figure 2.8.

Singlet peaks are seen for electrons originating from an s-level orbital. All other orbitals exhibit a doublet peak due to j-j coupling (spin-orbit coupling) of degenerate states. J is a vector sum between the orbital angular momentum (l) and the spin momentum (s). The doublet states are identical apart from their j values.

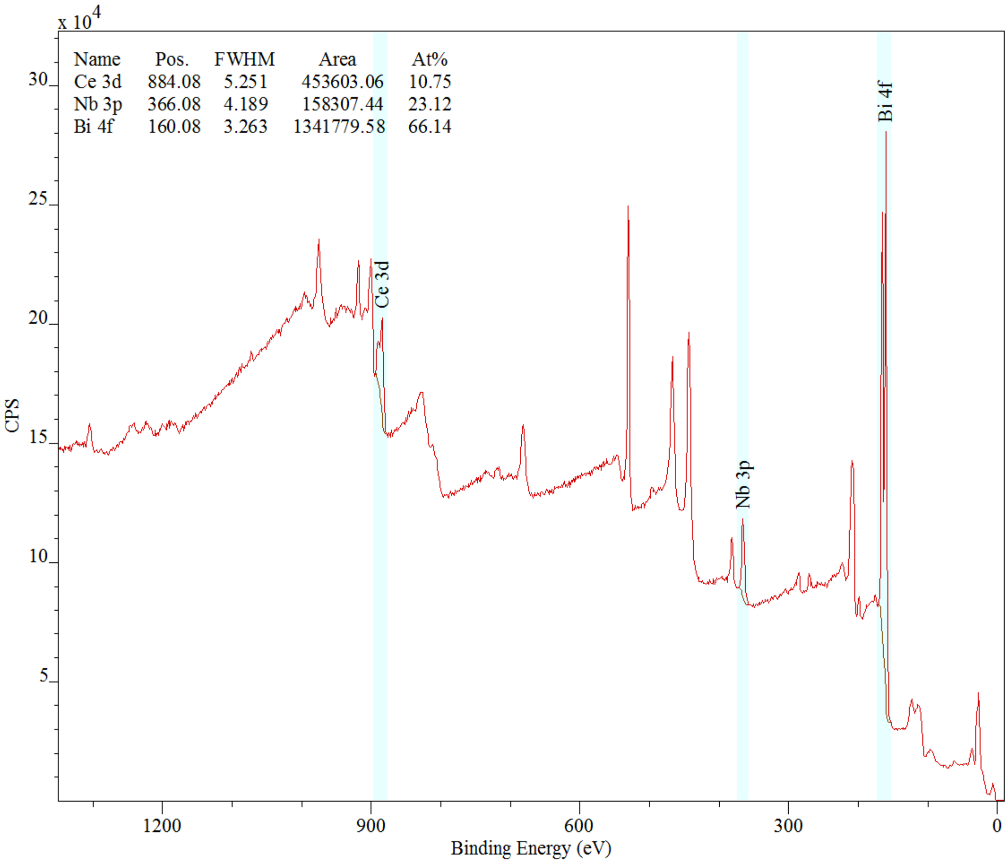

Figure 2.8. An example of an XPS spectrum showing the quantification regions. From these regions, the composition of the surface sample has been determined.

Analysis of the XPS spectrum is carried out using appropriate software, for example Casa XPS. This software is able to directly compare peaks by calculating a background using an algorithm and then subtracting the background from the spectrum. Peak areas are calculated and scaled relative to the total area using relative sensitivity factors. Relative atomic concentrations for the material can then be determined.

More detailed analyses can be carried out using XPS, for example depth profiling. This is where a series of XPS analyses are recorded at different depths of the material. After each XPS measurement a small amount of the material is etched away before repeating the cycle. The result is a series of XPS spectra showing how the material composition changes with depth. This method can be used to record data to a depth of approximately 1000 nm.

2.4.2 Experimental details and analysis of XPS data

- Monochromatic Al Kα X-rays are usually used for irradiating the surface atoms. These X-rays have an energy of 1486.68 eV.
- An ultra-high vacuum is required to prevent the electron undergoing collisions and changing its energy on the way to the detector. Typically the detector is 1 meter away from the sample. The vacuum also prevents sample surface contamination.
- A survey scan, which shows the elements present and how many electron counts from each, takes from 1 to 10 minutes to carry out. A depth profiling experiment can take from 1-4 hours to perform.

All of the XPS data presented in this thesis was carried out at the NEXUS nanoLAB facilities at the University of Newcastle, using the K-Alpha Thermo Scientific XPS spectrometer equipped with a 180° hemispherical analyser. Micro-focussed monochromatic Al Kα (1486.6 eV) was used as the X-ray source. The sample was also charge neutralised throughout the analysis.

For quantitative data to be generated the software Casa XPS was used, with permission of the NEXUS nanoLAB. A Shirley background was calculated for each spectra, which adjusts the background relative to the number of photoelectrons being emitted at each binding energy, and subtracted before the peaks were fitted using a Gaussian-Lorentzian model. Peaks are identified from the binding energies and comparison with the elemental library in Casa XPS. The binding energies were calibrated before quantitative regions were created, which calculated the elemental composition of the surface based on the peak areas. In order to make sure that the relative peak areas did, in fact, correspond to the concentration of each element in the sample, relative sensitivity factors (RSF) were used. These correspond to how likely it will be that an element will lose an electron at a certain energy. All peaks were normalised to carbon which has an RSF of 1. Therefore, the peak area (number of photoelectrons detected) does not necessarily correspond directly to atomic concentration until you divide the area by its RSF.

In addition to the survey scan (seen above in Figure 2.8), high resolution scans of the elemental energies of interest are also collected. In the case of the Ce-Nb-Bi mixed oxide samples these were the bismuth 4f, cerium 3d, niobium 3p and oxygen 1s energy regions. This allows any peak splitting due to different species to be identified, for example Ce^{3+} and Ce^{4+}. Single peaks were seen for oxygen 1s, bismuth 4f and niobium 3p indicating that only one oxidation state of each ion is present. Therefore, it can be assumed that all the bismuth is in the +3 state, the niobium in +5 state and the oxygen in -2 oxidation state.

The high resolution scans for cerium, however, were somewhat complicated by the presence of two oxidation states. The observed 3d peaks for the cerium ions can be grouped in three doublets indicating the presence of both Ce^{3+} and Ce^{4+}. The doublets are produced by the $3d_{3/2}$ and $3d_{5/2}$ splitting for the two species and are labelled as follows in Figure 2.9: u/v; ui/vi; uii/vii; uiii /viii. The $3d_{3/2}$ peaks are seen between 895–916 eV; the $3d_{5/2}$ peaks are seen between 880–895 eV.

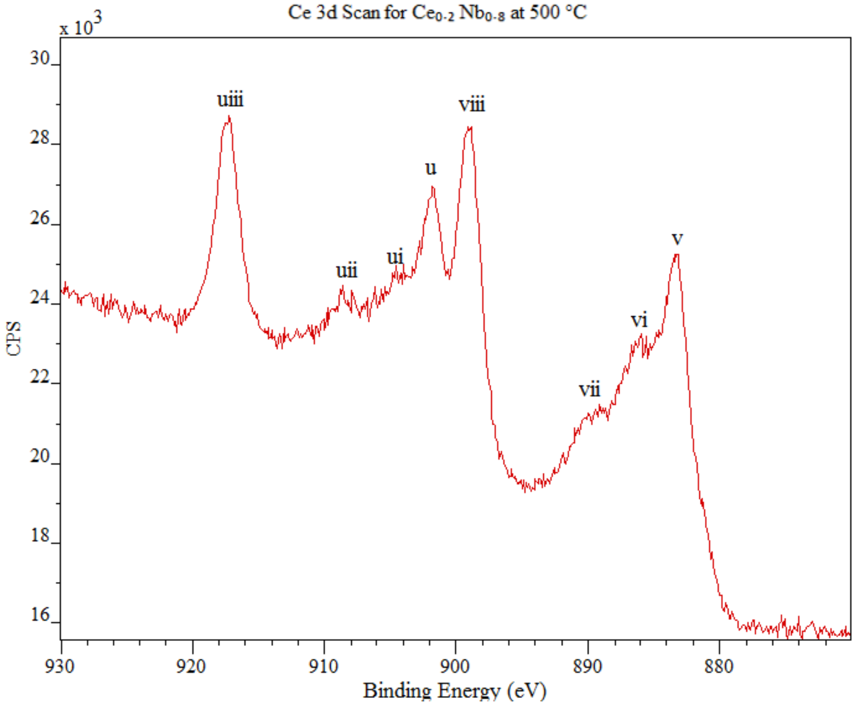

Figure 2.9. Ce 3d scan for the $Ce_{0.2}Nb_{0.8}$ oxide sample after heating at 500 °C showing peak splitting.

The most easily identifiable peak is that at 917 eV, labelled uiii, which is characteristic of the Ce^{4+} species. It has a high binding energy, which is be expected of the species with a higher oxidation state. This is due to the greater attraction felt by the electrons to the more positive nucleus in comparison with the Ce^{3+} species. The doublet peaks labelled uiii and viii are attributed to the Ce^{4+} $3d^9 4f^0 O2p^6$ state. The uii/vii and u/v doublets both originate from the Ce^{4+} $3d_{5/2}$ state, but the former is from the $3d^9 4f^1 O2p^5$ electronic arrangement while the latter is from $3d^9 4f^2$ $O2p^4$. Only one pair of doublets for the Ce^{3+} $3d^9 4f^2 O2p^6$ state can be seen (ui/vi). The second doublet for Ce^{3+} may be lost in the background. The doublets become more resolved with increased cerium concentration as expected. These results correlate strongly to XPS evidence for CeO_2 gathered by Reddy *et al*. [131].

2.4.3 Auger peaks

In addition to peaks generated directly from detection of photoelectrons, several other peaks are seen in the XPS spectrum. These Auger peaks are smaller peaks, which arise as a consequence of a core electron being ejected. The process for the generation of Auger electrons is shown in Figure 2.10. After the first core electron has been ejected by the X-ray photon, an electron with a higher energy drops down to fill the hole. The energy difference between these two electronic states causes a further outer shell electron to be emitted. The resulting atom is doubly ionised and needs to be stabilised by charge compensation during the XPS analysis. The charge is balanced by the instrument introducing low energy electrons to the sample.

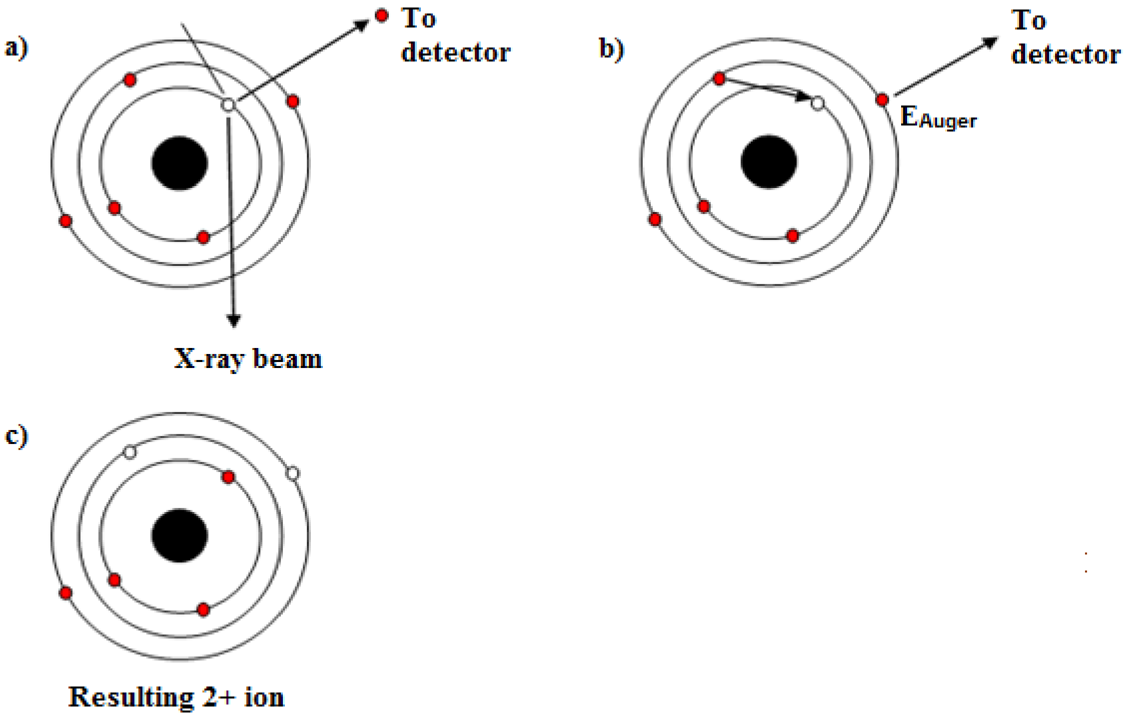

Figure 2.10. Illustration of an Auger electron being generated (b) following ejection of a core electron (a). The resulting 2+ ion is seen (c).

3. Synthetic methods

3.1 Introduction

This chapter discusses the variety of methods employed by chemists to synthesise mixed metal oxides as well as the experimental details of the thesis. There are variety of methods available to chemists for such syntheses including co-precipitation, solid state synthesis, resin-gel methods, sol-gel methods, hydrothermal and solvothermal techniques [132-137], with each method having advantages and disadvantages depending on the desired structural outcome. The synthesis of mixed metal oxide materials have been discussed at length in the literature and other published texts, however, the majority of discussion in this chapter is based on Sakka & Kozuka, (2005) [138].

The more traditional solid state method may be well understood and simple to carry out, but depends on interdiffusion of the various metal ions. This can result in inhomogeneous particles of varying sizes, usually on the micron scale, if temperatures are not high enough. The increased interest in nanoscience over the last century has consequently led to further techniques being developed to produce metal oxide particles on the nanoscale. Methods such as the sol-gel technique have become popular due to the lower experimental temperatures required, this in turn leading to smaller crystallites, and the flexibility of the synthesis means that the method can be adapted to control the particle size and crystal morphology. New techniques are constantly being developed to try and improve the control of crystal growth and the resulting properties of the particles. In recent years, research in the area of solid state chemistry has therefore shifted away from the classic ‘heat and beat’ solid state method and moved towards the solution based techniques, which give more control over the phases produced, as well as the crystal morphology.

The aim of this work was to synthesise nanoparticles of mixed metal oxides. It was immediately apparent that in order for nanoparticles to be synthesised, the solid state method was inappropriate due to the high temperatures required. However, it was a suitable method to synthesise the bulk samples of $BiNbO_4$, $CeNbO_4$ and Ce_2BiO_2. The bulk samples were used as standards for EDS analysis, as their overall composition was known, so that atomic percentages could be calculated accurately for the nanoparticles samples. A resin-gel method was used to synthesis all nanoparticles discussed in this thesis.

3.2 Solid state synthesis

The traditional solid state method (or ceramic method) for the synthesis of mixed metal oxides has been employed by chemists for many years. It involves heating the parent oxides or carbonates at high temperatures (greater than 1000 °C) for varying periods of time until the desired product is formed. Usually the reactants are removed and re-ground several times during the reaction to bring together new surfaces to react and aid diffusion. Sometimes months are required to get sufficient reaction between the starting materials as atoms have to diffuse over large distances. Although this is a very simple method, there are several other disadvantages aside from the slow reaction times. The resulting metal oxide particles can be inhomogeneous due to the presence of unreacted components and crystallite sizes tend to be in the micrometre range due to the high synthesis temperatures leading to sintering of particles. Sintering is a process whereby the atoms in each particle are able to diffuse across the particle boundary towards a neighbouring particle. This process fuses many neighbouring particles together, forming one solid crystal. Obviously at higher temperatures, the rate of diffusion is quicker, meaning particles sinter together more readily. Despite these complications, it is a method still regularly employed in industry as it is very straightforward to synthesise the required crystalline materials with good reproducibility.

3.3 The resin-gel method

The resin-gel method is a variation of the Pechini type polymeric gel method which was developed and patented in 1967 as a way to synthesise thin film capacitors of titinates and niobates [139]. The Pechini method uses citric acid as a chelating agent and ethylene glycol as gelling agent. The citric acid binds the metal ions in solution and stabilises them, preventing any separation of components. A polymer matrix is formed as the ethylene glycol is added due to the polycondensation of the citric acid and ethylene glycol at 100 °C (shown in Scheme 3.1). This restricts the movement of the ions and hence prevents isolation of any metal ions so a homogenous product is formed. As heating continues to 400 °C, pyrolysis of the polymer matrix leaves an amorphous precursor material. All of the organic material is removed from the reaction at this stage. The resulting powder can be a single amorphous or crystalline phase or a mixture of phases, which normally needs to be calcined in air at 400 °C to form a fully oxidised crystalline product. The method is used widely in research today for the synthesis of high temperature superconductors, magnetic materials and metal oxide particles.

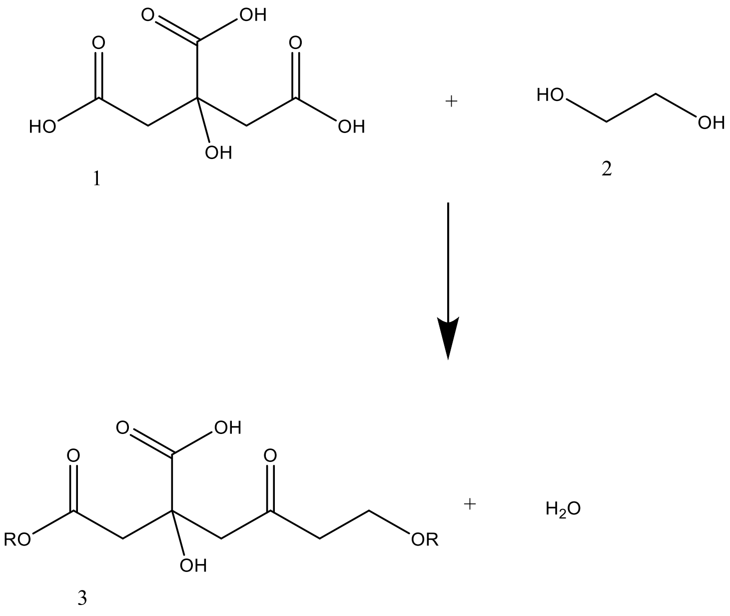

Scheme 3.1. The polymerisation reaction of citric acid (1) and ethylene glycol (2) is shown with the resultant polymer (3) forming the polymer matrix (metal ions chelated to the citric acid not shown).

The resin-gel method, used in the synthesis of nanoparticles in this work, is a modified version of this Pechini synthesis which has been adapted from that used by Li *et al.* [134] to form nanocrystalline particles. The method uses a long chain polymer, which in this research is PEG (mw = 20,000), as the binding agent to coordinate to the metal ions in solution indiscriminately via the oxygen atoms on the PEG. Polyethylene glycol is an ideal polymer for this purpose as it has many binding sites due to its length. In this respect it acts exactly like other potential binding agents such as citric acid and tartaric acid, both of which have been used successfully in producing nanoparticles [140, 141]. Figure 3.1 represents the binding mechanism of the polymer to the metal ions.

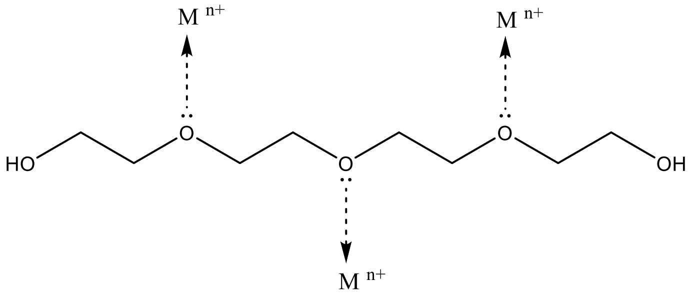

Figure 3.1. Representation of the PEG binding metal ions in solution via the oxygen lone pairs.

When compared with the solid-state method, the resin-gel method has the advantage that the starting materials are mixed at the atomic level so reaction times are much quicker and the homogeneity of the product is better. The PEG is used to chelate the metal ions and bring them in to close contact with one another which encourages a reaction especially when heat is applied. The polymer gel forms a matrix of ions and allows steady mixing of the ions through the matrix at low temperatures (350 °C).

Sol-gel methods have become the most popular choice in recent years for the synthesis of metal oxides as the binding agent and reaction temperatures can be varied depending on the properties required in the resulting particles. In the literature there are a plethora of examples of a ‘sol-gel method’ being used [142-144].

It should be noted, however, that there is a subtle difference between ‘gel’ methods, such as the Pechini synthesis, and a resin-gel method although both are commonly called ‘sol-gel’ methods in the literature. They are named as such due to the increase in the viscosity of the mixture as a polymeric network is formed. The traditional gel method uses an organic molecule such as citric acid to bind the metal ions in solution. After the addition of another organic species (e.g. ethylene glycol), a polycondensation reaction occurs to form a viscous gel. The resin-gel method however, does not require this polycondensation reaction, and any associated chemical processes, to form a gel. The long chain polymer is simply added to a solution of metal ions and binds to them indiscriminately, forming a polymer matrix. As the solvent evaporates, a hard waxy solid is left, which when heated and then ignited, results in the formation of mixed metal oxide nanoparticles.

3.4 Synthesis of standard samples in bulk form

Three bulk samples were synthesised via a solid state method to allow quantitative comparison between the known bulk phases and the nanoparticle phases via EDS analysis. All bulk samples were analysed by PXRD to confirm the target bulk phases had been synthesised before examination in the microscope.

Firstly, $CeNbO_4$ crystals were produced by mixing stoichiometric amounts of CeO_2 and Nb_2O_5 in a ceramic crucible. This was then heated at 1200 °C in a muffle furnace for 4 days. The sample was then removed, ground up with acetone and placed back in the furnace at 1200 °C for 4 days. The ramp rate of the furnace was 5 °C min^{-1} from room temperature up to the required temperature and was then held at this temperature for 96 hours. The same ramp rate was used for all samples.

Bulk $BiNbO_4$ was synthesised by mixing stoichiometric amounts of Bi_2O_3 and Nb_2O_5 and heating in a ceramic crucible for 5 days at 850 °C in the muffle furnace. Similarly, bulk Ce_2BiO_2 was synthesised by mixing stoichiometric amounts of Bi_2O_3 and CeO_2 and heating for 6 days at 850 °C. Samples containing bismuth oxide were heated at a slightly lower temperature to minimise any bismuth loss due to its volatility. Bismuth oxide may be lost to the gas phase from 825 °C [145].

3.5 Synthesis of ternary mixed metal oxides

Bismuth-Cerium Mixed Metal Oxides

The resin-gel technique was used to synthesise the Bi-Ce mixed oxide nanoparticles. Appropriate quantities of $Bi(NO_3)_3.5H_2O$ and $Ce(NO_3)_3.6H_2O$ were dissolved in concentrated nitric acid (40 mL) so as to produce solutions with varying quantities of each metal ion. Nitrates are ideal starting materials as the anion breaks down to produce gaseous products on heating. The samples were made up with the following percentages of bismuth nitrate: 20%, 40%, 60%, 80% dissolved with the following percentages of cerium nitrate respectively: 80%, 60%, 40% and 20%. Samples of pure bismuth nitrate and pure cerium nitrate were also prepared. The samples were left stirring overnight to dissolve in the acid. Polyethylene glycol (PEG mw = 20,000) was then added to each solution. It had been determined empirically that the optimum amount of PEG used was approximately equal to the volume of solvent. After the PEG had been added, the samples were heated to 80 °C until the solvent evaporated and a solid was formed. The solid was then heated with an IR lamp to achieve complete dehydration of the gel without boiling. It was found that boiling the gel could cause degradation of the polymer.

The waxy solid products were transferred to porcelain crucibles and heated, in a sand bath, with a Bunsen flame to approximately 450 °C until they were molten and hot enough to be ignited. The sand bath helped ensure even heating of the crucibles, so that all the crucibles could be ignited at approximately the same time and the Bunsen flame turned off as it was a self-propagating reaction. This experimental set up (seen in Figure 3.2) also helped to ensure that all the samples experienced the same heating conditions, although this could not always be guaranteed due to the amount of resin in each crucible and the position of the Bunsen flame under the sand bath. As the heating of the samples progressed, the colour of the samples changed from white or yellow to a dark brown and eventually black. At this point any remaining water and solvent was driven off and only the metal ions remained in the molten polymer. Once this stage was reached the polymer would either self-ignite, or could be ignited readily with a Bunsen flame. The samples burnt for approximately 10 minutes during which the sample volume decreased dramatically. As the polymer was burnt off, the nanocrystals of mixed metal oxides were able to form. The nanocrystalline particles remained in the crucibles as a powder product.

Bismuth-Niobium Mixed Metal Oxides

The method used for the synthesis of the bismuth-niobium nanoparticles was the same resin-gel technique used above. Calculated masses of $NbCl_5$ and $Bi(NO_3)_3$. $5H_2O$ were dissolved in HCl (30 mL) to give solutions containing 20%, 40%, 60% and 80% of bismuth nitrate with 80%, 60%, 40% and 20% niobium chloride respectively. A solution of 100% niobium chloride was also made. The solutions were left overnight to dissolve. PEG was added to all the solutions, as above, and then heated at 80 °C. When all the solvent had apparently evaporated, the samples were heated with an IR lamp to form the waxy solid. This waxy solid was transferred to a porcelain crucible and heated with a Bunsen burner, as with the bismuth-cerium samples, until they were molten and hot enough to ignite. The samples were ignited to burn off the polymer and leave the powdered solid nanoparticles in the crucibles.

Cerium-Niobium Mixed Metal Oxides

The synthesis of the Ce-Nb nanoparticles was again via a resin-gel technique. Calculated masses of $Ce(NO_3)_3.6H_2O$ and $NbCl_5$ were weighed out to give to give stoichiometric amounts of 20%, 40%, 60% and 80% $Ce(NO_3)_3.6H_2O$ to be mixed with 80%, 60%, 40% and 20% stoichiometric amounts of $Ce(NO_3)_3.6H_2O$ respectively. As the two compounds are not soluble in a common solvent, the $Ce(NO_3)_3.6H_2O$ was dissolved in water and the $NbCl_5$ in HCl. PEG was then added and mixed to each solution, before the two solutions for each ratio were mixed together. The four mixtures were then heated with an IR lamp to form a waxy solid. The waxy solids were transferred to a porcelain crucible and heated until molten and hot enough to ignite the polymer.

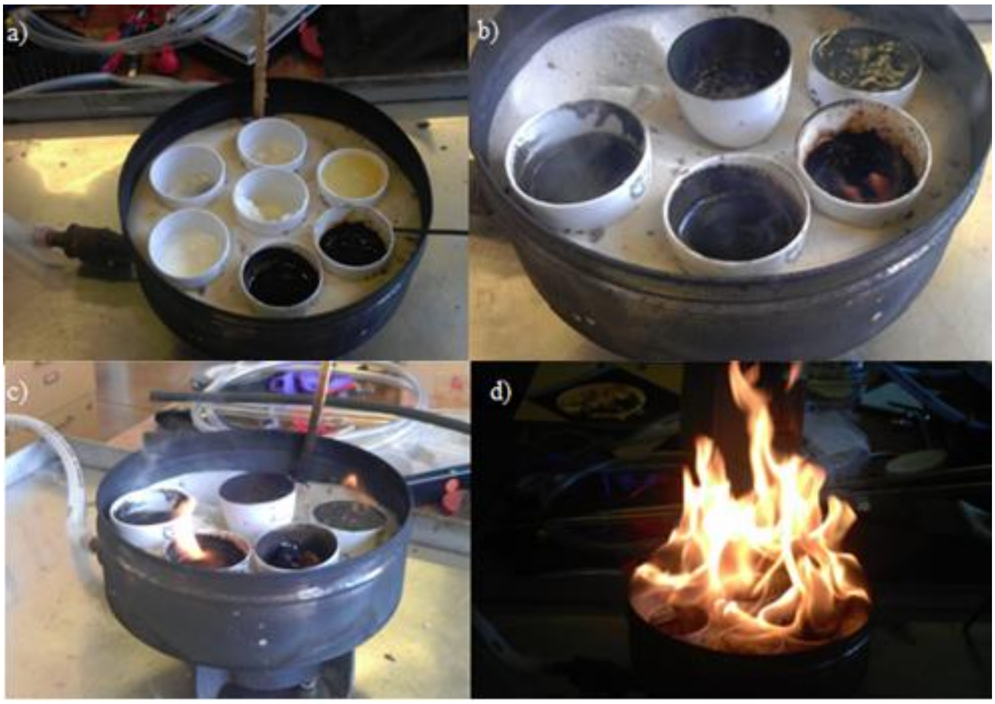

Figure 3.2 Images showing the progression of the pyrolysis stage of the resin-gel synthesis. Image a) shows the crucibles with the waxy solid evenly spaced in the sand bath (the two darker samples had already been heated for some time). Image b) shows the blackening of the samples with heating at 400 °C and spontaneous ignition of one sample. Images c) an d) show the more vigorous stages of the burn.

3.6 Synthesis of quaternary mixed metal oxides

$Bi(NO_3)_3.5H_2O$ and $Ce(NO_3)_3.6H_2O$ were solvated in nitric acid while $NbCl_5$ was dissolved in sulphuric acid in varying molar quantities to synthesise a full range of compositions. These compositions are shown in Table 3.1.

Table 3.1. Calculated masses for each of the starting compounds used to produce the four different resulting mixed metal oxide nanoparticles.

Molar ratio of Ce:Nb:Bi	*Mass of $Ce(NO_3)_3.6H_2O$ /g*	*Mass of $NbCl_5$ /g*	*Mass of $Bi(NO_3)_3.5H_2O$ /g*
2:1:1	0.535	0.166	0.299
1:2:1	0.297	0.370	0.332
1:1:2	0.259	0.161	0.579
1:1:1	0.365	0.227	0.408

PEG was added to each of the nitric acid and sulphuric acid solutions as a gelling agent and mixed thoroughly with a stirring rod before combining the two gels for further mixing. It was necessary to prepare the gels separately as the three metal salts were not all compatible in the same solvent. As before, the amount of PEG added was approximately equal to the volume of the metal ion solutions. The samples were placed under an IR lamp to attain dehydration of the gel without boiling. When the majority of the solvent had been evaporated, samples were moved to an oven and heated at 150 °C for 48 hours until a waxy solid remained. The resulting products were transferred to porcelain crucibles before being heated with a Bunsen flame to 450 °C. The polymer was then ignited and allowed to burn off. The polymer burnt with a yellow flame. The nanocrystalline particles remained as a powder product.

The quaternary oxides synthesised via a resin-gel method all produced mixed metal oxide nanoparticles successfully. For comparison, the same ratios of cerium, bismuth, and niobium were reacted in the bulk form, to see if a quaternary oxide of these metals was possible using a solid state synthesis. Therefore, appropriate masses of cerium oxide, niobium oxide and bismuth oxide were ground under acetone and placed in the muffle furnace at 850 °C with a ramp rate of 5 °C min^{-1} for 4 weeks to see if a reaction would occur. The samples were removed for grinding several times during the heating process. After 4 weeks, the samples were removed and analysed using PXRD and HRTEM.

3.7 Thermal treatments

Tube Furnace with Flowing Oxygen

To fully oxidise the nanoparticles, after the pyrolysis of the PEG, a tube furnace was used. The samples were inserted inside a quartz tube and calcined at 350 °C under flowing oxygen. The temperature was controlled by a thermocouple linked to a programmable heat controller. After heating the samples for 24 hours, it was apparent that all carbonaceous material from the organic polymer had been removed. This was seen as the colour of the powder samples changed from black to white or yellow depending on the composition. Further evidence that all the polymer residue had been removed was seen by elemental analysis (see section 3.9). An example of how the samples looked after full oxidation in the tube furnace is seen in Figure 3.3.

Figure 3.3 Image showing the calcined nanoparticles in the Bi-Ce series. From left to right shows pure CeO_2 through to pure Bi_2O_3

Usually after the removal of any organic residue from the nanoparticles, a crystalline phase or several phases were seen by PXRD. With some samples it was clear, from both observation in the HRTEM and the PXRD pattern, that an amorphous phase had been formed. In these cases further heating was required to see if a crystalline phase could be formed. It was necessary to still keep the temperature relatively low to avoid sintering of the nanoparticle. All samples, therefore, were further heated at 500 °C and 700 °C for one week under flowing oxygen. In addition to forming crystalline phases from amorphous product, the heating was also used to monitor any phase changes within the different nanoparticulate metal oxide systems at different temperatures. These two temperatures were chosen to give a relatively broad picture of the phases observed in these nanoparticulate systems at low temperatures. At temperatures above 700 °C it was found that sintering of particles became more evident, and above this temperature the bulk forms of the oxides were more likely to form rather than the solid solutions of interest in this project.

3.8 Ion exchange in solution

As the lattice structure of nanoparticles is believed to be more relaxed than that of bulk materials, it was hypothesised that this characteristic may facilitate ion exchange in solution. Therefore, a series of experiments were set up in order to test this. It was hoped that a change in overall particle composition would be observed, thus confirming the hypothesis. Two sets of experiments were devised: The first involved the addition of PEG as a binding agent; the second was based purely upon diffusion of ions in solution.

The method of the first experiment was as follows: The Bi-Nb nanoparticles previously synthesised via the resin-gel method were suspended in a solution of $Bi(NO_3)_3.5H_2O$. The bismuth ions in the solution were in great excess, so as to encourage diffusion of Bi^{+3} into the particles. The samples were stirred and heated at 50 °C for one week before being filtered, cleaned and dried. The particles were then analysed using PXRD, HRTEM and EDS to ascertain if the composition of the nanoparticles had changed.

The second series of experiments involved taking Bi-Nb nanoparticles with the same starting composition of those used in the first method and suspending them in a solution of $Bi(NO_3)_3.5H_2O$. These solutions were stirred and heated gently at 50 °C for one week. After this time PEG (mw=20,000) was added to the solutions. As above in the nanoparticle synthesis, the amount of PEG added was approximately equal to the volume of the metal ion solutions. The gel was dehydrated using an IR lamp before heating the samples to 450 °C and igniting the polymer to leave nanocrystalline products in powder form. The samples were then analysed using PXRD, HRTEM and EDS to see if there had been any change from the starting Bi-Nb oxide nanoparticle compositions.

3.9 Elemental analysis

In order to confirm that all the organic polymer had been removed from the nanoparticles in the calcination process, bulk elemental analysis was carried out. A combustion method was used to determine the percentages of carbon, hydrogen and nitrogen in the sample. It can be seen from the results, Table 3.2, that the temperatures in the tube furnace along with the flowing oxygen resulted in almost complete removal of the carbonaceous material coating the metal oxide nanoparticles. For all samples tested there was on average 0.268% carbon. This minimal amount of carbon would not affect any analyses of the nanoparticles.

Table 3.2. Results of the elemental analysis carried out on a selection of samples.

Sample	*% Carbon*	*% Hydrogen*	*% Nitrogen*
$CeNbBi_2$	0.02	0.02	0.00
CeNbBi	0.02	0.04	0.00
Ce_2NbBi	1.26	0.12	0.01
$CeNb_2Bi$	0.03	0.09	0.00
$Bi_{0.2}Ce_{0.8}$	0.28	0.10	0.09
$Bi_{0.4}Ce_{0.6}$	0.22	0.06	0.04
$Bi_{0.6}Ce_{0.4}$	0.23	0.04	0.12
$Bi_{0.8}Ce_{0.2}$	0.15	0.03	0.08
$Bi_{0.2}Nb_{0.8}$	0.36	0.06	0.00
$Bi_{0.4}Nb_{0.6}$	0.10	0.05	0.00
$Bi_{0.6}Nb_{0.4}$	0.20	0.03	0.02
$Bi_{0.8}Nb_{0.2}$	0.33	0.03	0.00
$Ce_{0.2}Nb_{0.8}$	0.56	0.18	0.02
$Ce_{0.4}Nb_{0.6}$	0.31	0.05	0.00
$Ce_{0.6}Nb_{0.4}$	0.19	0.08	0.04
$Ce_{0.8}Nb_{0.2}$	0.37	0.08	0.00
Ce 100%	0.22	0.09	0.11
Nb 100%	0.11	0.02	0.00
Bi 100%	0.14	0.00	0.00
Mean %	**0.268**	**0.061**	**0.027**

3.10 Discussion

As described in the following chapters, the resin-gel method was successful in the preparation of both ternary and quaternary oxides. This appears to confirm the hypothesis that the long-chain PEG does indeed co-ordinate the metal ions indiscriminately, resulting in the production of a mixed metal-containing phase, which after annealing in pure oxygen gives a mixed metal oxide. However, the actual nature of the precursor gel and the full mechanism of forming the mixed oxides remains an enigma. Previous attempts within the group to examine possible cation ordering in the gel using synchrotron radiation have all failed because the gel is too dilute. Similarly, any compositional examination in the electron microscope has proved impractical because the gel rapidly decomposes to give small particles under examination with high beam current density.

Although it must be assumed that the gel is approximately homogeneous the nanoparticles produced by decomposition are rarely so. A possible explanation for this is to consider the situation as the first particles are formed, which must be when the molten gel is decomposing. If this situation is likened to the equilibrium between solid and liquid solutions, then it may be represented by the phase diagram shown in Figure 3.4.

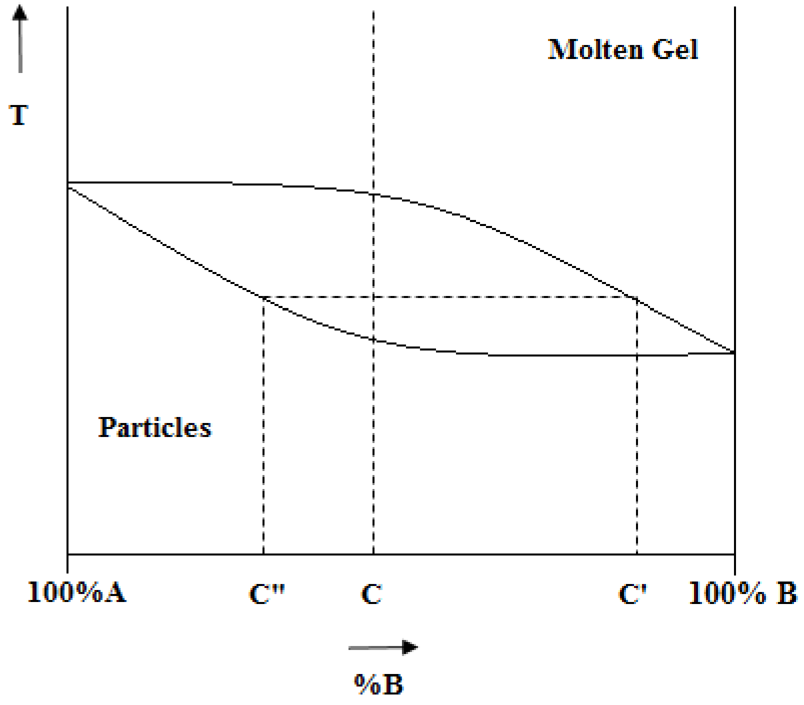

Figure 3.4. Phase diagram representing the equilibrium between solid and liquid solutions.

If this situation applied, then at a temperature T, we will have a gel of composition C’ in equilibrium with particles of composition C”, but as the temperature changes, so will these compositions, and if the overall temperature is insufficiently high to permit appreciable diffusion of cations, an inhomogeneous product will result. The extent of this behaviour will depend on the magnitude of the liquid/solidus gap, but it could explain the observed inhomogeneities.

4. Preliminary results

4.1 Bulk oxide samples

Three bulk oxides were prepared by solid state methods, described in Chapter 3, and analysed using PXRD, HRTEM and EDS. The purpose of synthesising these three bulk samples was to enable compositional analysis to be carried out on the subsequently synthesised Ce-Nb-Bi mixed oxide nanoparticles. By using standard samples with a known concentration of each metal, determined by EDS, the composition of the nanoparticles could be determined. The theory of this method can be found in Chapter 2 in the discussion of EDS analysis.

4.1.1 $BiNbO_4$

A bulk standard sample of $BiNbO_4$ was synthesised and calcined to produce a white ceramic solid. The white colour indicated that Bi^{3+} and Nb^{5+} were present, as expected for this compound. It can be seen from the PXRD pattern for the sample, Figure 4.1, that a pure $BiNbO_4$ phase was formed, with no starting material remaining, as the pattern matches exactly to the pattern found in the literature [146]. The sharp peaks in the pattern indicate a high degree of crystallinity in the sample.

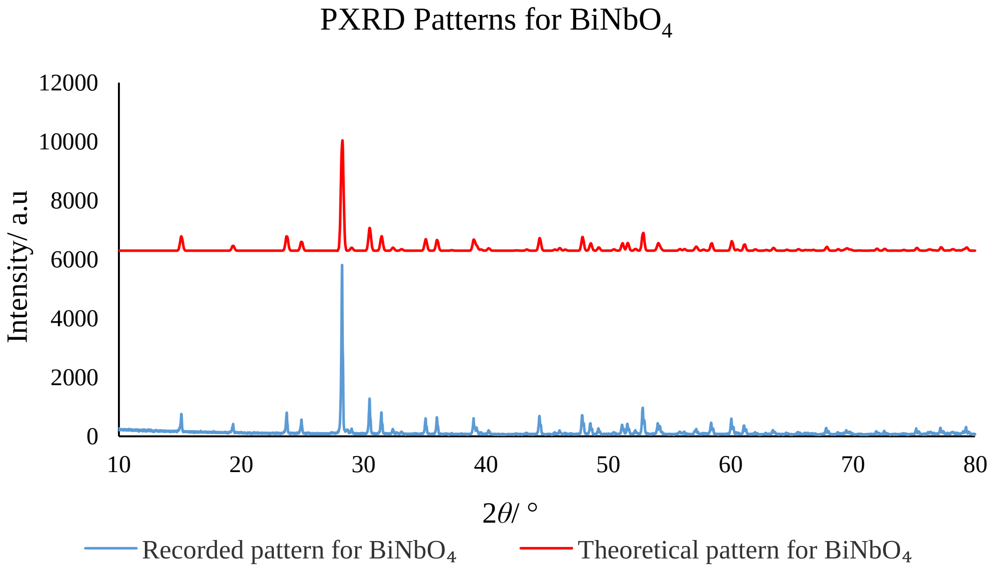

Figure 4.1. PXRD pattern for the recorded $BiNbO_4$ bulk sample compared with the theoretical PXRD pattern for $BiNbO_4$.

The mean crystallite size for the sample was calculated, using Scherrer analysis. Non-superimposed lines were chosen from the pattern to use in the analysis, thereby giving the most accurate crystallite size values. Table 4.1 gives the peaks used for Scherrer analysis, along with the values calculated for crystallite size. The mean crystallite size was found to be 56 ± 9 nm, which is smaller than might be expected for a bulk material. It is likely that the relatively low reaction temperature of 850 °C gave good control over the particle growth.

Table 4.1. Scherrer analysis for the recorded PXRD pattern of $BiNbO_4$ to calculate the mean crystallite size.

Index	*2θ/ °*	*θ/ °*	*θ/ rad*	*Peak Width/ °*	*Peak Width/ rad*	*L/ Å*	*L/ nm*
020	15.12	7.56	0.13	0.132	0.0023	593.91	59
101	23.72	11.86	0.21	0.150	0.0026	529.81	53
111	24.93	12.46	0.22	0.150	0.0026	531.01	53
121	28.24	14.12	0.25	0.120	0.0021	668.31	67
040	30.49	15.25	0.27	0.130	0.0023	620.08	62
200	31.46	15.73	0.27	0.151	0.0026	535.10	54
220	35.07	17.54	0.31	0.172	0.0030	474.21	47
002	35.99	18.00	0.31	0.118	0.0021	694.77	69
240	47.88	23.94	0.42	0.217	0.0038	392.14	39

The EDS data collected for the $BiNbO_4$ sample is shown in Figure 4.2. It can be seen from the plot that the majority of points sit on, or very close to the line of best fit. This is strong evidence for a single homogenous phase being formed and agrees well with the PXRD data. Some points were discarded due to absorption effects and some particles of pure Nb_2O_5 were also discarded. As no lines corresponding to the Nb_2O_5 phase were seen in the PXRD pattern it must be present in very small quantities so that lines corresponding to this phase were lost in the background. The PXRD and EDS data combined seem to indicate that only $BiNbO_4$ was formed from Bi_2O_3 and Nb_2O_5. The heating conditions were sufficient to ensure the oxide lattices of the starting materials interdiffused and the $BiNbO_4$ phase was formed.

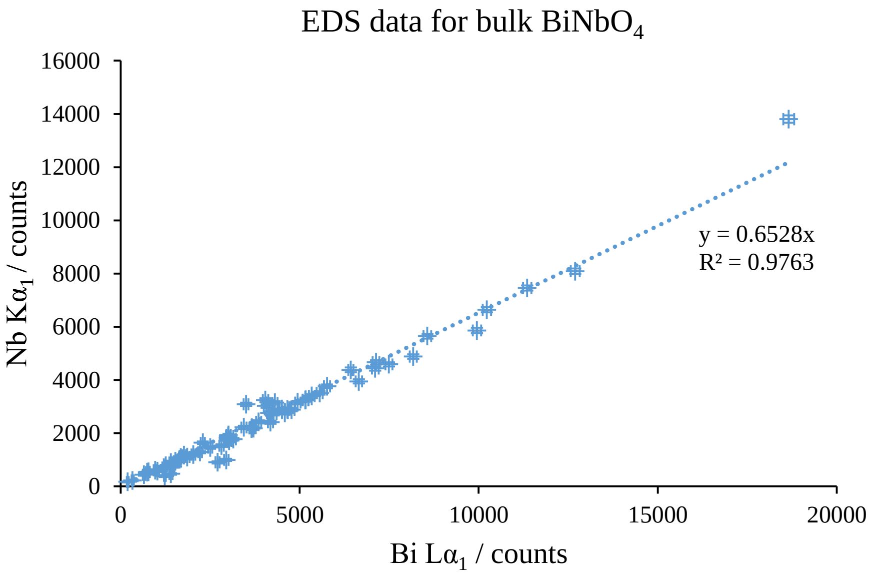

Figure 4.2. EDS plot of the Bi Lα$_1$ counts against the Nb Kα$_1$ counts for the bulk BiNbO$_4$ sample.

The Linest function in Excel was used to calculate the error in the slope of the EDS plot. It was found that the r^2 value was 0.98 and the percentage uncertainty in the slope was 1.83%, which indicates that the error for the data was small. Overall, it can be said that the sample was of uniform composition. From the equations laid out in Chapter 2 and the EDS data collected, the value for $K_{Nb:Bi}$ can be seen from the gradient of the line to be 0.6528. This ratio was later used to calculate the percentages of niobium and bismuth in the mixed oxide nanoparticles.

4.1.2 CeNbO$_4$

A bulk sample of CeNbO$_4$ was prepared by solid state methods, as described previously. The resultant black powder was analysed by EDS and PXRD. The PXRD pattern for the CeNbO$_4$ sample is shown in Figure 4.3 and provides good evidence for the formation of the desired phase. It can be seen that the CeNbO$_4$ phase produced is a combination of two different structures with the same chemical formula. There is evidently a very low energy barrier between the two phases. The pattern shown in red is Skinner's tetragonal CeNbO$_4$ structure, while the purple pattern is for Santoro's monoclinic structure [147, 118]. As the two phases are so similar and have the same chemical formula, the prepared bulk sample of CeNbO$_4$ was suitable for use in calculation relative compositions in the mixed metal oxide nanoparticles.

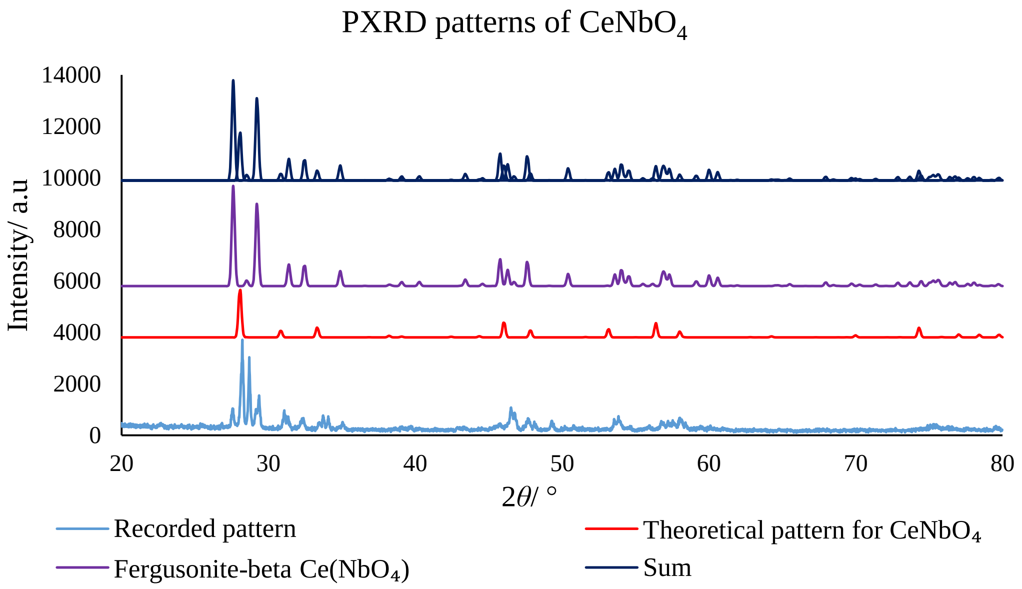

Figure 4.3. PXRD pattern for the recorded $CeNbO_4$ bulk sample compared with the theoretical PXRD patterns for $CeNbO_4$. [147, 118]

The mean crystallite size for the sample was calculated using Scherrer analysis and was found to be 24 ± 9 nm. A full table of Scherrer analysis can be seen in Table 4.2. The value calculated as the mean crystallite size may seem rather small considering the bulk synthesis method. This is because Scherrer analysis calculates the crystallite size only and the bulk crystals can be argued to be made up of many crystallites. Therefore, much larger crystals were actually seen in the HRTEM (~0.5 µm).

Table 4.2. Scherrer analysis for the recorded PXRD pattern of $CeNbO_4$ to calculate the mean crystallite size.

2θ/ °	*θ/ °*	*θ/ rad*	*Peak Width/ °*	*Peak Width/ rad*	*L/ Å*	*L/ nm*
27.25	13.62	0.24	0.34	0.0059	238.17	24
27.92	13.96	0.24	0.20	0.0035	398.71	40
28.38	14.19	0.25	0.43	0.0075	186.56	19
30.76	15.38	0.27	0.23	0.0040	350.70	35
33.77	16.88	0.29	0.34	0.0058	242.62	24
46.23	23.12	0.40	0.47	0.0082	180.81	18
53.55	26.78	0.47	0.59	0.0103	147.65	15
57.73	28.86	0.50	0.44	0.0077	201.83	20

The EDS data for the $CeNbO_4$ bulk sample can be seen in Figure 4.4. The plot is good evidence for a single composition being formed as the majority of points lie on the line, with a standard deviation of

0.016 and percent uncertainty in the slope of 2.22%, calculated using the Linest function. The two separate $CeNbO_4$ phases could not be differentiated using EDS as they have the same chemical formula.

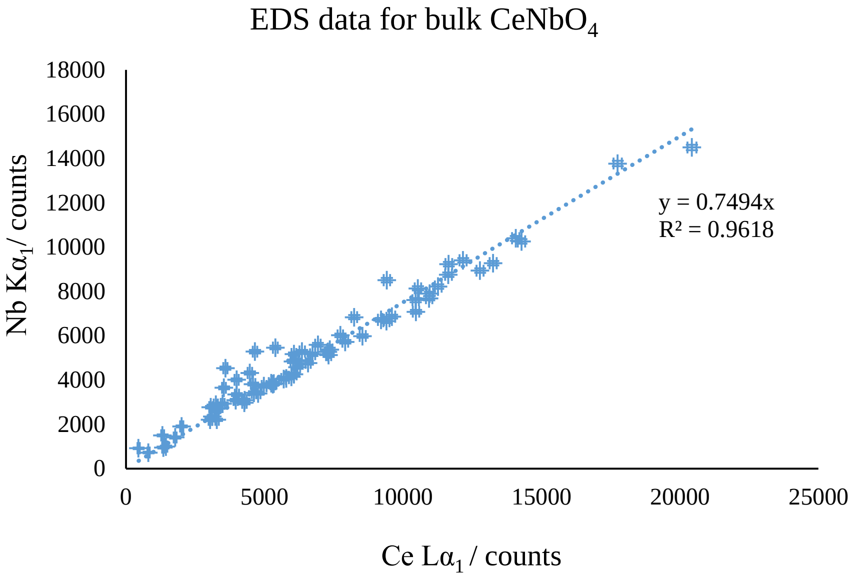

Figure 4.4. EDS plot of the Ce Lα_1 counts against the Nb Kα_1 counts for the bulk $CeNbO_4$ sample.

As with the $BiNbO_4$ standard EDS data, the gradient of the line gives the constant relating the ratio of the two elements to their concentration. In this case the $K_{Nb:Ce}$ value was found to be 0.7494, which was later used to quantify the EDS data in the mixed cerium-niobium nanoparticles.

4.1.3 Ce_2BiO_2

An attempt was also made to prepare Ce_2BiO_2 as a third standard. The PXRD data collected for the bulk Ce_2BiO_2 sample is shown in Figure 4.5. It can be seen that the recorded pattern for the sample synthesised does not match the theoretical pattern for Ce_2BiO_2, the intended phase [122]. In fact, it seems to match well to the CeO_2 fluorite phase [85]. This indicates that the bismuth ions were able to fit into the fluorite lattice in the cation sites to form a bulk mixed oxide. Due to the different ionic radii of Ce^{4+} and Bi^{3+} it is likely that the structure was disordered which may account for the extra peaks in the XRD pattern. There may also be a small proportion of α-Bi_2O_3 which would explain the many small peaks only just visible above the background.

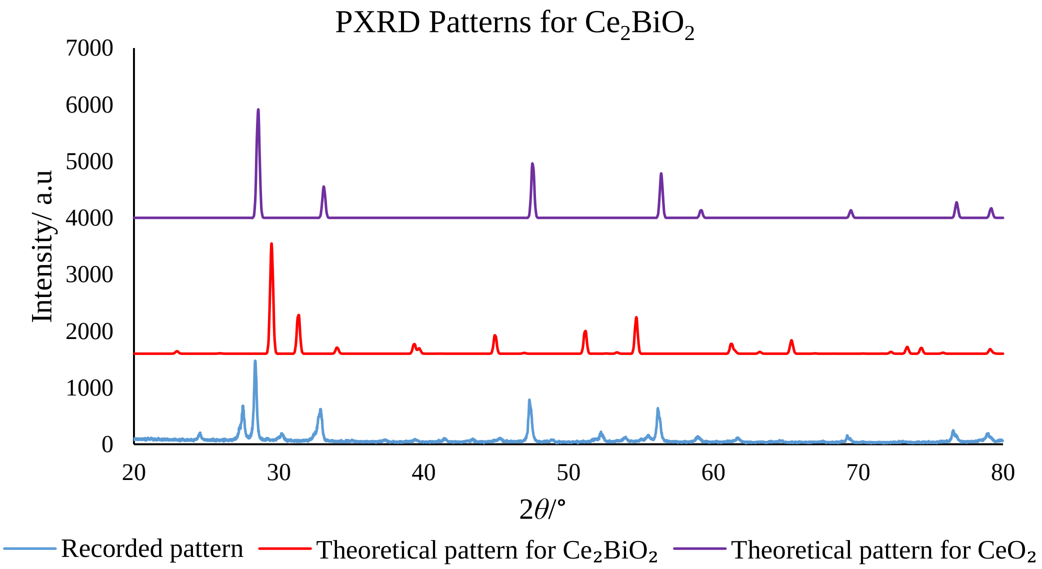

Figure 4.5. PXRD pattern for the recorded Ce_2BiO_2 bulk sample compared with the theoretical PXRD patterns for Ce_2BiO_2 and CeO_2. [122, 85]

Scherrer analysis was carried out to calculate the mean crystallite size, details seen in Table 4.3. This was found to be 22 ± 6 nm.

Table 4.3. Scherrer analysis for the recorded PXRD pattern of Ce_2BiO_2 to calculate the mean crystallite size.

2θ/ °	*θ/ °*	*θ/ rad*	*Peak Width/ °*	*Peak Width/ rad*	*L/ Å*	*L/ nm*
24.58	12.29	0.21	0.32	0.0056	248.74	25
27.50	13.75	0.24	0.28	0.0049	285.96	29
28.37	14.19	0.25	0.22	0.0038	364.64	36
32.90	16.45	0.29	0.37	0.0064	221.57	22
52.25	26.13	0.46	0.36	0.0063	240.62	24

The EDS data collected, shown in Figure 4.6, indicates that a range of compositions were present in the sample, which was not the intended outcome. It is possible that the sample was not heated for long enough or at a high enough temperature to form the Ce_2BiO_2 phase, or as many of the particles appear to be Ce rich, some bismuth may have escaped during the heating process as it is fairly volatile. It is also possible that the sample was a solid solution in the fluorite phase, although the presence of extra peaks would indicate that it was not a simple fluorite structure. As the PXRD pattern did not indicate any strong lines corresponding to α-Bi_2O_3, it must be assumed that the majority of the bismuth was incorporated into the fluorite structure rather than forming the Ce_2BiO_2 phase, which would be thermodynamically preferable, perhaps because the temperature of 850 °C were not sufficient for the phase to form.

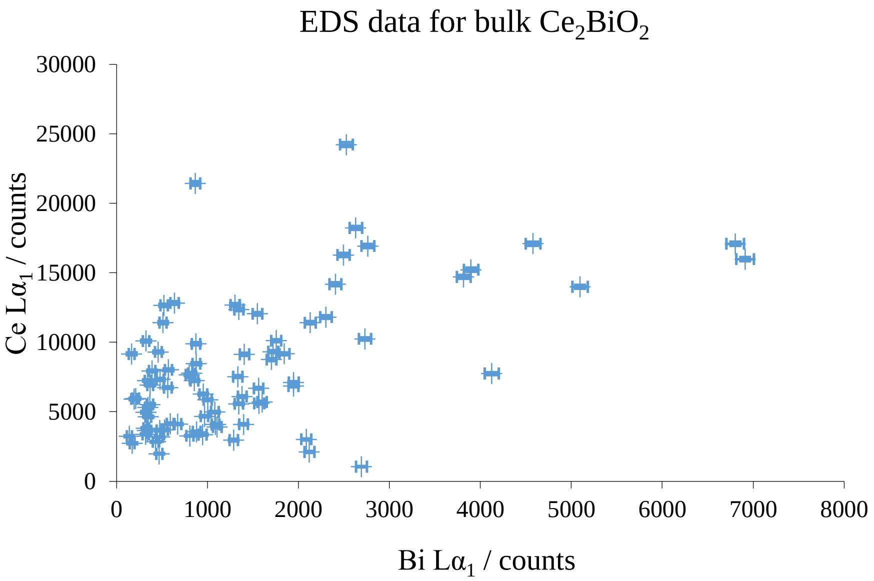

Figure 4.6. EDS plot of the Bi Lα_1 counts against the Ce Lα_1 counts for the bulk Ce_2BiO_2 sample.

As the required mixed Ce-Bi bulk oxide was not formed, it was necessary to compare the ratio of bismuth to cerium from the other two bulk oxides synthesised. By comparing the $CeNbO_4$ and $BiNbO_4$ samples, a ratio of bismuth: cerium could be calculated and applied to the mixed oxide nanoparticles. Once the $K_{Nb:Ce}$ and $K_{Bi:Nb}$ constants were calculated from the EDS data shown previously, a $K_{Bi:Ce}$value could be calculated as follows:

$$K_{Bi:Ce} = \frac{K_{Bi:Nb}}{K_{Ce:Nb}}$$

This calculation gave a value for $K_{Bi:Ce}$ as 1.33, which then allowed the composition of the Bi-Ce oxide nanoparticles to be subsequently calculated using this value and the EDS data for the Bi-Ce oxide nanoparticles.

4.2 Binary Oxides

The first nanoparticles synthesised were the binary oxides of cerium, niobium and bismuth. These were all synthesised using the resin-gel method, described in Chapter 3. As discussed in Chapter 1, all three of these metal oxides have extremely useful properties, which have the potential to be enhanced in nanoparticle form due to the increase in surface area and more relaxed lattice structure. It was, therefore, important to establish firstly if nanoparticles could be formed, and secondly if the phases synthesised were analogous to those found in the bulk. This was indeed found to be the case. All three target binary oxides were synthesised successfully and structural analysis was carried out using HRTEM, EDS and PXRD.

4.2.1 CeO_2

A very pale yellow solid was formed from the resin-gel synthesis, after calcination, indicating the presence of Ce^{4+} as expected. PXRD analysis, shown in Figure 4.7, indicates that one phase is present in the sample, with the pattern matching well to the CeO_2 phase [85]. The recorded pattern gave broad lines, indicating a small particle size, as well as the peaks being shifted slightly to the left, which is good evidence for a more relaxed crystal lattice.

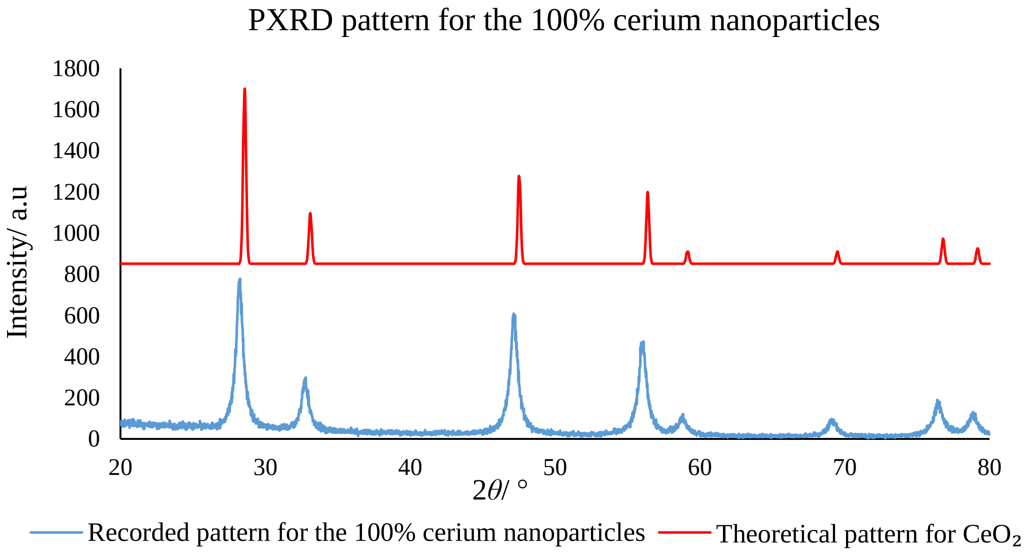

Figure 4.7. PXRD pattern for the CeO_2 nanoparticles in comparison with the theoretical pattern for CeO_2.

Scherrer analysis was carried out to give an idea of the mean crystallite size in the sample. This was found to be 14 ± 1 nm, with a full table of the analysis in Table 4.4.

Table 4.4. Scherrer analysis for the CeO$_2$ nanoparticulate sample.

Peak Index	*2θ/ °*	*θ/ °*	*θ/ rad*	*Peak Width/ °*	*Peak Width/ rad*	*L/ Å*	*L/ nm*
111	28.25	14.13	0.25	0.65	0.011	123.38	12
200	32.78	16.39	0.29	0.60	0.010	135.11	14
220	47.25	23.63	0.41	0.60	0.010	141.48	14
311	56.06	28.03	0.49	0.66	0.012	133.50	13
222	58.80	29.40	0.51	0.60	0.010	148.78	15
331	76.42	38.21	0.67	0.65	0.011	152.28	15

EDS data was collected for the CeO$_2$ nanoparticles confirming the presence of cerium and oxygen as expected. Calculated ratios for the Ce Lα_1 intensities vs Ce Lβ_1 were constant for the 36 particles analysed indicating there were no absorption effects in the microscope.

As expected, looking at the CeO$_2$ nanoparticles in the microscope confirmed that a pure phase had been synthesised. Micrographs seen in Figure 4.8 and 4.9 show small agglomerated CeO$_2$ particles with d-spacings characteristic of the fluorite structure.

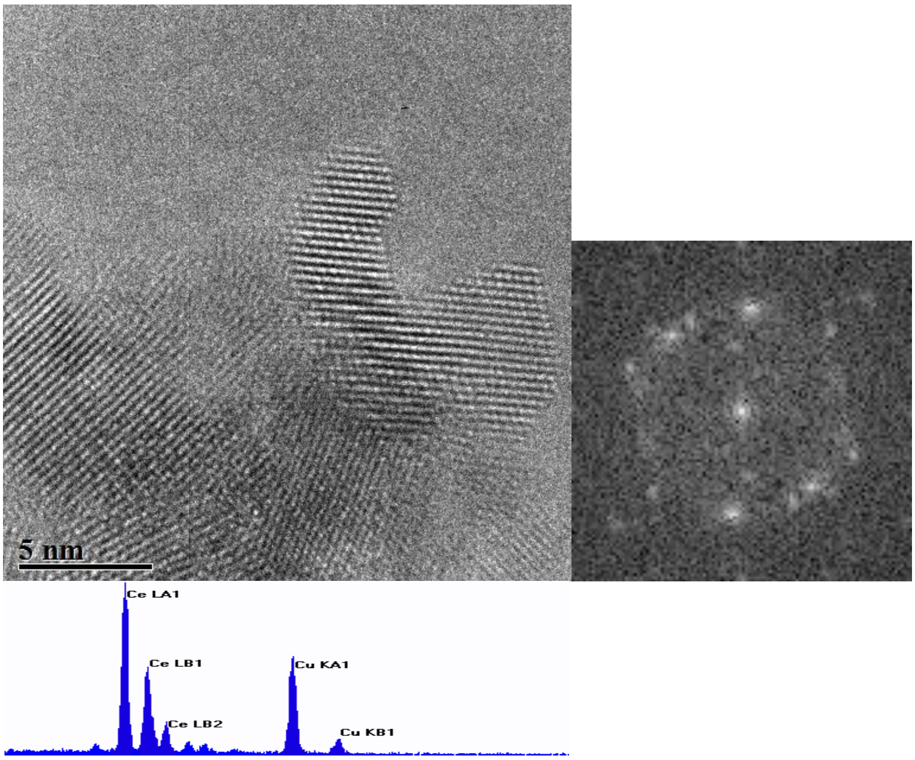

Figure 4.8. HRTEM micrograph of CeO$_2$ (l) with respective FFT (r). D-spacings calculated from the FFT correspond to the {111} and {200} lattice planes of fluorite. The EDS spectrum recorded for the area is shown underneath.

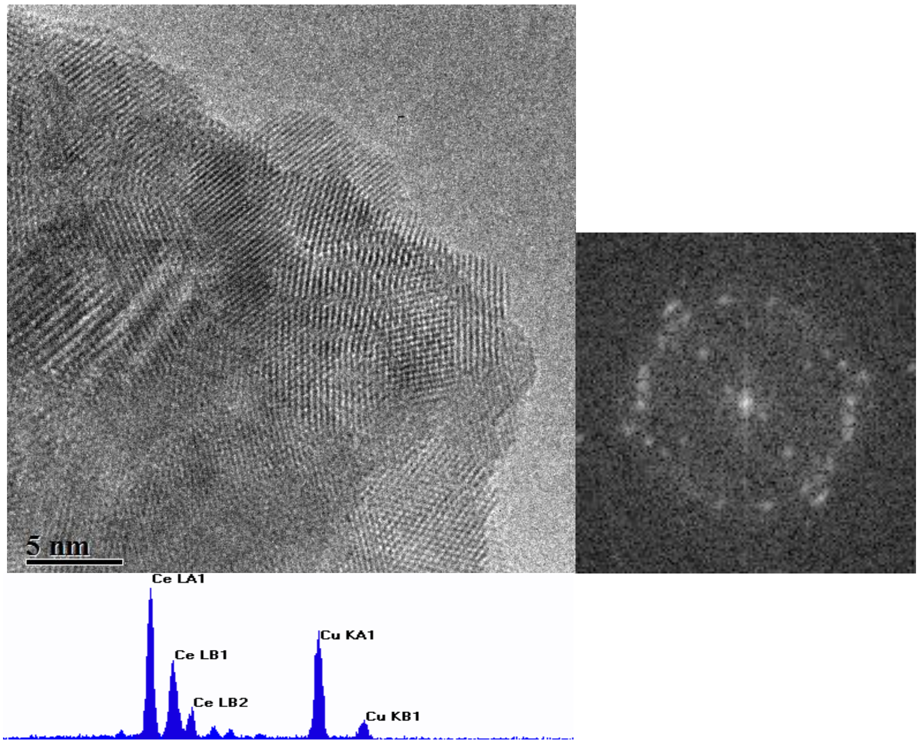

Figure 4.9. HRTEM micrograph of CeO_2 *(l) with respective FFT (r). D-spacings calculated from the FFT correspond to the {111}, {200} and {220} lattice planes of fluorite. The EDS spectrum recorded for the area is shown underneath.*

4.2.2 Bi_2O_3

The PXRD pattern for the bismuth oxide sample, shown in Figure 4.10, was a good match to the α-Bi_2O_3 phase found in the literature [35]. This was the expected phase due to the low temperature synthesis and calcination temperature, although, as the energy barriers between the polymorphs of bismuth oxide are relatively small, a higher temperature phase could have been attainable.

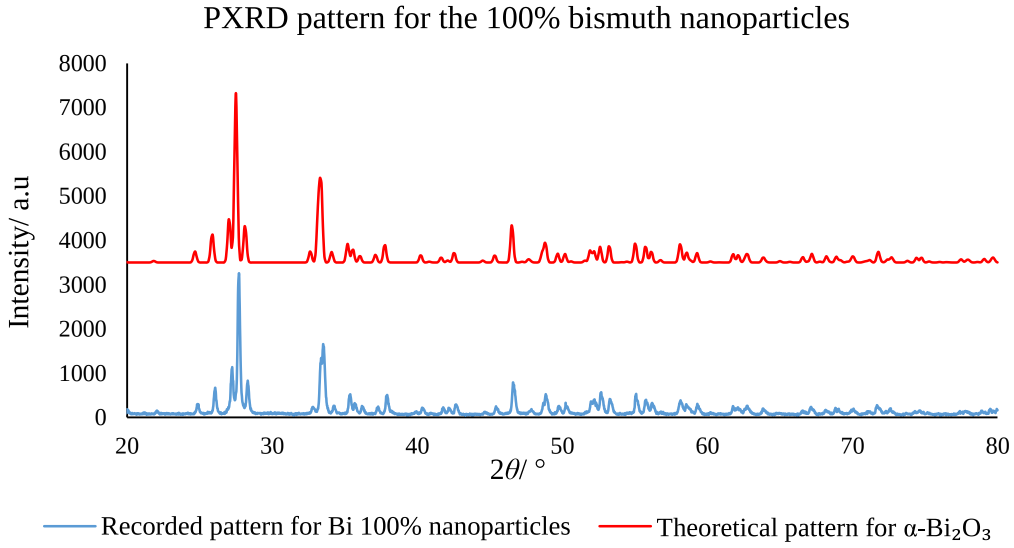

Figure 4.10. PXRD pattern for the Bi_2O_3 nanoparticles in comparison with the theoretical pattern for α-Bi_2O_3.

Scherrer analysis found that the mean crystallite size was 34 ± 8 nm, with a full analysis shown in Table 4.5. The crystallite size calculated was significantly larger than those of the CeO_2 and Nb_2O_5 nanoparticulate samples and is reflected in the lack of broadening of the peaks.

Table 4.5. Scherrer analysis for the Bi_2O_3 nanoparticulate sample.

Peak Index	*2θ/ °*	*θ/ °*	*θ/ rad*	*Peak Width/ °*	*Peak Width/ rad*	*L/Å*	*L/nm*
102	24.88	12.44	0.22	0.17	0.0030	465.75	47
002	26.08	13.04	0.23	0.22	0.0038	367.55	37
112	27.25	13.63	0.24	0.22	0.0038	368.41	37
121	27.72	13.86	0.24	0.20	0.0035	399.47	40
200	33.53	16.77	0.29	0.38	0.0067	211.31	21
221	37.31	18.66	0.33	0.28	0.0050	288.94	29
220	42.68	21.34	0.37	0.30	0.0052	277.77	28
22-1	46.60	23.30	0.41	0.26	0.0046	324.45	32

EDS data was collected for the Bi_2O_3 sample, with a ratio calculated for the Bi Lα_1 and Bi Lβ_1 intensities of 0.7117. This value was constant over the 30 particles analysed and, again, shows that absorbance did not significantly affect the measurements.

Micrographs taken in the HRTEM showed large crystals of α-Bi_2O_3, confirmed by the fringe spacings calculated from the FFTs, which were typical of the α-Bi_2O_3 phase. The area shown in Figure 4.11 is a representative region of α-Bi_2O_3 observed in the microscope. D-spacings of 2.61 Å, 2.91 Å and 3.30 Å were found from the FFT. These values correspond to the {202}, {211} and {11-1} lattice planes respectively. It is can also be seen that there appears to be another species evolving out of the main crystal. This could be a small amount of carbon impurity from the PEG being 'burnt off' under the energy of the electron beam. Alternatively it could be bismuth metal particles gaining energy from the electron beam and evolving out of the main crystal. The EDS spectrum confirms that bismuth is the only element present in the sample.

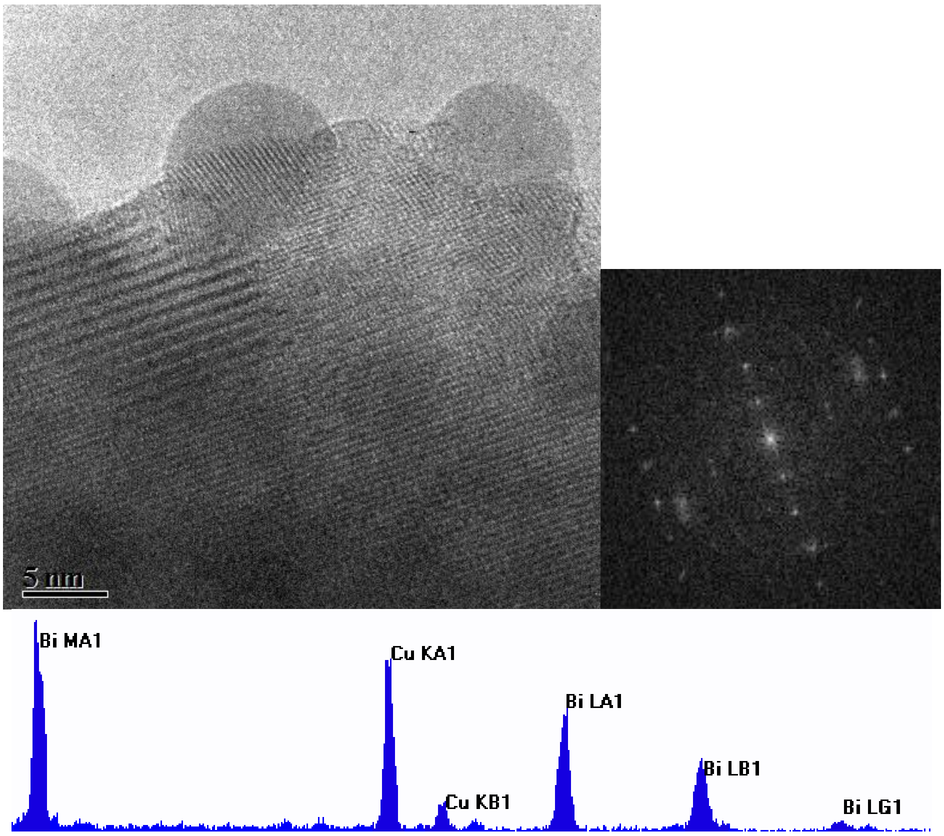

Figure 4.11. HRTEM micrograph of α-Bi_2O_3 (l) with respective FFT (r). D-spacings calculated from the FFT correspond to the {202}, {211} and {11-1} lattice planes. The EDS spectrum recorded for the area is shown underneath.

A second region of α-Bi_2O_3 is shown in Figure 4.12. The d-spacings calculated for this region are typical of α-Bi_2O_3 but in this case the crystal has a distinctive rod shape. D-spacings of 3.19 Å and 6.39 Å were calculated, indicating the {012} lattice plane being observed. The larger fringe spacing is indicative of a doubling of the unit cell. Smaller crystals of bismuth oxide can be seen evolving from the main crystal due to the energy from the electron beam. This was commonly seen when studying any region containing bismuth. As bismuth oxide is fairly volatile and there are several accessible polymorphs available at the temperature of the electron beam it is perhaps not surprising. Especially as it is suspected that less energy is required to transform between polymorphs in the nanoparticle form as the energy barrier is lower. The EDS spectrum also confirms that the sample is pure α-Bi_2O_3.

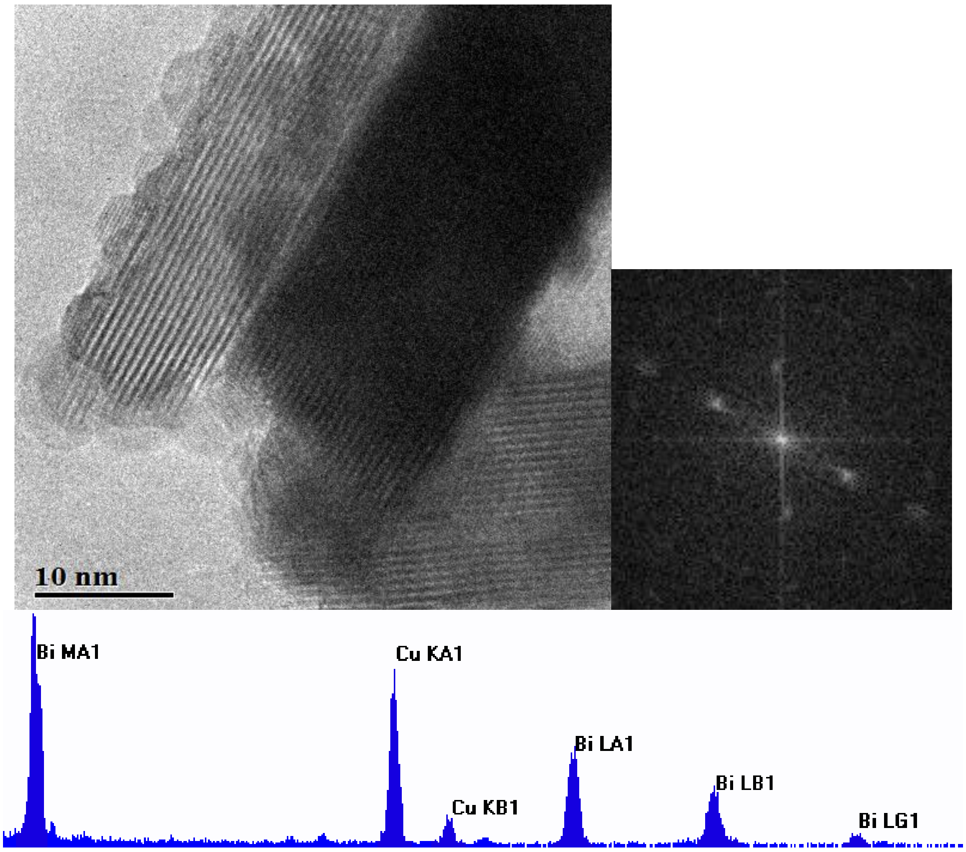

Figure 4.12. HRTEM micrograph of α-Bi_2O_3 (l) with respective FFT (r). D-spacings calculated from the FFT correspond to the {012} lattice plane. The EDS spectrum recorded for the area is shown underneath.

4.2.3 Nb_2O_5

The PXRD pattern for the 100% niobium oxide sample is shown in Figure 4.13. It is immediately apparent that more than one phase was present; due to niobium oxide's extensive polymorphism this was not an unexpected result. By comparing the recorded pattern to the literature it is clear that a mixture of T-Nb_2O_5 and M-Nb_2O_5 had formed [65, 70]. It could also be deduced that there is a higher proportion of the low temperature T-Nb_2O_5 present in the sample as these peaks dominate the pattern. In addition, the peak at 12.3 ° which should be seen in the recorded pattern corresponding to M-Nb_2O_5 is too weak and is, therefore, lost in the background noise. Nevertheless, the stronger peaks in the M-Nb_2O_5 peaks can be discerned. Peak broadening is also noticeable in the pattern as expected for a nanoparticulate sample.

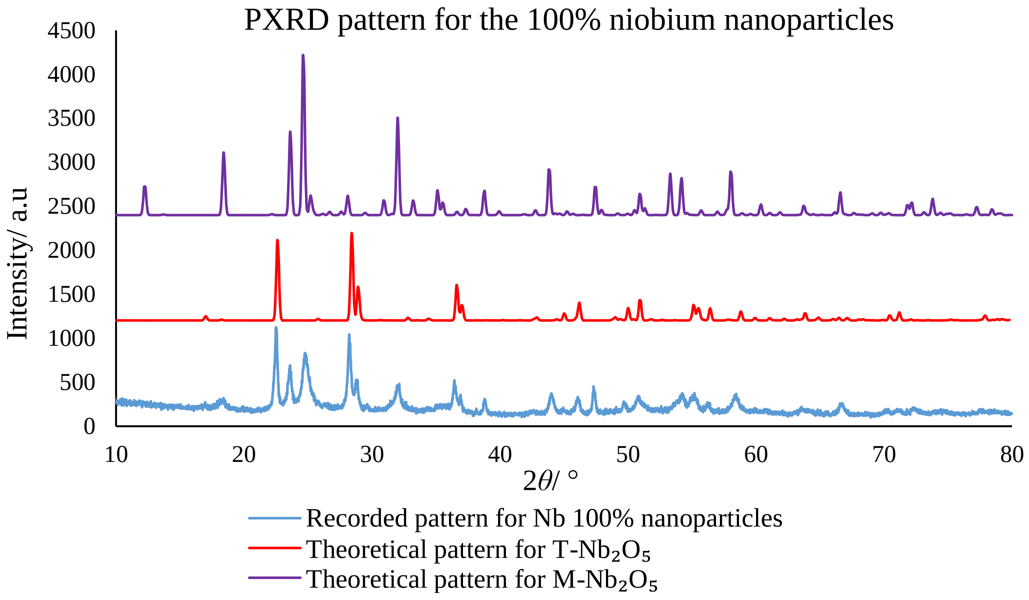

Figure 4.13. PXRD pattern for the 100%Nb nanoparticles in comparison with the theoretical pattern for the T- and M- polymorphs of Nb_2O_5*.*

Scherrer analysis was carried out on the niobium oxide sample with the mean crystallite size in the sample calculated as 17 ± 5 nm. A full table of the analysis is seen in Table 4.6.

Table 4.6. Scherrer analysis for the Nb_2O_5 *nanoparticulate sample.*

Phase	*Peak Index*	*2θ/ °*	*θ/ °*	*θ/ rad*	*Peak Width/ °*	*Peak Width/ rad*	*L/ Å*	*L/ nm*
$T\text{-}Nb_2O_5$	001	22.50	11.25	0.20	0.32	0.0056	247.80	25
$M\text{-}Nb_2O_5$	400	23.56	11.78	0.21	0.56	0.0098	141.87	14
$M\text{-}Nb_2O_5$	101	24.78	12.39	0.22	0.74	0.0129	107.61	11
$T\text{-}Nb_2O_5$	111	28.24	14.12	0.25	0.35	0.0061	229.13	23
$T\text{-}Nb_2O_5$	220	28.77	14.39	0.25	0.50	0.0087	160.58	16
$T\text{-}Nb_2O_5$	201	36.44	18.22	0.32	0.52	0.0091	157.46	16

To have accurate quantitative values for the proportion of each polymorph in the Nb_2O_5 sample, a Rietveld refinement was carried out on the PXRD pattern using FullProf. The results of this are shown in Figure 4.14. The refinement confirmed that both T- and M-Nb_2O_5 were present in the sample and that T-Nb_2O_5 composed 61.47 ± 5.44 % of the sample while the M- polymorph made up 38.53 ± 1.95 % of the sample. The χ^2 value for the refinement was 6.09, which is good considering the fit was relatively poor for the shape of the peaks due to the line broadening.

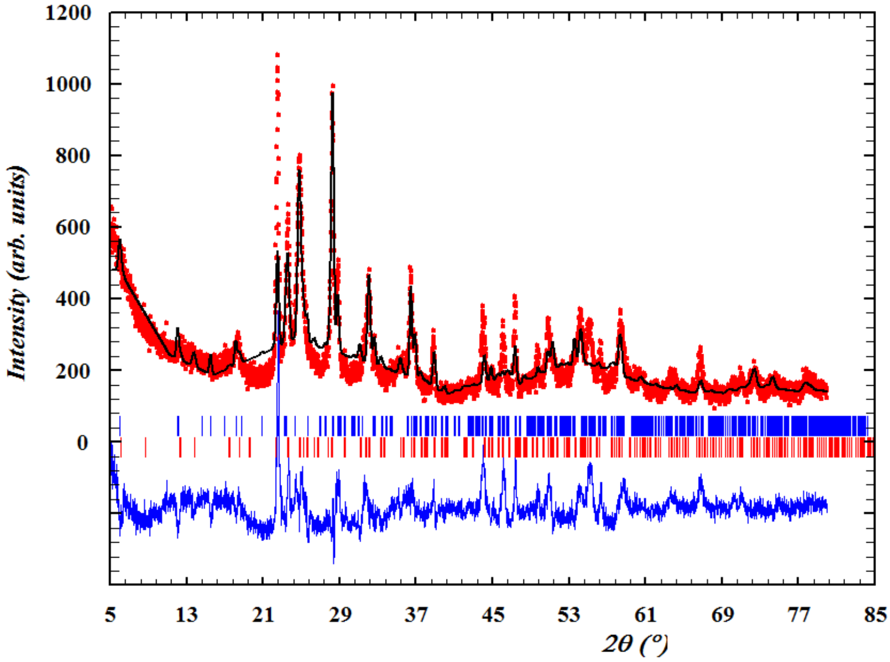

Figure 4.14. Rietveld refinement for the Nb_2O_5 nanoparticulate sample.

EDS was used to record the Nb Lα_1 and Nb Kα_1 intensities in the Nb_2O_5 nanoparticles to check for absorption effects in the microscope. Again, the ratio of these intensities across the 37 particles analysed remained constant verifying that the EDS data from the nanoparticulate sample was not subject to absorption effects.

The presence of the two polymorphs was confirmed by HRTEM, with fringe spacings corresponding to both T-Nb_2O_5 and M-Nb_2O_5 calculated from the FFTs of the micrographs. Examples of both phases can be seen in Figure 4.15. D-spacings for the T-Nb_2O_5 phase were found to be 3.92 Å and 1.95 Å corresponding to the {001} and {291} lattice planes. The d-spacings of 2.75 Å and 3.62 Å calculated from the FFT for the M-Nb_2O_5 phase indicated the {501} and the {101} planes being observed.

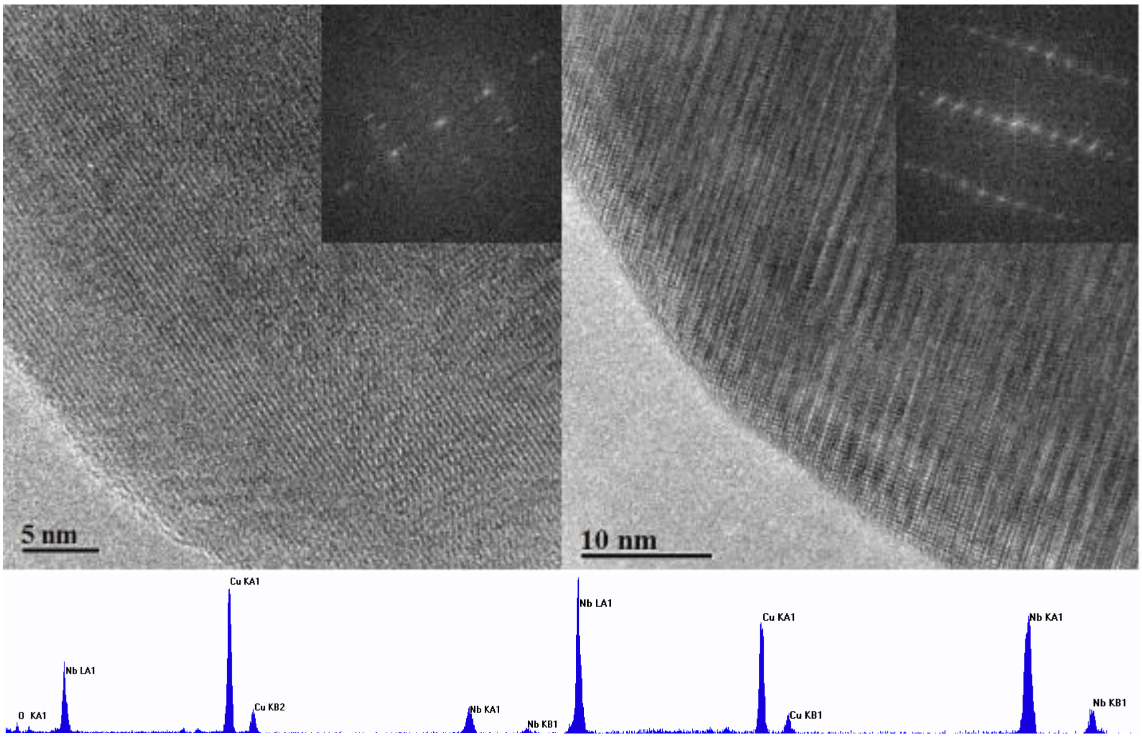

Figure 4.15. HRTEM micrograph of T-Nb_2O_5 (l) and HRTEM micrograph of M-Nb_2O_5(r) with their respective FFTs (inset). D-spacings calculated from the FFT correspond to the {001} and {291} lattice planes of T-Nb_2O_5 and the {501} plane of M-Nb_2O_5. EDS data for each area is shown underneath the respective micrograph.

5. The Bi_2O_3-CeO_2 system

5.1 Introduction

Many studies have previously been carried out on each of the ternary systems of interest, however, as yet no samples have been prepared using the resin-gel method to produce nanoparticles in these systems. Examples seen in the literature use a variety of methods to form Bi-Ce, Ce-Nb and Bi-Nb oxides, such as ball milling, hydrothermal, sol-gel and high temperature ceramic methods [148-151]. It was, therefore, interesting to compare the results gathered from samples formed using the resin-gel method, to the structures formed previously using alternative methods.

Initially all samples were calcined at 350 °C and studied using HRTEM, PXRD, EDS and XPS. The samples then underwent a series of heat treatments to see how this affected the homogeneity of the samples. In general, it was found that heating the samples did not change the distribution of metal ions in the structure showing that, although the particles were very small and it may be expected that the arrangement would be more fluid, a significant amount of order was present within the structure. This shows that the enthalpic interactions within the crystallite are the dominant factors in the total free energy of the system. It was found, on the whole, that similar phases were synthesised to those investigated previously, with a range of solid solutions being formed.

The first ternary system investigated was that of Bi_2O_3-CeO_2. The resin-gel synthesis proved successful in producing yellow powders of nanocrystalline mixed oxide nanoparticles, which were then studied using the techniques described above. Compositional analysis using EDS and XPS indicated that the particles were not homogeneous, with bismuth showing a strong preference for surface site occupation.

5.2 Initial results for samples calcined at 350 °C

The PXRD results shown in Figure 5.1 provide good evidence for the formation of a solid solution in the CeO_2-Bi_2O_3 system up until 60% doping of the CeO_2 structure with Bi^{3+} ions. For the first two samples, those of $Bi_{0.2}Ce_{0.8}$ and $Bi_{0.4}Ce_{0.6}$, the only lines present in the pattern are those characteristic of the CeO_2 fluorite structure. Therefore, the Bi^{3+} ions must have been incorporated into the fluorite lattice. As the bismuth concentration is increased to 60% a second phase seems to emerge, as extra peaks can be seen in the pattern, however, it appears that fluorite is still the majority phase. At 80% bismuth substitution a complete phase change occurs to form the α-Bi_2O_3 phase.

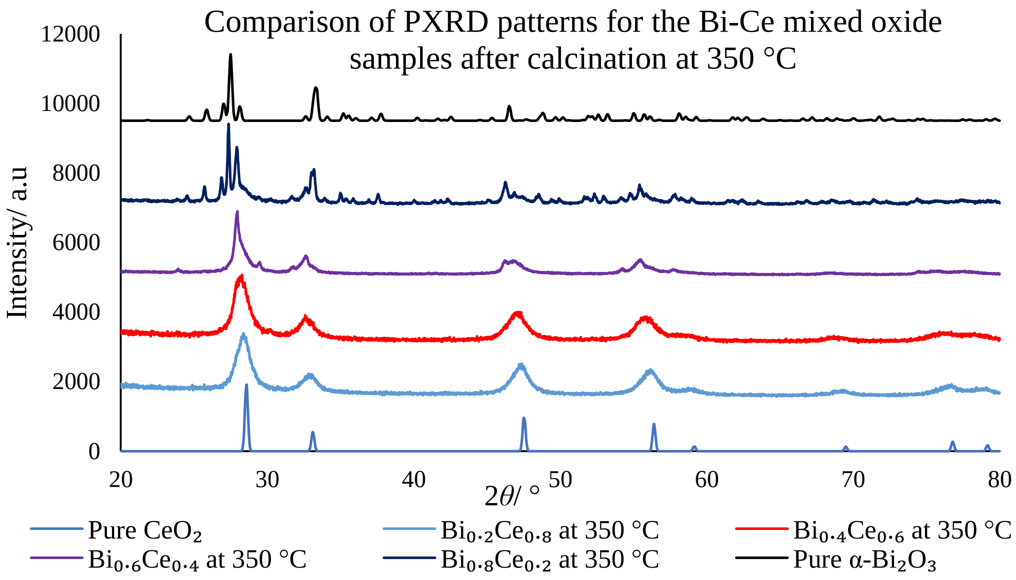

Figure 5.1. PXRD patterns for the range of Bi-Ce oxide compositions synthesised.

Although previous studies have shown that fluorite is relatively tolerant of doping, levels of 60% are particularly high. It may be that the tolerance of the structure is exaggerated in nanoparticle form due to the more relaxed lattice structure. Dikmen *et al*. [152] found that in the Ce-Bi oxide system, the solubility limit was 20% Bi which agreed well with the study carried out by Bourjai *et al*. [153] who also found the solubility limit in the fluorite structure to be 20%. These studies were carried out on particles ranging in size from 20 nm-85 nm. This is substantially larger than the crystallites studied here.

Zhao *et al*. [154] used a Pechini synthesis to produce mixed Bi-Ce oxide nanoparticles of 30 nm in size. They found a fluorite solid solution was produced for samples up to 40% bismuth. After this an α-Bi_2O_3 phase was formed preferentially. These results also agree well with previous studies by Hund who found the emergence of the α-Bi_2O_3 phase after 40% doping [155]. A comparable study carried out by Prekajski *et al*. [156] showed that the solubility limit of the fluorite Bi-Ce oxide particles can be increased to 50% in nanoparticles of 2-3 nm. Li *et al*. [157] and Sardar *et al*. [158] used hydrothermal methods to produce mixed bismuth-cerium oxide nanoparticles of 10-19 nm in size with a solubility limit of 60%. These results agree well with the PXRD evidence from this study.

Consequently, it can be seen from this work and previous studies that solid solutions based on the fluorite structure can readily be formed with bismuth and cerium, with the solubility limit depending heavily on particle size and synthetic method. As particle size decreases, the solubility limit increases due to the more relaxed nature of the crystal lattice which can accommodate the slightly larger bismuth ion more readily. The ionic radius of Bi^{3+} is 1.17 Å compared to 1.15 Å in Ce^{3+} and 1.01 Å in Ce^{4+} [159].

At concentrations of 80% bismuth it appears that there is some rearrangement in the structure as the simple fluorite lattice can no longer accommodate the bismuth ions. The PXRD pattern for the $Bi_{0.8}Ce_{0.2}$ oxide particles matches well to the theoretical pattern for α-Bi_2O_3 structure. Therefore, it appears a phase change takes place moving from the fluorite structure to the α-Bi_2O_3 structure above 60% bismuth doping.

It can also be seen that there is a significant amount of line broadening in the patterns. This is characteristic of nanoparticulate samples as well as the values of 2θ shifting to slightly lower values. Peak broadening can occur in powder diffraction, not only due to crystallite size, but also due to inhomogeneity in the sample. In these samples the formation of a non-ideal solid solution producing regions of differing lattice strain in the crystal could also contribute to peak broadening.

Scherrer analysis was carried out on the PXRD patterns to calculate the mean crystallite value for all samples. The results of this are shown in Figure 5.2. The analysis shows that the crystallite size generally increases as the bismuth concentration is increased. Nevertheless, all samples had calculated crystallite sizes of less than 35 nm, with the mean being 15.18 nm, indicating that the resin-gel method was highly successful in creating nanoparticles.

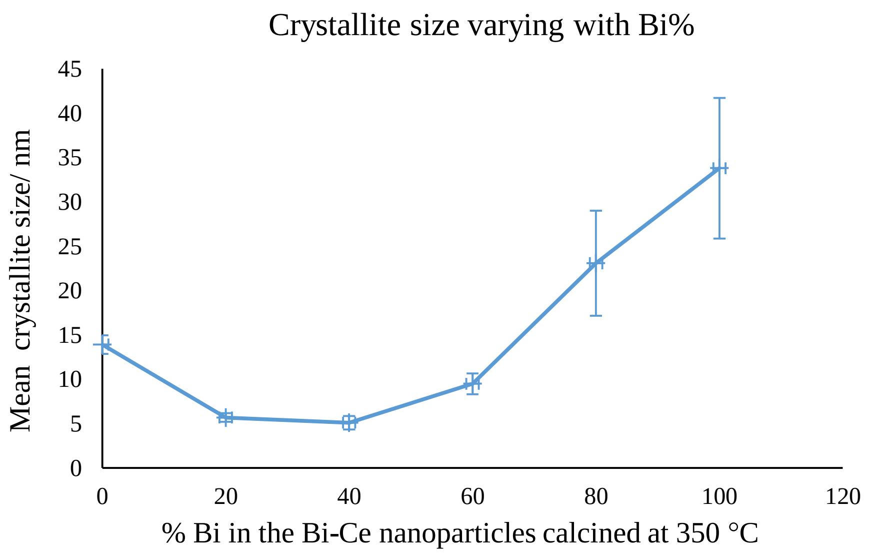

Figure 5.2. Plot showing the relationship between composition and mean crystallite size.

It is important to note, however, that Scherrer analysis can underestimate the crystallite size due to several factors affecting the degree of peak broadening. These factors include: inhomogeneous lattice strain, crystal imperfections such as dislocations, grain boundaries and stacking faults, as well as crystallite size.

EDS data was collected for all samples in order to calculate elemental compositions. Approximately 30 particles were analysed in each sample to get an accurate assessment of how homogeneous the particles were. The resulting data, shown in Figures 5.3-5.6, indicates the relative counts of Ce Lα_1 and Bi Lα_1 across all samples. It can be seen that for the $Bi_{0.2}Ce_{0.8}$, $Bi_{0.4}Ce_{0.6}$ and $Bi_{0.6}Ce_{0.4}$ oxide samples, the compositions appear relatively constant with little deviation of the points from the line of best fit. However, the composition for the $Bi_{0.8}Ce_{0.2}$ oxide sample appear much more inhomogeneous with a large range of different compositions being present in the sample.

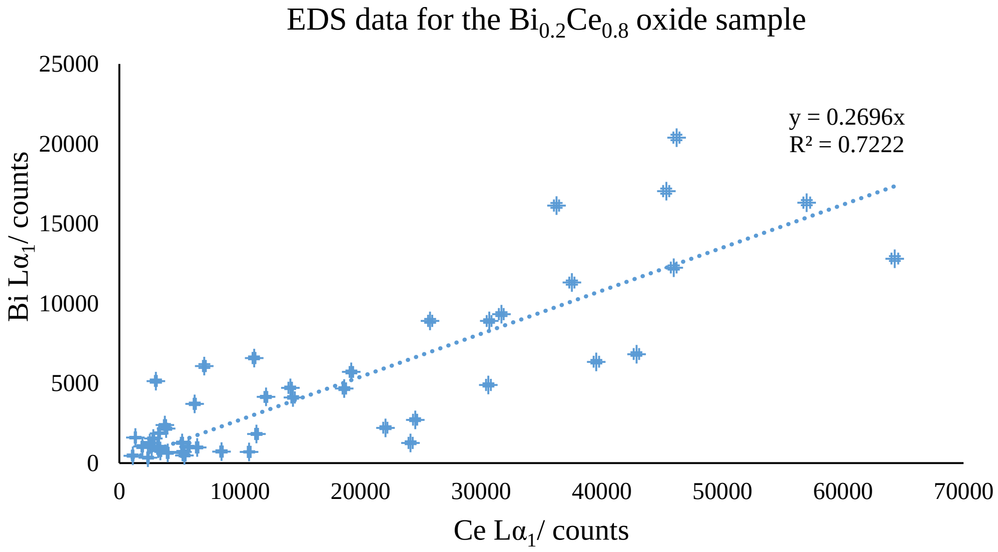

Figure 5.3. EDS plot of Ce Lα_1 counts against Bi Lα_1 for the $Bi_{0.2}Ce_{0.8}$ oxide sample

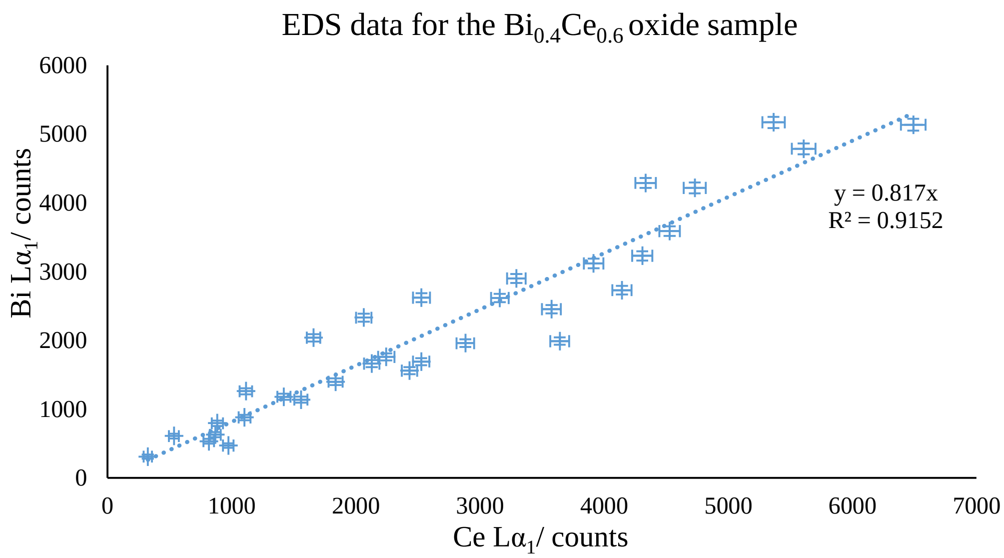

Figure 5.4. EDS plot of Ce $L\alpha_1$ counts against Bi $L\alpha_1$ for the $Bi_{0.4}Ce_{0.6}$ oxide sample.

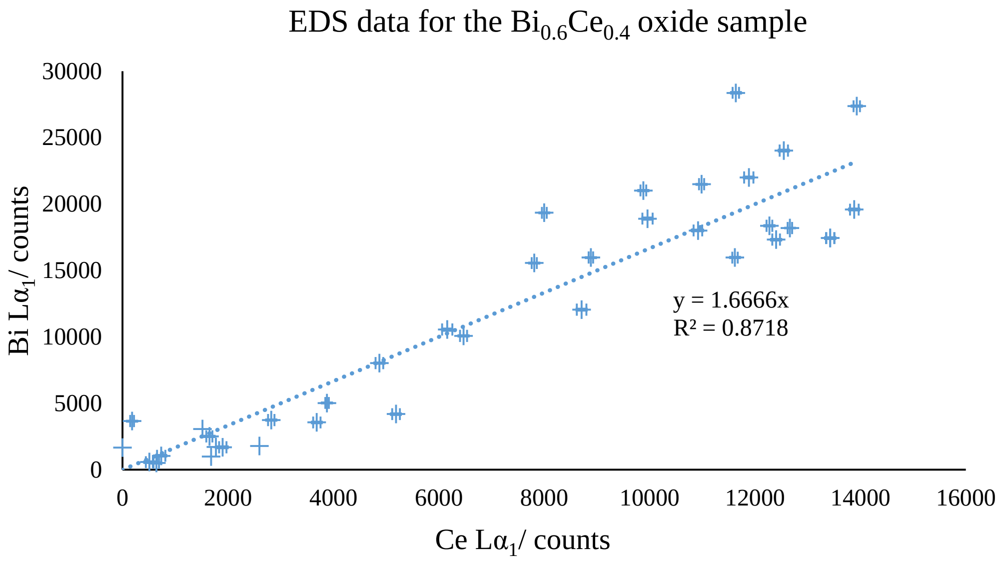

Figure 5.5. EDS plot of Ce $L\alpha_1$ counts against Bi $L\alpha_1$ for the $Bi_{0.6}Ce_{0.4}$ oxide sample

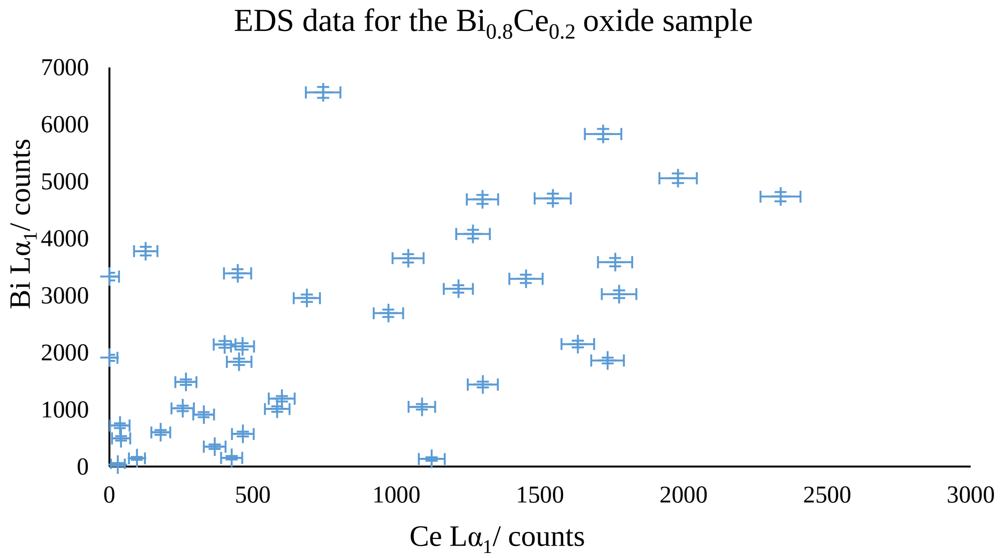

Figure 5.6. EDS plot of Ce Lα₁ counts against Bi Lα₁ for the $Bi_{0.8}Ce_{0.2}$ oxide sample

Some pure Bi_2O_3 nanoparticles were observed in the microscope across all sample compositions indicating that an ideal solid solution had not been formed. The fact that there is no evidence for the α-Bi_2O_3 phase in the PXRD patters for the $Bi_{0.2}Ce_{0.8}$, $Bi_{0.4}Ce_{0.6}$ and $Bi_{0.6}Ce_{0.4}$ oxide samples indicates that it is very much a minority phase which is lost in the background of the PXRD patterns. It should be noted that the EDS spot used for analysis had dimensions of approximately 50-100 Å. This is greater than the mean particle size of 15.18 nm. Therefore, it is possible that the signal was collected from not only the particle being focussed on, but also from surrounding particles. It was hoped that this effect would be minimised by selecting particles on the edge of an agglomerate, however, it is possible that interfering signals from neighbouring particles contributed towards the range in values observed.

From the EDS data, compositions for each sample were calculated using the ratio of Bi:Ce, as seen from the EDS plot, and adjusted using the $K_{Bi:Ce}$value, as calculated from the standard samples. The calculated compositions for each sample can be seen in Table 5.1.

Table 5.1. Calculated composition of the mixed phase in each of the Bi-Ce oxide samples from EDS data.

Sample Bi_2O_3-CeO_2	*Expected % Bi*	*Calculated % Bi from EDS*	*Expected % Ce*	*Calculated % Ce from EDS*
$Bi_{0.2}Ce_{0.8}$	20.00	23.67	80.00	76.33
$Bi_{0.4}Ce_{0.6}$	40.00	48.44	60.00	51.56
$Bi_{0.6}Ce_{0.4}$	60.00	65.71	40.00	34.29
$Bi_{0.8}Ce_{0.2}$	80.00	72.90	20.00	27.10

The calculated compositions from EDS agree fairly well with the expected percentages. As only a small number of particles are observed and analysed in the microscope it is possible that some larger bismuth rich particles were overlooked as they are less suitable for EDS analysis. This could explain why the bismuth percentage is slightly lower than expected for the $Bi_{0.8}Ce_{0.2}$ oxide sample. Contrastingly, the $Bi_{0.6}Ce_{0.4}$ and $Bi_{0.4}Ce_{0.6}$ oxide samples both contained more bismuth than expected. This could be because there were some pure CeO_2 particles which were not analysed as they were smaller in size and, therefore, harder to find in the microscope.

Further structural analysis was carried out in the microscope by calculating lattice spacings for individual crystals using the FFT of the HRTEM images. The results of average d-spacings for the different planes of the fluorite structure in comparison to literature values are seen in Table 5.2.

Table 5.2. Observed d-spacings for each index of the fluorite structure across all Bi-Ce oxide compositions in comparison with literature values. [85]

	Index of fluorite structure							
Sample Bi_2O_3-CeO_2	*Average d-spacing for 111/ Å*	*Literature value/ Å*	*Average d-spacing for 200/ Å*	*Literature value/ Å*	*Average d-spacing for 220/ Å*	*Literature value/ Å*	*Average d-spacing for 311/ Å*	*Literature value/ Å*
Ce100 %	3.16 ± 0.06	3.12	2.78 ± 0.12	2.71	1.92 ± 0.06	1.91	1.7 ± 0.02	1.63
$Bi_{0.2}Ce_{0.8}$	3.23 ± 0.08	3.12	2.89 ± 0.13	2.71	2.28 ± 0.47	1.91	-	-
$Bi_{0.4}Ce_{0.6}$	3.33 ± 0.17	3.12	2.77 ± 0.09	2.71	2.21 ± 0.26	1.91	1.86 ± 0.02	1.63
$Bi_{0.6}Ce_{0.4}$	3.23 ± 0.11	3.12	2.80 ± 0.09	2.71	2.39 ± 0.00	1.91	1.61 ± 0.04	1.63
$Bi_{0.8}Ce_{0.2}$	3.19 ± 0.10	3.12	-	-	-	-	-	-

These results show that the observed d-spacings across all the mixed oxide nanoparticles compositions are considerably larger than standard values observed in the literature. This is what was expected due to the more relaxed crystal lattice in nanoparticles. From these values the unit cell lattice parameters could be calculated according to the following relationship for a cubic lattice and compared to literature values:

$$d_{hkl} = \frac{a}{\sqrt{h^2 + k^2 + l^2}}$$

The results of these calculations are seen in Table 5.3. All values for the α-Bi_2O_3 cell parameters were calculated from FullProf analysis of the PXRD patterns for these samples. Calculated errors for these measurements were < 1% The general trend in unit cell parameters was as expected, with the nanoparticles showing slightly higher values in comparison with the literature due to the decreased lattice strain in nanoparticles and, therefore, a more relaxed and larger unit cell. As the bismuth concentration increased, generally the lattice parameters increased proportionally more due to the bismuth ions having a larger ionic radius.

Table 5.3. Unit cell parameters calculated for all Bi-Ce oxide samples compared to literature values. [160, 35]

					Unit Cell Parameter Length/ Å			*Unit Cell Parameter Literature Length/ Å*		
Ratio Bi:Ce	*Phase*	*θ/ rads*	*Index*	*d_{hkl}/ Å*	*a*	*b*	*c*	*a*	*B*	*c*
0:100	CeO_2	0.247 0.286 0.412 0.490	111 200 220 311	3.16 2.73 1.92 1.64	5.47	5.47	5.47	5.41	5.41	5.41
20:80	CeO_2	0.249 0.287 0.413 0.491	111 200 220 311	3.14 2.72 1.92 1.64	5.44	5.44	5.44	5.41	5.41	5.41
40:60	CeO_2	0.246 0.285 0.410 0.489	111 200 220 311	3.17 2.74 1.93 1.64	5.49	5.49	5.49	5.41	5.41	5.41
60:40	CeO_2	0.244 0.284 0.403	111 200 220	3.19 2.75 1.97	5.53	5.53	5.53	5.41	5.41	5.41
80:20	α-Bi_2O_3	0.225 0.244 0.290	002 112 200	3.46 3.19 2.70	5.85	8.17	7.51	5.85	8.17	7.51
100:0	α-Bi_2O_3	0.290 0.170 0.225	200 020 002	2.70 4.44 3.46	5.87	8.18	7.52	5.85	8.17	7.51

A plot of the data shown above in Table 5.3 is represented in Figure 5.7. It shows clearly at what point a phase change occurs in the bismuth-cerium mixed oxide solid solution system as there is a large increase in lattice parameter a with 80% bismuth concentration. It is at this point that the fluorite structure is forced to change and adopt the α-Bi_2O_3 monoclinic structure.

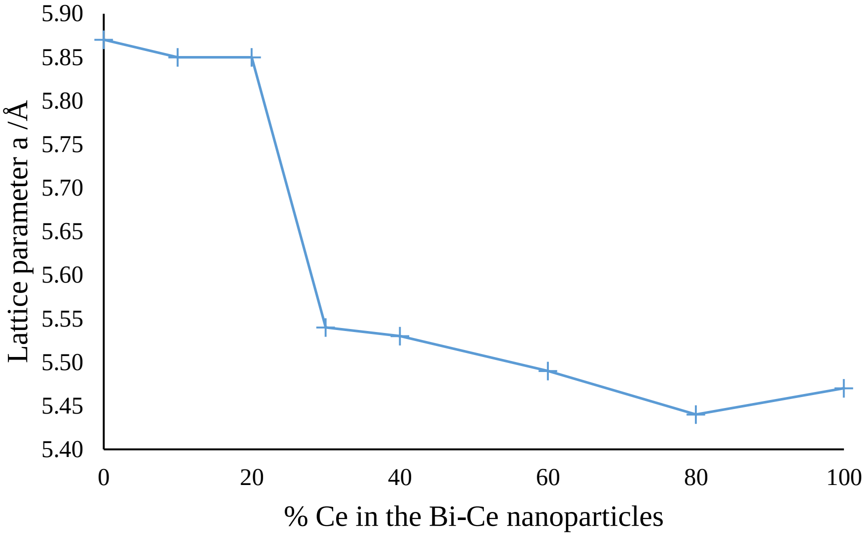

Figure 5.7. Plot showing how the lattice parameter, a, varies with composition.

5.2.1 HRTEM imaging

A large range of particles were studied and imaged in the HRTEM. This allowed comparison of particle sizes with the values calculated from Scherrer analysis and also allowed identification of phases in the samples due to fringe spacing analysis. The micrographs seen in Figures 5.8 to 5.15 are representative examples of the particles seen in the HRTEM for the Bi-Ce oxide nanoparticles.

Figure 5.8 shows a typical region of fluorite nanoparticles from the $Bi_{0.2}Ce_{0.8}$ oxide sample. The small size of the particles (~ 5 nm) agrees well with Scherrer analysis. D-spacings were calculated from the FFT in order to confirm which phase was present. The values calculated corresponded well to the spacings of the {111} and {200} fluorite lattice planes, in agreement with PXRD data. The micrograph shows a large agglomerated region of nanoparticles which was typical across all samples. As the samples tended to agglomerate in this way, imaging of a single isolated nanoparticle was difficult. Despite the agglomeration of nanoparticles, clear fringes could still be observed. Figure 5.9 is a further example of the micrographs collected for the $Bi_{0.2}Ce_{0.8}$ oxide sample. It shows several overlapping nanoparticles with fringe spacings correlating to the {111} and {200} fluorite lattice planes. The EDS spectra, included in Figures 5.8 and 5.9, both indicate the presence of bismuth and cerium in the particles showing a mixed oxide has been formed. The gold and copper signals are from the TEM grid and the specimen holder in the microscope.

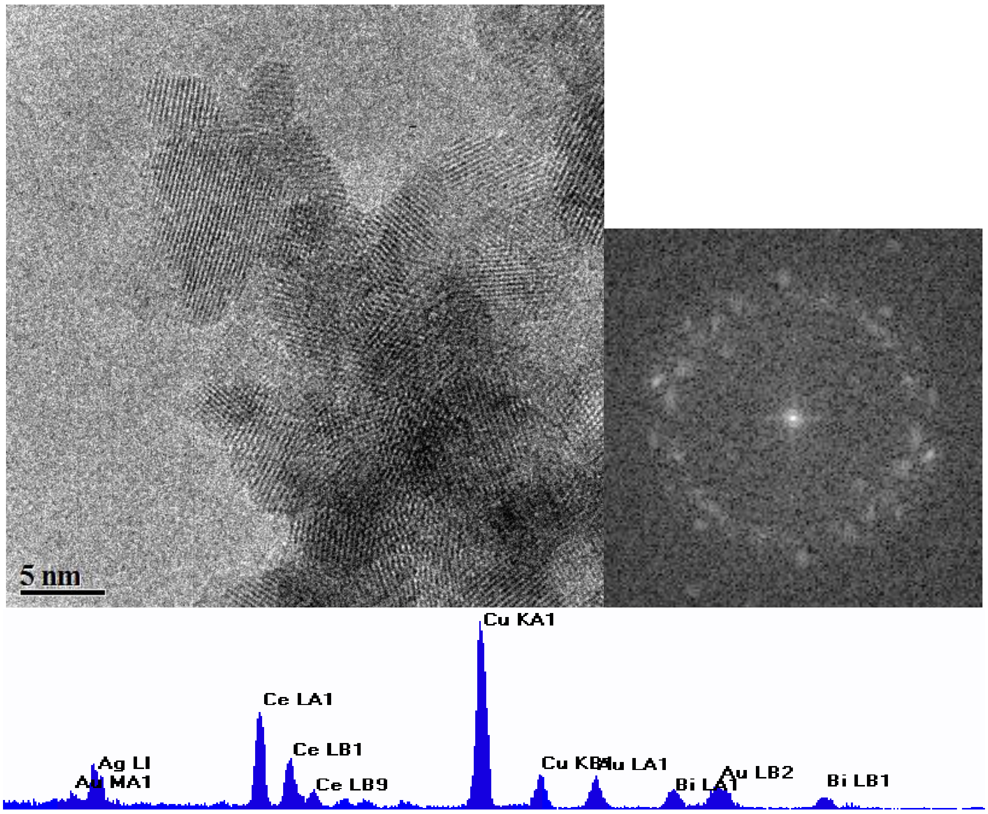

Figure 5.8. HRTEM micrograph of a polycrystalline region of the $Bi_{0.2}Ce_{0.8}$ *sample (l) with corresponding FFT (r). EDS spectra for the area shown below.*

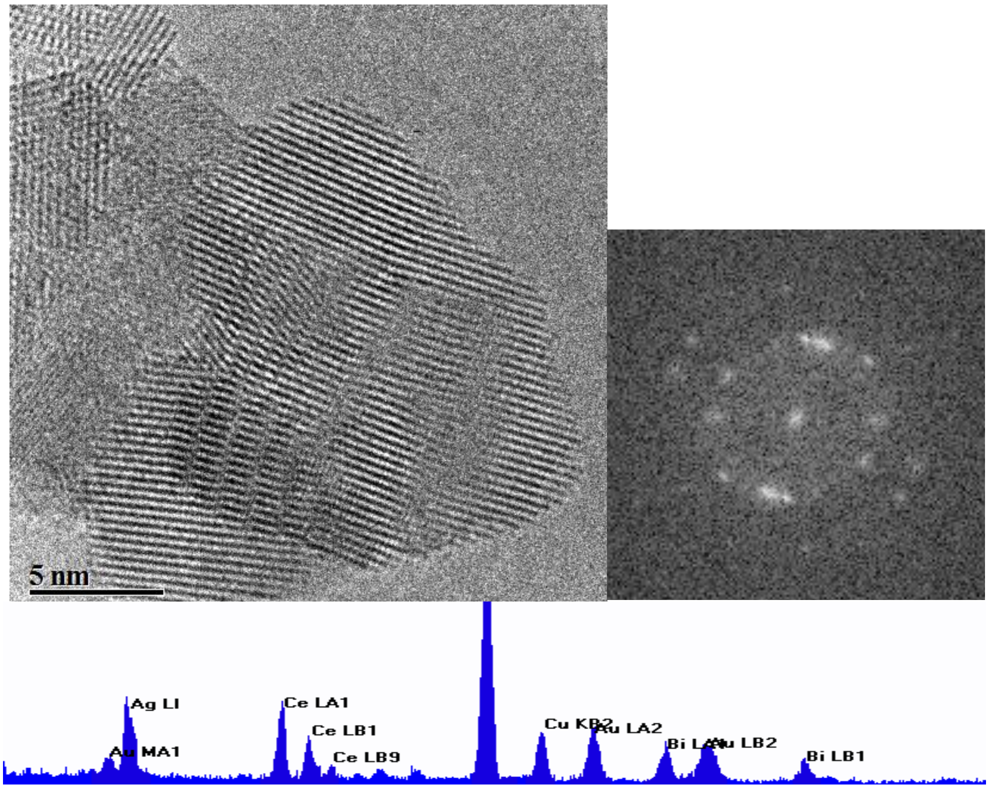

Figure 5.9. HRTEM micrograph of the $Bi_{0.2}Ce_{0.8}$ *sample (l) with corresponding FFT (r). EDS spectra for the area shown below.*

The micrographs shown in Figures 5.10 and 5.11 are from the $Bi_{0.4}Ce_{0.6}$ oxide sample. They, again, show agglomerated regions of fluorite nanoparticles, confirmed by fringe spacing analysis. The particles shown in Figure 5.10, have calculated d-spacings of 3.14 and 2.92 Å, indicating the {111} and the {200} lattice planes of a fluorite crystal are being observed. Again, this agrees well with the PXRD data. Similarly, fringe spacing analysis for the crystal shown in Figure 5.11 indicates the {200} lattice plane of fluorite being observed. For both regions of crystals, EDS indicated that both cerium and bismuth were present in the nanoparticles.

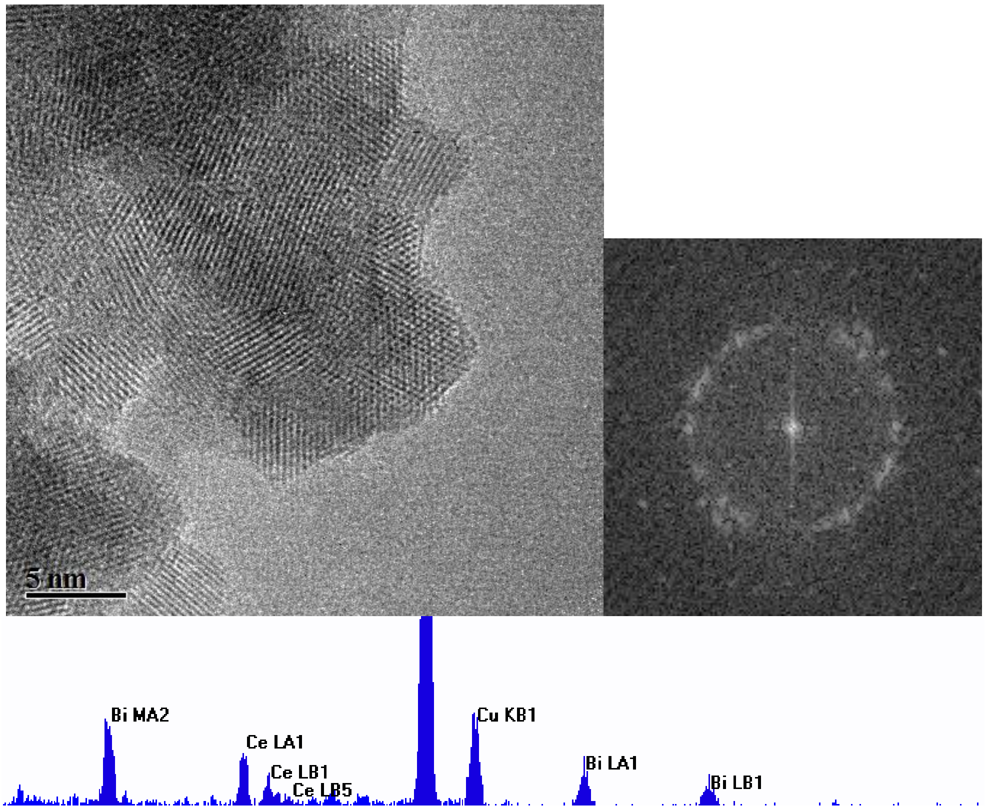

Figure 5.10. HRTEM micrograph of the $Bi_{0.4}Ce_{0.6}$ *sample (l) with corresponding FFT (r). EDS spectra for the area shown below.*

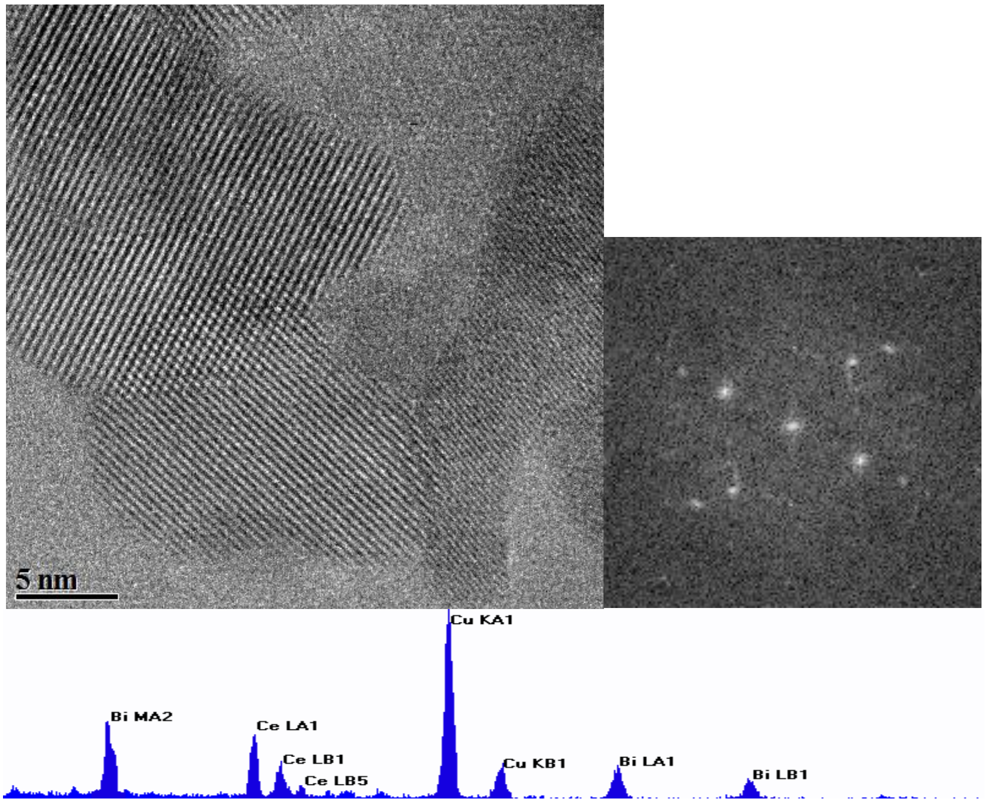

Figure 5.11. HRTEM micrograph of the $Bi_{0.4}Ce_{0.6}$ *sample (l) with corresponding FFT (r). EDS spectra for the area shown below.*

When the $Bi_{0.6}Ce_{0.4}$ oxide sample was analysed in the HRTEM, it was apparent that two phases were present. This was expected from the PXRD results, as there were lines in addition to the expected fluorite pattern. Fringe space analysis showed that there were large crystals of α-Bi_2O_3 present in the sample. An example of this is seen in Figure 5.12. EDS confirmed that the large crystals consisted only of bismuth oxide as no cerium peaks were observed. D-spacings for this region were calculated to be 3.57, 3.33 and 3.26 Å indicating the {102}, {121} and {11-1} lattice planes were observed.

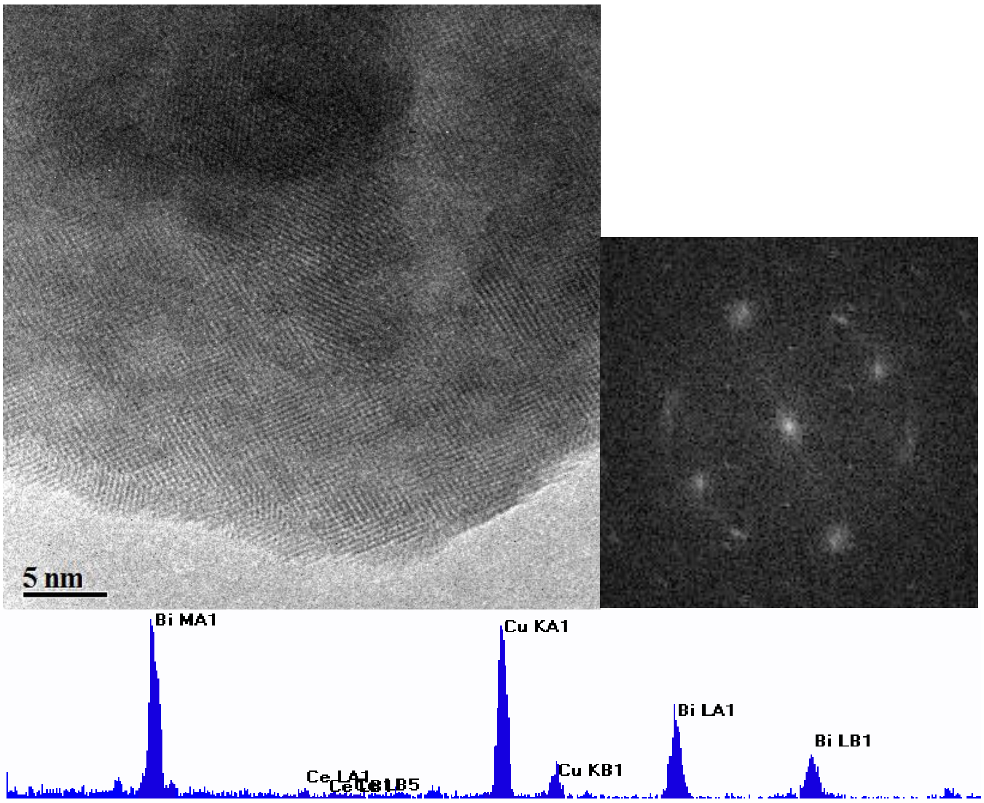

Figure 5.12. HRTEM micrograph of the $Bi_{0.6}Ce_{0.4}$ sample (l) with corresponding FFT (r). EDS spectra for the area shown below.

Figure 5.13 also presents a micrograph from the $Bi_{0.6}Ce_{0.4}$ oxide sample, however, this region shows an agglomerate of fluorite nanoparticles, as confirmed by fringe spacing analysis indicating d-spacings corresponding to the {111} and {200} lattice planes. EDS for this area shows that a mixed oxide has been formed as there are peaks indicating the presence of bismuth and cerium.

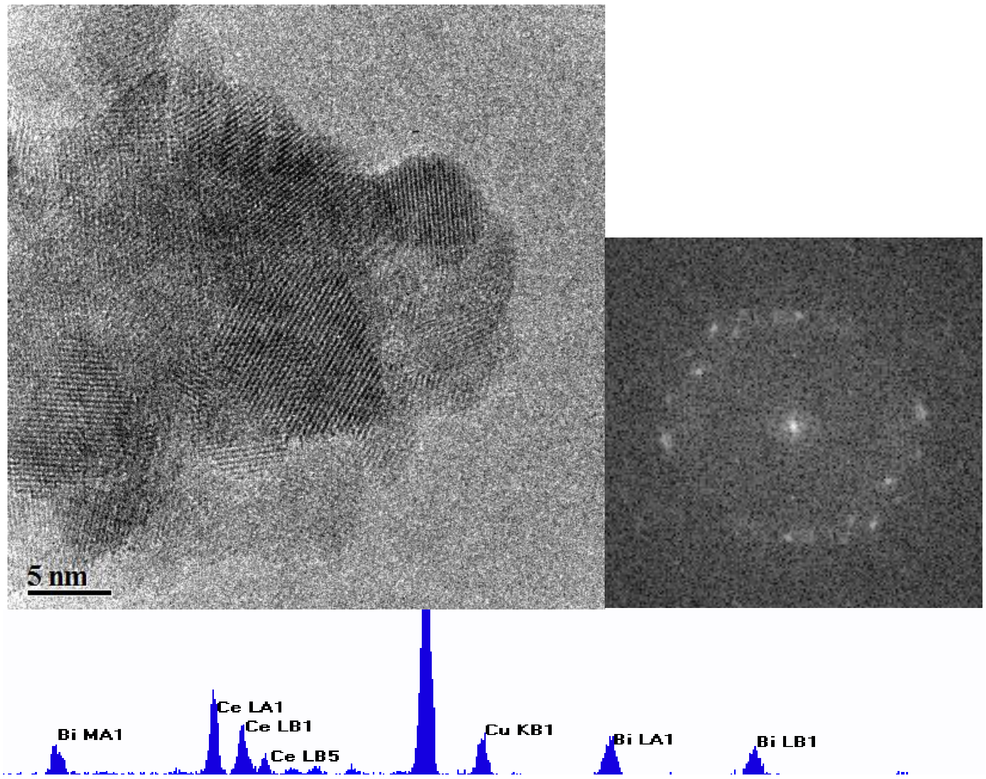

Figure 5.13. HRTEM micrograph of the $Bi_{0.6}Ce_{0.4}$ sample (l) with corresponding FFT (r). EDS spectra for the area shown below. D-spacings of 3.15 Å and 2.82 Å indicate the {111} and {200} lattice planes of fluorite.

Finally, the micrographs for the $Bi_{0.8}Ce_{0.2}$ oxide sample are seen in Figure 5.14 and 5.15. The vast majority of particles seen in this sample had the α-Bi_2O_3 structure. An example of this is seen in Figure 5.14. Calculated d-spacings for this crystal were found to be 2.96 Å, indicating that the {012} lattice plane was being observed. EDS showed that there was no cerium present in the α-Bi_2O_3 phase.

There was second minority phase with the fluorite structure, an example of which can be seen in Figure 5.15. The micrograph show an agglomerate of fluorite particles, with the FFT indicating d-spacings of 3.18 Å. This is indicative of the {111} plane in the fluorite structure. The EDS spectrum indicates that both bismuth and cerium are present in these particles.

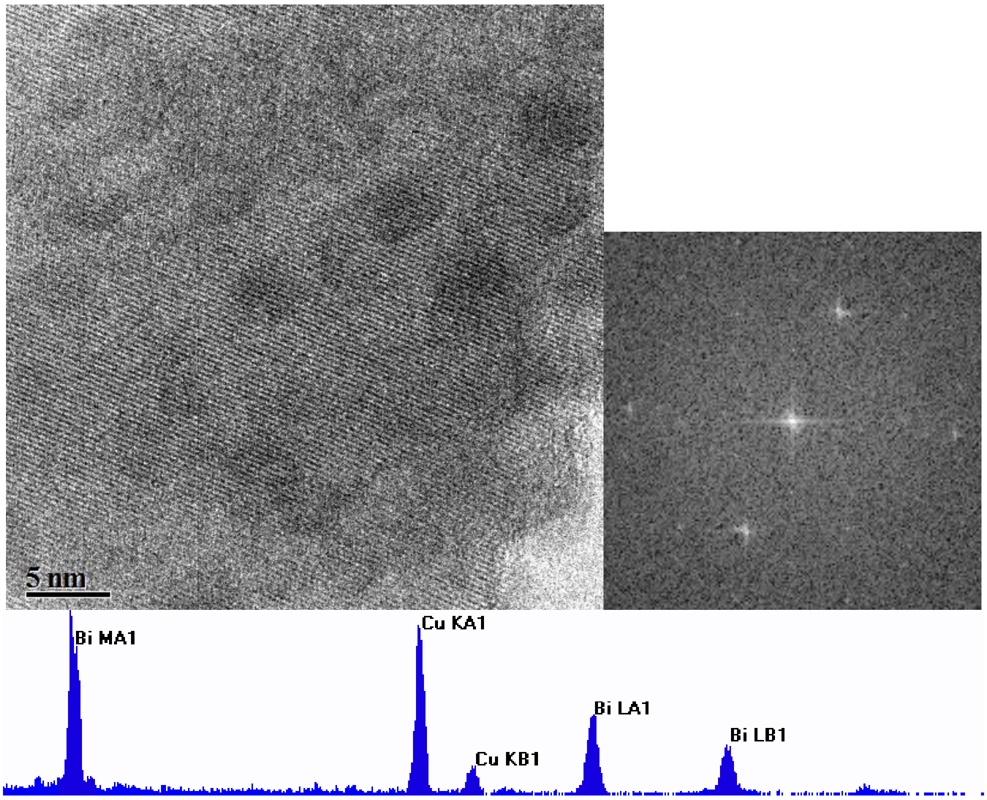

Figure 5.14. HRTEM micrograph of the $Bi_{0.8}Ce_{0.2}$ sample (l) with corresponding FFT (r). EDS spectra for the area shown below.

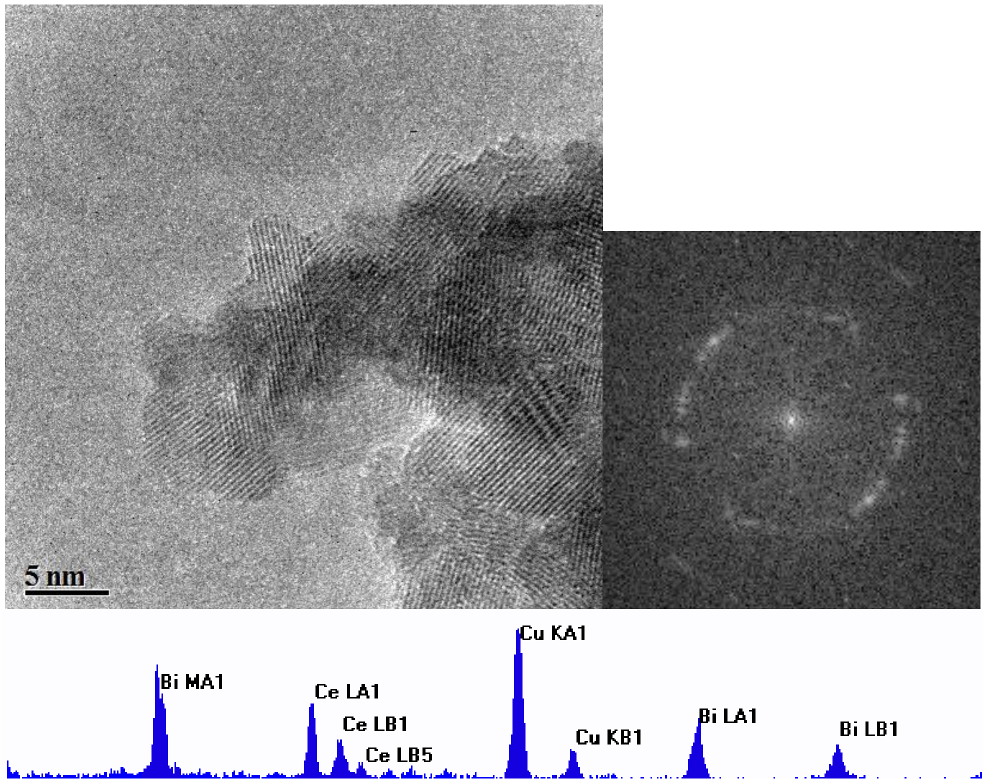

Figure 5.15. HRTEM micrograph of a polycrystalline region of the $Bi_{0.8}Ce_{0.2}$ sample (l) with corresponding FFT (r). EDS spectra for the area shown below.

5.2.2 XPS analysis

After initial analysis using HRTEM and PXRD data, it was decided to probe the structures further using XPS. This would enable comparison between the overall composition of the nanoparticles as calculated from EDS and the surface compositions, which could be acquired from XPS analysis. This would conclusively determine if the nanoparticles were homogeneous and had formed ideal solid solutions, or if certain metal ions showed site preferences giving a more ordered structure.

A representative XPS survey scan is shown in Figure 5.16, indicating the peaks corresponding to the Ce 3d, the O 1s and the Bi 4f electron binding energies, as well as the overall surface composition of the sample.

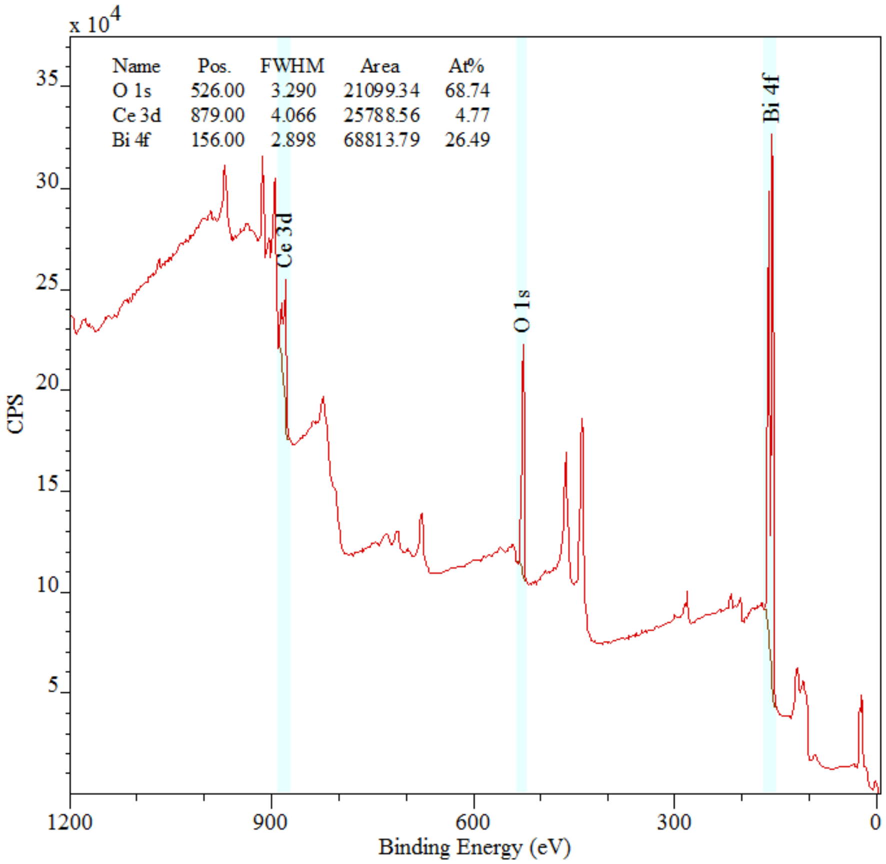

Name	Pos.	FWHM	Area	At%
O 1s	526.00	3.290	21099.34	68.74
Ce 3d	879.00	4.066	25788.56	4.77
Bi 4f	156.00	2.898	68813.79	26.49

Figure 5.16. XPS survey scan for the $Bi_{0.4}Ce_{0.6}$ *oxide sample.*

Results from XPS analysis can be seen in Table 5.4. They show a much higher percentage of bismuth present at the surface, in all samples, than expected indicating bismuth has a very strong preference to occupy surface sites.

Table 5.4. XPS results for the Bi-Ce oxide nanoparticles showing the surface composition.

Sample Bi_2O_3-CeO_2	Atom & Orbital	Binding Energy/ eV	Atomic Concentration/ %
$Bi_{0.2}Ce_{0.8}$ at 350 °C	Bismuth 4f	161.08	80.16
	Cerium 3d	885.08	19.84
$Bi_{0.4}Ce_{0.6}$ at 350 °C	Bismuth 4f	156.00	84.74
	Cerium 3d	879.00	15.26
$Bi_{0.6}Ce_{0.4}$ at 350 °C	Bismuth 4f	155.00	88.44
	Cerium 3d	878.00	11.56
$Bi_{0.8}Ce_{0.2}$ at 350 °C	Bismuth 4f	155.00	93.35
	Cerium 3d	878.00	6.65

Comparing the particle compositions as shown by EDS to those by XPS (Table 5.5), it becomes clear that the mixed oxide particles are far from homogeneous, with bismuth showing strong preference for surface site occupation. Olsen *et al*. [161] studied the electronic structure of bismuth in Bi_2S_3, using DFT calculations, in order to understand how the bismuth lone pair effects the local geometry and coordination environment. Their results agreed strongly with previous studies [162, 163, 47], which suggest that bismuth prefers to coordinate asymmetrically to accommodate its lone pair of s electrons. This argument is also applicable to the studies carried out in this thesis and would explain why there is such discrepancy between the compositions calculated from EDS and XPS results. By coordination at surface site, the bismuth atoms have more room to accommodate the lone pair as they are coordinated asymmetrically due to the nature of the surface arrangement. The cerium atoms have no preference for surface sites and will maximise the enthalpy of the structure by occupying the 8 coordination sites in the structure.

Table 5.5. Comparison of overall particle composition calculated from EDS analysis and surface composition from XPS.

Sample Bi_2O_3-CeO_2	%Ce from EDS	%Ce from XPS	%Bi from EDS	%Bi from XPS
$Bi_{0.2}Ce_{0.8}$ at 350 °C	75.30	19.84	24.70	80.16
$Bi_{0.4}Ce_{0.6}$ at 350 °C	51.56	15.26	48.44	84.74
$Bi_{0.6}Ce_{0.4}$ at 350 °C	34.29	11.56	65.71	88.44
$Bi_{0.8}Ce_{0.2}$ at 350 °C	27.10	6.65	72.90	93.35

From XPS it is also possible to calculate the proportion of Ce^{3+} to Ce^{4+} due to the various doublets that both species produce of slightly differing binding energies. Peak fitting analysis was carried out on the high resolution Ce 3d scan in order to differentiate between the two Ce species and generate quantitative data relating the proportions of the two Ce oxidation states present at the surface of the particles. A representative Ce 3d scan showing the peak fitting routine is shown in Figure 5.17. A Shirley background is also used in this process.

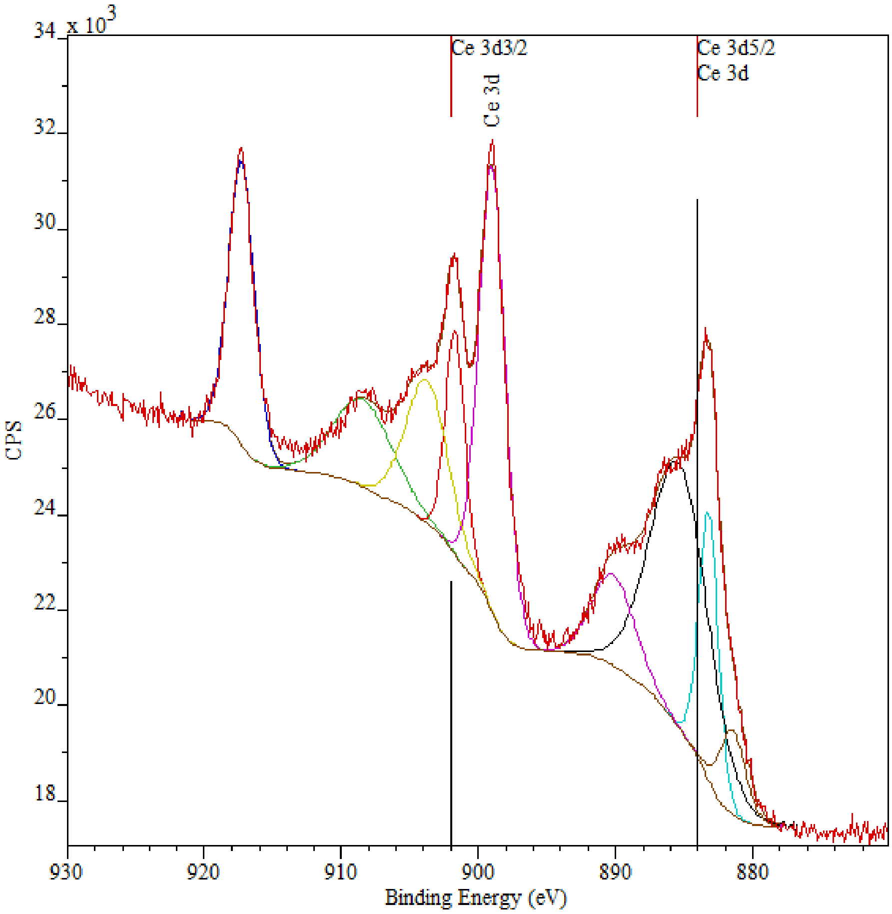

Figure 5.17. Representative scan of Ce 3d showing peak fitting to calculate proportions of Ce^{3+} and Ce^{4+} present at the surface of the samples.

The results in Table 5.6 show the percentages calculated for each Ce species in the Bi-Ce samples. It can be seen that there is very little variation in the percentages of each species across the four compositions. On average 82.91% of Ce^{4+} and 17.09% of Ce^{3+} is found at the surface, meaning there is considerably more Ce^{3+} present in these mixed oxide nanoparticles than have been found in previous XPS studies of CeO_2. For example, Noronha *et al*. found 10.48% Ce^{3+} present at the surface of their CeO_2 catalyst on a Pt support [164]. This value is similar to calculated percentages on pure CeO_2 samples by Shyu *et al*. [165] of 13.4% Ce^{3+} and 13.5% by Abi-aad *et al*. [166]. These studies were not on nanoparticles which may explain the difference in Ce(III) and Ce(IV) proportions.

Table 5.6. Results from peak fitting analysis showing the relative proportions of Ce^{3+} and Ce^{4+} species in each sample.

Sample Bi_2O_3-CeO_2	% Ce^{3+}	STDEV	%Ce^{4+}	STDEV
$Bi_{0.2}Ce_{0.8}$ at 350 °C	16.40	1.87	83.60	1.87
$Bi_{0.4}Ce_{0.6}$ at 350 °C	16.32	0.76	83.68	0.76
$Bi_{0.6}Ce_{0.4}$ at 350 °C	17.14	0.81	82.86	0.81
$Bi_{0.8}Ce_{0.2}$ at 350 °C	18.52	1.30	81.48	1.30

5.2.3 Analysis of trends and correlation of all analytical data

Here it has been shown that mixed metal oxide nanoparticles in the Bi-Ce system can be synthesised successfully using a resin-gel method. Looking in detail at the phases seen using HRTEM and PXRD, we can see that up to and including 40% bismuth substitution, the structure adopts a fluorite-based CeO_2 phase. Based on the EDS data, it seems a fluorite solid solution has formed. This was expected due to the lattice structure being more relaxed in nanoparticles making a solid solution more accessible due to greater ease of permeation of atoms. PXRD results are also in agreement with the hypothesis that the lattice relaxes due to the slight peak shifts observed. Line broadening Scherrer analysis approximates the particles size range as 5-23 nm. At 60% substitution of bismuth, the PXRD pattern becomes more complicated than the standard CeO_2 pattern. EDS suggests two phases are present, both mixed bismuth-cerium phases but with one richer in cerium than the other. However, at 80% bismuth substitution the pattern changes significantly and matches well to the pattern of α-Bi_2O_3. It therefore appears that between 60% and 80% bismuth substitution, the structure must undergo a phase change, as the CeO_2 fluorite structure is no longer able to accommodate the bismuth. EDS data indicates that a range of compositions are present.

Overall, the results concur with those from Sardar *et al.* [158] who demonstrated that the CeO_2 structure is highly tolerant of bismuth substitution down to the nominal composition $Ce_{0.4}Bi_{0.6}O_{1.7}$. This level of substitution is higher than seen previously, for example in studies by Li *et al.* [157] the maximum bismuth substitution was seen to be 50%. The study indicated that the anion vacancies accompanying the bismuth substitution were disordered, although the pair distribution function suggested that some local ordering of the oxygen vacancies was occurring. Therefore, the limiting factor of bismuth substitution within the CeO_2 structure must be the ordering of the anion vacancies causing the distortion of the anion framework leading to the formation of the α-Bi_2O_3 structure with some ceria impurities.

A possible explanation for the phase change between 60% and 80% bismuth substitution follows from the explanation in Chapter 3 describing the equilibrium of the ions in the gel:

The nanoparticles can only form once the ions have been deposited into the matrix by the molten polymer during the 'burn off'. Throughout this process, the metal ions in solution with molten polymer are in equilibrium with the solid matrix. This can be compared to the equilibrium between solid and liquid solutions (see Figure 5.18).

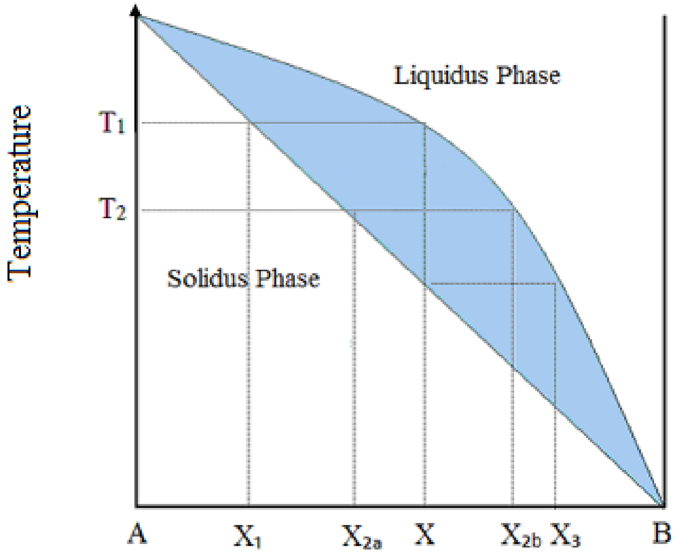

Figure 5.18. Phase diagram for a solid solution in equilibrium with liquid.

This phase diagram demonstrates how a liquid of composition, X, heated at temperature T_1 will form a solid with composition of X_1 which is more rich in element A than the original composition. As the temperature is lowered to T_2, the solid formed has a composition of X_{2a} which is less rich in A than the previous temperature. This process continues and eventually, as the temperature is lowered, all of the solid will have the required composition X, and the liquid has composition X_3. Annealing the sample for an extended period can form a homogeneous solid, but usually a solid with a variable composition results. It is likely that this is the case for the CeO_2-Bi_2O_3 system up to approximately 60% bismuth, but as the percentage of bismuth increases, a more complicated system emerges. The possible phase diagram for the entire CeO_2-Bi_2O_3 system is shown in Figure 5.19.

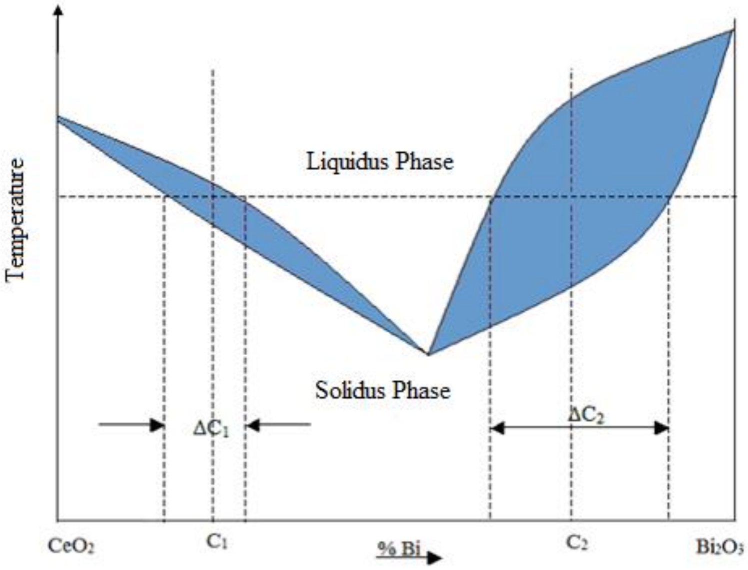

Figure 5.19. Proposed phase diagram for the CeO_2*-*Bi_2O_3 *system.*

In this diagram the behaviour at the two ends of the system varies greatly. At the cerium rich end, the difference between the solidus and liquidus curves is small in comparison to the bismuth rich end. As the difference is small at the cerium rich end, there is not a huge range of compositions formed making the specimen relatively homogeneous. However, at the bismuth rich end, as the difference between the solidus and liquidus curves is quite large, the particles produced are more likely to have variable composition. It is highly possible this is the case in the CeO_2-Bi_2O_3 system as the gap between the solid and liquid phase is a function of the latent heat of melting. Changing from a disordered fluorite structure to a more ordered monoclinic phase is therefore likely to produce a large change in enthalpy. A comparison between the cubic and monoclinic structures is shown in Figure 5.20.

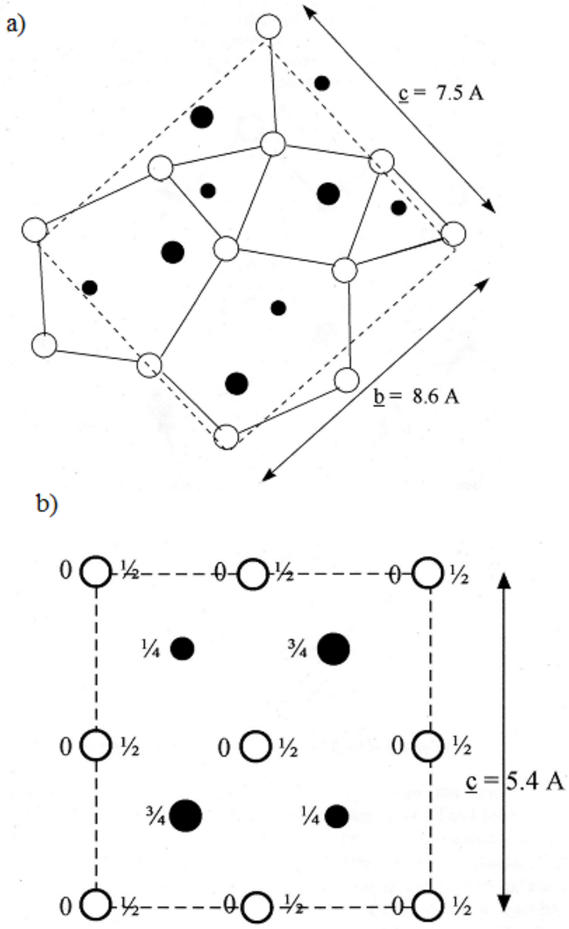

Figure 5.20. a) shows the monoclinic structure of the Bi_2O_3 phase, b) shows the structure of CeO_2, with both being projected on the 100) planes (black spheres represent anions, white spheres represent cations).

A possible mechanism for the transformation of the cubic phase to the monoclinic phase is shown below (Figure 5.21). It involves a series of oxygen removals coupled with oxygen and cation shifts to produce the α-Bi_2O_3 structure.

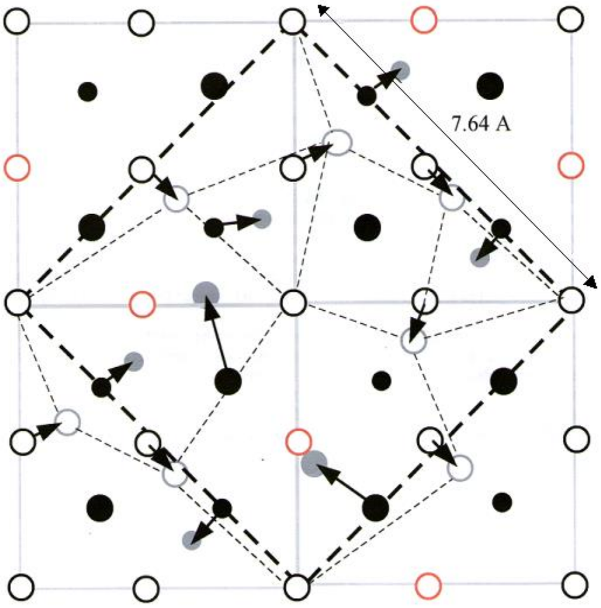

Figure 5.21. The monoclinic α-Bi_2O_3 structure and cubic CeO_2 structure projected onto the (100) planes of their respective unit cells.

Although there is little similarity between the two structures, |b| and |c| in the monoclinic cell are approximately equal to √ 2 x |c| for the cubic cell. The diagram shows the oxygen layer at x= ½ in four unit cells of CeO_2 with the associated bismuth atoms at x= ½ and ¾, depicted by small and large filled circles respectively. If the oxygen atoms in red are removed and other bismuth and oxygen atoms are displaced, then an α-Bi_2O_3 layer is created. The Bi^{3+} ion can be either 5 or 6 coordinate due to the lone pair of electrons.

5.3 Thermal treatments

Samples were heated at 500 °C and 700 °C for 7 days under flowing oxygen in order to see how the particles changed with temperature. It was theorised that by heating at these temperatures, the particles would become more homogenous, with a consistent composition seen in each sample, without any substantial sintering of nanoparticles. Above these temperature, studies would not be reliable as bismuth is very volatile and likely to be lost. In addition to any loss of bismuth, a significant amount of sintering would occur, defeating the purpose of studying nanoparticulate behaviour.

The PXRD patterns for the $Bi_{0.2}Ce_{0.8}$ oxide nanoparticles calcined at 350 °C, 500 °C and 700 °C are seen in Figure 5.22. It can be seen from the patterns that no phase changes occurred whilst heating at these temperatures and the fluorite phase remained stable. The only difference between the patterns is that the peaks become sharper and less broad as the temperature increases. This is due to improved crystallinity and a larger particle size.

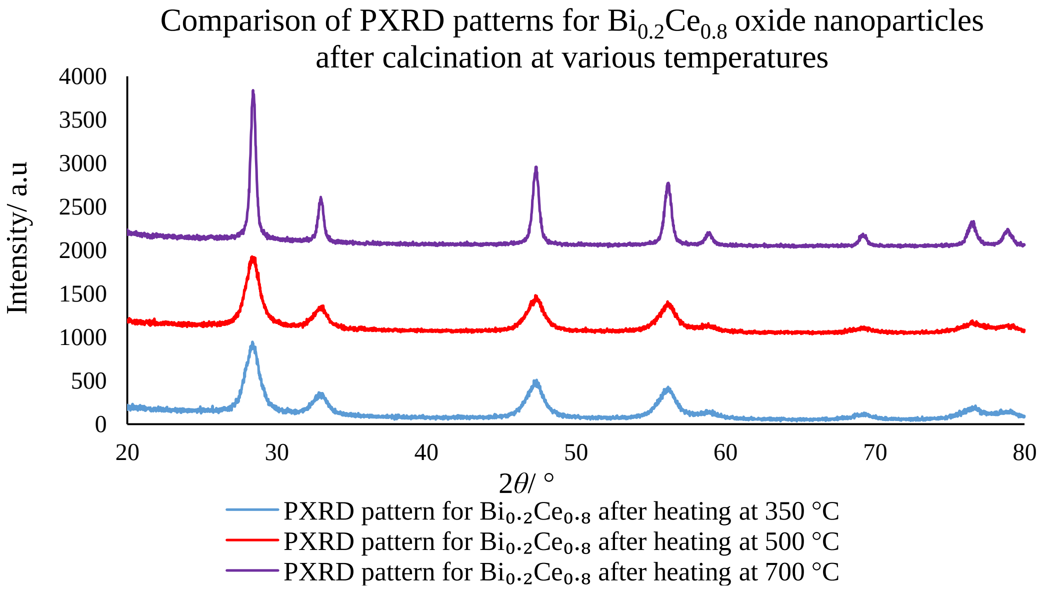

Figure 5.22. PXRD patterns of the $Bi_{0.2}Ce_{0.8}$ oxide nanoparticles after heating in the tube furnace at various temperatures for 7 days.

Likewise, the series of patterns for the $Bi_{0.4}Ce_{0.6}$ oxide sample, seen in Figure 5.23, show that the fluorite phase remains stable up to 500 °C. At 700 °C, however, an extra peak is seen in the pattern at 30 ° which could suggest a change in the fluorite F-lattice structure. Either a new minority phase is emerging or there is sufficient structure change in the fluorite structure to cause new peaks.

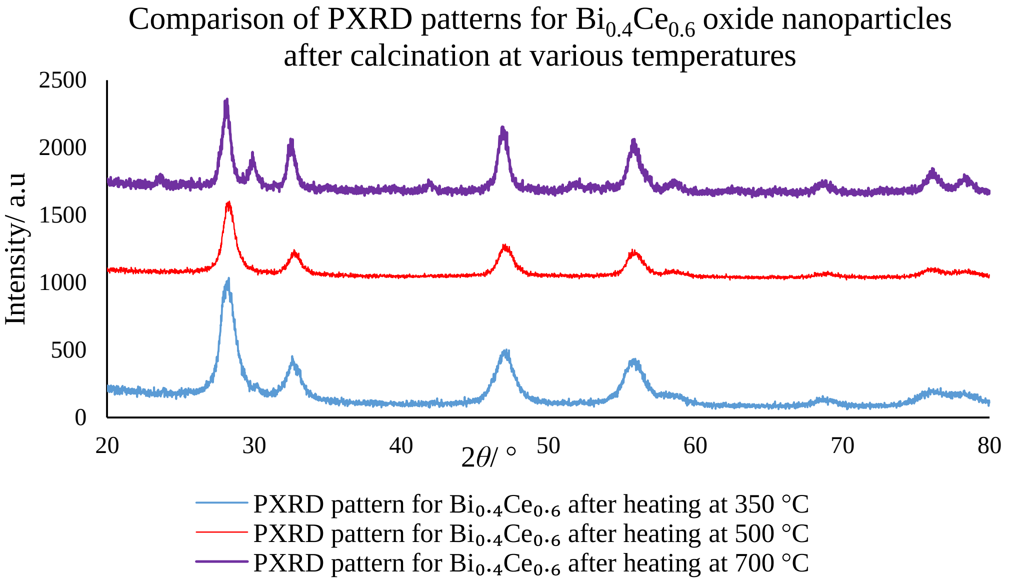

Figure 5.23. PXRD patterns of the $Bi_{0.4}Ce_{0.6}$ *oxide nanoparticles after heating in the tube furnace at various temperatures for 7 days.*

The PXRD patterns for the $Bi_{0.6}Ce_{0.4}$ oxide sample, seen in Figure 5.24, indicate that a phase change may have occurred through the heating process as several new peaks appeared at higher temperatures. However, it could also be the case that the peaks were just more resolved due to the decreased peak broadening at higher temperatures. If this is the case then the sample would consist of two phases: fluorite and α-Bi_2O_3. Both these phases had previously been identified in the microscope. It is also possible that more α-Bi_2O_3 evolved from the mixed phase at higher temperature as this is more thermodynamically favourable.

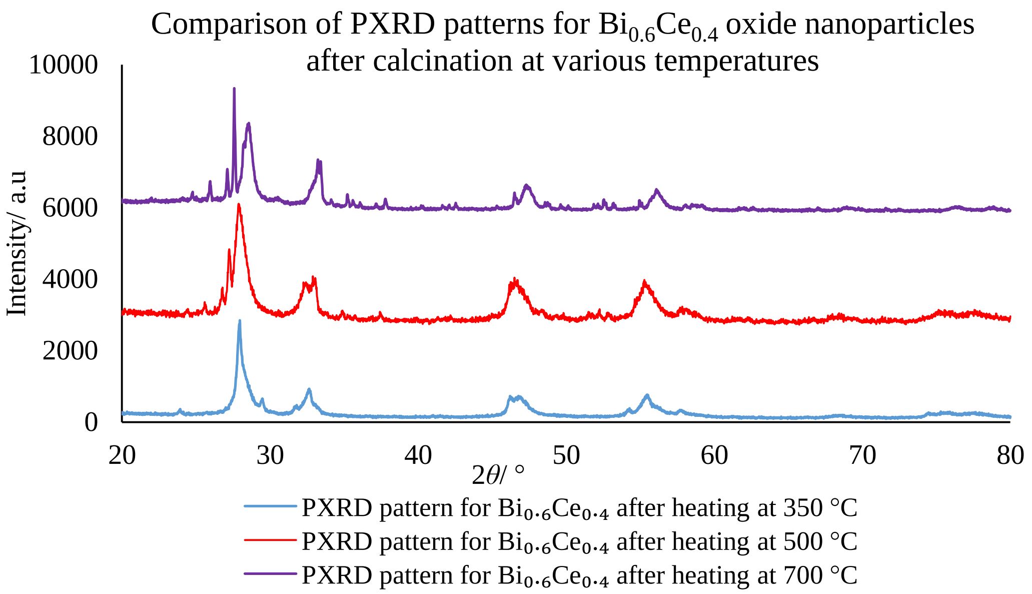

Figure 5.24. PXRD patterns of the $Bi_{0.6}Ce_{0.4}$ *oxide nanoparticles after heating in the tube furnace at various temperatures for 7 days.*

The patterns for the $Bi_{0.8}Ce_{0.2}$ oxide sample heated at different temperatures are seen in Figure 5.25. From this data it can be seen that the α-Bi_2O_3 phase remains stable up to 700 °C and this remains the majority phase.

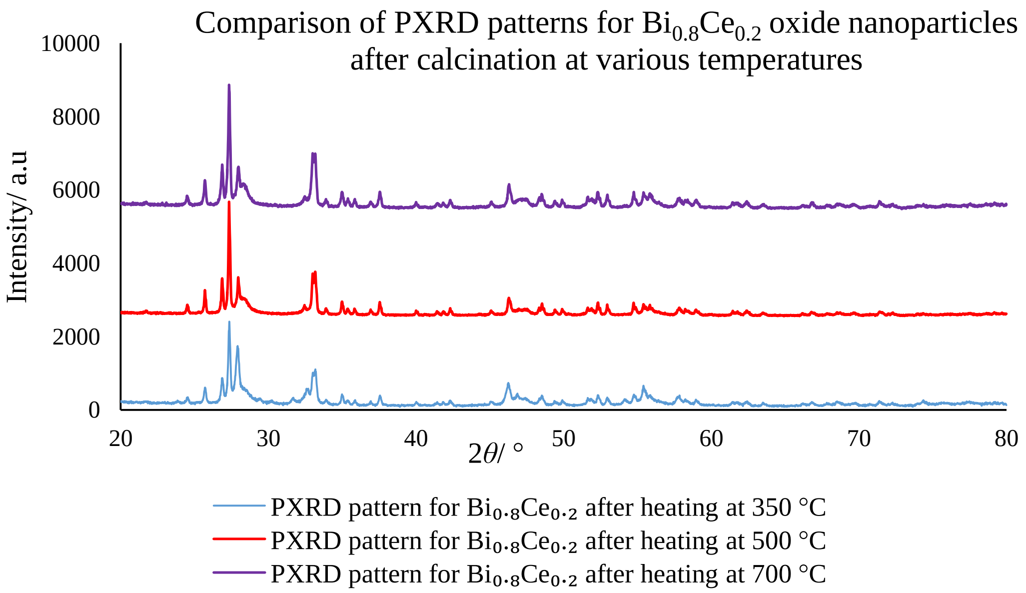

Figure 5.25. PXRD patterns of the $Bi_{0.8}Ce_{0.4}$ *oxide nanoparticles after heating in the tube furnace at various temperatures for 7 days.*

Scherrer analysis was carried out on the PXRD patterns in order to calculate the mean crystallite size for each sample. This also allowed comparison of crystallite size with increasing temperature. As can be seen from Figure 5.26, there was very little variation in crystallite size as the temperature increased. In general, the same trend of increasing particle size with increasing bismuth concentration applied across all compositions. It would be expected that the particles calcined at 700 °C would have a larger crystallite size than those calcined at 350 °C due to sintering. This does seem to be the case for the 20 and 40% bismuth samples, however, the particles with 60% and 80% bismuth seem to have very similar sizes regardless of the calcination temperature. It may be that in the temperature increase was not great enough to provide enough energy for the atoms to move significant distances over the time period.

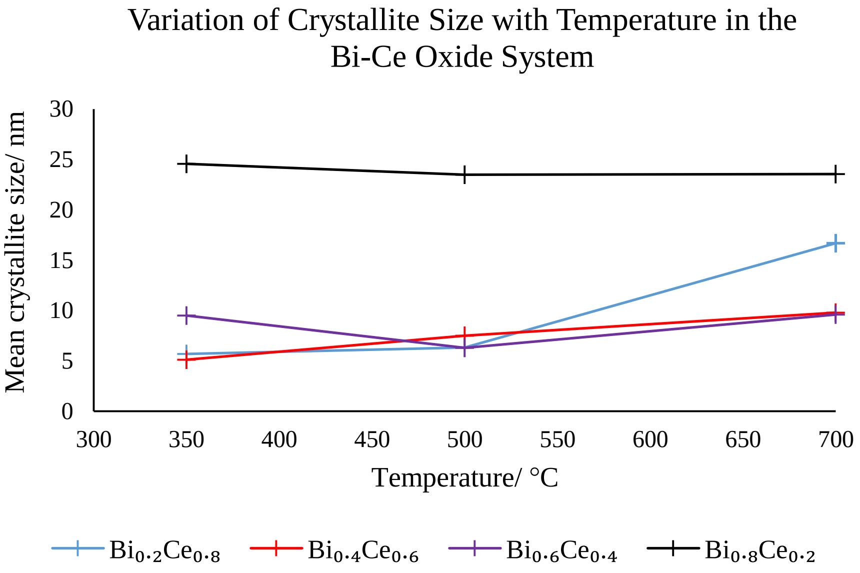

Figure 5.26. Plot showing the relationship between composition and mean crystallite size at various temperatures.

From PXRD analysis it was concluded that from 350-700 °C, for the $Bi_{0.2}Ce_{0.8}$ and $Bi_{0.8}Ce_{0.2}$ samples, no phase changes occurred. However, for the $Bi_{0.4}Ce_{0.6}$ and $Bi_{0.6}Ce_{0.4}$ samples there did appear to be more structural change at 700 °C. It is unknown quite how the structures changed at this temperature to cause the extra peaks in the pattern. It was also still unknown if the composition of the nanoparticles had changed. Therefore, compositional analysis was carried out using EDS. The results of this are shown in Table 5.7. They show that for the $Bi_{0.2}Ce_{0.8}$ and $Bi_{0.4}Ce_{0.6}$ oxide samples, there is very little change in composition with temperature, <5%, which is well within error. However, for the $Bi_{0.6}Ce_{0.4}$ and $Bi_{0.8}Ce_{0.2}$ oxide samples, the compositions vary more significantly with temperature. The trend for these two samples is that as the temperature increases, the percentage of cerium in the mixed oxide particles increases. It is possible that with temperature the bismuth evolves out of the main mixed phase and exists purely as α-Bi_2O_3, which has the effect of enhancing the proportion of cerium in the mixed phase.

Table 5.7. Composition of the Bi-Ce oxide nanoparticles varying with temperature.

Sample Bi_2O_3-CeO_2	*Calcination temperature/ °C*	*%Bi*	*%Ce*
$Bi_{0.2}Ce_{0.8}$	350	23.67	76.33
	500	26.32	73.68
	700	22.64	77.36
$Bi_{0.4}Ce_{0.6}$	350	48.44	51.56
	500	49.03	50.97
	700	51.10	48.90
$Bi_{0.6}Ce_{0.4}$	350	65.71	34.29
	500	48.94	51.06
	700	35.80	64.20
$Bi_{0.8}Ce_{0.2}$	350	72.90	27.10
	500	63.82	36.18
	700	41.73	58.27

All Bi-Ce oxide samples were investigated in the microscope after heating in order to identify any new phases. Generally it was found that the particles had changed very little with heating. The same fluorite agglomerates were found across all sample compositions as well as crystals of pure α-Bi_2O_3. Therefore, it can be concluded, that the Bi-Ce oxide system is relatively stable to heat treatments and the fluorite structure remains a favourable crystal structure for the system in solid solution.

Examples of particles observed in the microscope from samples heated at 500 °C can be seen in Figures 5.27-5.30. For the $Bi_{0.2}Ce_{0.8}$ oxide sample seen in Figure 5.27, an agglomerate of fluorite particles can be seen. D-spacings were calculated from the FFT giving values of 3.20 Å, 2.76 Å and 2.05 Å indicating the {111}, {200} and {220} lattice planes were present.

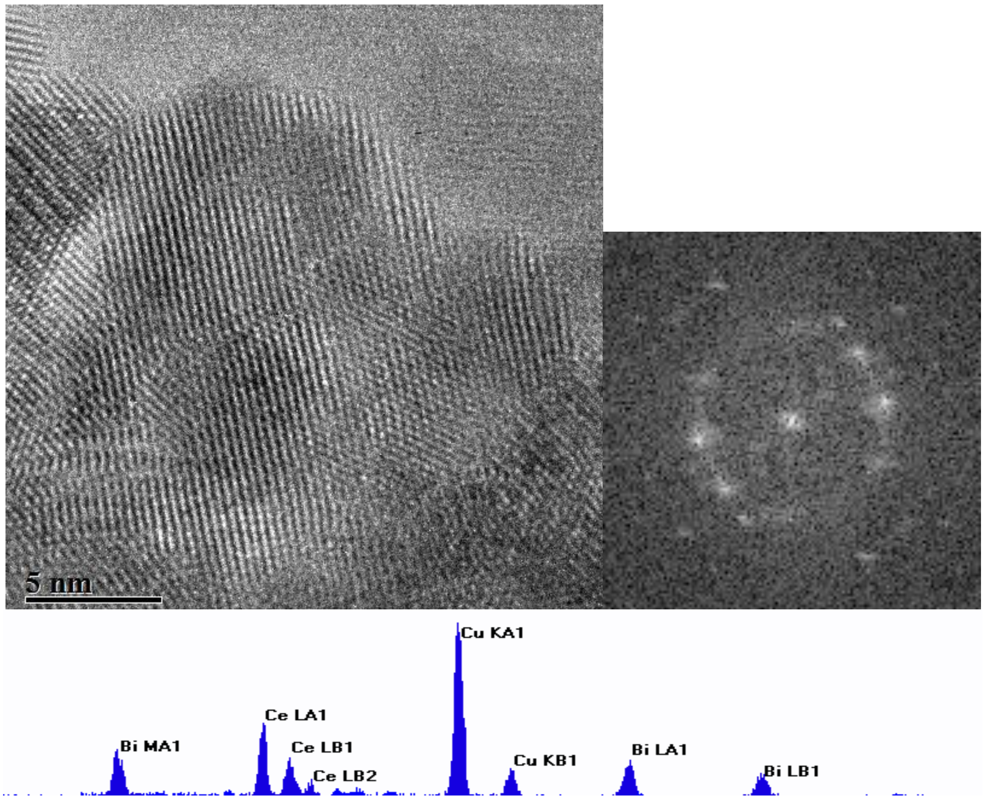

Figure 5.27. HRTEM micrograph of the $Bi_{0.2}Ce_{0.8}$ *sample after calcination at 500 °C (l) with corresponding FFT (r). EDS spectra for the area shown below.*

Similarly, the micrographs for the $Bi_{0.4}Ce_{0.6}$ oxide sample seen in Figure 5.28, show mixed oxide nanoparticles based on the fluorite structure. The d-spacings calculated from the FFT indicated that the {111}, {200} and the {220} lattice planes were present.

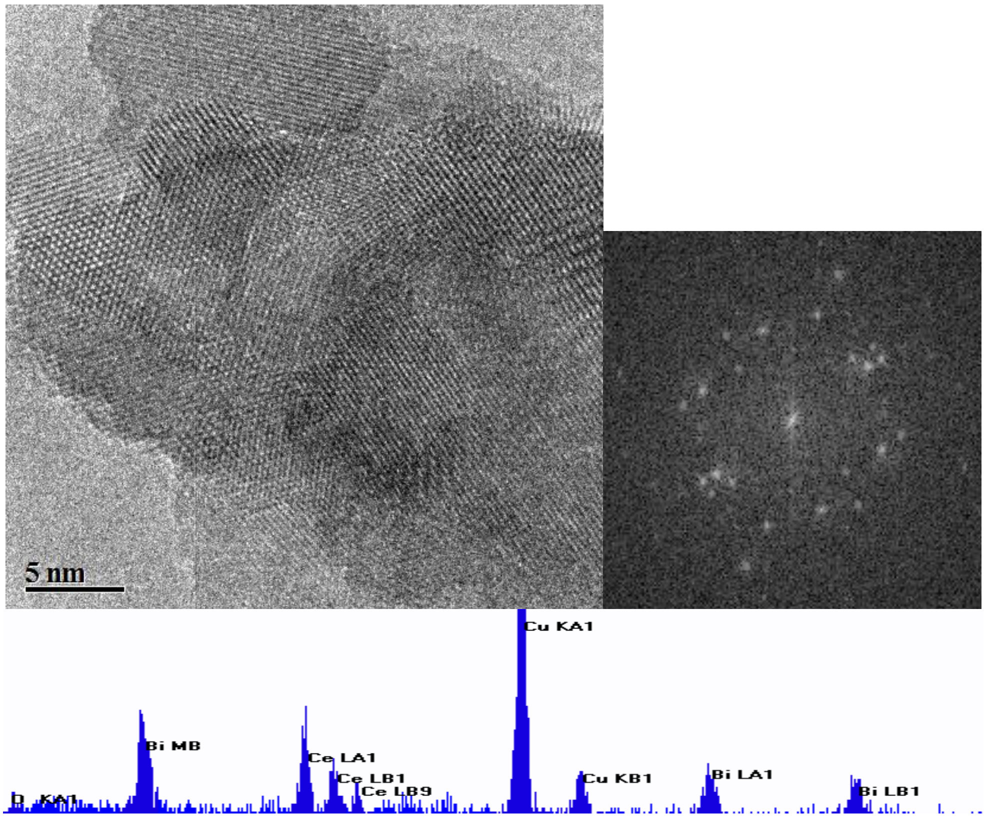

Figure 5.28. HRTEM micrograph of the $Bi_{0.4}Ce_{0.6}$ *sample after calcination at 500 °C (l) with corresponding FFT (r). EDS spectra for the area shown below.*

The micrograph shown in Figure 5.29 shows a cluster of fluorite type particles from the $Bi_{0.6}Ce_{0.4}$ sample, but they are noticeably larger than those with less bismuth content as expected. From the FFT, d-spacings of 3.18 Å and 2.75 Å were calculated, corresponding to the {111} and {220} fluorite lattice planes.

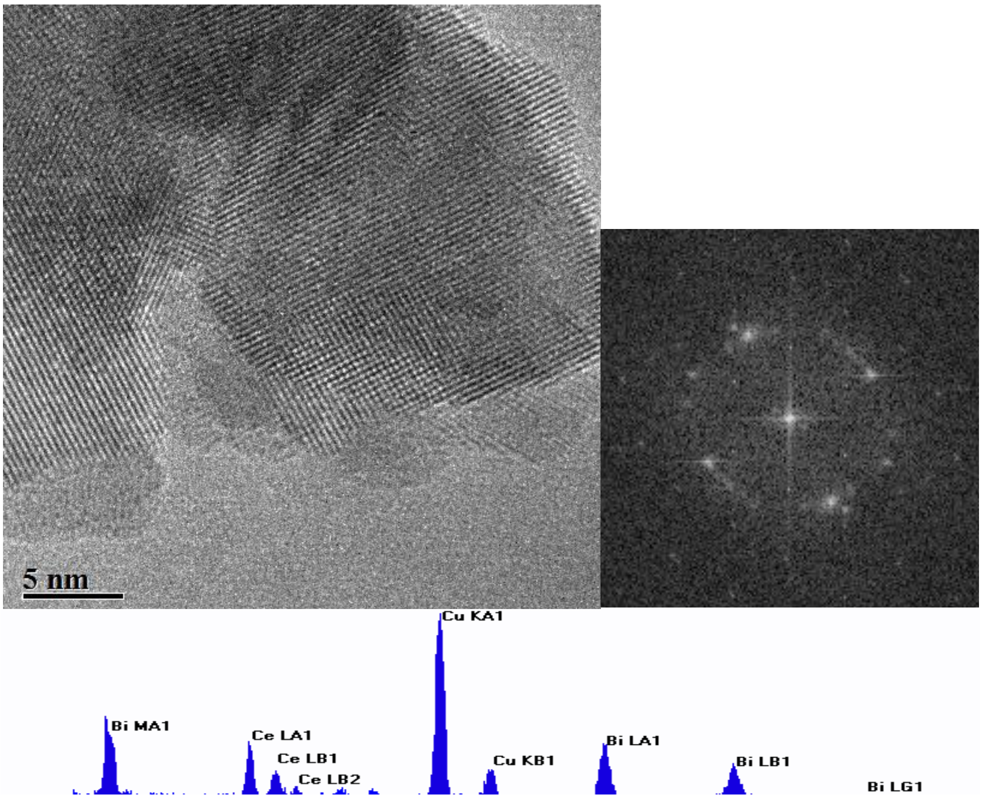

Figure 5.29. HRTEM micrograph of a polycrystalline region of the Bi$_{0.6}$Ce$_{0.4}$ *sample after calcination at 500 °C (l) with corresponding FFT (r). EDS spectra for the area shown below.*

Figure 5.30 presents a micrograph of the Bi$_{0.8}$Ce$_{0.2}$ oxide sample. It can be seen from the FFT and the look of the crystal that α-Bi$_2$O$_3$ is present, as expected from the PXRD pattern. This sample was not ideal for imaging as the α-Bi$_2$O$_3$ crystals tended to be too thick to observe fringes and to focus easily. EDS shows that the crystal is very bismuth rich, although there does appear to be a small amount of cerium present. Fringe spacing analysis indicated that the {012} lattice plane was being observed in this micrograph.

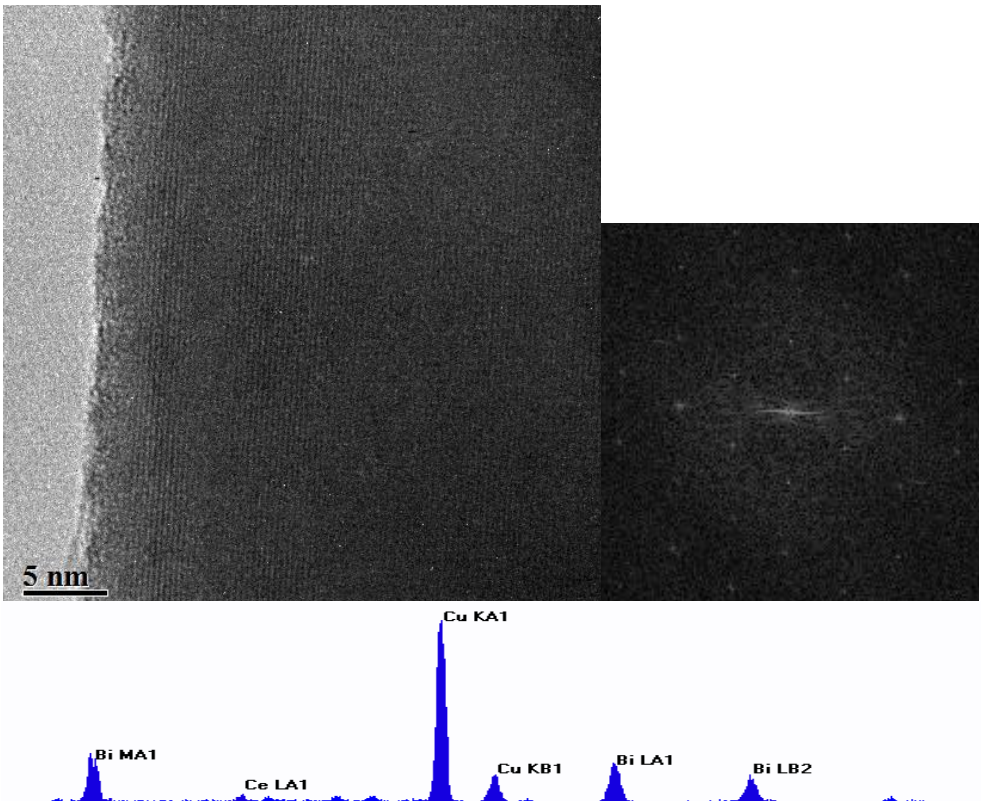

Figure 5.30. HRTEM micrograph of the $Bi_{0.8}Ce_{0.2}$ *sample after calcination at 500 °C (l) with corresponding FFT (r). EDS spectra for the area shown below.*

Examples of images acquired while investigating the Bi-Ce oxide nanoparticles after calcination at 700 °C are shown in Figures 5.31-5.34. Although the phases observed are the same as at previous temperatures, the micrographs show a wider spread of fringes throughout the sample indicating a greater degree of crystallinity. For example, the micrograph shown in Figure 5.31 is an example of a fluorite crystal from the $Bi_{0.2}Ce_{0.8}$ oxide sample. It shows a particle approximately 10 nm in diameter with strong fringes indicating a d-spacings of 3.21 Å, typical of the {111} plane of fluorite. There is also a second relatively large crystal shown below which appears to display crystal twinning.

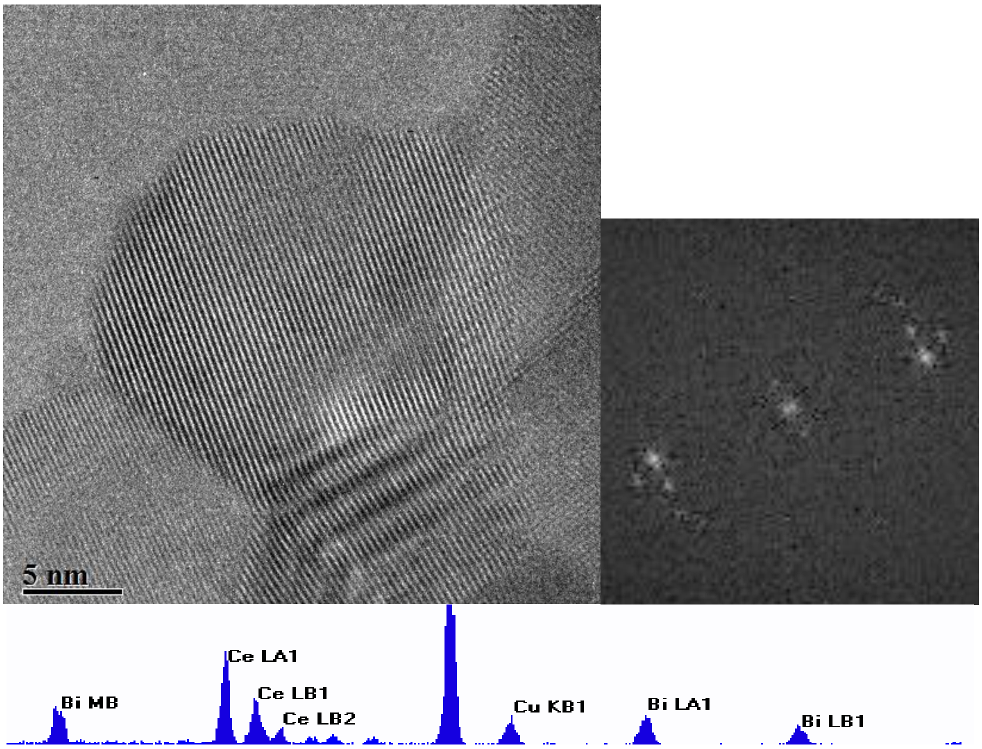

Figure 5.31. HRTEM micrograph of the $Bi_{0.2}Ce_{0.8}$ *sample after calcination at 700 °C (l) with corresponding FFT (r). EDS spectra for the area shown below.*

Figure 5.32 presents a micrograph taken of the $Bi_{0.4}Ce_{0.6}$ oxide sample showing a large fluorite particle. The d-spacings for this particle were calculated to be 3.20 Å, representative of the {111} lattice plane.

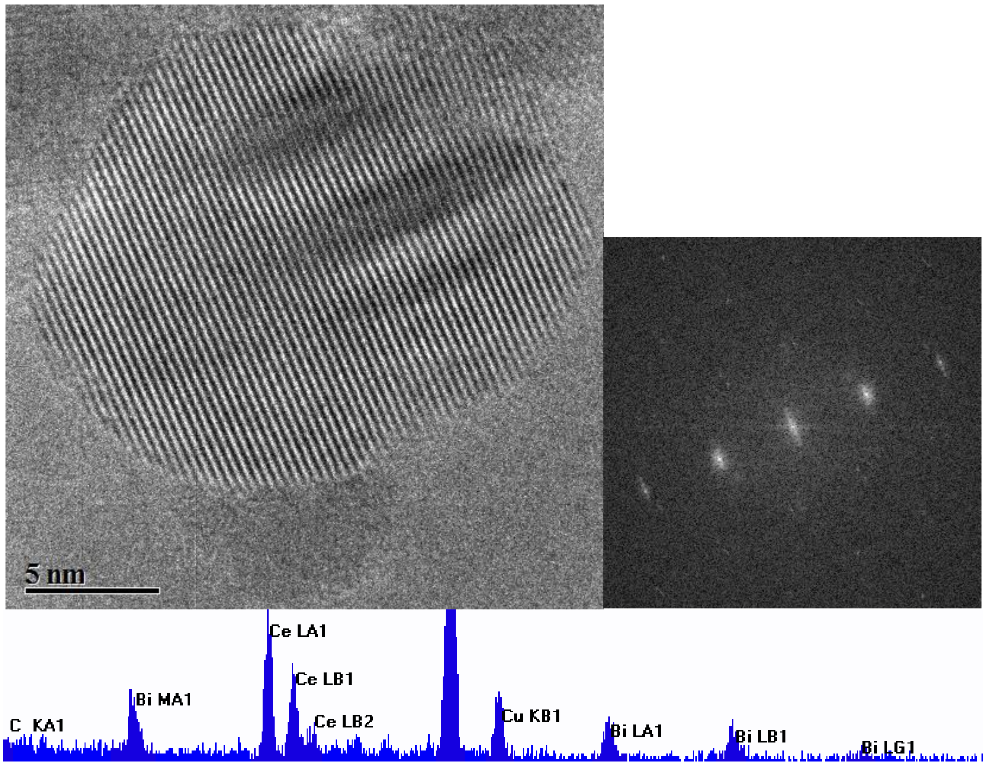

Figure 5.32. HRTEM micrograph of the $Bi_{0.4}Ce_{0.6}$ *sample after calcination at 700 °C (l) with corresponding FFT (r). EDS spectra for the area shown below.*

The micrograph taken of the $Bi_{0.6}Ce_{0.4}$ oxide sample shown in Figure 5.33, is interesting as it shows a rod shaped crystal of α-Bi_2O_3 surround by fluorite particles. This is confirmed by fringe spacing analysis from the FFT, which shows d-spacings of 3.47 Å relating to the {021} plane of α-Bi_2O_3, and of 3.21 Å, 1.82 Å and 1.38 Å from the surrounding particles relating to the {111}, {220} and {311} planes of fluorite. Figure 5.34 also shows a crystalline region from the $Bi_{0.6}Ce_{0.4}$ oxide sample, this time just showing particles with the fluorite structure as confirmed by FFT analysis. The d-spacings values correspond to the {111}, {200}, {220} and {311} planes being observed. This agrees well with the PXRD data which suggests that two phases are present in the sample.

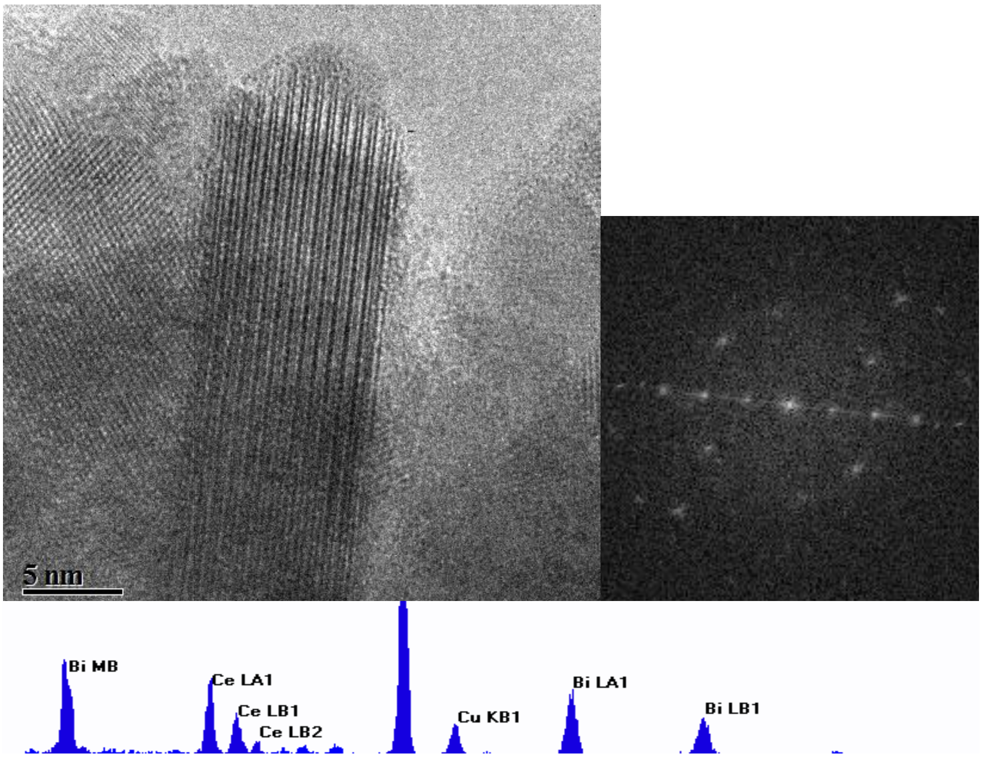

Figure 5.33. HRTEM micrograph of the $Bi_{0.6}Ce_{0.4}$ sample after calcination at 700 °C showing a rod shaped crystal of α-Bi_2O_3 surrounded by fluorite (l) with corresponding FFT (r). EDS spectra for the area shown below.

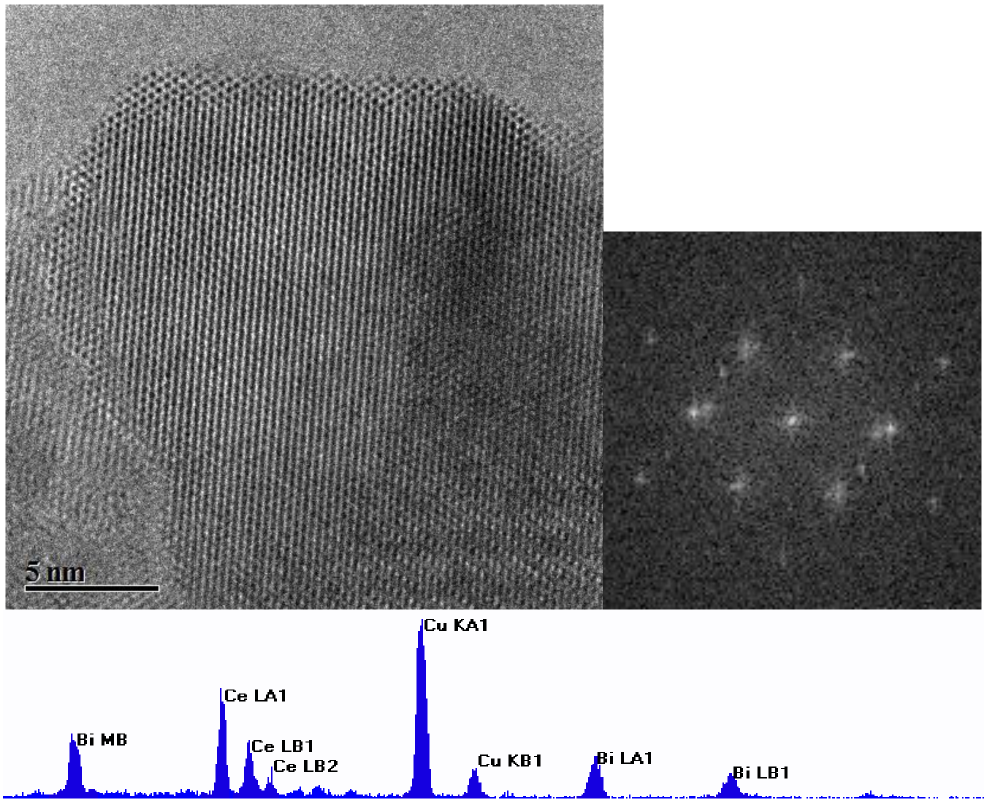

Figure 5.34. HRTEM micrograph of the $Bi_{0.6}Ce_{0.4}$ sample after calcination at 700 °C showing a region of fluorite crystals (l) with corresponding FFT (r). EDS spectra for the area shown below.

XPS analysis was carried out on the Bi-Ce oxide particles heated at 500 °C to see if any change in surface composition occurred with temperature change. The results are seen in Table 5.8. It can be seen that the surface composition stays relatively constant over this temperature range meaning that the particles are strongly ordered, giving further evidence that the system is far from an ideal solid solution.

Table 5.8. Comparison of XPS data for the Bi-Ce oxide nanoparticles after calcination at 350 °C and 500 °C.

Sample Bi_2O_3-CeO_2	*Atom & Orbital*	*Binding Energy/ eV*	*Atomic Concentration/ %*
$Bi_{0.2}Ce_{0.8}$ at 350 °C	Bismuth 4f	161.08	20.28
	Cerium 3d	885.08	5.02
	Oxygen 1s	161.08	74.70
$Bi_{0.2}Ce_{0.8}$ at 500 °C	Bismuth 4f	156.00	20.24
	Cerium 3d	879.00	6.68
	Oxygen 1s	526.00	73.08
$Bi_{0.4}Ce_{0.6}$ at 350 °C	Bismuth 4f	156.00	26.49
	Cerium 3d	879.00	4.77
	Oxygen 1s	526.00	68.74
$Bi_{0.4}Ce_{0.6}$ at 500 °C	Bismuth 4f	155.00	25.48
	Cerium 3d	879.00	4.90
	Oxygen 1s	526.00	69.62
$Bi_{0.6}Ce_{0.4}$ at 350 °C	Bismuth 4f	155.00	20.06
	Cerium 3d	878.00	2.62
	Oxygen 1s	526.00	77.32
$Bi_{0.6}Ce_{0.4}$ at 500 °C	Bismuth 4f	156.00	30.08
	Cerium 3d	879.00	3.57
	Oxygen 1s	526.00	66.35
$Bi_{0.8}Ce_{0.2}$ at 350 °C	Bismuth 4f	155.00	35.81
	Cerium 3d	878.00	2.55
	Oxygen 1s	526.00	61.64
$Bi_{0.8}Ce_{0.2}$ at 500 °C	Bismuth 4f	255.00	32.79
	Cerium 3d	878.00	3.00
	Oxygen 1s	526.00	64.21

Likewise, the calculated Ce(III) and Ce(IV) proportions across all compositions remain constant, as seen from Table 5.9.

Table 5.9. Comparison of the Ce(III) and Ce(IV) percentages across the Bi-Ce oxide system.

Sample Bi_2O_3-CeO_2	% Ce^{3+}	STDEV	%Ce^{4+}	STDEV
$Bi_{0.2}Ce_{0.8}$ at 350 °C	16.40	1.87	83.60	1.87
$Bi_{0.2}Ce_{0.8}$ at 500 °C	18.50	0.68	81.50	0.68
$Bi_{0.4}Ce_{0.6}$ at 350 °C	16.32	0.76	83.68	0.76
$Bi_{0.4}Ce_{0.6}$ at 500 °C	20.04	0.77	79.96	0.77
$Bi_{0.6}Ce_{0.4}$ at 350 °C	17.14	0.81	82.86	0.81
$Bi_{0.6}Ce_{0.4}$ at 500 °C	17.38	1.96	82.62	1.96
$Bi_{0.8}Ce_{0.2}$ at 350 °C	18.52	1.30	81.48	1.30
$Bi_{0.8}Ce_{0.2}$ at 500 °C	17.78	1.24	82.22	1.24

5.4 Summary of the Bi_2O_3-CeO_2 system

It has been shown that mixed metal oxide nanoparticles of bismuth and cerium can be formed by the resin-gel method. Average crystallite sizes of 5-23 nm were calculated for the various samples via Scherrer analysis. Data from PXRD and HRTEM allowed phases of fluorite and α-Bi_2O_3 to be identified in the system and indicated that the fluorite structure prevails with α-Bi_2O_3 present as a minority phase until 60% bismuth doping. This data compares well to previous studies in the Bi-Ce oxide system. After 60% bismuth doping, the α-Bi_2O_3 structure was dominant with fluorite as the minority phase. A mechanism for the transformation of the fluorite to the α-Bi_2O_3 phase has been postulated, involving the loss of two oxygen ions coupled with several cation shifts.

XPS confirmed suspicions from EDS analysis that the particles formed were not homogeneous. Analysis of the data revealed that bismuth showed a strong preference for surface sites, which agrees well with the previous literature aforementioned. Homogeneity did not improve with temperature as might be expected. With increasing temperature, the ions have more energy to diffuse through the lattice, meaning the particles should become more homogenous. As this was not the case, it must be concluded that due to the bismuth lone pair, the most favourable ionic arrangement involves having a bismuth rich surface.

6. The CeO_2-Nb_2O_5 system

6.1 Introduction

The CeO_2-Nb_2O_5 system was the second ternary system investigated. The resin-gel synthesis was again successful in producing mixed oxide nanoparticles in this system. Unfortunately at low calcination temperatures (350 °C), the resulting product was mainly amorphous. At higher temperatures, however, phases of T- and M-Nb_2O_5 and fluorite phases were found in solid solution, via PXRD and HRTEM analysis. Compositional analysis using EDS and XPS indicated that the particles were not homogenous, with niobium showing a preference for surface site occupation.

Very few previous structural studies have been carried out on the Ce-Nb mixed oxide system at low temperatures, therefore, it was not known what phases would be seen and if a solid solution would be formed. It was expected that the fluorite structure would be tolerant to doping with niobium ions, as seen with the Bi-Ce oxide system, and possibly at higher concentrations of niobium the T-Nb_2O_5 phase would dominate. It is, therefore, interesting that although the fluorite phase was found at all calcination temperatures, the T-Nb_2O_5 phase did not form until 700 °C, highlighting the preference for fluorite formation at low temperatures.

6.2 Initial results for samples calcined at 350 °C

After the particles had been calcined at 350 °C, their crystal structures were investigated using PXRD. The results of this are seen in Figure 6.1. It can be seen that for the samples with a larger proportion of niobium present, it appears the material is less crystalline, with very small broad peaks almost obscured by the background. This high background indicates a large proportion of an amorphous phase being present, with the weak peaks correlating to the fluorite phase. It was not expected to find any of the $CeNbO_4$ phase as generally this does not form at temperatures below 1000 K [147]. As the cerium concentration in the sample increases, the peaks become stronger and more discernible indicating there is an increasing degree of crystallinity in the sample. Therefore, it can be concluded that at this low calcination temperature, the fluorite phase can be formed, but any of the niobium oxide phases require a higher temperature for formation. It appears that a mixture of fluorite and amorphous phases are present throughout all samples, with the crystalline fluorite phase increasing in proportion with increasing cerium concentration.

Poor crystallinity in mixed Ce-Nb oxides has been noted in previous studies. For example, Stošić *et al*. [121] conducted studies on mixed Ce-Nb oxides for catalysis and found results similar to those discussed here, with two phases being present: a crystalline fluorite phase present and a niobium rich amorphous phase. They proposed that it was the presence of cerium which prevented the crystallisation of niobia at temperatures below 500 °C.

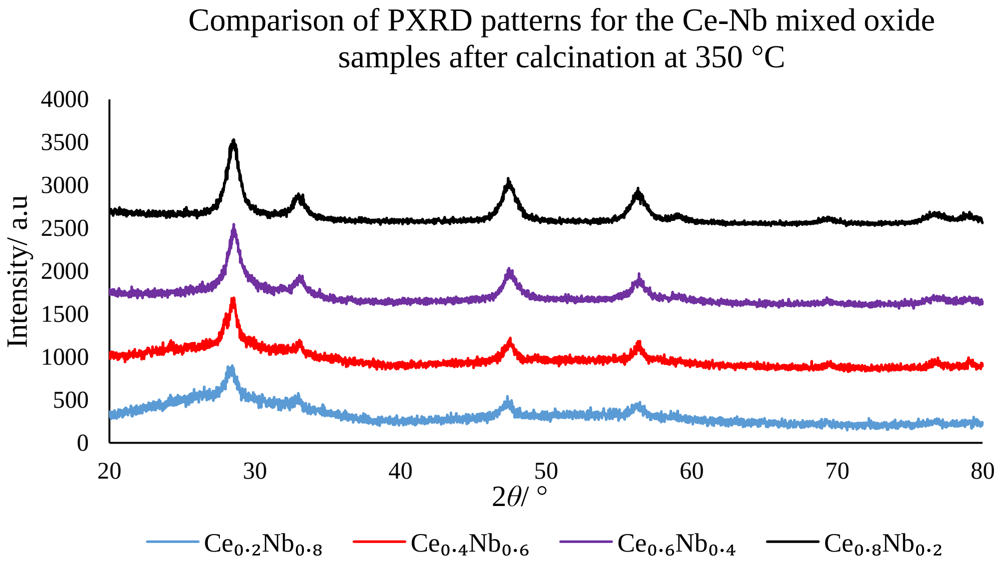

Figure 6.1. PXRD patterns for the range of Ce-Nb oxide compositions synthesised.

From the PXRD patterns, Scherrer analysis could be carried out, giving mean crystallite sizes for the fluorite particles in each sample. These results are shown in Figure 6.2. It can be seen that, as expected, the crystallite size increases with increased cerium content. The range of crystallite sizes is from 3.84-7.21 nm in the mixed nanoparticles, again showing that the resin-gel method is highly successful at producing nanoparticles.

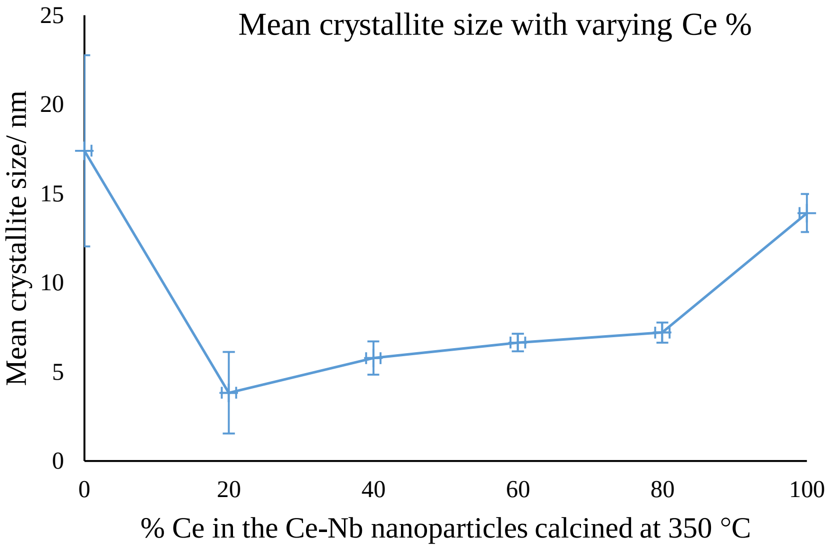

Figure 6.2. Plot showing the relationship between composition and mean crystallite size.

The samples were next looked at in the HRTEM to further explore the fluorite and amorphous structures, as well as their elemental compositions. It was apparent from viewing particles in the microscope that two phases existed in all samples. A crystalline fluorite phase, with EDS showing primarily the presence of cerium, and a mixed amorphous phase containing both cerium and niobium. EDS plots for all mixed oxide samples are seen in Figures 6.3-6.6.

For the $Ce_{0.2}Nb_{0.8}$ oxide sample, the EDS data, Figure 6.3, shows clearly that two phase have been formed, as all the points fit well on two lines of best fit. Within these two series there is little deviation from the line of best fit. Therefore, it can be concluded that each phase has a fairly constant composition and it is likely the ions are in solid solution. The composition of the mixed amorphous phase was calculated using the ratio of Nb:Ce, as seen from the EDS plot, and adjusted using the $K_{Nb:Ce}$ value, as calculated from the standard samples. The percentage of Nb in the mixed phase was found to be 66.03% with linest analysis giving a 4.70% error in the line of best fit. An explanation for why there is less niobium than expected in particles analysed may be that there was also some pure Nb_2O_5 in the sample which was not examined. The fluorite phase had a composition of 98.30% cerium and 1.70% niobium.

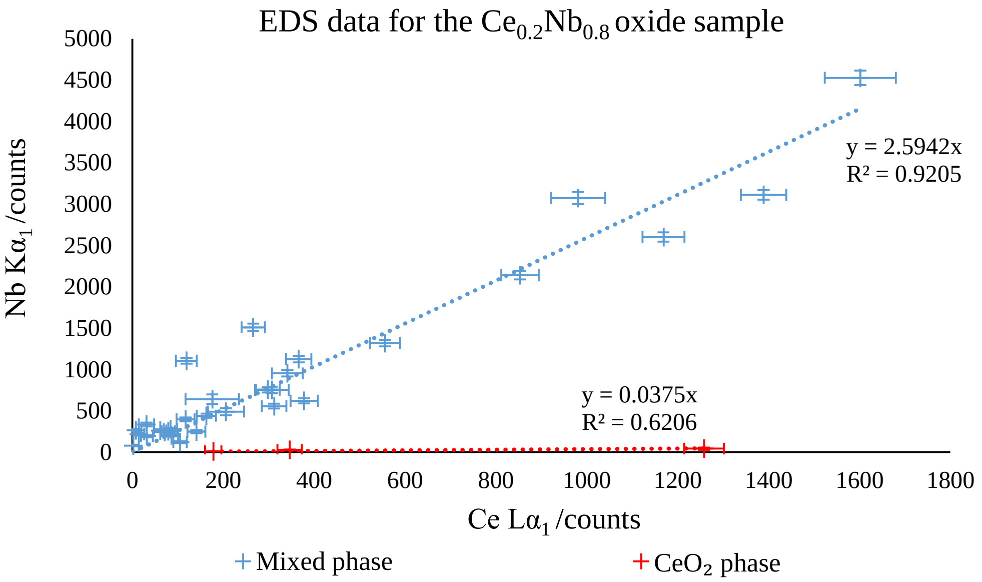

Figure 6.3. EDS plot of Ce Lα₁ counts against Nb Kα₁ counts for the $Ce_{0.2}Nb_{0.8}$ *oxide sample.*

The EDS plot for the $Ce_{0.4}Nb_{0.6}$ (Figure 6.4) presents good evidence for the formation of only one phase. However, considering this observed phase was amorphous, and the PXRD pattern shows evidence of a crystalline fluorite structure there must be some CeO_2 present in the sample which was not found in the microscope. This is one of the main downfalls of microscopy: only a small proportion of particles can be observed. However, in combination with other techniques such as PXRD, it is possible to gain a full picture of the sample. As for the previous sample, the amorphous phase seems to have a constant composition with an R^2 value of 0.98 for the line of best fit. The calculated composition for the mixed phase was 53.88% niobium and 46.12% cerium. This is close to the intended composition. Linest analysis gave an error in the line of best fit as 2.44%.

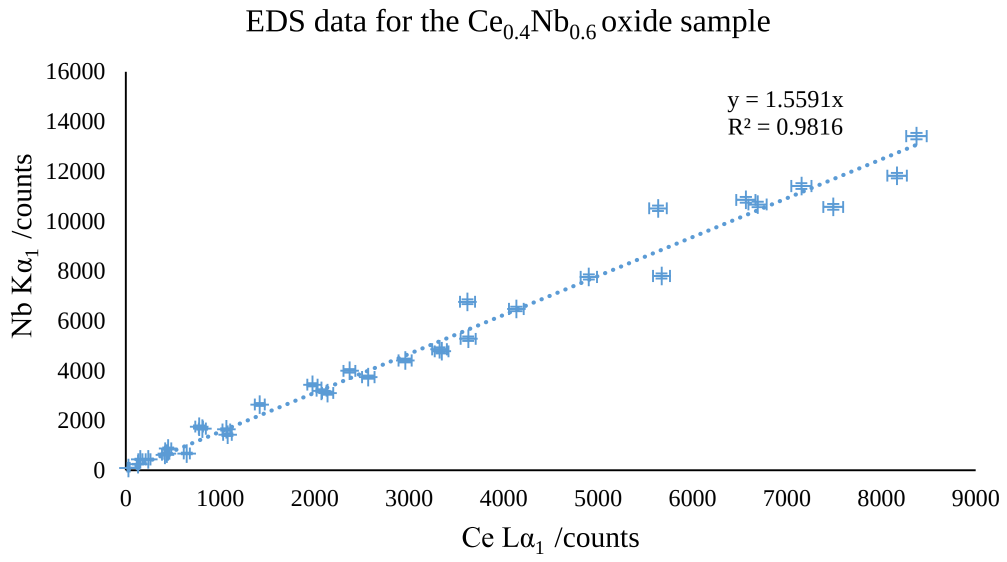

Figure 6.4. EDS plot of Ce Lα₁ counts against Nb Kα₁ counts for the $Ce_{0.4}Nb_{0.6}$ *oxide sample.*

The trend of two phases being seen in the microscope continues for the $Ce_{0.6}Nb_{0.4}$ and $Ce_{0.8}Nb_{0.2}$ oxide samples, with their EDS data seen in Figures 6.5 and 6.6. Composition calculations for the $Ce_{0.6}Nb_{0.4}$ oxide sample found 34.67% niobium and 65.33% cerium in the mixed amorphous phase, with a 12.87% error in the line of best fit.

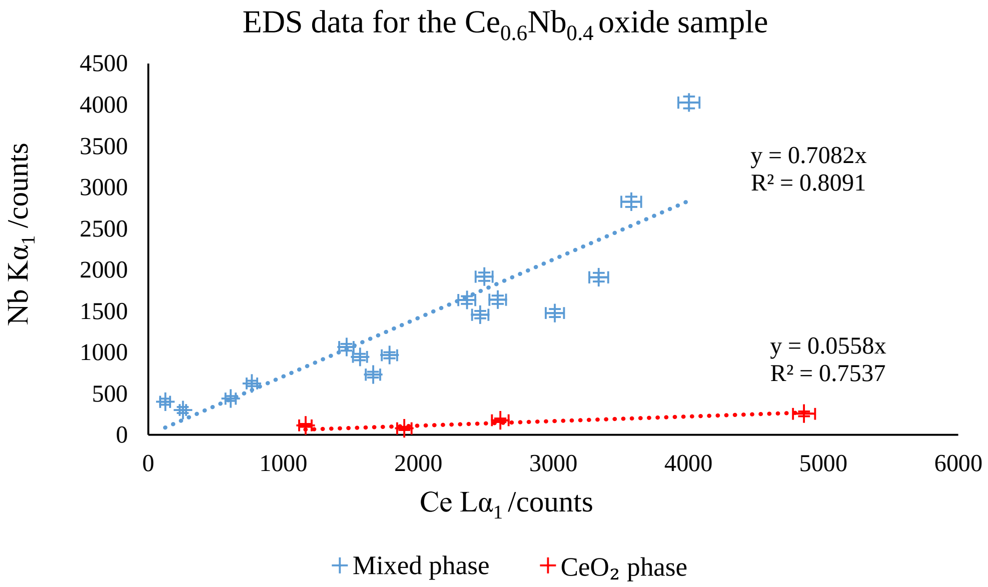

Figure 6.5. EDS plot of Ce Lα₁ counts against Nb Kα₁ counts for the $Ce_{0.6}Nb_{0.4}$ *oxide sample.*

The composition of the mixed phase in the $Ce_{0.8}Nb_{0.2}$ oxide sample was found to be 82.22% niobium and 17.78% cerium, which may be slightly surprising as those figures are not at all close to the target composition. However, many particles of near pure CeO_2 were observed, which agrees well with the

PXRD data which had strong fluorite peaks. Therefore, it can be inferred that almost complete phase separation occurred, with the amorphous niobium oxide phase being formed, taking up a small proportion of cerium ions, and a fluorite CeO_2 phase being formed from the excess cerium ions. This was not the expected or intended outcome as clearly a solid solution of ions was not formed.

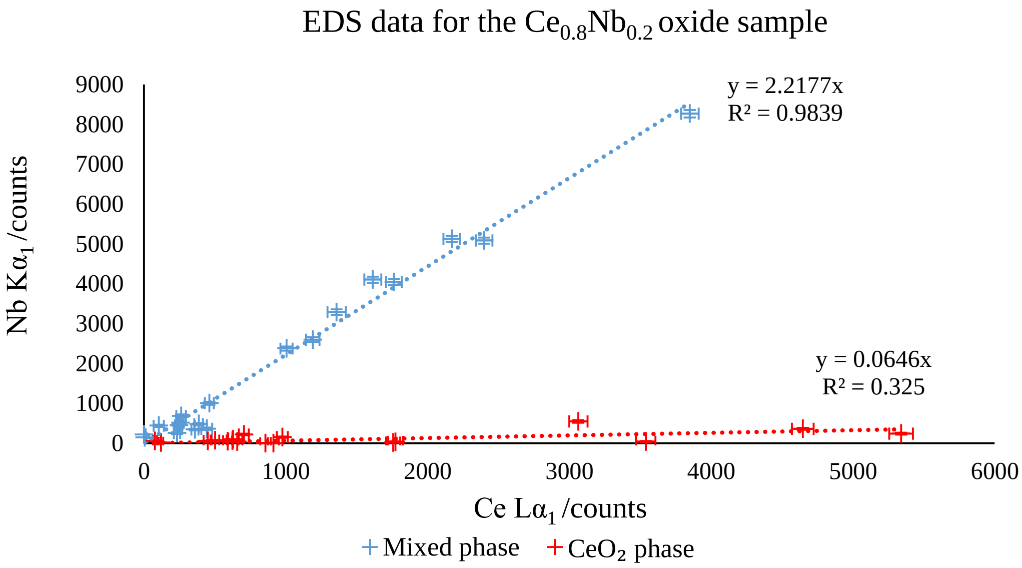

Figure 6.6. EDS plot of Ce Lα₁ counts against Nb Kα₁ counts for the $Ce_{0.8}Nb_{0.2}$ oxide sample.

A summary of the mixed oxide compositions (blue points on EDS plots) for each Ce-Nb oxide sample are shown in Table 6.1. As discussed above, the mixed compositions were generally as expected, however, it appears that almost complete phase separation occurred in the $Ce_{0.8}Nb_{0.2}$ sample which was not the intended result.

Table 6.1. Calculated composition of the mixed phase in each of the Ce-Nb oxide samples from EDS data.

Sample CeO_2-Nb_2O_5	Expected % Ce	Calculated % Ce from EDS	Expected % Nb	Calculated % Nb from EDS
$Ce_{0.2}Nb_{0.8}$	20.00	33.97	80.00	66.03
$Ce_{0.4}Nb_{0.6}$	40.00	46.12	60.00	53.88
$Ce_{0.6}Nb_{0.4}$	60.00	65.33	40.00	34.67
$Ce_{0.8}Nb_{0.2}$	80.00	17.78	20.00	82.22

The particles analysed in the microscope were confirmed as fluorite structures by their d-spacings, as calculated from the FFT of the image. The results of the average d-spacings assigned to their respective lattice planes for fluorite are seen in Table 6.2 and compared to literature values. It can be seen, on the whole, that the observed lattice planes were slightly larger than their literature counterparts. This is expected due to lattice relaxation in nanoparticles.

Table 6.2. Observed d-spacings for each index of the fluorite structure across all Ce-Nb oxide compositions. [85]

	Index of fluorite structure							
Sample CeO_2-Nb_2O_5	Average d-spacing for 111/ Å	Literature value/ Å	Average d-spacing for 200/ Å	Literature value/ Å	Average d-spacing for 220/ Å	Literature value/ Å	Average d-spacing for 311/ Å	Literature value/ Å
$Ce_{0.2}Nb_{0.8}$	3.26 ± 0.11	3.12	2.81 ± 0.06	2.71	2.17 ± 0.18	1.91	1.64 ± 0.01	1.63
$Ce_{0.4}Nb_{0.6}$	3.18 ± 0.05	3.12	2.84 ± 0.24	2.71	-	-	-	-
$Ce_{0.6}Nb_{0.4}$	3.27 ± 0.07	3.12	2.78 ± 0.08	2.71	2.02 ± 0.01	1.91	-	-
$Ce_{0.8}Nb_{0.2}$	3.23 ± 0.12	3.12	2.83 ± 0.08	2.71	1.99 ± 0.05	1.91	1.79 ± 0.01	1.63

As calculations showed the d-spacings in the fluorite phase were slightly higher than the literature values of bulk material, it was expected that the unit cell parameters would increase accordingly. This was indeed found to be the case, with full results seen in Table 6.3.

Table 6.3. Unit cell parameters calculated for all Ce-Nb oxide samples compared to literature values. [65, 70, 85]

					Unit Cell Parameter Length/ Å			*Unit Cell Parameter Literature Length/ Å*		
Sample CeO_2-Nb_2O_5	Phase	θ/ rads	Index	d_{hkl}/ Å	a	b	c	a	b	c
Nb_2O_5		0.196	001	3.96						
	T-Nb_2O_5	*0.206*	*400*	*3.77*						
		0.216	*101*	*3.60*	6.18	29.29	3.93	6.18	29.18	3.93
	M-Nb_2O_5	0.246	111	3.17	*20.23*	*20.23*	*3.82*	*20.44*	*20.44*	*3.83*
		0.251	220	3.10						
		0.318	201	2.47						
$Ce_{0.2}Nb_{0.8}$	CeO_2	0.248	111	3.14	5.44	5.44	5.44	5.41	5.41	5.41
		0.413	220	1.92						
$Ce_{0.4}Nb_{0.6}$	CeO_2	0.249	111	3.13	5.42	5.42	5.42	5.41	5.41	5.41
		0.415	220	1.91						
		0.491	311	1.63						
$Ce_{0.6}Nb_{0.4}$	CeO_2	0.249	111	3.13	5.42	5.42	5.42	5.41	5.41	5.41
		0.416	220	1.91						
		0.492	311	1.63						
$Ce_{0.8}Nb_{0.2}$	CeO_2	0.250	111	3.12	5.40	5.40	5.40	5.41	5.41	5.41
		0.288	200	2.71						
		0.414	220	1.92						
		0.492	311	1.63						
CeO_2	CeO_2	0.247	111	3.16	5.47	5.47	5.47	5.41	5.41	5.41
		0.286	200	2.73						
		0.412	220	1.92						
		0.490	311	1.64						

The calculated lattice parameter a is plotted against elemental composition in Figure 6.7. The results show that the unit cell parameters are relatively constant across all compositions, apart from pure T-Nb_2O_5 which has an orthorhombic unit cell.

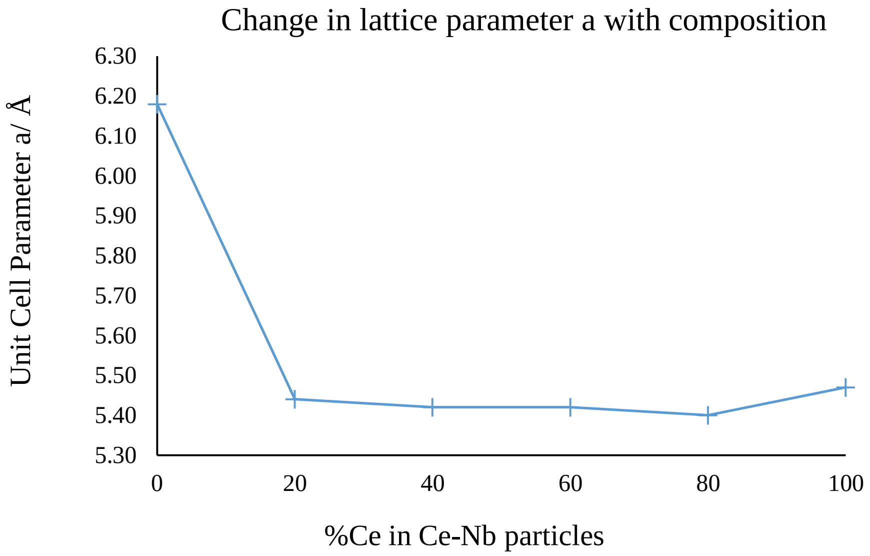

Figure 6.7. Plot showing how the lattice parameter, a, varies with composition.

6.2.1 HRTEM imaging

As with the Bi-Ce oxide nanoparticles, imaging was carried out on many particles in the Ce-Nb oxide samples to better understand the phases identified by PXRD. The micrographs seen in Figures 6.8 to 6.13 are representative examples of the particles seen in the HRTEM for the Ce-Nb oxide nanoparticles.

Most commonly seen in the microscope were amorphous regions of sample, an example of which is seen in Figure 6.8. These could be particularly hard to image and focus in the beam as they were usually thicker than the crystalline nanoparticles. The area of the $Ce_{0.2}Nb_{0.8}$ sample shown is niobium rich, as seen in the EDS spectrum, with a small cerium peak. The copper and gold signals are from the microscope pole piece and the TEM grid respectively. In addition to the regions of amorphous material, some particles of fluorite were also found, as expected from the PXRD pattern. An example of these particles is seen in Figure 6.9. The d-spacings, as calculated from the FFT, were found to be 2.76 Å and 1.92 Å, indicative of the {200} and {220} lattice planes of fluorite. EDS data shows the particles are rich in cerium.

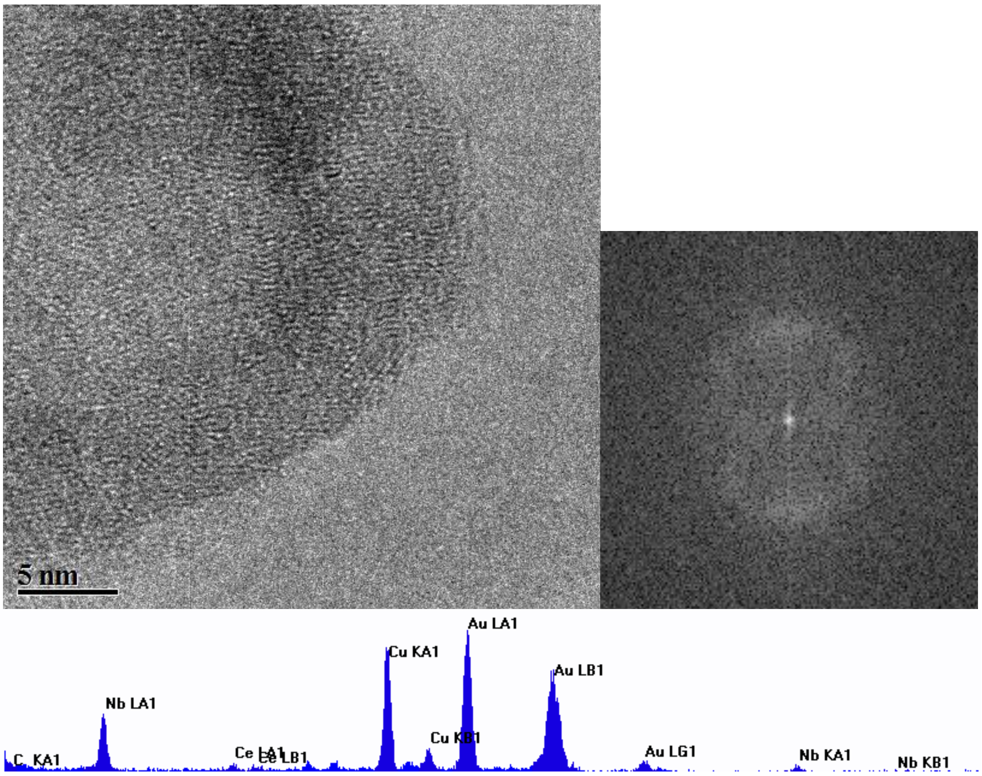

Figure 6.8. HRTEM micrograph of an amorphous region from the $Ce_{0.2}Nb_{0.8}$ *oxide sample (l) with corresponding FFT (r). EDS spectra for the area shown below.*

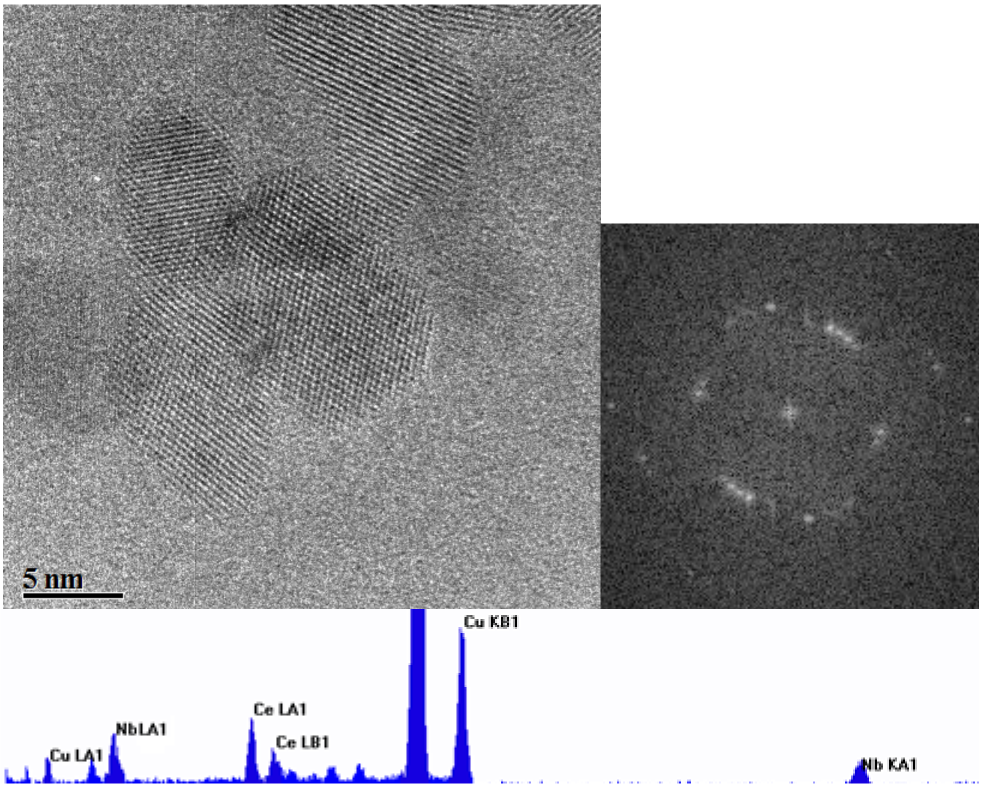

Figure 6.9. HRTEM micrograph of crystalline fluorite particles in the $Ce_{0.2}Nb_{0.8}$ *oxide sample (l) with corresponding FFT (r). EDS spectra for the area shown below.*

In the $Ce_{0.4}Nb_{0.6}$ sample, there were many regions of amorphous material observed as well as some fluorite particles, both similar to those seen above. Interestingly, there were also several particles of T- and M-Nb_2O_5 observed. This was suspected from the EDS calculations which gave a smaller percentage of niobium than expected, leaving the excess niobium to form a more niobium rich phase. As there was no evidence for an Nb_2O_5 phase in the PXRD pattern it can be assumed that this phase was present in very small amounts. An example of a crystal of M-Nb_2O_5 can be seen in Figure 6.10. The d-spacings calculated from the FFT give values of 5.08 Å, 3.78 Å and 2.86 Å indicating the {330}, {101} and {501} lattice planes were being observed.

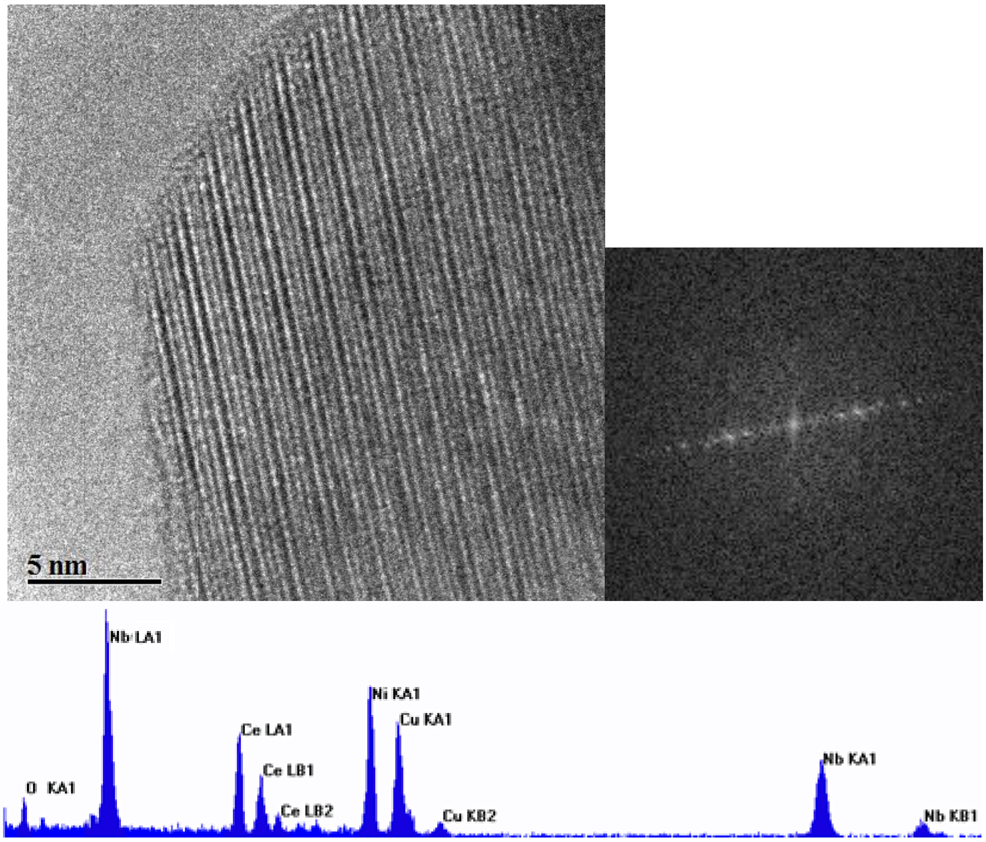

Figure 6.10. HRTEM micrograph of a crystalline M-Nb_2O_5 region in the $Ce_{0.4}Nb_{0.6}$ oxide sample (l) with corresponding FFT (r). EDS spectra for the area shown below.

When observing the $Ce_{0.6}Nb_{0.4}$ oxide sample in the microscope many more fluorite particles were seen than for the previous samples due to the increased cerium concentration. An example of a fluorite particle in this sample can be seen in Figure 6.11. A d-spacing of 3.28 Å was calculated from the FFT indicating the {111} lattice plane of the fluorite structure.

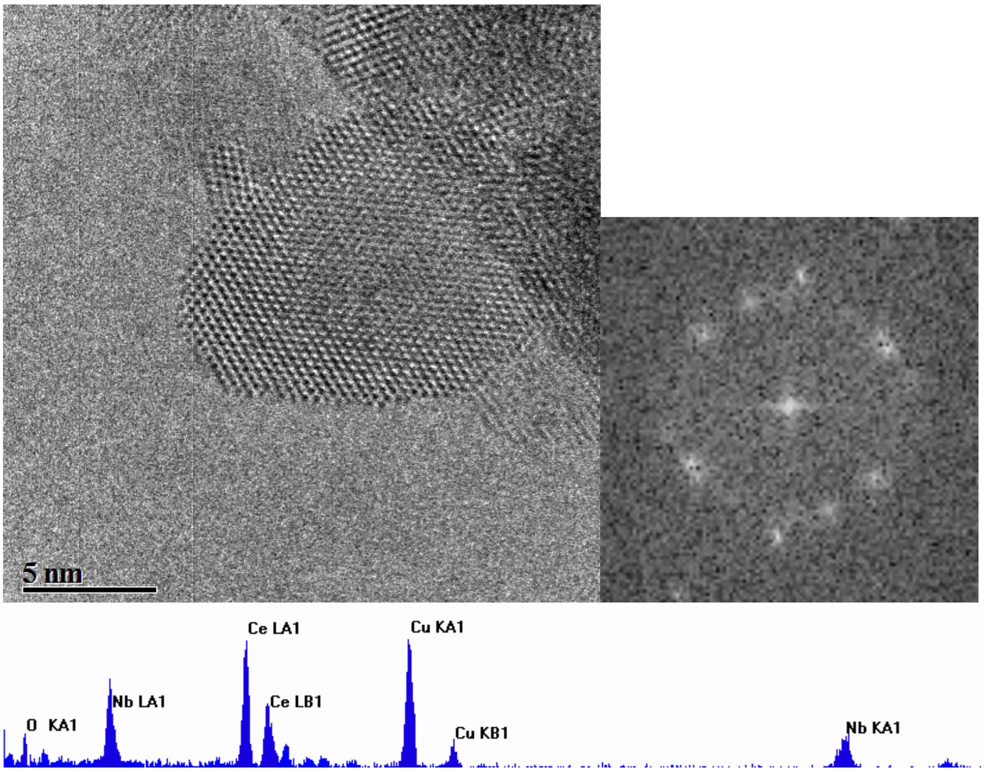

Figure 6.11. HRTEM micrograph of a fluorite particle in the $Ce_{0.6}Nb_{0.4}$ oxide sample (l) with corresponding FFT (r). EDS spectra for the area shown below.

Figure 6.12 shows an agglomerate of fluorite particles in the $Ce_{0.8}Nb_{0.2}$ oxide sample. The EDS, also shown in the Figure, indicates that the particles contain only cerium. The d-spacings for this particle were found to be 3.13 Å and 2.98 Å indicating the {111} and {200} lattice plane. As suspected from the EDS data shown previously, the amorphous phase, shown in Figure 6.13, was niobium rich with only a small cerium signal seen in the EDS spectrum.

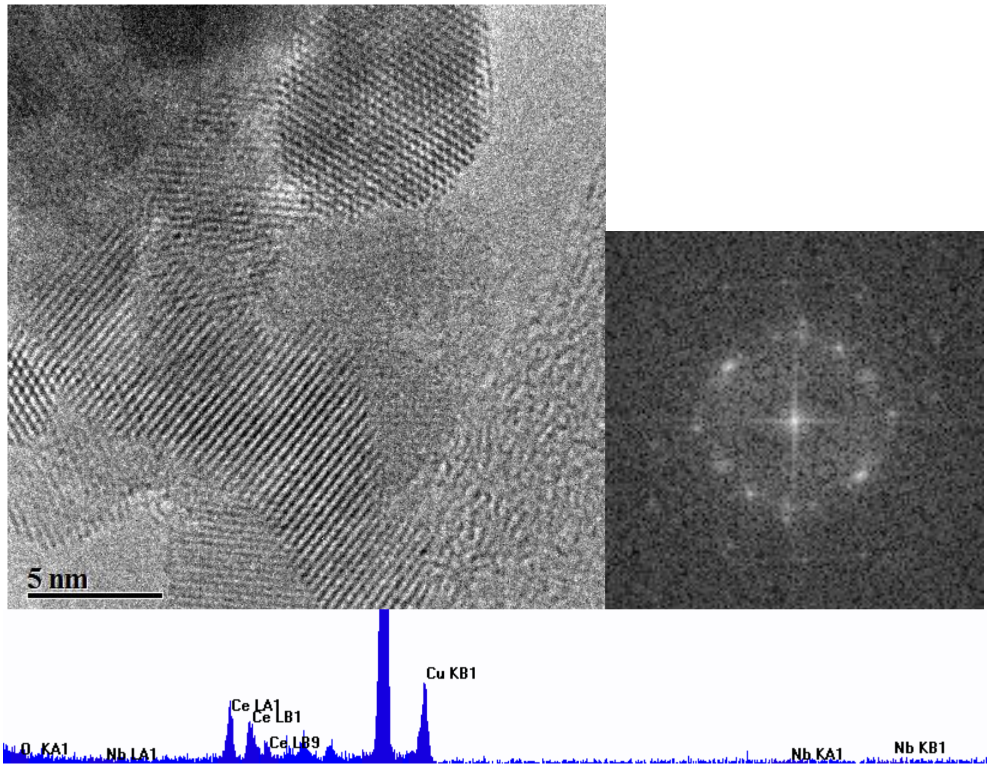

Figure 6.12. HRTEM micrograph of a fluorite agglomerate in the $Ce_{0.8}Nb_{0.2}$ oxide sample (l) with corresponding FFT (r). EDS spectra for the area shown below.

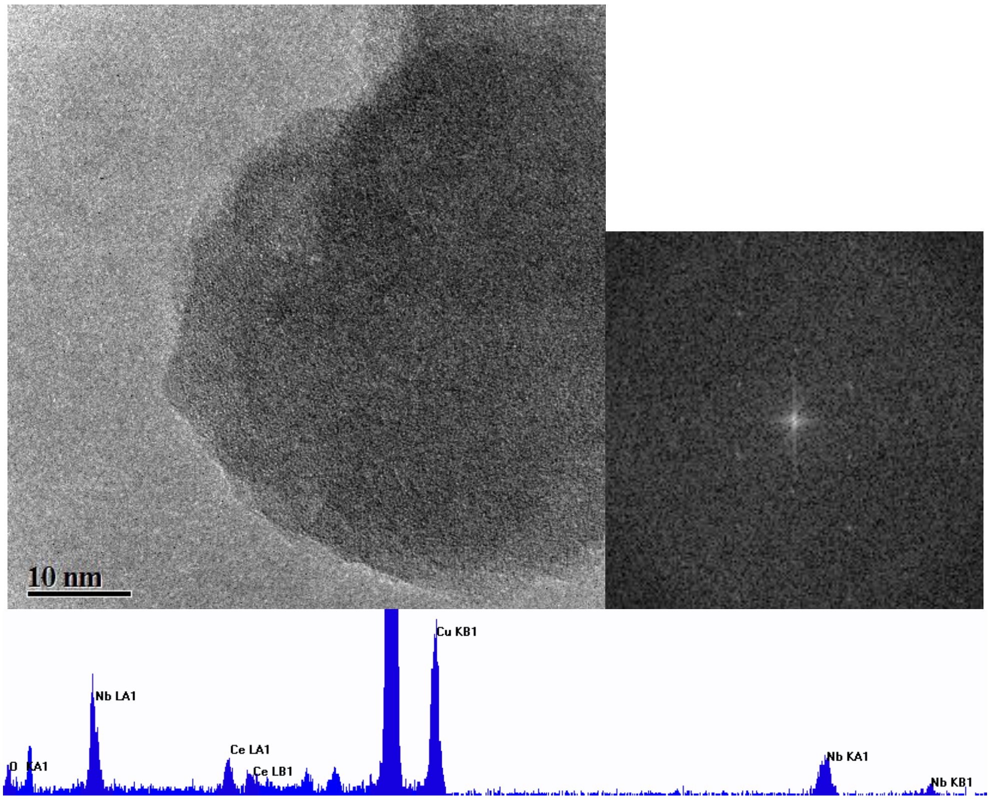

Figure 6.13. HRTEM micrograph of an amorphous region in the $Ce_{0.8}Nb_{0.2}$ oxide sample (l) with corresponding FFT (r). EDS spectra for the area shown below.

6.2.2 XPS analysis

As with the Bi-Ce oxide samples, XPS analysis was carried out on the Ce-Nb oxide samples in order to compare the particle compositions calculated from EDS with those calculated from XPS. Therefore, it could be seen if the surface composition was the same as the overall particle composition and consequently an image of the metal ion distribution in the particles could be built up.

An example XPS survey scan recorded of the $Ce_{0.2}Nb_{0.8}$ oxide sample is seen in Figure 6.14. The survey scan and high resolution scans for all the samples showed a single doublet for the Nb 3d signal (example in Figure 6.15) indicating that niobium was only present in the 5+ state, with the doublet being assigned to the Nb $3d_{5/2}$ and Nb $3d_{3/2}$ spin states. Many split peaks were seen for the Ce 3d signal, indicating cerium was present in the +3 and +4 state.

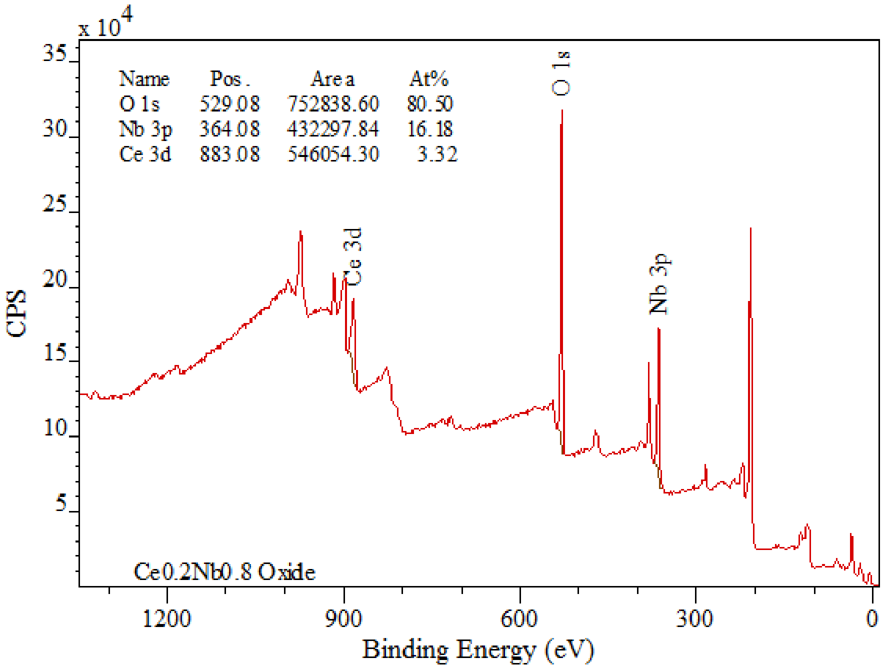

Figure 6.14. XPS survey scan for the $Ce_{0.2}Nb_{0.8}$ oxide sample.

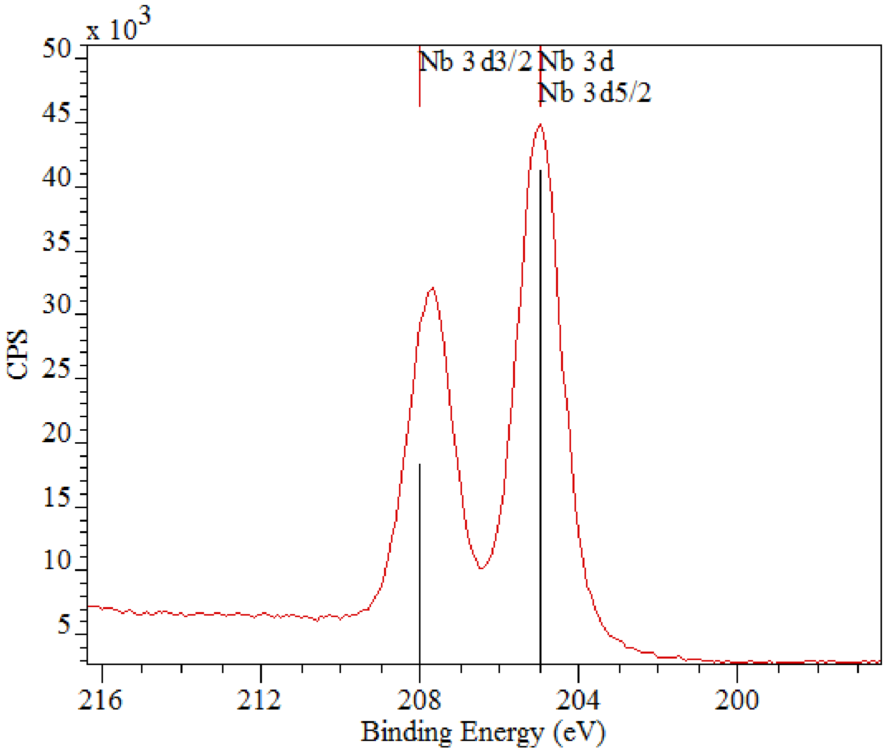

Figure 6.15. High resolution XPS scan of the Nb 3d region for the $Ce_{0.2}Nb_{0.8}$ *oxide sample*

Full results of the XPS analysis can be seen in Table 6.4. They show that the surface is highly niobium rich, regardless of the cerium concentration. This implies that niobium has a strong preference for surface site occupation. These results agree strongly with studies carried out by Stošić *et al*. [121] who found that their mixed Ce-Nb oxide samples also had niobium rich particle surfaces. For example their oxide sample with an average composition of $Ce_{0.75}Nb_{0.25}$ had a surface composition of 64% niobium and 36% cerium (relative metal percentages excluding oxygen content). This is very similar to the surface ratio of Ce:Nb found in the $Ce_{0.8}Nb_{0.2}$ oxide sample in this study. Stošić *et al*. also found that the surface enrichment of niobium increased as the overall concentration of niobium increased, again agreeing well with the results shown below.

Table 6.4. XPS results for the Ce-Nb oxide nanoparticles showing the surface composition.

Sample CeO_2-Nb_2O_5	Atom & Orbital	Binding Energy/ eV	Atomic Concentration /%	Std Dev
$Ce_{0.2}Nb_{0.8}$	Niobium 3p	365.08	83.18	0.31
	Cerium 3d	883.08	16.82	0.31
$Ce_{0.4}Nb_{0.6}$	Niobium 3p	365.08	78.95	0.46
	Cerium 3d	883.08	21.05	0.46
$Ce_{0.6}Nb_{0.4}$	Niobium 3p	365.08	47.00	0.09
	Cerium 3d	883.08	53.00	0.09
$Ce_{0.8}Nb_{0.2}$	Niobium 3p	365.08	64.28	1.27
	Cerium 3d	883.08	35.72	1.27

Overall, as with the Bi-Ce oxide nanoparticles, the XPS analysis has shown that the particles have not formed an ideal solid solution. A comparison of the elemental compositions as calculated from XPS and EDS are shown in Table 6.5. The results show that overall there is a large discrepancy between the composition calculated from the EDS data and the composition of the particles calculated from XPS. The discrepancy is largest for samples with the lowest proportion of niobium where it is most obvious that the niobium ions prefer surface site occupation. The most likely reason for niobium preferring to occupy the surface sites is that niobium can form stable compounds with a lower coordination number. For example, niobium is able to form compounds with 4-fold coordination, whereas cerium is much more stable with higher coordination numbers such as 6- or 8- fold coordination [159, 167].

Table 6.5. Comparison of overall particle composition calculated from EDS analysis and surface composition from XPS.

Sample CeO_2-Nb_2O_5	%Ce from EDS	%Ce from XPS	%Nb from EDS	%Nb from XPS
$Ce_{0.2}Nb_{0.8}$	16.52	16.82	83.47	83.18
$Ce_{0.4}Nb_{0.6}$	23.01	21.05	76.99	78.95
$Ce_{0.6}Nb_{0.4}$	43.15	53.00	56.95	47.00
$Ce_{0.8}Nb_{0.2}$	17.78	35.72	82.22	64.28

The results in Table 6.6 show the percentages calculated for each Ce species in the Ce-Nb samples. It can be seen that there is slightly more variation in the percentages of each species across the four compositions than seen for the Bi-Ce samples, with the percentage of Ce^{3+} increasing substantially with niobium concentration. On average 79.27% of Ce^{4+} and 20.73% of Ce^{3+} is found at the surface, still showing that there is considerably more Ce^{3+} present in these mixed oxide nanoparticles than has been found in previous XPS studies of CeO_2. It has been suggested by Stošić *et al*. [121] that the increased proportion of Ce^{3+} in these mixed oxide species is due to reduction of the Ce^{4+} ions by oxygen ions diffusing through the structure to reach the surface. Cerium is easily able to change between the 3+ and 4+ oxidation state, allowing for addition or removal of oxygen in the structure. This is the underlying mechanism for its application in solid oxide fuel cells, whereby oxygen vacancies created in the crystal by reducing Ce^{4+} to Ce^{3+} allows the diffusion of oxygen ions through the structure. This would also explain why the percentage of Ce^{3+} present increases with increasing Nb^{5+} concentration, to allow for charge balancing in the structure.

Table 6.6. Results from peak fitting analysis showing the relative proportions of Ce^{3+} and Ce^{4+} species in each sample.

Sample CeO_2-Nb_2O_5	% Ce^{3+}	STDEV	%Ce^{4+}	STDEV
$Ce_{0.2}Nb_{0.8}$	28.37	6.41	68.30	0.71
$Ce_{0.4}Nb_{0.6}$	24.61	0.51	75.39	6.03
$Ce_{0.6}Nb_{0.4}$	14.33	0.09	85.67	0.09
$Ce_{0.8}Nb_{0.2}$	15.60	2.37	84.41	2.37

6.2.3 Analysis of trends and correlation of all analytical data

The results of the Ce-Nb mixed oxide system presented here show that although there is good evidence for mixed oxide particles being formed, it is clear that calcination temperatures of 350 °C are not sufficient to form entirely crystalline samples. The PXRD data showed that across all compositions there was evidence of a CeO_2 fluorite phase, but there was also a high proportion of an amorphous phase present. This was confirmed by HRTEM where mixed particles of fluorite and amorphous material were both observed with the CeO_2 phase being close to 100% cerium. Unlike the Bi-Ce oxide system where a phase change occurs across the system, from fluorite to α-Bi_2O_3, with increased bismuth concentration, here it seems that two phase persist throughout the system as a whole. XPS analysis showed that the mixed particles were not homogeneous with niobium showing surface site preference in all samples, presumably due to niobium's ability to form compounds with a lower coordination number than cerium.

6.3 Thermal treatments

As with the Bi-Ce oxide nanoparticles, the Ce-Nb samples were heated at 500 °C and 700 °C for 7 days under flowing oxygen in the tube furnace in order to see how the particles changed with temperature. It was hoped that with heating the particles would become more crystalline and more information about the structural arrangements of these mixed oxides could be gathered.

The PXRD patterns for the $Ce_{0.2}Nb_{0.8}$ oxide nanoparticles calcined at 350 °C, 500 °C and 700 °C are seen in Figure 6.16. It can be seen from the patterns that although no phase changes occurred at 500 °C, the fluorite peaks appear more pronounced and sharper, indicating increased crystallinity in the fluorite phase. At 700 °C, however, an additional phase is observed in addition to the fluorite peaks. These can be assigned to the T-Nb_2O_5 phase. The peaks of the pattern at 700 °C are also much sharper and less broad than the patterns recorded after calcination at lower temperatures indicating improved crystallinity of the sample as well as larger particle sizes.

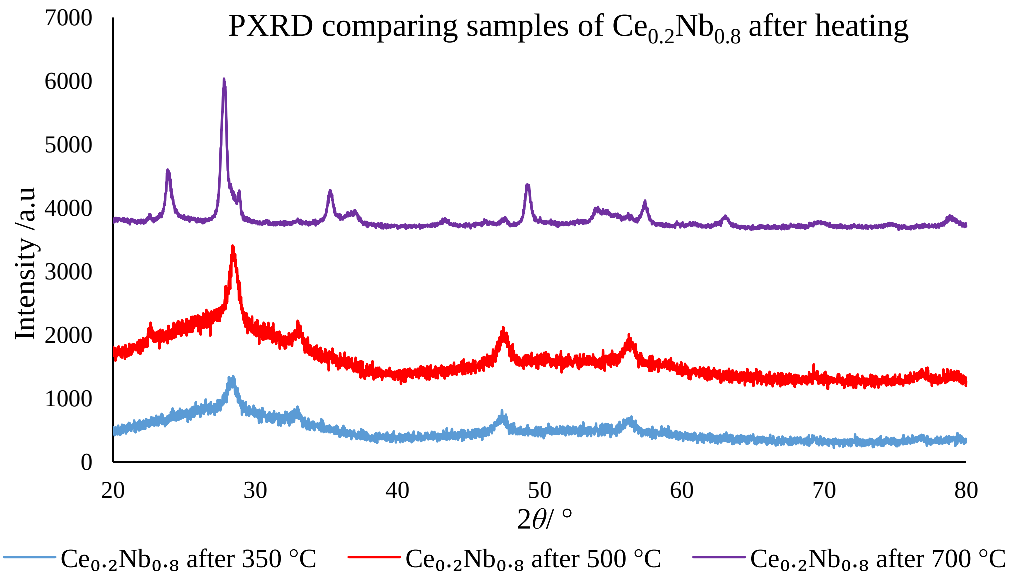

Figure 6.16. PXRD patterns of the $Ce_{0.2}Nb_{0.8}$ oxide nanoparticles after heating in the tube furnace at various temperatures for 7 days.

The PXRD patterns for the $Ce_{0.4}Nb_{0.6}$ oxide sample are seen in Figure 6.17. They show that little change occurred when the sample was heated to 500 °C, but at 700 °C another phase did emerge in addition to the fluorite phase. The additional peaks could be ascribed to the T-Nb_2O_5 phase. Therefore, it can be said that temperature of 700 °C were required to provided enough energy for the crystallisation of these phases. It was unknown, however, at this stage if each of the phases identified contained a mixture of cations.

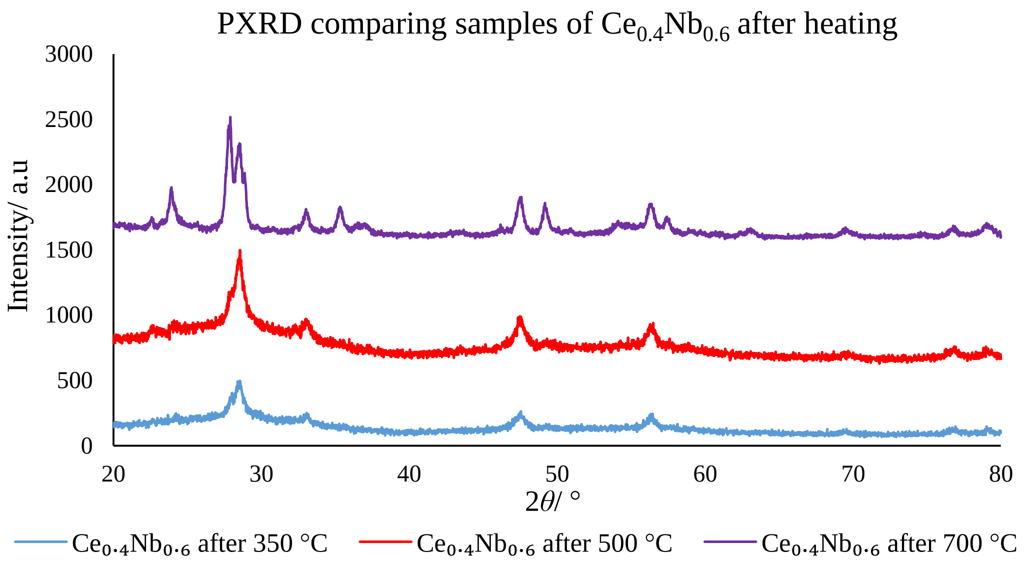

Figure 6.17. PXRD patterns of the $Ce_{0.4}Nb_{0.6}$ oxide nanoparticles after heating in the tube furnace at various temperatures for 7 days.

The cerium rich oxide samples of $Ce_{0.6}Nb_{0.4}$ and $Ce_{0.8}Nb_{0.2}$ have very similar PXRD patterns after calcination at 500 °C and 700 °C. The patterns, as seen in Figures 6.18 and 6.19, show that the majority phase present in these samples is fluorite. This must mean that the majority of the niobium ions are substituted into the fluorite lattice. However, it could be said that a second phase is present at 700 °C, as a shoulder appears on the peak at 28.6 °. As the pattern for $Ce_{0.4}Nb_{0.6}$ shows peaks for several phases at 700 °C, it can be inferred that the solubility limit of niobium ions in the fluorite lattice is approximately 40%.

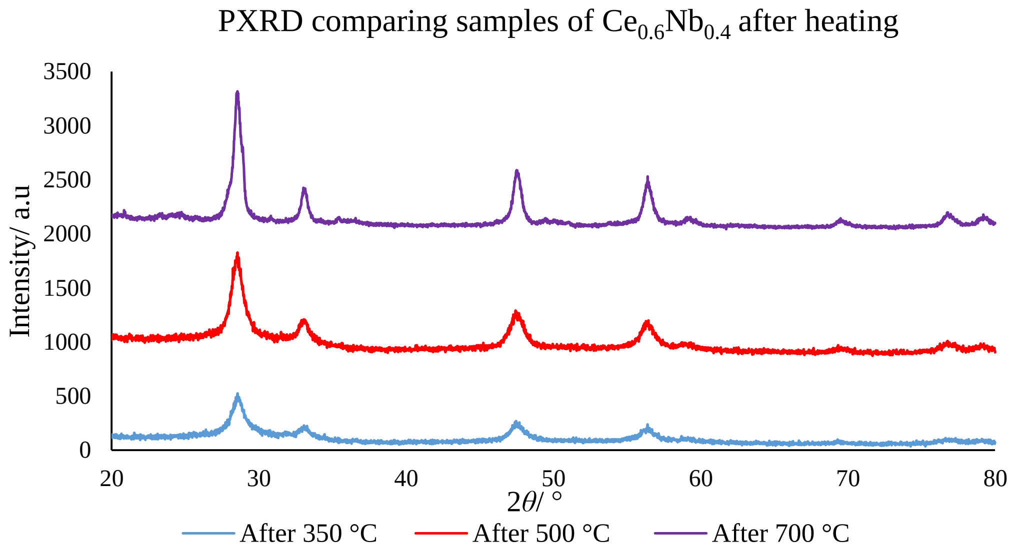

Figure 6.18. PXRD patterns of the $Ce_{0.6}Nb_{0.4}$ oxide nanoparticles after heating in the tube furnace at various temperatures for 7 days.

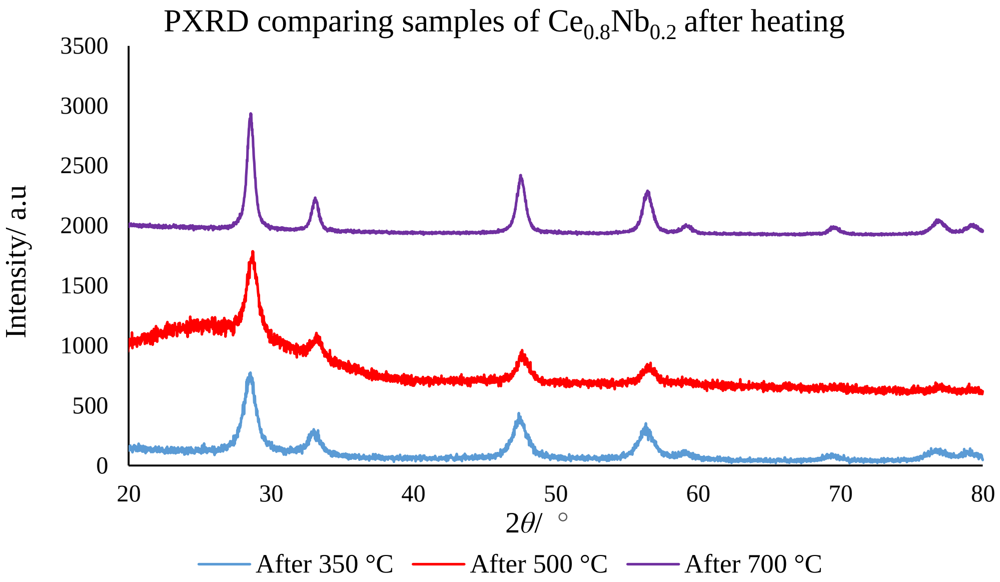

Figure 6.19. PXRD patterns of the $Ce_{0.8}Nb_{0.2}$ oxide nanoparticles after heating in the tube furnace at various temperatures for 7 days.

Scherrer analysis was carried out on all PXRD data in order to compare crystallite size of the different samples at different calcination temperatures. The results of this are seen in Figure 6.20.

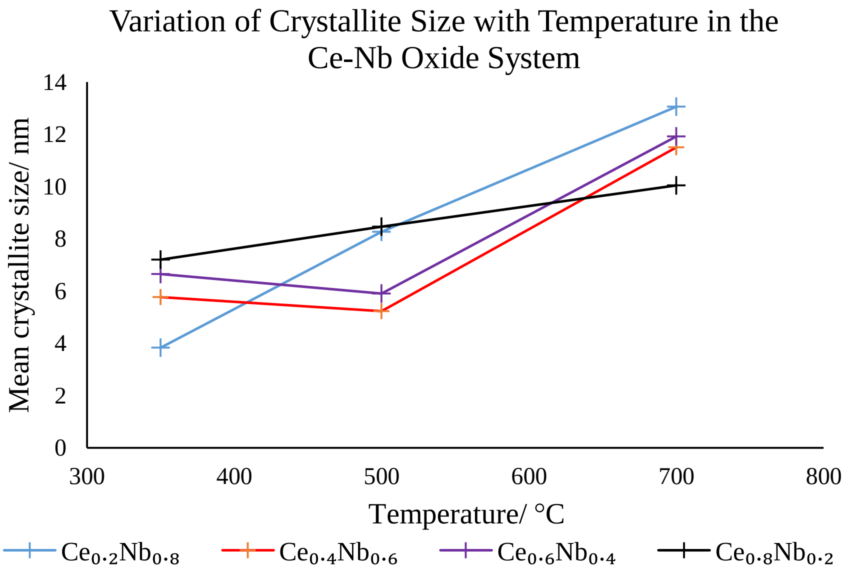

Figure 6.20. Plot showing the relationship between composition and mean crystallite size at various temperatures.

The results show that generally, as expected, crystallite size of all samples increased with temperature due to sintering of particles. The largest change in crystallite size with increasing temperature was seen for the $Ce_{0.2}Nb_{0.8}$ sample. This is because at 350 °C mainly an amorphous phase was seen, with only a few CeO_2 particles being observed in the HRTEM. As the sample was heated, however, a large proportion of crystalline T-Nb_2O_5 was formed, which generated much larger crystallites than CeO_2, hence the large average increase. The smallest increase in crystallite size with temperature was seen for $Ce_{0.8}Nb_{0.2}$ as there was no phase change or new any phases being introduced as the temperature increased. Therefore, the slight increase in the mean crystallite size is likely to be due to sintering of nanoparticles rather than a change in phase.

Similar size changes were seen for $Ce_{0.4}Nb_{0.6}$ and $Ce_{0.6}Nb_{0.4}$, with very little crystallite size change from 350 °C to 500 °C as no phase change occurred, just crystalline CeO_2 and an Nb rich amorphous phase were present. At 700 °C, the T-Nb_2O_5 phase emerged in the sample forming much larger crystallites in comparison to the CeO_2, hence the significant increase in the mean crystallite size as seen in the graph.

The calcined samples were investigated in the microscope to see how the crystallinity of the particles had changed with temperature, as well as how the composition of the mixed particles had changed as new phases were introduced with increased temperature. The results of the compositional analysis, using EDS, for the mixed phase are seen in Table 6.7. These results show that there was a significant change in the elemental composition of these particles after calcination from 350 °C to 500 °C. This may imply that although no phase changes were observed at this temperature, the system was moving towards a more homogenous amorphous phase. As the samples were heated further, to temperatures of 700 °C, the composition of the mixed phase seemed to remain constant, suggesting that the amorphous phase crystallised to T-Nb_2O_5 with the same elemental composition seen at 500 °C. The exception to this trend is the $Ce_{0.8}Nb_{0.2}$ oxide sample, as its composition changes dramatically from 500 °C to 700°C. At this temperature, the particles can form highly crystalline CeO_2 with no amorphous phase present. The CeO_2 phase can accommodate the 20% niobium ions and the composition is close to what is expected with only slightly less niobium than expected. It is possible that a small amount of Nb_2O_5 also formed from this sample explaining the slight deficit of niobium ions in the mixed phase. This small proportion of Nb_2O_5 would be lost in the background of the PXRD pattern so could only be identified in the microscope.

Table 6.7. Composition of the mixed Ce-Nb oxide nanoparticles varying with temperature.

Sample CeO_2-Nb_2O_5	*Calcination temperature/ °C*	*%Ce*	*%Nb*
$Ce_{0.2}Nb_{0.8}$	350	16.52	83.47
	500	36.66	63.34
	700	31.53	59.58
$Ce_{0.4}Nb_{0.6}$	350	23.01	76.99
	500	48.82	51.18
	700	40.42	59.58
$Ce_{0.6}Nb_{0.4}$	350	43.15	56.95
	500	72.67	27.33
	700	69.40	30.60
$Ce_{0.8}Nb_{0.2}$	350	17.78	82.22
	500	35.87	64.13
	700	85.93	14.07

Many particles were viewed in the microscope to see how the crystallinity of the particles had changed with heating. Examples of particles calcined at 500 °C are seen in the micrographs in Figures 6.21-6.24. Generally, although it has already been discussed that the composition of the mixed phase changed substantially upon heating to 500 °C, the phases seen in the micrograph were very similar to those at 350 °C. This also agrees well with the PXRD data, which shows evidence of the fluorite phase only as the amorphous phase cannot be detected by XRD. Figure 6.21 is a representative example of the amorphous phase which was seen across all the samples of the Ce-Nb oxide nanoparticles. The FFT indicates that the sample is non-crystalline, with the EDS spectrum showing that the area contains cerium and niobium ions, therefore, confirming a mixed oxide has been formed.

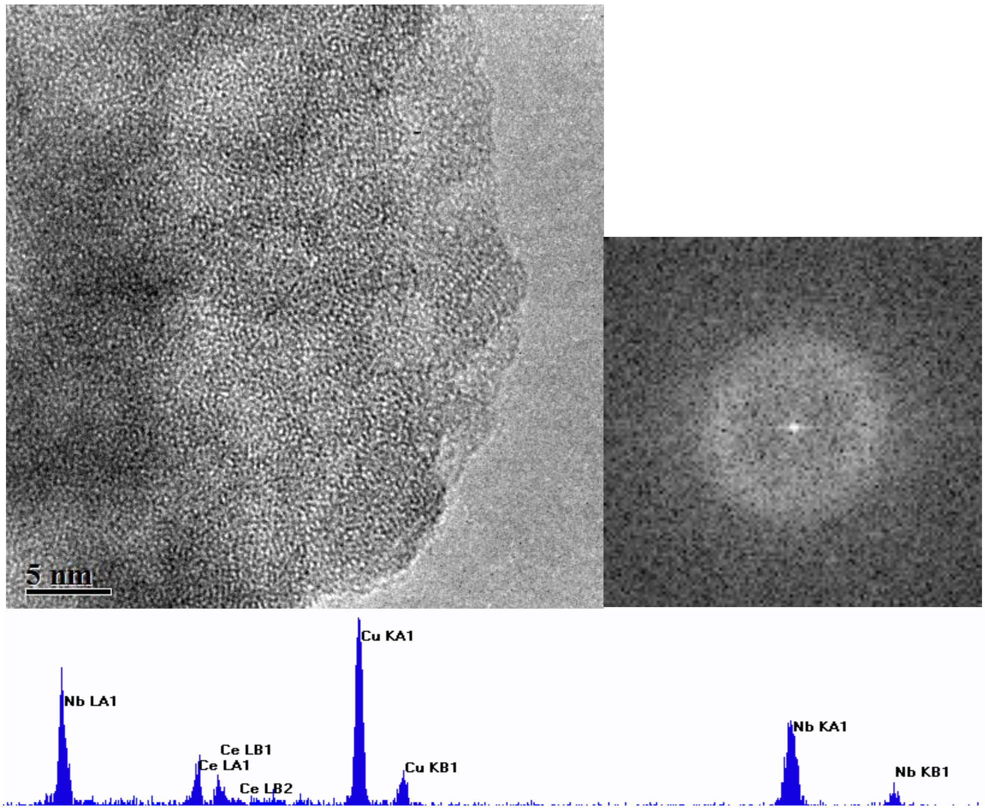

Figure 6.21. HRTEM micrograph of the $Ce_{0.2}Nb_{0.8}$ sample after calcination at 500 °C (l) with corresponding FFT (r). EDS spectra for the area shown below.

The micrograph presented in Figure 6.22 is an example of a crystal of T-Nb_2O_5 seen in the $Ce_{0.4}Nb_{0.6}$ oxide sample. The crystal was identified as the T-Nb_2O_5 phase due to the d-spacings of 3.84 Å, 3.32 Å and 2.87 Å, calculated from the FFT which are indicative of the {001}, {111} and {201} lattice planes of T-Nb_2O_5 respectively. Although no T-Nb_2O_5 peaks were seen in the PXRD pattern from this sample, they may have been concealed by the broad fluorite peaks and high background.

Figure 6.23 presents a micrograph of several overlapping fluorite particles seen in the $Ce_{0.6}Nb_{0.4}$ oxide sample. The d-spacing for the observed lattice plane was found to be 3.31 Å, indicative of the {111} plane of fluorite. Generally, more fluorite particles were observed with increasing cerium content as expected.

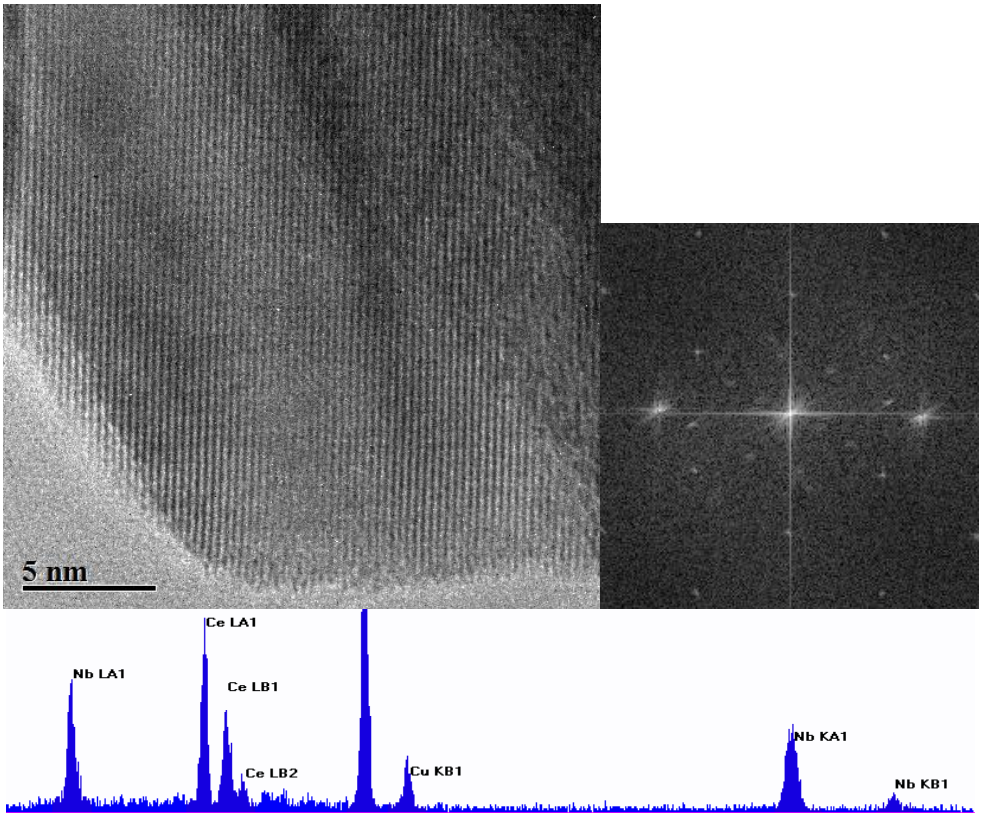

Figure 6.22. HRTEM micrograph of the $Ce_{0.4}Nb_{0.6}$ sample after calcination at 500 °C (l) with corresponding FFT (r). EDS spectra for the area shown below.

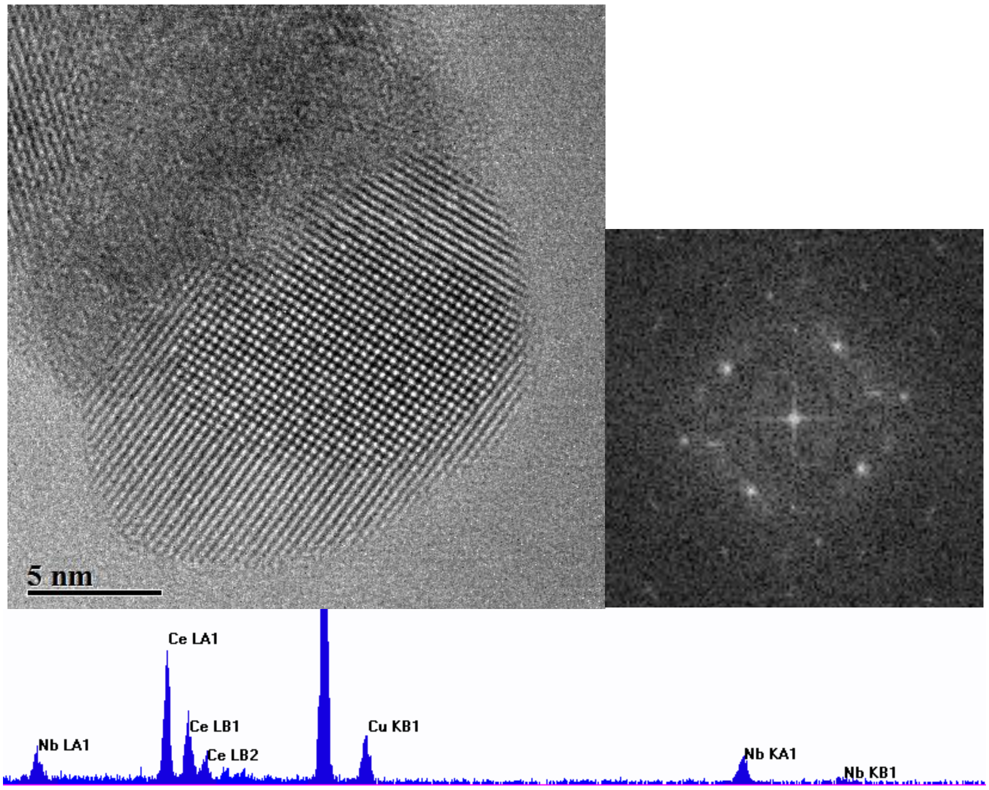

Figure 6.23. HRTEM micrograph of the $Ce_{0.6}Nb_{0.4}$ sample after calcination at 500 °C (l) with corresponding FFT (r). EDS spectra for the area shown below.

A large number of fluorite particles can also be seen in Figure 6.24, which shows a micrograph of the $Ce_{0.8}Nb_{0.2}$ oxide sample with d-spacings of 3.18 Å and 1.98 Å calculated, corresponding to the {111} and {220} lattice planes of fluorite. The EDS spectrum for this area shows that only cerium is present in the particles.

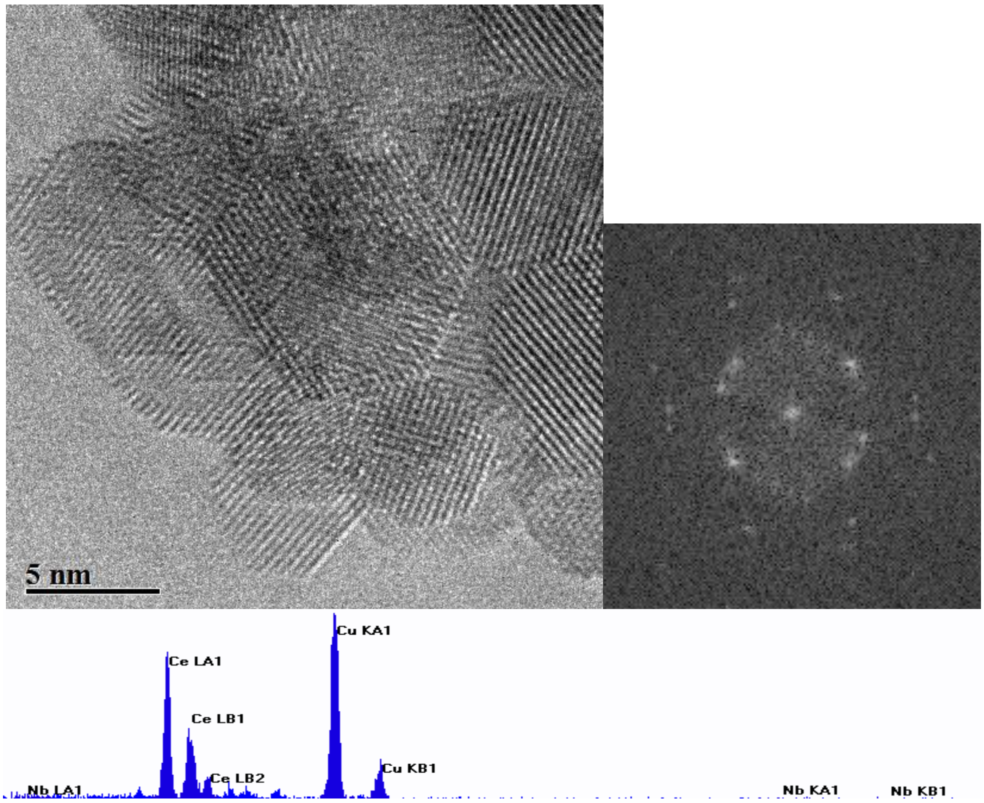

Figure 6.24. HRTEM micrograph of the $Ce_{0.8}Nb_{0.2}$ sample after calcination at 500 °C (l) with corresponding FFT (r). EDS spectra for the area shown below.

Examples of particles calcined at 700 °C can be seen in the micrographs in Figures 6.25-6.28. Generally particles calcined at this temperature were much more crystalline than the previous samples. For example, the micrograph in Figure 6.25 shows an area of T-Nb_2O_5, found in the $Ce_{0.2}Nb_{0.8}$ oxide sample, identified by d-spacings calculated from the FFT of 3.09 Å and 1.55 Å corresponding to the {220} and {118} lattice planes respectively of the T- polymorph of niobium oxide. The corresponding EDS spectrum for the crystal indicates that both cerium and niobium are present showing a mixed oxide has been formed. Several crystals of M-Nb_2O_5 were also found in this sample, and the $Ce_{0.4}Nb_{0.6}$ oxide sample.

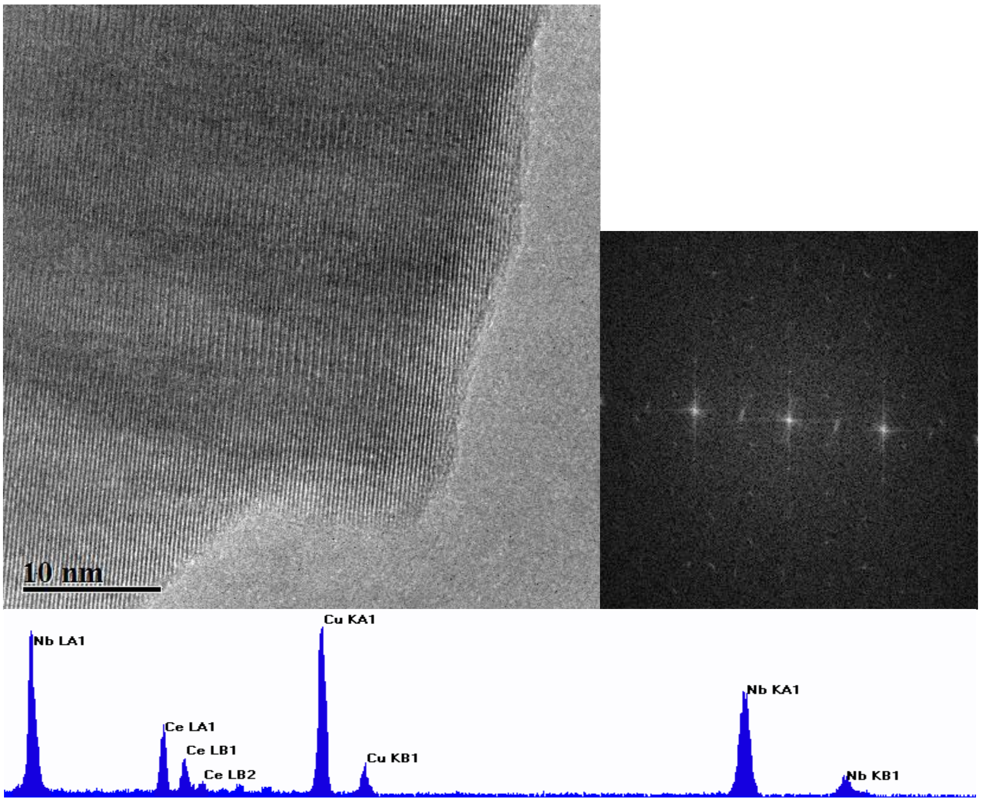

Figure 6.25. HRTEM micrograph of the $Ce_{0.2}Nb_{0.8}$ sample after calcination at 700 °C (l) with corresponding FFT (r). EDS spectra for the area shown below.

The micrograph seen in Figure 6.26 shows an area of the $Ce_{0.4}Nb_{0.6}$ sample. Two distinct phases can be distinguished in the image: an amorphous phase and a crystalline area of T-Nb_2O_5. The d-spacings of the crystalline area, as calculated from the FFT, are 3.17 Å indicative of the {111} lattice plane of T-Nb_2O_5. These results show that in the Ce-Nb mixed oxide system, temperatures of greater than 700 °C are required for full crystallisation of the sample.

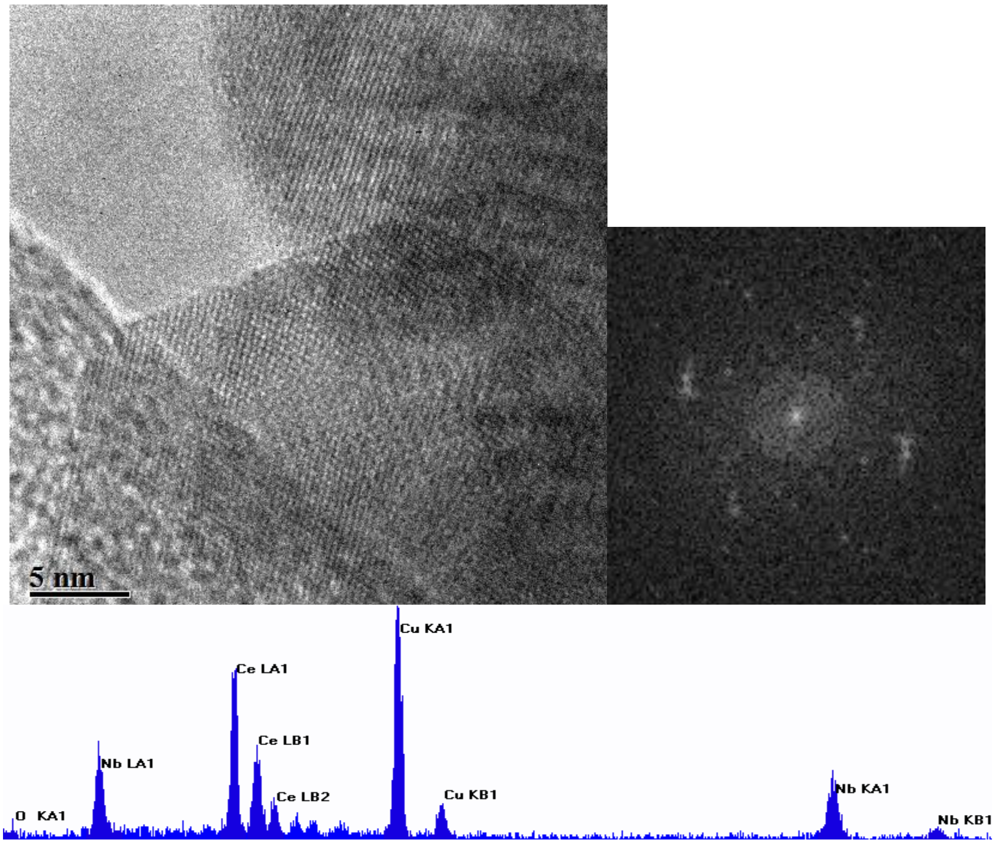

Figure 6.26. HRTEM micrograph of the $Ce_{0.4}Nb_{0.6}$ sample after calcination at 700 °C (l) with corresponding FFT (r). EDS spectra for the area shown below.

Figure 6.27 presents a micrograph of several overlapping fluorite particles seen in the $Ce_{0.6}Nb_{0.4}$ oxide sample after calcination at 700 °C. The FFT gave d-spacings of 3.07 Å and 1.91 Å indicative of the {111} and {220} lattice planes. As expected from the PXRD patterns, the only crystalline phase observed in the microscope was fluorite, with the EDS spectrum showing the presence of both niobium and cerium. Similarly, Figure 6.28 shows an agglomerate of fluorite particles in the $Ce_{0.8}Nb_{0.2}$ oxide sample, with EDS confirming the presence of both metal ions. The calculated d-spacing for this area was 3.19 Å, indicative of the {111} plane.

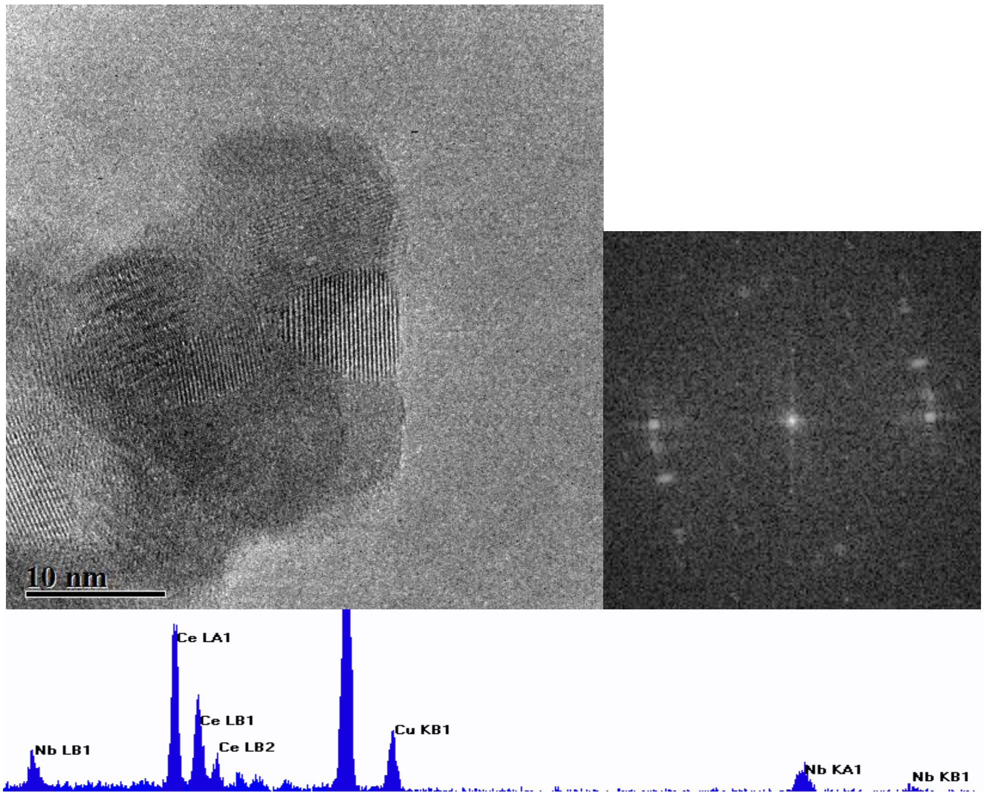

Figure 6.27. HRTEM micrograph of the $Ce_{0.6}Nb_{0.4}$ sample after calcination at 700 °C (l) with corresponding FFT (r). EDS spectra for the area shown below.

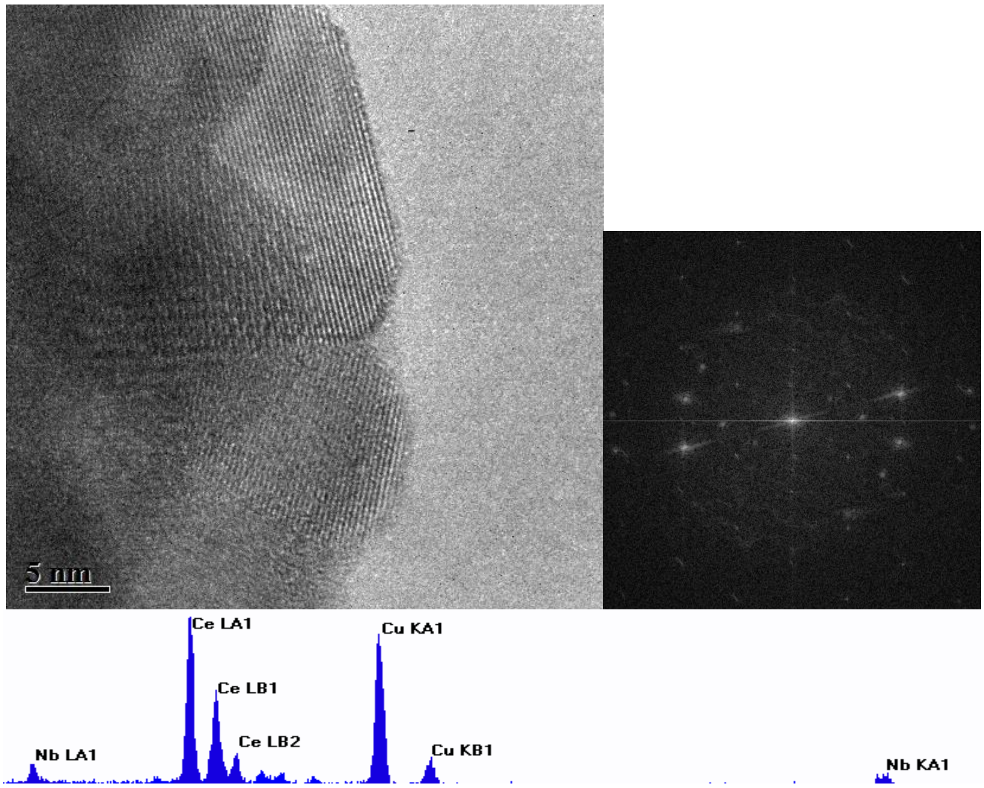

Figure 6.28. HRTEM micrograph of the $Ce_{0.8}Nb_{0.2}$ sample after calcination at 700 °C (l) with corresponding FFT (r). EDS spectra for the area shown below.

XPS analysis was carried out on the samples calcined at both 500 °C and 700 °C to see if the surface composition changed with heating. The results are seen below in Table 6.8. As with the Bi-Ce oxide samples, it can be seen that the surface compositions for each sample stays relatively constant with temperature. As it has already been discussed that the overall composition does change with temperature, it must be concluded that having a niobium rich surface is very energetically favourable for these particles and there is a strong degree of order in the surface structure of the particles.

Table 6.8. Comparison of cerium and niobium percentages from XPS data for the Ce-Nb oxide nanoparticles after calcination at 350 °C, 500 °C and 700 °C, excluding the oxygen signal.

Sample CeO_2-Nb_2O_5	*Atom & Orbital*	*Binding Energy/ eV*	*Atomic Concentration /%*	*Std Dev*
$Ce_{0.2}Nb_{0.8}$ at 350 °C	Niobium 3p	365.08	83.18	0.31
	Cerium 3d	883.08	16.82	0.31
$Ce_{0.2}Nb_{0.8}$ at 500 °C	Niobium 3p	366.08	85.64	0.47
	Cerium 3d	884.08	14.36	0.47
$Ce_{0.2}Nb_{0.8}$ at 700 °C	Niobium 3p	365.08	88.21	0.22
	Cerium 3d	883.08	11.86	0.24
$Ce_{0.4}Nb_{0.6}$ at 350 °C	Niobium 3p	365.08	78.95	0.46
	Cerium 3d	883.08	21.05	0.46
$Ce_{0.4}Nb_{0.6}$ at 500 °C	Niobium 3p	366.08	81.31	0.87
	Cerium 3d	884.08	18.69	0.87
$Ce_{0.4}Nb_{0.6}$ at 700 °C	Niobium 3p	366.08	80.75	0.49
	Cerium 3d	883.08	19.25	0.49
$Ce_{0.6}Nb_{0.4}$ at 350 °C	Niobium 3p	365.08	47.00	0.09
	Cerium 3d	883.08	53.00	0.09
$Ce_{0.6}Nb_{0.4}$ at 500 °C	Niobium 3p	366.08	65.52	1.45
	Cerium 3d	884.08	34.48	1.45
$Ce_{0.6}Nb_{0.4}$ at 700 °C	Niobium 3p	366.08	68.46	0.38
	Cerium 3d	883.08	31.54	0.38
$Ce_{0.8}Nb_{0.2}$ at 350 °C	Niobium 3p	365.08	64.28	1.27
	Cerium 3d	883.08	35.72	1.27
$Ce_{0.8}Nb_{0.2}$ at 500 °C	Niobium 3p	366.08	70.80	0.99
	Cerium 3d	884.08	29.54	0.55
$Ce_{0.8}Nb_{0.2}$ at 700 °C	Niobium 3p	366.08	63.12	0.83
	Cerium 3d	883.08	36.88	0.83

Likewise, the calculated Ce(III) and Ce(IV) proportions across all compositions remain constant, as seen from Table 6.9.

Table 6.9. Comparison of the Ce(III) and Ce(IV) percentages across the Ce-Nb oxide system.

Sample CeO_2-Nb_2O_5	% Ce^{3+}	STDEV	%Ce^{4+}	STDEV
$Ce_{0.2}Nb_{0.8}$ at 350 °C	28.37	6.41	68.30	0.71
$Ce_{0.2}Nb_{0.8}$ at 500 °C	25.82	7.97	73.59	7.36
$Ce_{0.2}Nb_{0.8}$ at 700 °C	26.00	6.61	74.00	6.61
$Ce_{0.4}Nb_{0.6}$ at 350 °C	24.61	0.51	75.39	6.03
$Ce_{0.4}Nb_{0.6}$ at 500 °C	15.42	5.37	84.49	5.47
$Ce_{0.4}Nb_{0.6}$ at 700 °C	20.60	3.20	79.46	3.29
$Ce_{0.6}Nb_{0.4}$ at 350 °C	14.33	0.09	85.67	0.09
$Ce_{0.6}Nb_{0.4}$ at 500 °C	28.64	0.89	71.92	0.64
$Ce_{0.6}Nb_{0.4}$ at 700 °C	26.36	11.01	73.64	11.01
$Ce_{0.8}Nb_{0.2}$ at 350 °C	15.60	2.37	84.41	2.37
$Ce_{0.8}Nb_{0.2}$ at 500 °C	26.17	10.00	73.83	10.00
$Ce_{0.8}Nb_{0.2}$ at 700 °C	26.70	1.82	73.30	1.82

6.4 Summary of the CeO_2-Nb_2O_5 system

The results presented here of investigations into the Ce-Nb mixed oxide system show that although the resin-gel method was successful at producing mixed oxide nanoparticles, further heat treatments were required to form fully crystalline samples. The nanoparticles produced at 350 °C were mostly amorphous, with some cerium rich fluorite particles also being formed. These results agree well with previous studies which found that the presence of cerium in the niobia structure dramatically affects its crystallinity.

As the particles were heated at various temperatures, EDS data indicated that the particle composition changed substantially, but XPS showed that the surface remained highly niobium rich. Therefore, it can be deduced that having a niobium rich surface is energetically preferable possibly due to niobium’s ability to form bonds with a lower coordination number than cerium, and also due to this arrangement causing the least disruption to the fluorite structure. Data from PXRD and HRTEM allowed several phases to be identified in the system including fluorite and an amorphous phase across all compositions and T- and M-Nb_2O_5 emerging at higher concentrations of niobium. Unlike the Bi-Ce oxide system, a mixture of phases was found in every sample and at every temperature. So, overall it can be said that in this system only limited solubility of niobium ions was found in the fluorite structure with an amorphous niobium rich phase also forming readily at lower temperatures. It was found that with heating, this amorphous phase crystallised to Nb_2O_5.

7. The Bi_2O_3-Nb_2O_5 system

7.1 Introduction

The Bi-Nb oxide system was the final ternary oxide system investigated. The resin-gel synthesis was again successful in producing mixed oxide nanoparticles, however, the system proved to be highly complex, with many phases being identified over different elemental compositions and temperatures. These phases included fluorite, pyrochlore, perovskite, T-Nb_2O_5 and $BiNbO_4$. The results found were similar to previous investigations into this system by Zhou *et al*., who described the solid solution Bi-Nb oxide in terms of four phase types from I-IV [168]. Evidence for two of these phases were found in this study.

The samples underwent heat treatments at 500 °C and 700 °C in order to assess the stability of the phases. It was found that little change occurred when heating to 500 °C but at 700 °C the samples underwent a phase change to the well-studied $BiNbO_4$ phase. As with the other ternary oxide systems, analysis was carried out using PXRD, HRTEM, EDS and XPS.

7.2 Initial results for samples calcined at 350 °C

After calcination of the four Bi-Nb oxide samples at 350 °C, PXRD data was recorded to identify which phases had been formed. The results of this analysis are seen in Figure 7.1. It is apparent that the resulting particles formed a mixture of phases.

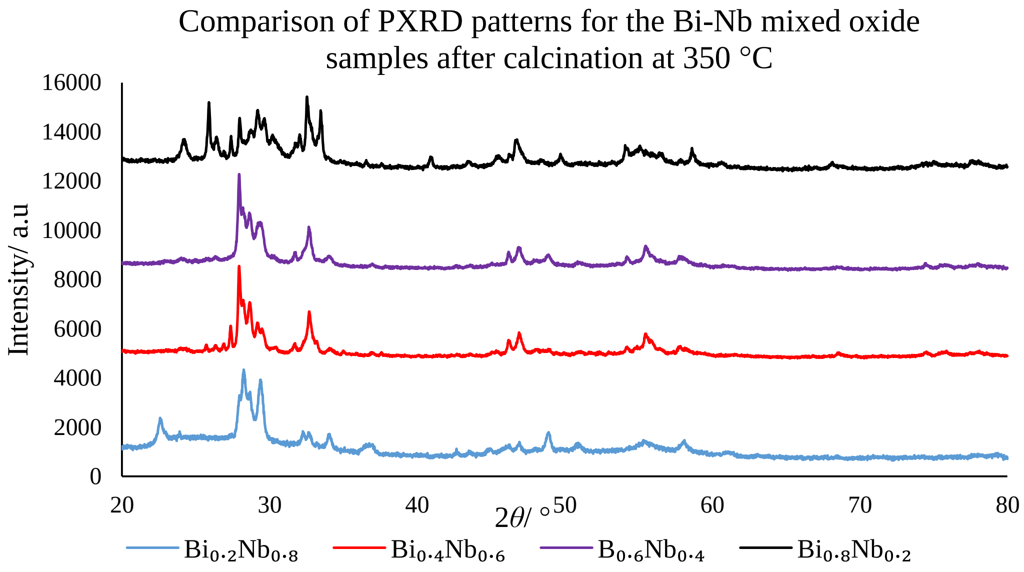

Figure 7.1. PXRD patterns for the range of Bi-Nb oxide compositions synthesised.

The PXRD pattern for the $Bi_{0.2}Nb_{0.8}$ oxide sample shows peaks which can be indexed to the T-Nb_2O_5 phase with the characteristic {001} peak visible at 22.7° , however, there are also some additional peaks, some of which overlap slightly with the niobium oxide peaks. These extra peaks can be indexed to the pyrochlore phase. This is perhaps unexpected as it may be predicted that the α-Bi_2O_3 structure could form a solid solution with a small percentage of niobium ions and the remainder would form T-Nb_2O_5, however, this is not the case as there is no evidence of the α-Bi_2O_3 phase in the pattern. Zhou *et al.* [168] previously identified a defect pyrochlore type structure in their studies on the Bi_2O-Nb_2O_5 system, which they named the type II structure. It may be this same structure type being observed in the $Bi_{0.2}Nb_{0.8}$ oxide sample. Zhou *et al.* reported that the type II structure appeared at compositions of $12Bi_2O_3$. Nb_2O_5 to $4Bi_2O_3$. Nb_2O_5. This would explain why two phases are seen as there is an excess of niobium in the $Bi_{0.2}Nb_{0.8}$ oxide sample, if the type II structure has formed, which could then crystallise at T-Nb_2O_5. If this is the case then it can be inferred that the type II phase forms preferentially leaving the remaining niobium to form T-Nb_2O_5. Ling *et al.* [169] also carried out studies on the bismuth rich end of the Bi_2O-Nb_2O_5 system and produced good evidence for solid solutions of the type II structure being formed. The pyrochlore structure has also previously been seen in the Bi-Nb oxide system by Piir *et al.* [170], who found evidence of the pyrochlore phase forming when a further transition metal species is also introduced to the system. Therefore it is highly likely that the $Bi_{0.2}Nb_{0.8}$ oxide sample contains two phases: the type II pyrochlore phase and T-Nb_2O_5.

The patterns for the $Bi_{0.4}Nb_{0.6}$ and $Bi_{0.6}Nb_{0.4}$ oxide sample were both very similar, with peaks indexed to the fluorite, pyrochlore and perovskite phases. It seems likely that these samples have formed the type III structure, as defined by Zhou *et al.*, which is described as a composite phase made up of units of fluorite, pyrochlore and perovskite. They postulated that the only way the δ-Bi_2O_3 fluorite structure could accommodate increasing niobium content was to form these additional phase units.

The PXRD pattern for the $Bi_{0.8}Nb_{0.2}$ oxide sample was also complicated by the presence of several phases. Firstly, the same δ-Bi_2O_3 fluorite peaks were identified in this sample, as for the other Bi-Nb oxide samples, at 29.03°, 32.67°, 46.83° and 57.72°. In addition to this phase, peaks corresponding to β-Bi_2O_3 were observed at 28.0°, 32.5° and 33.4°. The β-Bi_2O_3 phase is usually formed by cooling of the δ-Bi_2O_3 phase. Therefore, it appears that in this sample some of the δ-Bi_2O_3 particles may have cooled down more rapidly than others and formed a mixture of bismuth oxide polymorphs. The β- polymorph is known to be structurally related to fluorite but has a different arrangement of oxygen vacancies [171]. Therefore, the δ- and β- polymorphs would be indistinguishable by HRTEM, which only records the cation arrangement. The low temperature α-Bi_2O_3 polymorph was also seen. After assigning the peaks corresponding to these three phases there were still several peaks unaccounted for. This is likely due to the defect fluorite nature of the majority of the nanoparticles, meaning that in addition to the face centred cubic lines of the fluorite phases, new lines are present corresponding to the disorder in the structure. These results support the theory that at this particle size solid solution structures form readily due to the increased quantum effects at this scale.

Crystallite sizes of the mixed Bi-Nb oxide samples were found using Scherrer analysis and the results can be seen in Figure 7.2. The plot shows the general trend of crystallite size increasing as the bismuth concentration in the mixed oxide particles increases. The $Bi_{0.4}Nb_{0.6}$ and $Bi_{0.6}Nb_{0.4}$ oxide samples seem to have very similar crystallite sizes despite the slightly different compositions, which is likely due to the same phases being formed for both samples, as seen from the PXRD data, so the crystallite size difference is minimal.

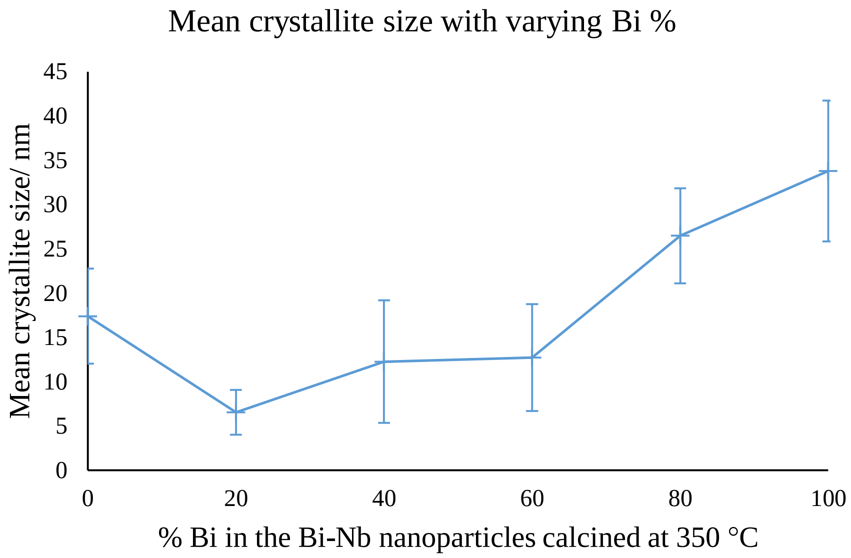

Figure 7.2. Plot showing the relationship between composition and mean crystallite size.

The samples were analysed microscopically, in order to observe the various phases present in the sample and to form an idea of how the metal ions were distributed in the different phases. EDS data collected for each of the samples is shown in Figures 7.3-7.6. The plots show the number of Bi Lα_1 counts against the Nb Kα_1 counts for approximately 30 particles in each sample. It can be seen from this data that 3 phases of different compositions were seen in every sample. The plot for the $Bi_{0.2}Nb_{0.8}$ oxide sample, seen in Figure 7.3, indicates that two mixed oxide phases were formed, along with some pure Nb_2O_5. This agrees well with the PXRD pattern for this sample which indicated that T-Nb_2O_5 was present along with a pyrochlore phase. Of the two mixed phases observed, one was highly bismuth rich, while the second majority phase was more niobium rich. The more niobium rich mixed phase was found to be poorly crystalline which, therefore, may not be represented in the PXRD pattern, while the more bismuth rich phase was highly crystalline and is likely to be the pyrochlore type II phase seen in the PXRD pattern. The majority mixed phase had a calculated composition of 74.75% niobium and 25.25% bismuth in solid solution. It is possible that this was the maximum percentage of bismuth that could be accommodated in the structure, therefore a second mixed phase with a higher proportion of bismuth but less niobium was formed. The remaining niobium was then free to form Nb_2O_5.

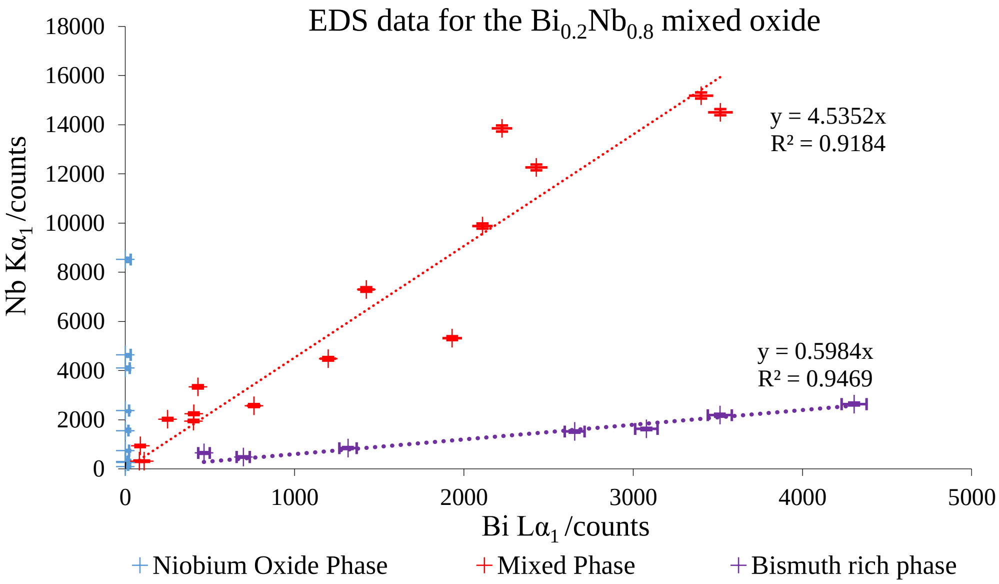

Figure 7.3. EDS plot of Bi Lα$_1$ counts against Nb Kα$_1$ counts for the $Bi_{0.2}Nb_{0.8}$ oxide sample.

The EDS data for the $Bi_{0.4}Nb_{0.6}$ oxide sample, shown in Figure 7.4, also provides evidence of a pure niobium oxide phase as well as a highly bismuth rich phase. The mixed oxide phase seen in red shows a large range of compositions is present which is a good indication the ions are in solid solution. This is what would be expected given that the temperatures used in the synthesis were far too low to form the distinct $BiNbO_4$ phase. Similarly, the $Bi_{0.6}Nb_{0.4}$ oxide sample, Figure 7.5, shows a similar range of compositions for the mixed phase, also indicating the ions are in solid solution. The composition calculations show there is more bismuth than expected in the mixed phase. This can be accounted for by the fact that there were some large niobium oxide crystals also examined in the microscope, which would decrease the amount of niobium available to be incorporated into the mixed phase. As well as the pure Nb_2O_5 being examined, there were a few crystals of pure bismuth oxide also present in the sample. The reason for several phases being formed across all concentration ranges could be because of the synthetic process, where there may be regions of bismuth or niobium ions trapped separately from each other in the polymer matrix. These may then form binary oxides before coming into contact with the other metal ion. These results generally agree well with the phases found using X-ray diffraction, however no lines corresponding to T-Nb_2O_5 were found for these two samples. This is likely because the proportion of T-Nb_2O_5 in the samples was low and therefore, masked by the other phases. This makes sense as the ‘excess’ of niobium in these samples is much less as the proportion of the two metal ions is approximately equal.

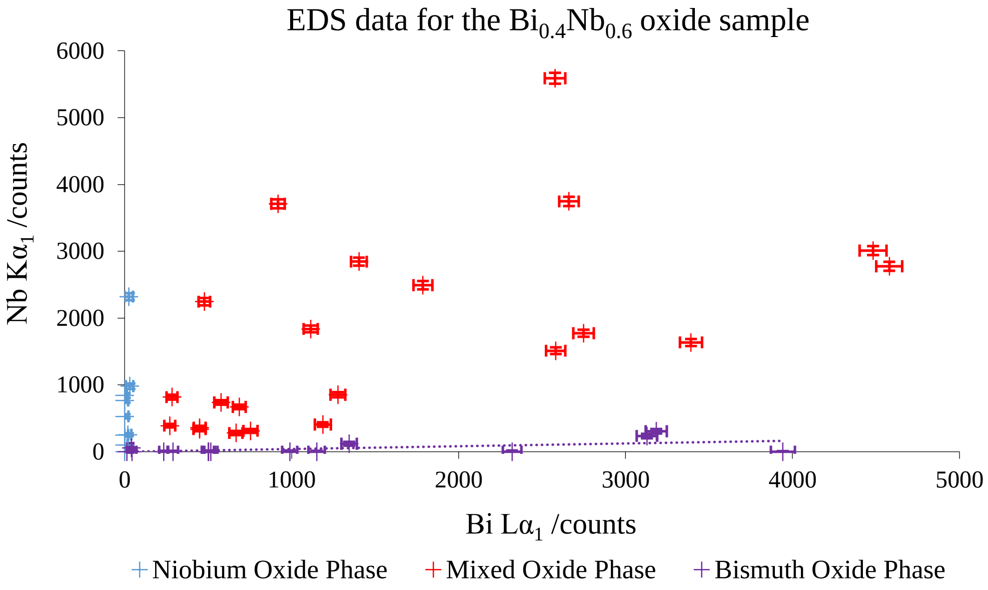

Figure 7.4. EDS plot of Bi Lα_1 counts against Nb Kα_1 counts for the $Bi_{0.4}Nb_{0.6}$ oxide sample.

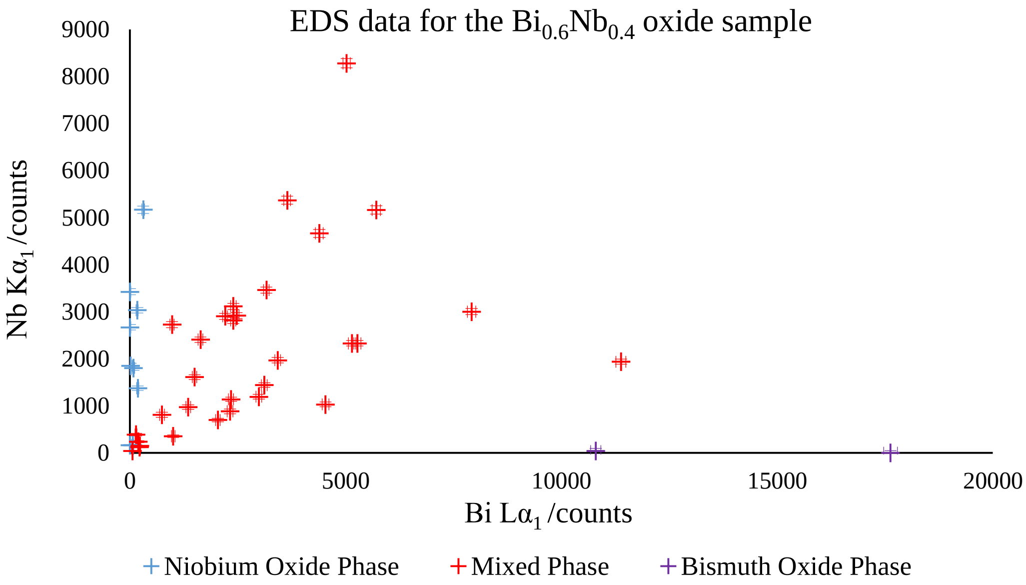

Figure 7.5. EDS plot of Bi Lα_1 counts against Nb Kα_1 counts for the $Bi_{0.6}Nb_{0.4}$ oxide sample.

Finally, the EDS plot for the $Bi_{0.8}Nb_{0.2}$ oxide sample is seen in Figure 7.6. The same trend is seen here, with three distinct phases being observed. In this case however, there were far more pure bismuth oxide particles observed due to the excess of bismuth in the sample.

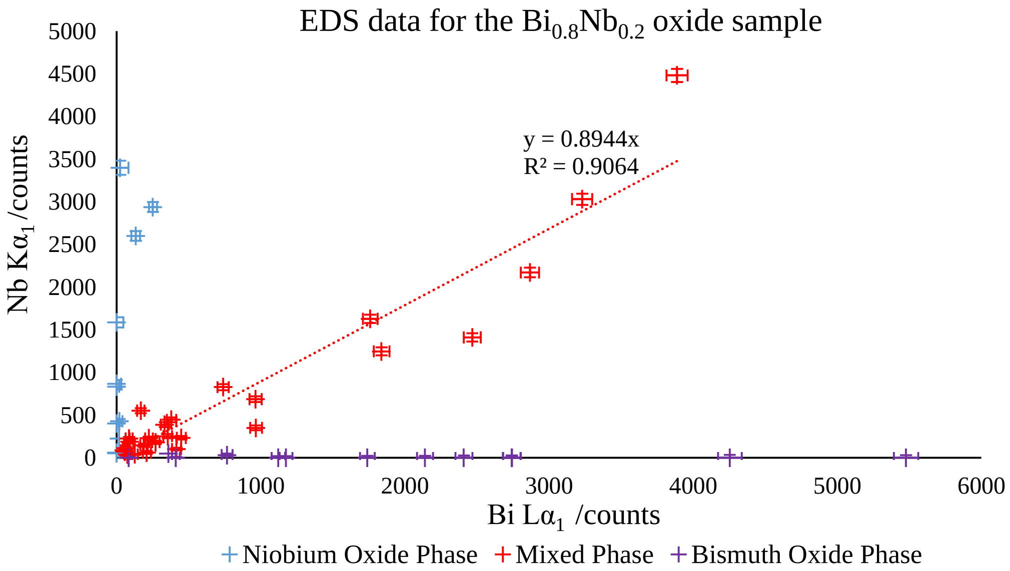

Figure 7.6. EDS plot of Bi $L\alpha_1$ counts against Nb $K\alpha_1$ counts for the $Bi_{0.8}Nb_{0.2}$ oxide sample.

As with the Ce-Nb oxide samples, the fact that multiple phases were seen in all samples, indicates that an ideal solid solution was not formed for any of the compositions synthesised here. As already suggested, this could be due to the synthetic process where ‘pockets’ of bismuth or niobium ions may be isolated in the polymer and form binary oxides. The calcination which takes place after the synthesis is only at sufficient temperatures to remove any residual polymer and not allow for diffusion of ions across particles.

From the EDS data, compositions for the mixed phase in each sample were calculated using the ratio of Bi:Nb, as seen from the EDS plot, and adjusted using the $K_{Bi:Nb}$ value, as calculated from the standard samples. The calculated compositions for each sample can be seen in Table 7.1. The results show that the composition for the mixed phase in each sample is quite different from what was expected. For the $Bi_{0.2}Nb_{0.8}$ oxide sample there appears to be slightly more bismuth than expected in the mixed phase. However, this is compensated by the fact that there was a large proportion of Nb_2O_5 also present in the sample. The $Bi_{0.4}Nb_{0.6}$ and $Bi_{0.6}Nb_{0.4}$ oxide samples both have substantially more bismuth present in the mixed phase than expected, but again, there is evidence for pure Nb_2O_5 also being present in the sample. Conversely, the $Bi_{0.8}Nb_{0.2}$ oxide sample had a calculated mixed phase composition which was bismuth deficient in comparison to the expect result. However, a large number of pure bismuth oxide particles were also seen. Again, these results provide evidence that an ideal solid solution was not formed in the Bi-Nb oxide system with a variety of phases and compositions seen.

Table 7.1. Calculated composition of the mixed phase in each of the Bi-Nb oxide samples from EDS data.

Sample Bi_2O_3-Nb_2O_5	*Expected % Bi*	*Calculated % Bi from EDS*	*Expected % Nb*	*Calculated % Nb from EDS*
$Bi_{0.2}Nb_{0.8}$	20	25.25	80	74.75
$Bi_{0.4}Nb_{0.6}$	40	63.17	60	36.83
$Bi_{0.6}Nb_{0.4}$	60	72.37	40	27.37
$Bi_{0.8}Nb_{0.2}$	80	63.14	20	36.86

Further structural analysis was carried out in the microscope by calculating lattice spacings for individual crystals using the FFT of the HRTEM images. The results of average d-spacings for the different planes of the fluorite structure in comparison to literature values are seen in Table 7.2. It can be seen that d-spacing evidence of the fluorite phase was found in three of the mixed Bi-Nb oxide samples, those of $Bi_{0.4}Nb_{0.6}$, $Bi_{0.6}Nb_{0.4}$ and $Bi_{0.8}Nb_{0.2}$. The calculated d-spacings for these samples were slightly larger than the literature values indicating a more relaxed crystal structure. The results agree well with the PXRD which gave evidence for the three compositions seen to contain fluorite particles.

Table 7.2. Observed d-spacings for each index of the fluorite structure across all Bi-Nb oxide compositions. [85]

	Index of fluorite structure with corresponding d-spacing							
Sample Bi_2O_3-Nb_2O_5	Average d-spacing for {111}/ Å	Literature value/ Å	Average d-spacing for {200}/ Å	Literature value/ Å	Average d-spacing for {220}/ Å	Literature value/ Å	Average d-spacing for {311}/ Å	Literature value/ Å
$Bi_{0.2}Nb_{0.8}$	-	-	-	-	-	-	-	-
$Bi_{0.4}Nb_{0.6}$	3.18 ± 0.12	3.12	-	-	2.16 ± 0.18	1.91	-	-
$Bi_{0.6}Nb_{0.4}$	3.21 ± 0.10	3.12	2.98 ± 0.12	2.71	1.91 ± 0.17	1.91	1.70 ± 0.07	1.63
$Bi_{0.8}Nb_{0.2}$	3.22 ± 0.08	3.12	2.75 ± 0.15	2.71	-	-	-	-

Average d-spacings found for the pyrochlore and perovskite phases can be seen in Tables 7.3 and 7.4. The observed phases in the microscope generally correlate well to the phases seen in the PXRD patterns, with the exception of some pyrochlore particles being seen in the $Bi_{0.2}Nb_{0.8}$ sample, of which there was no evidence in the PXRD pattern. This is undoubtedly because the proportion of pyrochlore formed in this sample was too small to be seen in the pattern. Generally, the particles analysed in the microscope give further weight to the theory that a combination of type II and type III phases have been formed across this solid solution Bi-Nb oxide system, due to the identification of fluorite, pyrochlore and perovskite phases.

Table 7.3. Observed d-spacings for each index of the pyrochlore structure across all Bi-Nb oxide compositions. [107]

Sample Bi_2O_3-Nb_2O_5	**Index of pyrochlore phase with corresponding d-spacing** Average d-spacing for {111}/ Å	Literature value/ Å	Average d-spacing for {311}/ Å	Literature value/ Å	Average d-spacing for {222}/ Å	Literature value/ Å
$Bi_{0.2}Nb_{0.8}$	6.22 ± 0.02	6.03	3.12 ± 0.03	3.15	3.07 ± 0.03	3.02
$Bi_{0.4}Nb_{0.6}$	-	-	-	-	-	-
$Bi_{0.6}N_{0.4}$	6.15 ± 0.17	6.03	3.31 ± 0.01	3.15	3.03 ± 0.04	3.02
$Bi_{0.8}Nb_{0.2}$	-	-	-	-	3.02 ± 0.03	3.02

Table 7.4. Observed d-spacings for each index of the perovskite structure across all Bi-Nb oxide compositions. [172]

Sample Bi_2O_3-Nb_2O_5	**Index of perovskite phase with corresponding d-spacing** Average d-spacing for {110}/ Å	Literature value/ Å	Average d-spacing for {112}/ Å	Literature value/ Å	Average d-spacing for {220}/ Å	Literature value/ Å
$Bi_{0.2}Nb_{0.8}$	-	-	-	-	-	-
$Bi_{0.4}Nb_{0.6}$	4.04 ± 0.11	3.82	3.05 ± 0.07	2.71	2.07 ± 0.14	1.92
$Bi_{0.6}Nb_{0.4}$	3.99 ± 0.08	3.82	2.96 ± 0.03	2.71	1.96 ± 0.07	1.92
$Bi_{0.8}Nb_{0.2}$	3.92 ± 0.06	3.82	2.98 ± 0.06	2.71	2.09 ± 0.20	1.92

As calculations showed the d-spacings in all three phases were slightly higher than the literature values of bulk material, it was expected that the unit cell parameters would increase accordingly. This was indeed found to be the case, with full results seen in Table 7.5. The table shows the isolated indexed peaks in each sample used to calculate the unit cell parameters. For the more complex patterns where the peaks of different phases were less easily distinguishable, FullProf was used to fit the patterns and calculate the unit cell parameters. Where this was the case the errors for the FullProf calculations are given in brackets.

Table 7.5. Unit cell parameters calculated for all Bi-Nb oxide samples compared to literature values. Indexed peaks for each phase are also given. [35, 39, 107, 172]

					Unit Cell Parameter Length/ Å			*Unit Cell Parameter Literature Length/ Å*		
Sample Bi_2O_3-Nb_2O_5	Phase	*θ*/ rads	Index	d_{hkl}/ Å	a	b	c	A	b	c
Nb_2O_5	T-Nb_2O_5 *M-Nb_2O_5*	0.196 *0.206* *0.216* 0.246 0.251 0.318	001 *400* *101* 111 220 201	3.96 *3.77* *3.60* 3.17 3.10 2.47	6.18 *20.23*	29.29 *20.23*	3.93 *3.82*	6.18 *20.44*	29.18 *20.44*	3.93 *3.83*
$Bi_{0.2}Nb_{0.8}$	T-Nb_2O_5 *Pyrochlore*	0.197 *0.256* *0.426*	100 *222* *440*	3.94 *3.04* 1.87	6.19 (0.00095) *10.76* *(0.00427)*	29.23 (0.00354) *10.76* *(0.00427)*	3.91 (0.000420) *10.76* *(0.00427)*	6.18 *10.79*	29.18 *10.79*	3.93 *10.79*
$Bi_{0.4}Nb_{0.6}$	δ-Bi_2O_3	0.243 0.284	111 200	3.20 2.75	5.68 (0.00063)	5.68 (0.00063)	5.68 (0.00063)	5.65	5.65	5.65
$Bi_{0.6}Nb_{0.4}$	Perovskite *δ-Bi_2O_3*	0.285 *0.484*	200 *311*	2.74 *1.66*	3.78 (0.00118) *5.63* *(0.00914)*	3.78 (0.00118) *5.63* *(0.00914)*	3.78 (0.00118) *5.63* *(0.00914)*	3.90 *5.65*	3.90 *5.65*	3.90 *5.65*
$Bi_{0.8}Nb_{0.2}$	Perovskite	0.284 0.407	112 220	2.75 1.95	3.78	3.78	3.78	3.80	3.80	3.80
Bi_2O_3	α-Bi_2O_3	0.290 0.170 0.225	200 020 002	2.70 4.44 3.46	5.87	8.18	7.52	5.85	8.17	7.51

7.2.1 HRTEM imaging

As with the other two ternary systems, imaging was carried out on many particles in the Bi-Nb oxide samples to better understand the phases identified by PXRD. The micrographs seen in Figures 7.7 to 7.15 are representative examples of the particles seen in the HRTEM for the Bi-Nb oxide nanoparticles.

The micrograph in Figure 7.7 shows a T-Nb_2O_5 particle in the $Bi_{0.2}Nb_{0.8}$ oxide sample. This was the most abundant phase, as expected from the PXRD data which showed the most intense peaks for this niobium oxide. The d-spacings for this area, as calculated from the FFT, were 3.97 Å, 2.54 Å and 1.98 Å corresponding to the {001}, {201} and {291} lattice planes of T-Nb_2O_5. The EDS spectrum indicates that the crystal contained only niobium. Another region of the $Bi_{0.2}Nb_{0.8}$ sample is shown in Figure 7.8. This micrograph presents a crystalline region containing both niobium and bismuth, as shown in the EDS spectrum. The d-spacings were found to be 6.17 Å and 3.06 Å indicative of the {111} and {222} lattice planes of pyrochlore, which agrees well with the PXRD data. The final micrograph of the $Bi_{0.2}Nb_{0.8}$ oxide sample, seen in Figure 7.9, shows a quasi-crystalline region of sample. As it is not crystalline the phase is not represented in the PXRD pattern. These three different phases can all be differentiated crystallographically and compositionally, as seen in the EDS plot for the sample (Figure 7.3). The quasi-crystalline phase was present across all compositions of the Bi-Nb samples, with EDS finding the areas were niobium rich. This is similar to the results found for the Ce-Nb system where it was suggested that the niobium inhibits the formation of a crystalline phase by disrupting the cation arrangement in some way.

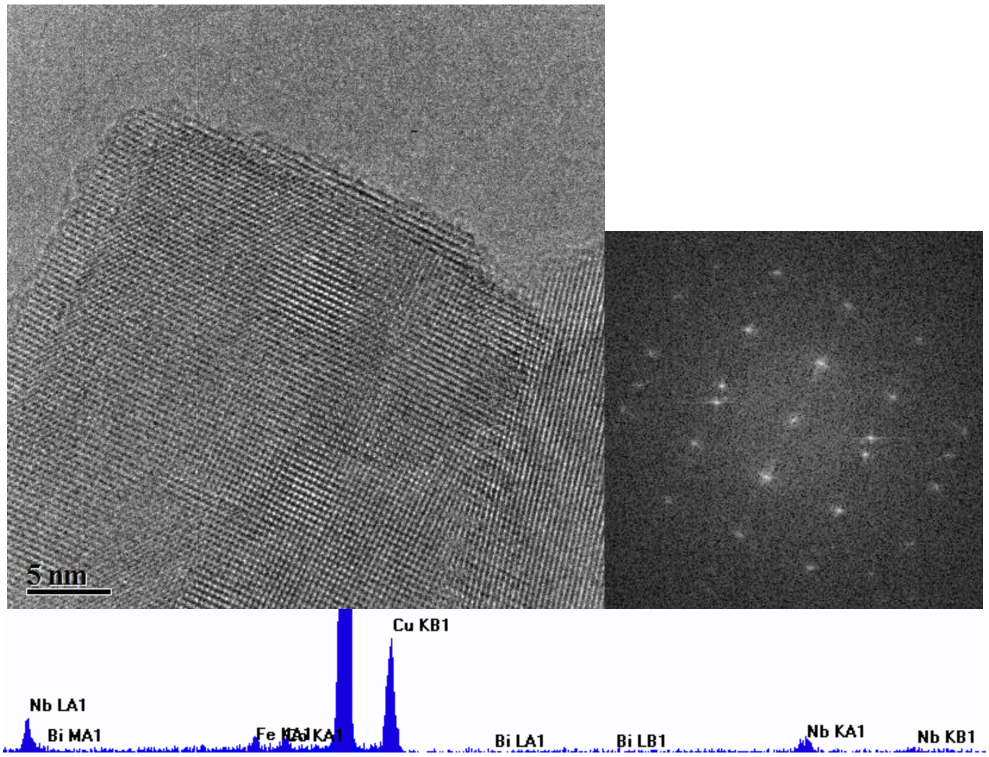

Figure 7.7. HRTEM micrograph of a highly crystalline region of T-Nb_2O_5 from the $Bi_{0.2}Nb_{0.8}$ oxide sample (l) with corresponding FFT (r). EDS spectra for the area shown below.

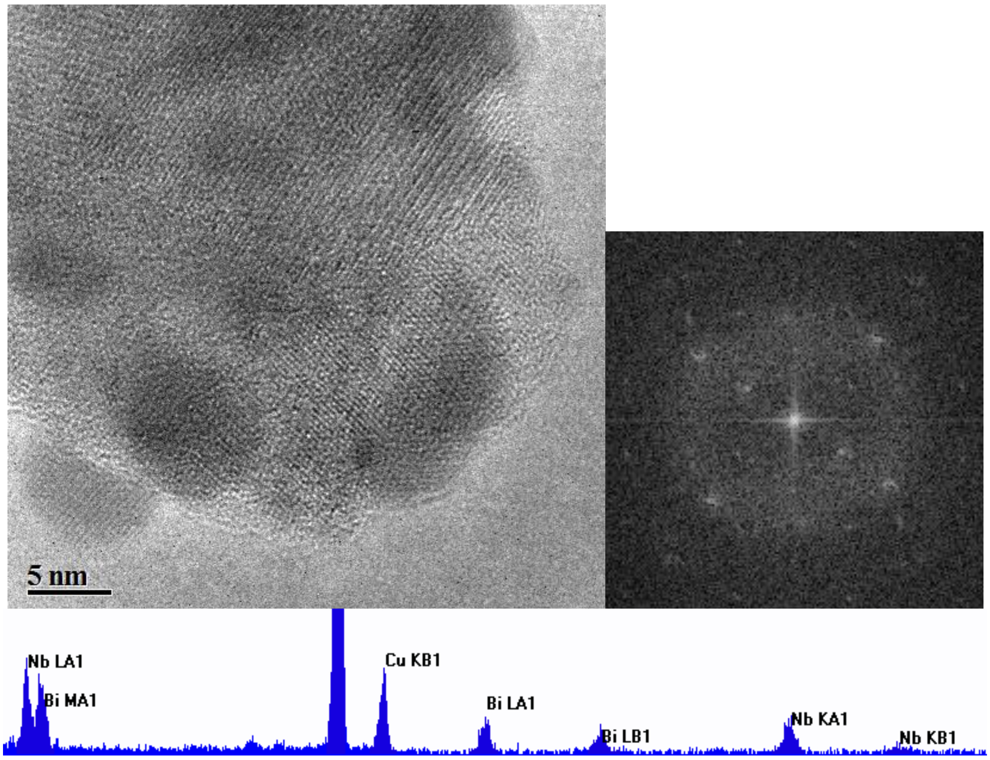

Figure 7.8. HRTEM micrograph of a region of pyrochlore from the $Bi_{0.2}Nb_{0.8}$ oxide sample (l) with corresponding FFT (r). EDS spectra for the area shown below.

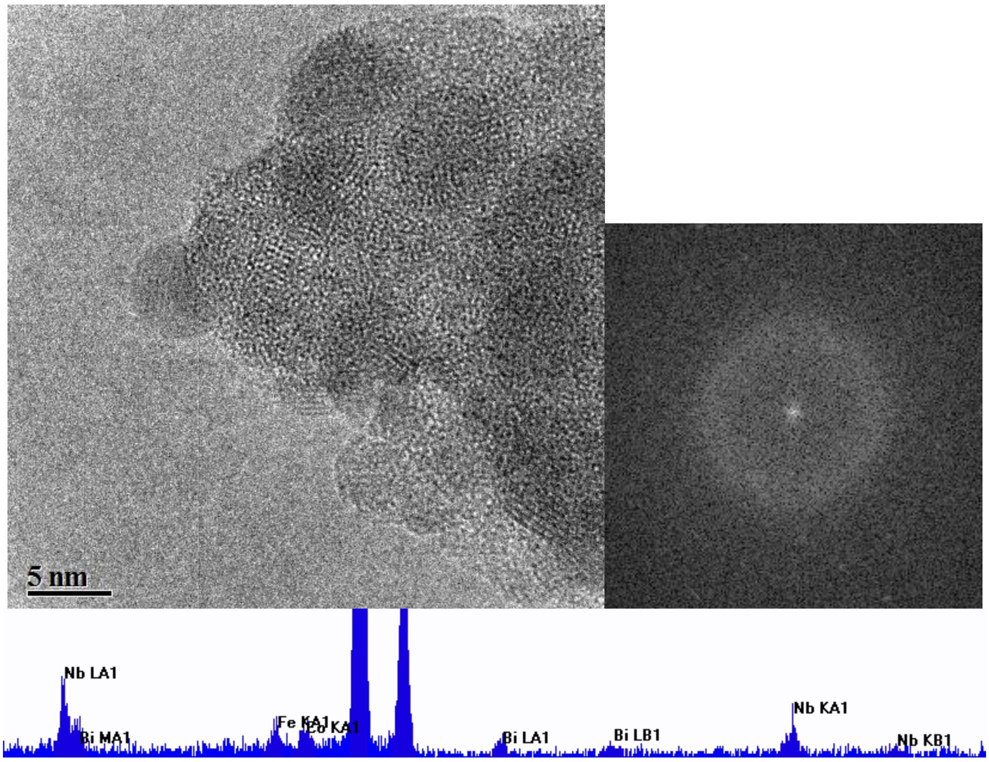

Figure 7.9. HRTEM micrograph of a region a quasi-crystalline area from the $Bi_{0.2}Nb_{0.8}$ *oxide sample (l) with corresponding FFT (r). EDS spectra for the area shown below*

.

A crystal of fluorite can be identified in the $Bi_{0.4}Nb_{0.6}$ oxide sample, Figure 7.10, with calculated d-spacing of 2.00 Å indicating the {220} plane of the phase. The EDS spectrum shows the presence of niobium and bismuth indicating the crystal is a mixed oxide. Quasi-crystalline regions were also seen in this sample, Figure 7.11, containing bismuth and niobium.

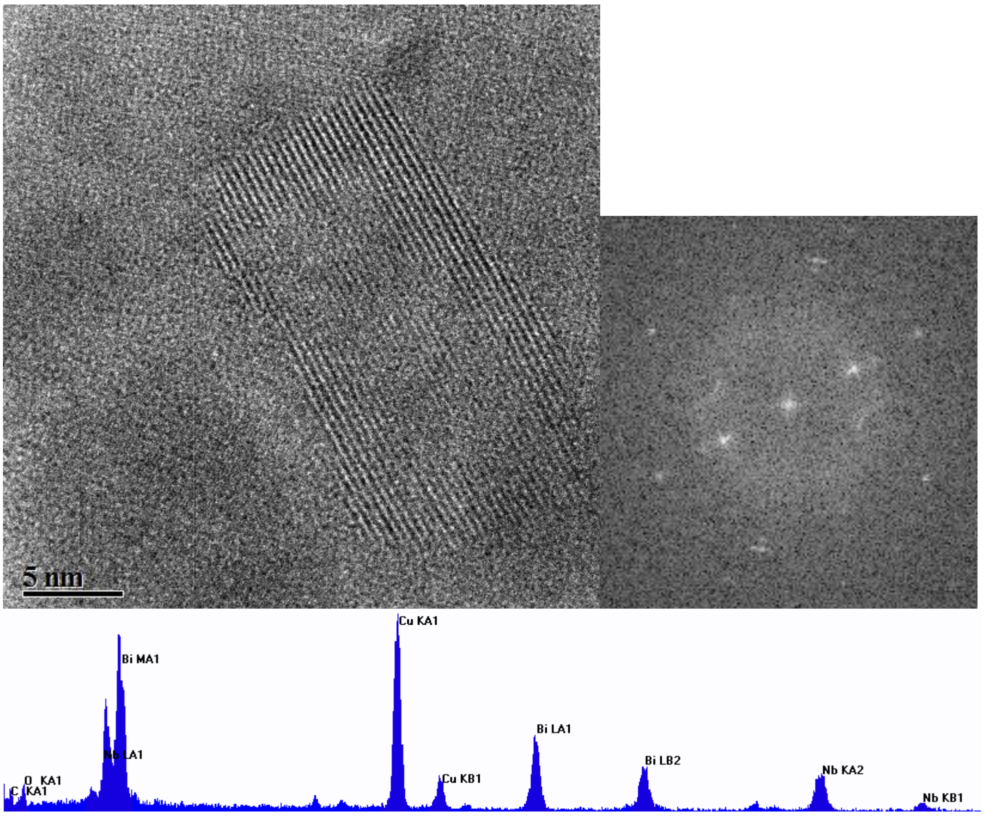

Figure 7.10. HRTEM micrograph of a crystal from the $Bi_{0.4}Nb_{0.6}$ *oxide sample (l) with corresponding FFT (r). EDS spectra for the area shown below.*

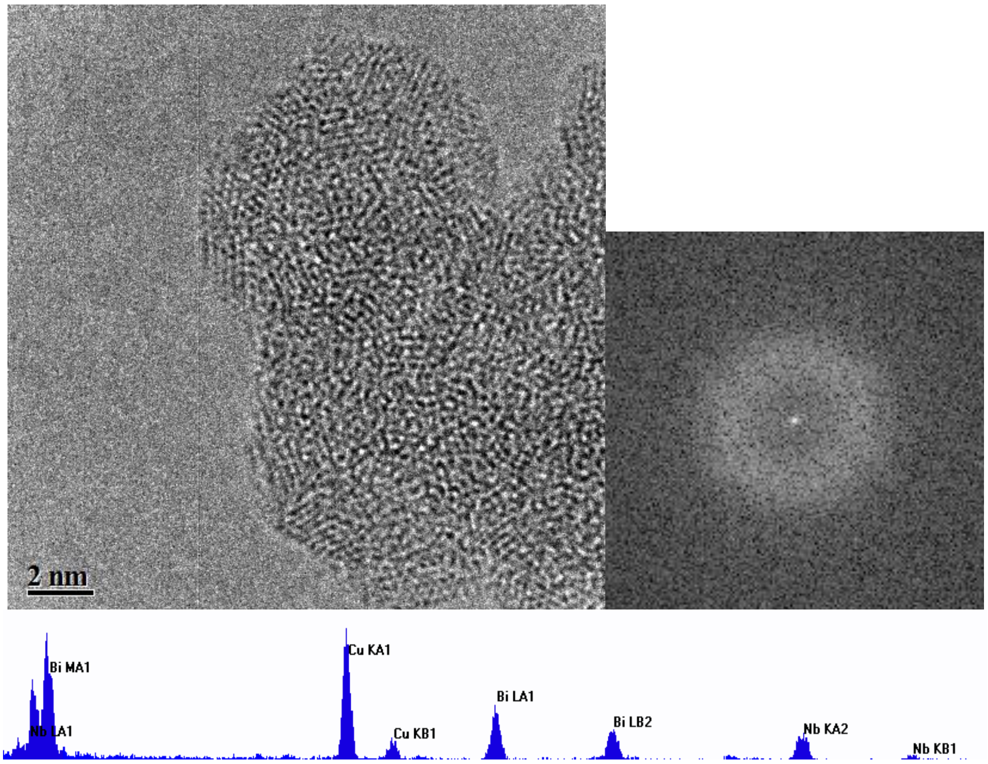

Figure 7.11. HRTEM micrograph of quasi-crystalline nanoparticles from the $Bi_{0.4}Nb_{0.6}$ *oxide sample (l) with corresponding FFT (r). EDS spectra for the area shown below.*

A mixture of phases can be identified in the micrograph of the Bi$_{0.6}$Nb$_{0.4}$ oxide sample, Figure 7.12, with d-spacings of 6.27 Å, 4.00 Å, 3.27 Å and 1.99 Å being calculated. These correspond to the {111} plane of pyrochlore, the {110} plane of perovskite and the {111} and {220} planes of fluorite respectively. This is strong evidence for the type III phase being formed and supports the PXRD data. EDS shows that both metal ions are present in the area.

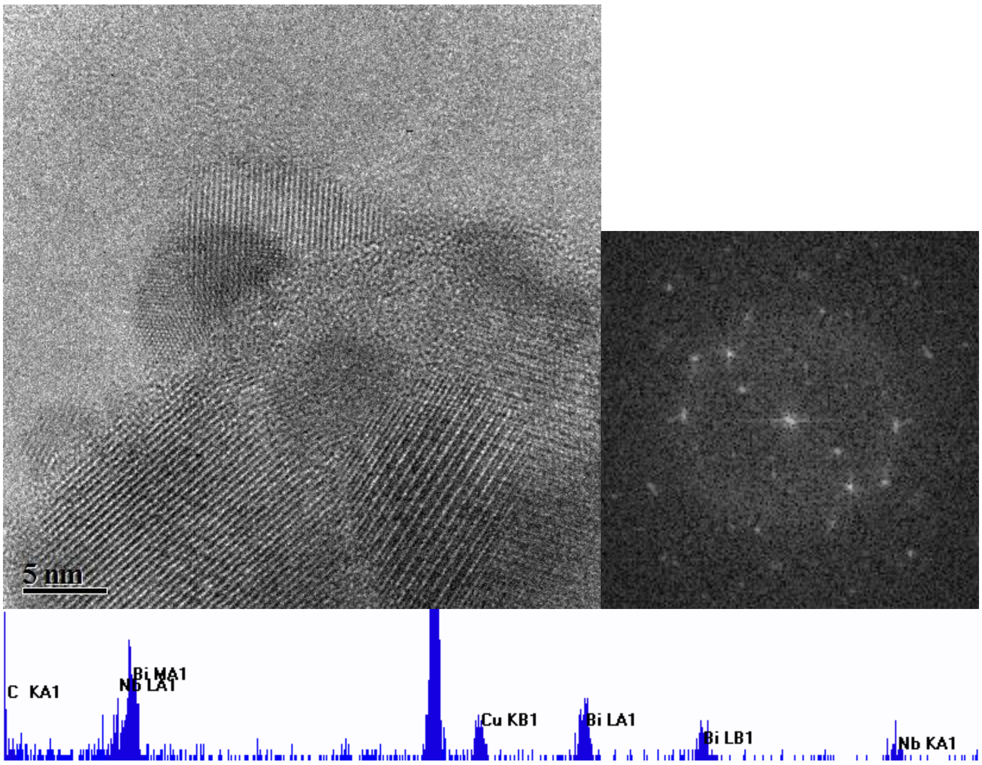

Figure 7.12. HRTEM micrograph of a region a crystalline area from the Bi$_{0.6}$Nb$_{0.4}$ oxide sample (l) with corresponding FFT (r). EDS spectra for the area shown below.

A further example of a quasi-crystalline region, this time in the Bi$_{0.6}$Nb$_{0.4}$ oxide sample, is seen in Figure 7.13, with EDS showing the presence of bismuth and niobium.

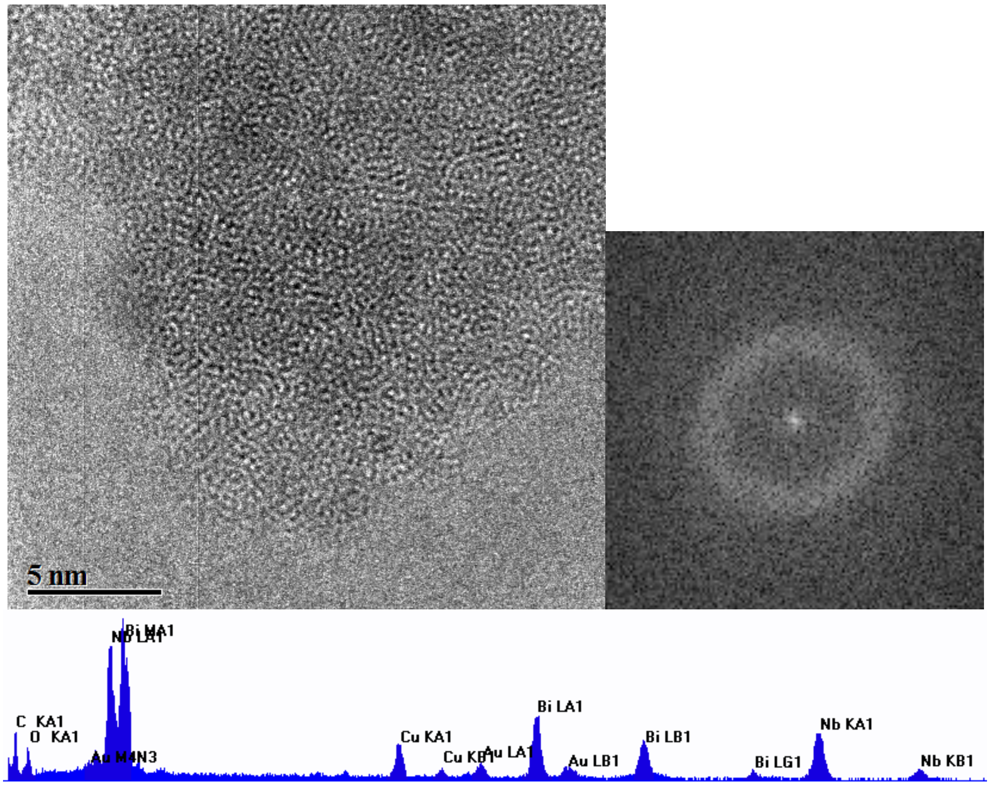

Figure 7.13. HRTEM micrograph of a quasi-crystalline area from the $Bi_{0.6}Nb_{0.4}$ *oxide sample (l) with corresponding FFT (r). EDS spectra for the area shown below.*

In the highly bismuth rich end of the system evidence of δ-Bi_2O_3 was found, which has a defect fluorite structure. An example of a large crystal of δ-Bi_2O_3 is seen in Figure 7.14, with d-spacings calculated from the FFT as 3.20 Å and 1.64 Å, indicative of the {111} and {311} lattice planes of fluorite respectively. The EDS spectrum indicated that only bismuth was present in this crystal. As seen in the other compositional ranges, quasi-crystalline particles were also observed, Figure 7.15, containing bismuth and niobium ions.

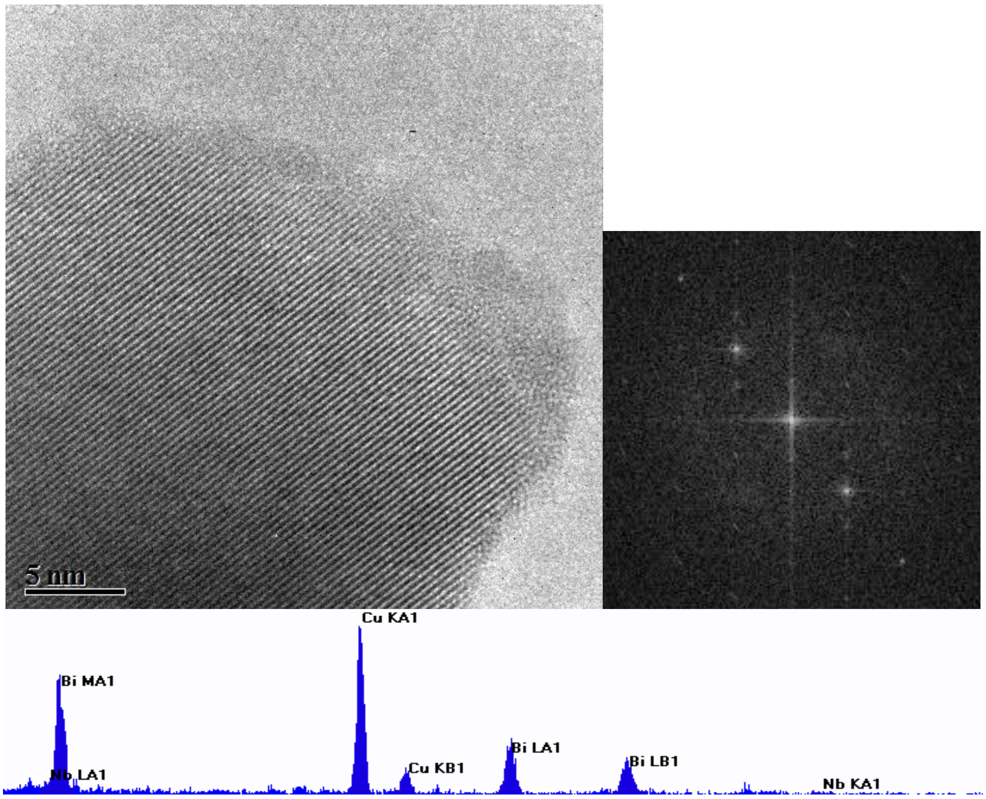

Figure 7.14. HRTEM micrograph of a crystalline area from the $Bi_{0.8}Nb_{0.2}$ *oxide sample (l) with corresponding FFT (r). EDS spectra for the area shown below.*

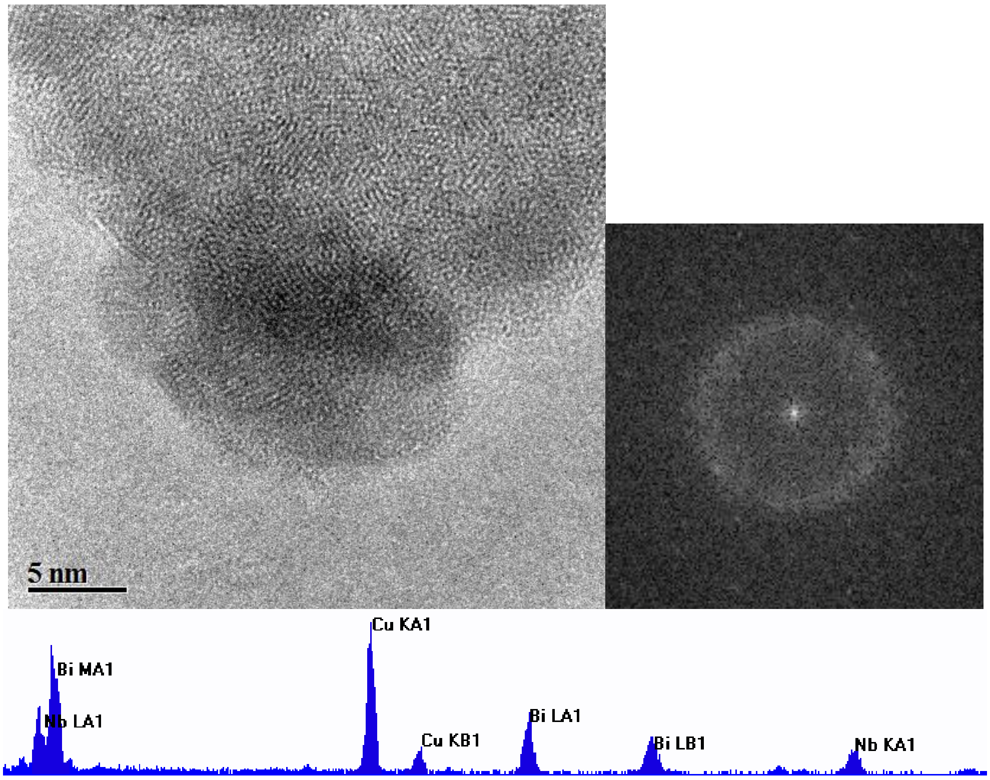

Figure 7.15 HRTEM micrograph of an amorphous area from the $Bi_{0.8}Nb_{0.2}$ *oxide sample (l) with corresponding FFT (r). EDS spectra for the area shown below.*

7.2.2 XPS analysis

As with other ternary oxide samples, XPS analysis was carried out on the Bi-Nb oxide samples in order to compare average particle compositions from EDS with the surface compositions of the particles, calculated from XPS, and determine if a homogenous solid solution had been formed.

A representative XPS survey scan is shown in Figure 7.16, indicating the peaks corresponding to the Nb 3p, the O 1s and the Bi 4f electron binding energies, as well as the overall surface composition of the sample.

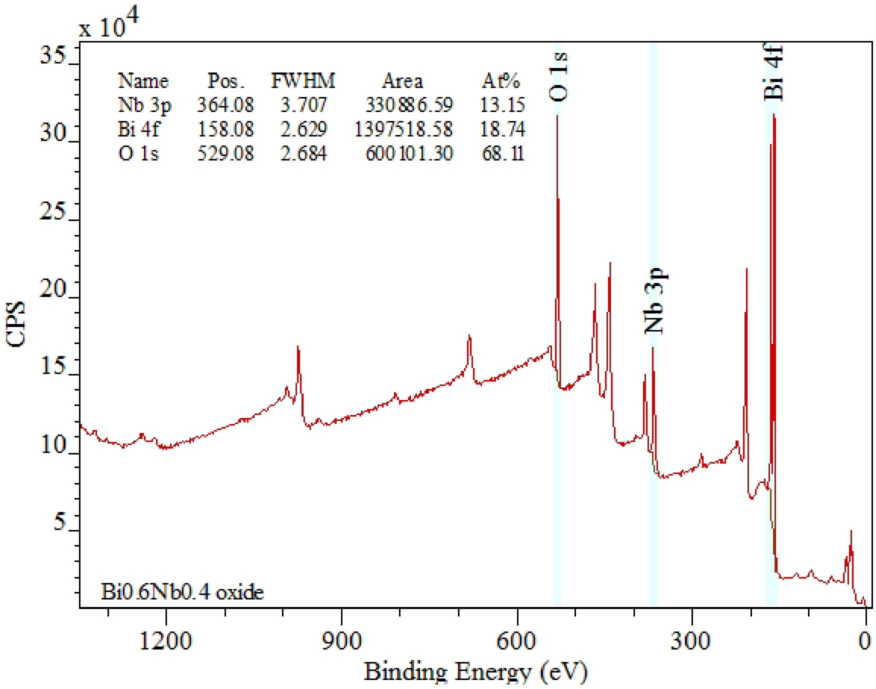

Figure 7.16. XPS survey scan for the $Bi_{0.6}Nb_{0.4}$ oxide sample.

From the XPS data, it was determined that the bismuth was present in exclusively in the +3 oxidation state as seen from the high resolution bismuth scan, Figure 7.17. Only 1 doublet is seen for the 4f component which can be assigned to the $4f_{5/2}$ and $4f_{7/2}$ spin states. Similarly, the niobium 3d signal is seen as one doublet, Figure 7.18, which can be assigned to the $3d_{3/2}$ and $3d_{5/2}$ spin states.

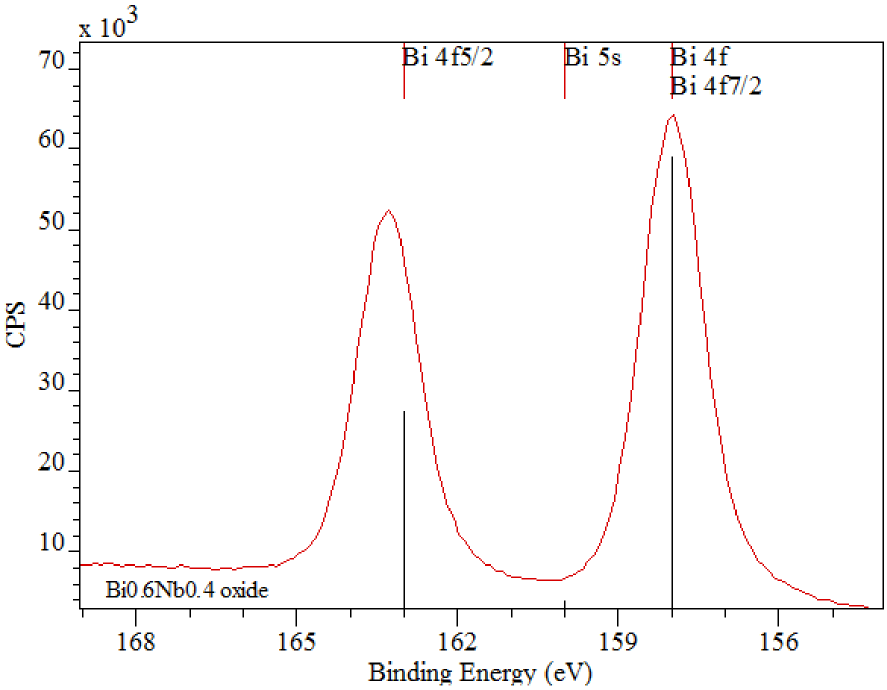

Figure 7.17. XPS high resolution scan of the bismuth 4f region for the $Bi_{0.6}Nb_{0.4}$ *oxide sample.*

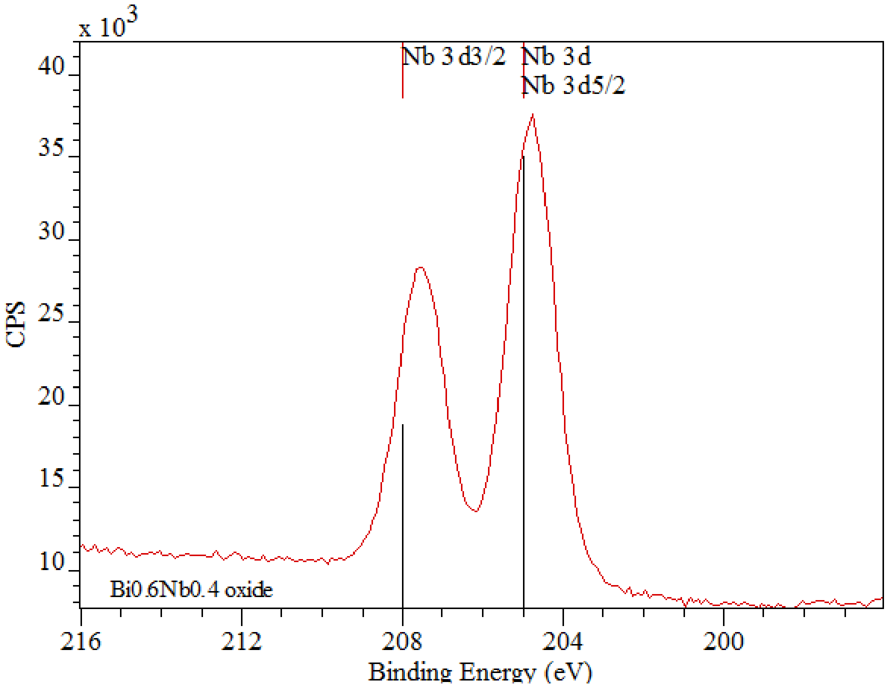

Figure 7.18. XPS high resolution scan of the niobium 3d region for the $Bi_{0.6}Nb_{0.4}$ *oxide sample.*

Full analysis of the XPS data for the Bi-Nb oxide system, Table 7.6, revealed that at the niobium rich end of the system the particle surfaces were slightly bismuth enriched, however, for the $Bi_{0.6}Nb_{0.4}$ and $Bi_{0.8}Nb_{0.2}$ oxide samples, the surface compositions matched well to the nominal compositions. This shows that at the bismuth rich end of the system the particles were reasonably homogenous. As discussed earlier, due to bismuth's lone pair, it often prefers to coordinate asymmetrically, which is why the surface is bismuth enriched at the niobium rich end of the system. However, as the bismuth concentration increases, there is a large excess of bismuth which cannot be accommodated at the surface, therefore the particles are more mixed.

Table 7.6. XPS results for the Bi-Nb oxide nanoparticles showing the surface composition.

Sample Bi_2O_3-Nb_2O_5	*Atom & Orbital*	*Binding Energy/ eV*	*Atomic Concentration /%*	*Std Dev*
$Bi_{0.2}Nb_{0.8}$	Bismuth 4f	159.08	32.71	0.15
	Niobium 3p	365.08	67.29	0.23
$Bi_{0.4}Nb_{0.6}$	Bismuth 4f	159.08	69.61	2.42
	Niobium 3p	365.08	30.39	0.91
$Bi_{0.6}Nb_{0.4}$	Bismuth 4f	159.08	59.01	0.20
	Niobium 3p	364.08	40.99	0.22
$Bi_{0.8}Nb_{0.2}$	Bismuth 4f	159.08	80.55	0.35
	Niobium 3p	364.08	19.45	0.12

A comparison of atomic compositions calculated from XPS and EDS for each sample is seen in Table 7.7. The compositions seen for EDS are the majority mixed phases seen in each sample. The results show that there is some degree of discrepancy between the surface and bulk composition in all samples, but is most pronounced for the $Bi_{0.4}Nb_{0.6}$ and $Bi_{0.8}Nb_{0.2}$ oxide samples. This could be because the $Bi_{0.4}Nb_{0.6}$ oxide sample contained a large range of mixed particle compositions, therefore, the average elemental percentages for this sample are likely to have a high percentage error. To explain the discrepancy in the $Bi_{0.8}Nb_{0.2}$ oxide sample, it should be mentioned that the sample contained many pure δ-Bi_2O_3 particles which could have artificially enhanced the XPS bismuth percentage. As there were multiple phases present in all samples it is hard to draw any real conclusions from this data about the degree of homogeneity in the particles.

Table 7.7. Comparison of overall particle composition calculated from EDS analysis and surface composition from XPS.

Sample Bi_2O_3-Nb_2O_5	*%Nb from EDS*	*%Nb from XPS*	*% Bi from EDS*	*% Bi from XPS*
$Bi_{0.2}Nb_{0.8}$	74.75	67.29	25.25	32.71
$Bi_{0.4}Nb_{0.6}$	63.17	30.39	36.83	69.61
$Bi_{0.6}Nb_{0.4}$	27.40	40.99	72.60	59.01
$Bi_{0.8}Nb_{0.2}$	36.86	19.45	63.14	80.55

7.2.3 Analysis of trends and correlation of all analytical data

It can be seen from the results presented that the Bi_2O_3-Nb_2O_5 system is highly complicated with the growth of many phases across the various compositions. However, it has been shown that the resin-gel method is successful in producing mixed metal oxide nanoparticles in this system, with resultant phases similar to those seen previously by Zhou *et al*., Ling *et al*. and Piir *et al*. [168-170]. As many different phases were identified, it was difficult to determine the atomic arrangements with each phase, however, it can be said that the compositions of the particles were variable and non-homogenous, indicating that the ions were in solid solution within the various structure types.

7.3 Thermal treatments

Samples were heated at 500 °C and 700 °C for 7 days under flowing oxygen in order to see how the particles changed with temperature. This was carried out in order to see how stable the type II and type III phases were at higher temperatures and if any new phases appeared. It was also hoped that the quasi-crystalline phases observed in the samples would crystallise at higher temperatures. Again, these temperatures were chosen to avoid substantial sintering of nanoparticles and to avoid the loss of any bismuth.

The PXRD patterns for the $Bi_{0.2}Nb_{0.8}$ oxide nanoparticles calcined at 350 °C, 500 °C and 700 °C are seen in Figure 7.19. It can be seen from the patterns that no phase changes occurred between 350° C and 500 °C, with the same T-Nb_2O_5 and pyrochlore lines being visible. However, at 700 °C a clear phase change occurs, with the formation of the $BiNbO_4$ phase. Lines corresponding to the T-Nb_2O_5 phase are still present as expected due to the stoichiometry of the mixed $BiNbO_4$ phase and the starting composition of the sample. The peaks corresponding to both phases are much sharper and less broad than the previous patterns, indicating an increase in crystallinity and larger particle size.

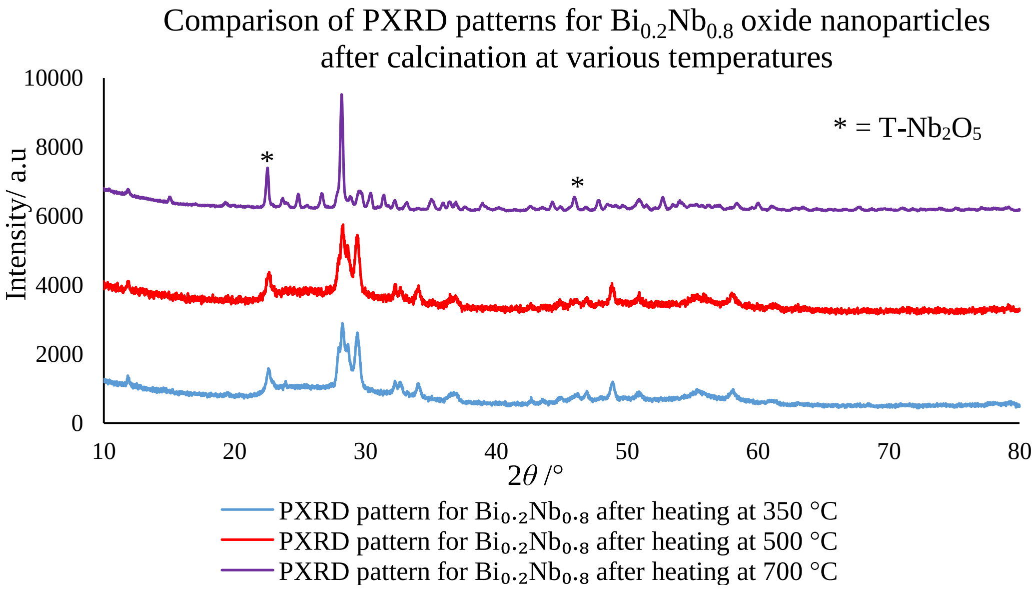

Figure 7.19. PXRD patterns of the $Bi_{0.2}Nb_{0.8}$ oxide nanoparticles after heating in the tube furnace at various temperatures for 7 days.

A similar trend is seen for the $Bi_{0.4}Nb_{0.6}$ oxide and $Bi_{0.6}Nb_{0.4}$ oxide samples, Figures 7.20 and 7.21, with little change in the patterns between 350 °C and 500 °C, which may be due to small ratio differences between several phases present, followed by an obvious change at 700 °C when the $BiNbO_4$ phase is formed. The sharper peaks again indicate the materials at 700 °C are highly crystalline.

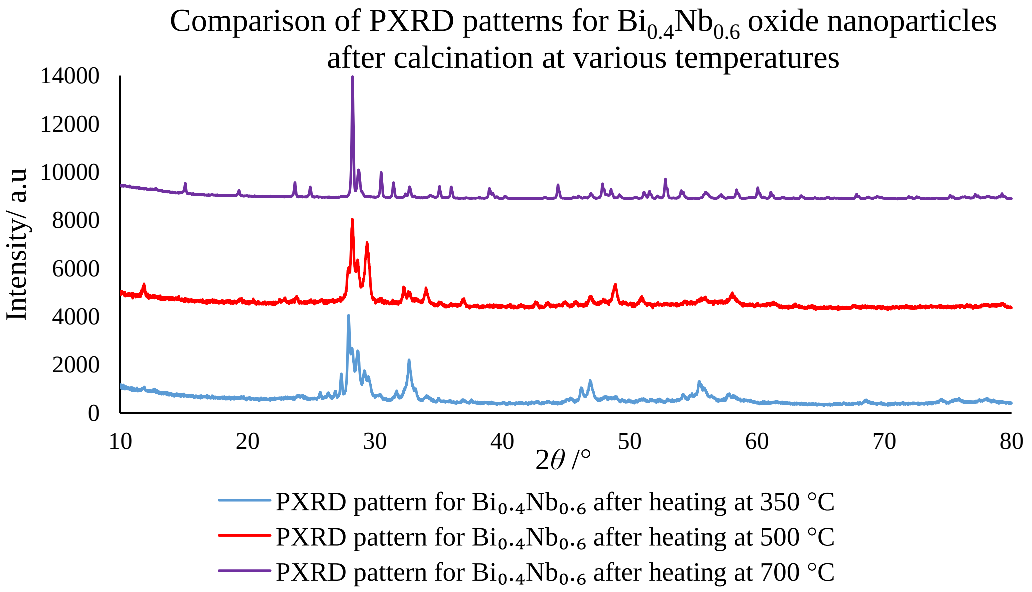

Figure 7.20. PXRD patterns of the $Bi_{0.4}Nb_{0.6}$ oxide nanoparticles after heating in the tube furnace at various temperatures for 7 days.

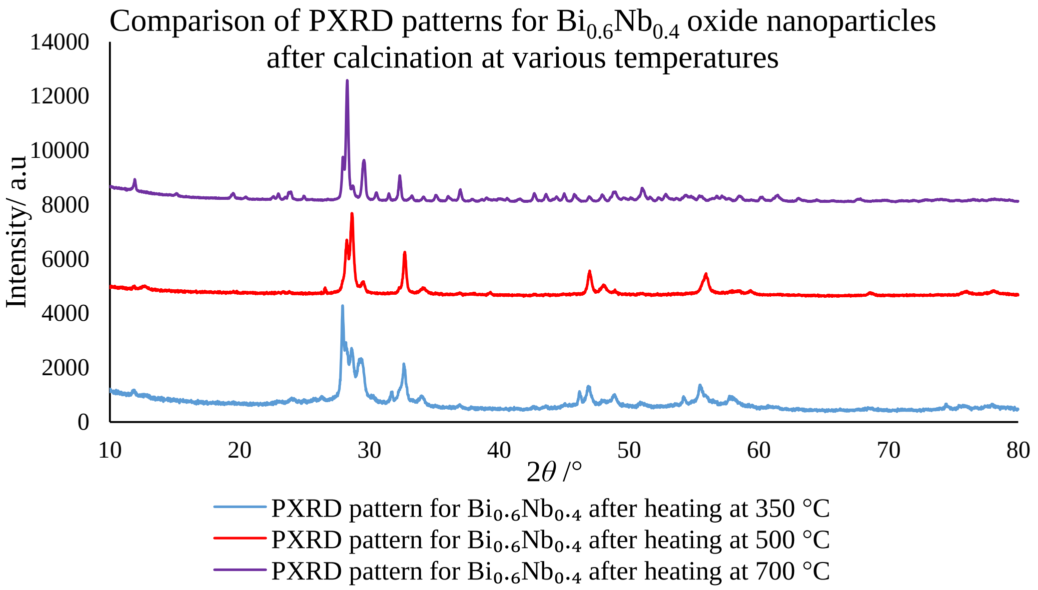

Figure 7.21. PXRD patterns of the Bi$_{0.6}$Nb$_{0.4}$ oxide nanoparticles after heating in the tube furnace at various temperatures for 7 days.

The PXRD patterns for the Bi$_{0.8}$Nb$_{0.2}$, Figure 7.22, show that heating the sample does not promote the formation of a single phase and there are still several phases present, even after heating at 700 °C. The phases formed include the α-, β- and δ- polymorphs of Bi_2O_3, seen at low temperature, as well as a minority phase of $BiNbO_4$.

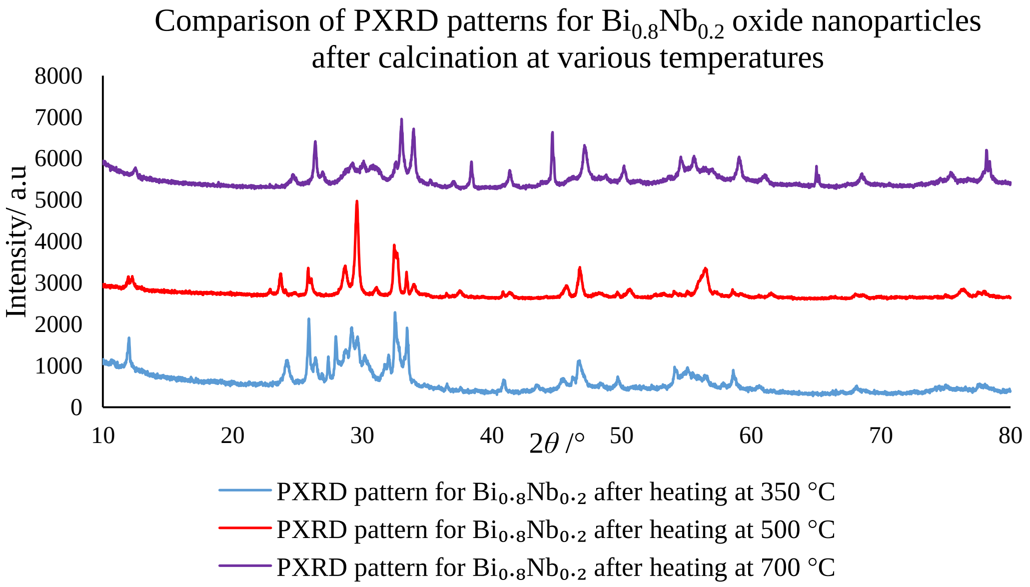

Figure 7.22. PXRD patterns of the Bi$_{0.8}$Nb$_{0.2}$ oxide nanoparticles after heating in the tube furnace at various temperatures for 7 days.

It is perhaps surprising that $BiNbO_4$ is seen across the whole Bi_2O_3-Nb_2O_5 at 700 °C as this phase is not usually seen at temperatures below 800 °C when synthesised by the solid state method. However, an example of formation of $BiNbO_4$ at low temperature was seen by Radhaa *et al*. [173], in their co-precipitation synthesis of $BiNbO_4$ at 600 °C. The fact that $BiNbO_4$ was formed at a lower temperature than usual is also probably a consequence of working at the nanoscale, as it takes less energy for these phases to form.

Scherrer analysis was carried out on all PXRD data in order to compare crystallite size of the different samples at different calcination temperatures, Figure 7.23. The results show that generally an increase of temperature does increase the mean crystallite size as expected due to the sintering of nanoparticles, and the phase change from fluorite based structures, to the $BiNbO_4$ structure. However, the $Bi_{0.8}Nb_{0.2}$ oxide sample does not follow this trend at all, with an average crystallite size decrease with temperature. A possible explanation for this is the exsolution of bismuth and niobium to form two distinct phases which, on average, give a lower crystallite size. It is possible that as the $Bi_{0.8}Nb_{0.2}$ oxide sample was heated, it became more favourable for the bismuth and niobium to separate into different phases. This suggestion seems probable given that HRTEM for the $Bi_{0.8}Nb_{0.2}$ oxide sample showed the presence of α-Bi_2O_3 particles and fluorite particles even at higher temperatures which were not present in the other samples where the $BiNbO_4$ phase was dominant.

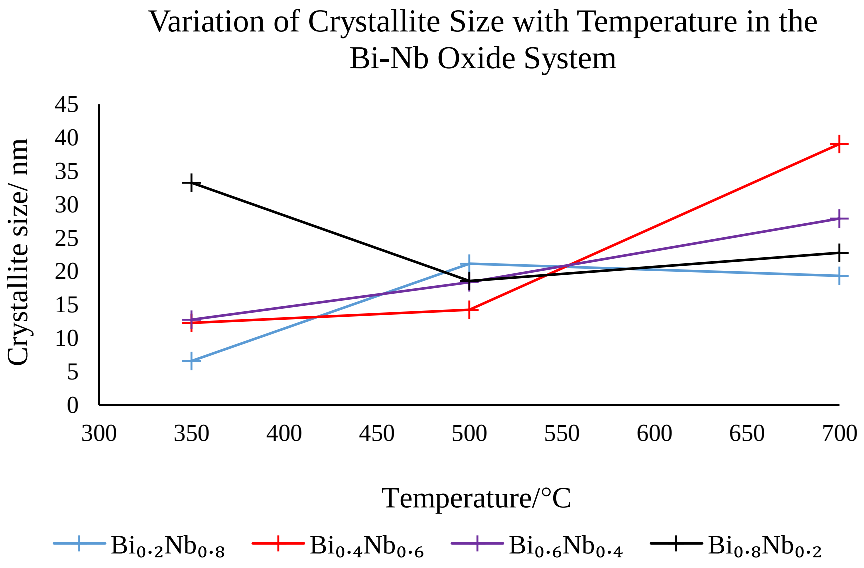

Figure 7.23. Plot showing the relationship between composition and mean crystallite size at various temperatures.

The calcined samples were investigated in the microscope to see how the crystallinity of the particles had changed with temperature, as well as how the composition of the mixed particles had changed as new phases were introduced with increased temperature. The results of the compositional analysis, using EDS, for the mixed phase are seen in Table 7.8. It can be seen that there was very little change in the average particle composition with temperature and the elemental compositions remained constant. This could be predicted for the particles analysed at 350 °C and 500 °C as it has already been established that there was no phase change, and from this data it can be assumed that the atomic arrangement was relatively stable at both these temperatures. However, as a phase change has been identified in all samples upon heating at 700 °C, it may be expected that the elemental ratios would change too. As this is not the case, it can be assumed that a complete solid solution in the $BiNbO_4$ structure was formed.

Table 7.8. Composition of the Bi-Nb oxide nanoparticles, from EDS, varying with temperature.

Sample Bi_2O_3-Nb_2O_5	Calcination temperature/ °C	%Bi	%Nb
$Bi_{0.2}Nb_{0.8}$	350	25.25	74.75
	500	31.52	68.48
	700	18.88	81.12
$Bi_{0.4}Nb_{0.6}$	350	63.17	36.83
	500	64.31	35.69
	700	68.90	31.10
$Bi_{0.6}Nb_{0.4}$	350	72.37	27.37
	500	81.54	18.46
	700	71.69	28.31
$Bi_{0.8}Nb_{0.2}$	350	63.14	36.86
	500	78.16	21.84
	700	67.91	32.09

Many particles were viewed in the microscope to see how the crystallinity of the particles had changed with heating. Examples of particles calcined at 500 °C are seen in the micrographs in Figures 7.24-7.27. As already discussed, the phases and the compositions of the particles had changed very little from the samples calcined at 350 °C.

Figure 7.24 shows an area of overlapping fluorite type particles from the $Bi_{0.2}Nb_{0.8}$ oxide sample, identified by d-spacings of 3.18 Å, with some larger d-spacings (4.10 Å) also being calculated which could indicate some perovskite growth as well. The accompanying EDS spectrum indicates the area is niobium rich with some bismuth also present. This could indicate a change from the type II phase found at 350 °C to the type III phase which incorporates units of perovskite and fluorite in addition to the pyrochlore phase. This change would make little difference to the PXRD pattern. A crystal of pyrochlore was identified in the $Bi_{0.4}Nb_{0.6}$ oxide sample, Figure 7.25, from the observed d-spacings of 6.15 Å and 3.01 Å, correlating to the {111} and {222} lattice planes of pyrochlore respectively. EDS shows that the crystal contains both niobium and bismuth ions.

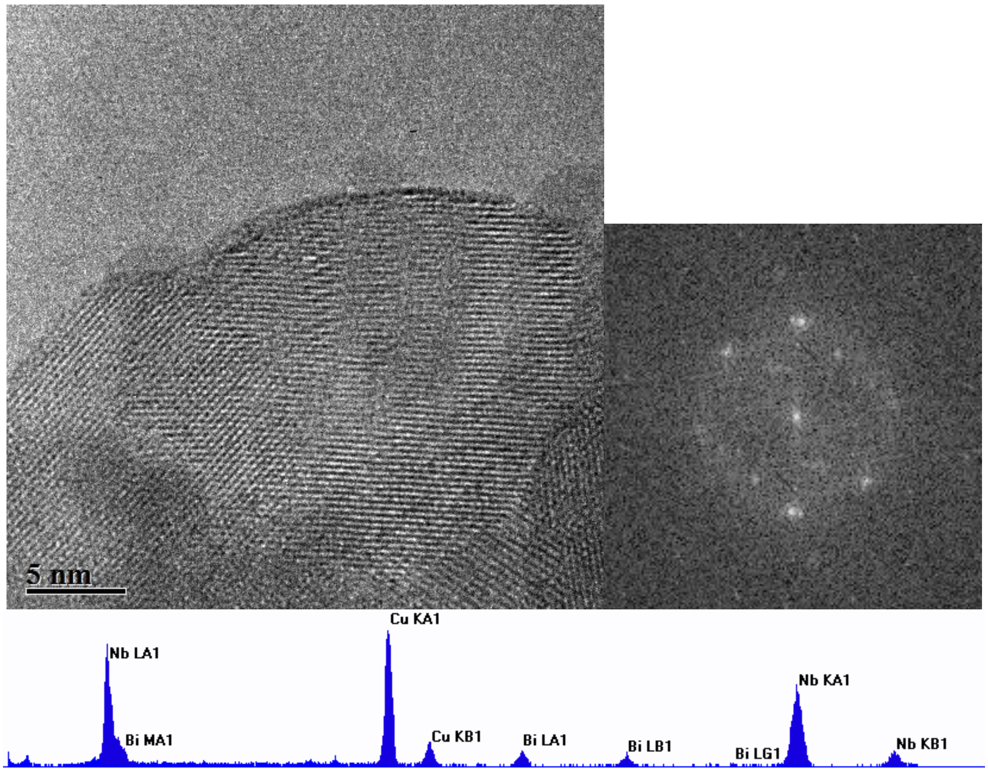

Figure 7.24. HRTEM micrograph of the $Bi_{0.2}Nb_{0.8}$ sample after calcination at 500 °C (l) with corresponding FFT (r). EDS spectra for the area shown below.

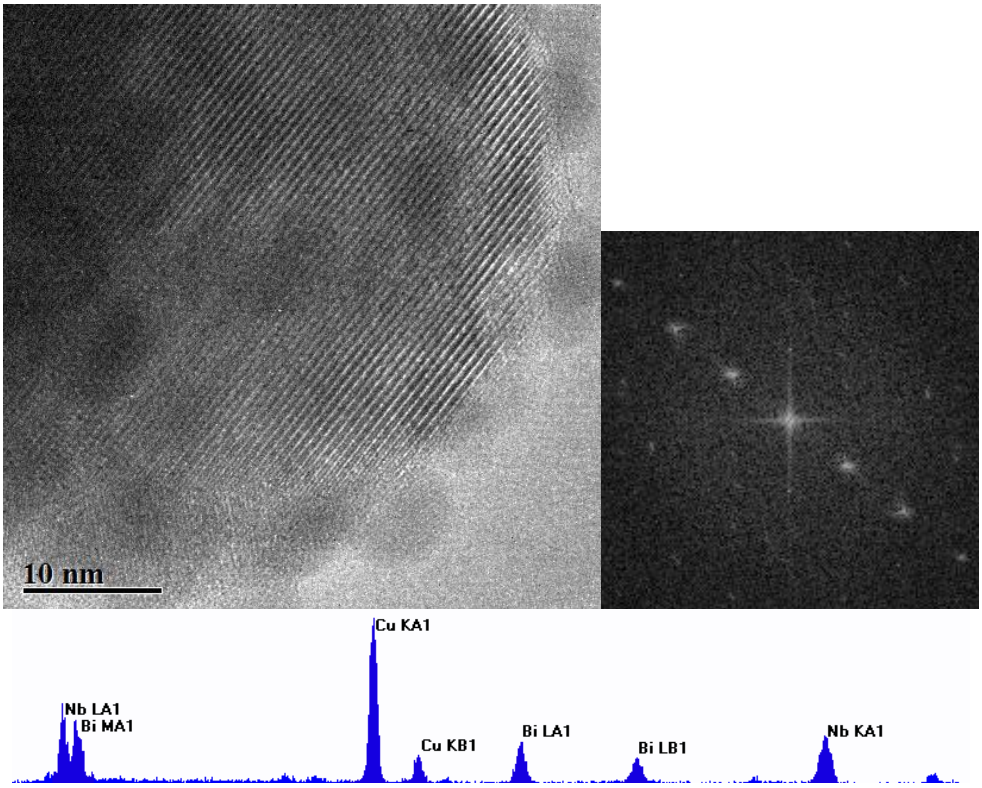

Figure 7.25. HRTEM micrograph of the $Bi_{0.4}Nb_{0.6}$ *sample after calcination at 500 °C (l) with corresponding FFT (r). EDS spectra for the area shown below.*

An example of the poorly crystalline phase found in all samples is seen in Figure 7.26. This area was seen in the $Bi_{0.6}Nb_{0.4}$ oxide sample, with EDS showing the presence of both niobium and bismuth. The d-spacings calculated from the FFT give values of 2.86 Å. These spacings could indicate the fluorite δ -Bi_2O_3 structure, as it seemed as though this phase was forming under the electron beam.

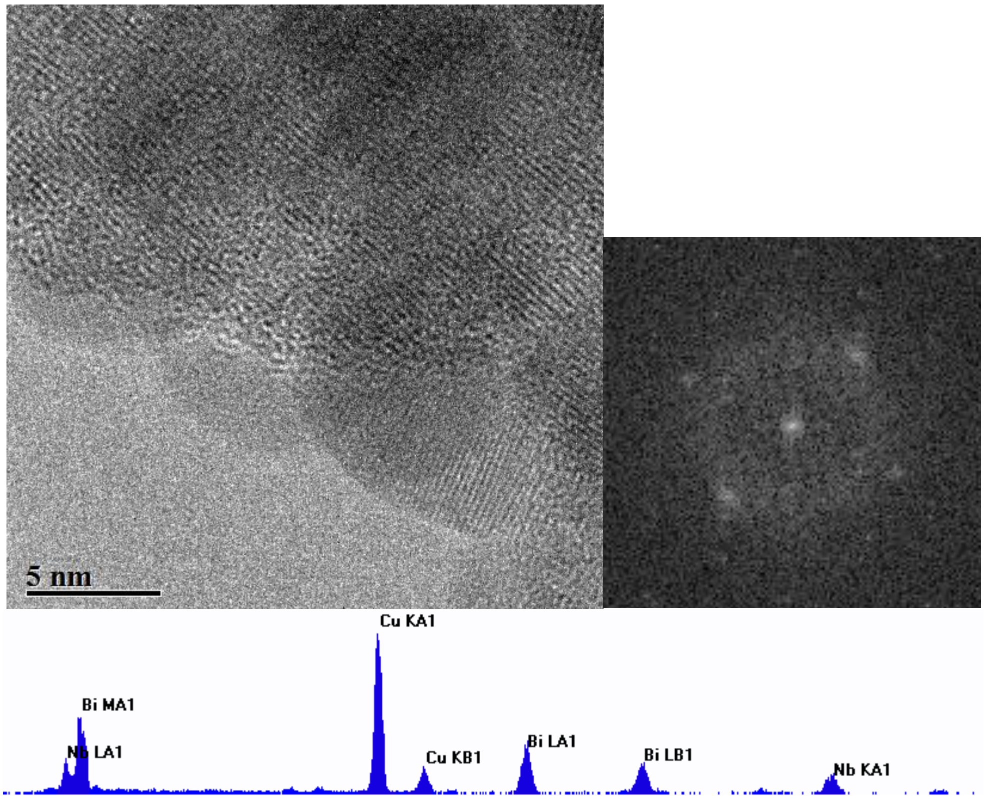

Figure 7.26. HRTEM micrograph of the $Bi_{0.6}Nb_{0.4}$ *sample after calcination at 500 °C (l) with corresponding FFT (r). EDS spectra for the area shown below.*

At the bismuth rich end of the system, crystals of α-Bi_2O_3 were observed, Figure 7.27. The micrograph shows a highly crystalline region of the $Bi_{0.8}Nb_{0.2}$ oxide sample, with d-spacings of 3.82 Å and 2.79 Å calculated from the FFT. These values correspond to the {102} and {211} lattice planes of α-Bi_2O_3. The EDS spectrum indicates that only bismuth is present in the crystal, which may explain the high degree of crystallinity, as well as the increased calcination temperature. Several crystals of this type were observed in the $Bi_{0.8}Nb_{0.2}$ oxide sample.

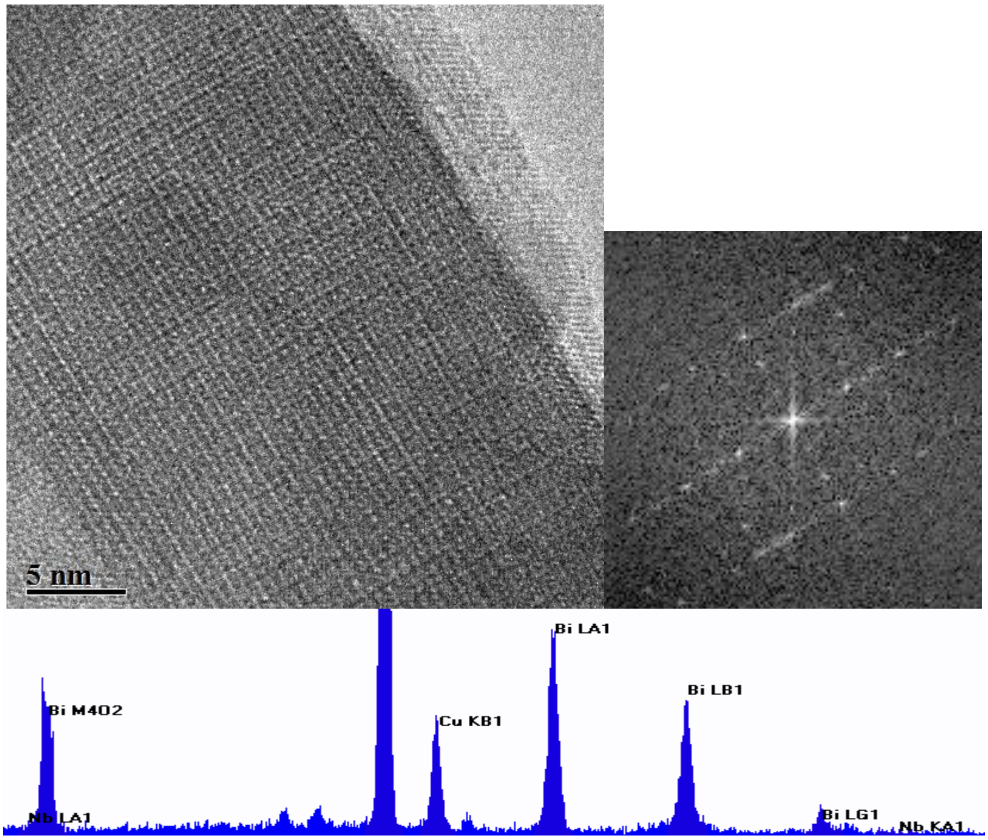

Figure 7.27. HRTEM micrograph of the $Bi_{0.8}Nb_{0.2}$ sample after calcination at 500 °C (l) with corresponding FFT (r). EDS spectra for the area shown below.

The imaging of the samples calcined at 700 °C proved to be more difficult, as the $BiNbO_4$ phase formed thick crystals which are not particularly suitable for imaging. Although $BiNbO_4$ was the majority phase found in all the samples calcined at 700 °C, there were still particles of fluorite, T-Nb_2O_5 and quasi-crystalline regions found in the microscope for all sample compositions. Several examples of the crystals found can be seen in Figures 7.28-7.31.

A large crystal of T-Nb_2O_5 can be seen the micrograph for the $Bi_{0.2}Nb_{0.8}$ oxide sample, Figure 7.28, identified by d-spacings of 3.97 Å. EDS shows that only niobium is present in the crystal and that heating up to 700 °C does not form a uniform mixed oxide. A crystal of $BiNbO_4$ was identified in the $Bi_{0.4}Nb_{0.6}$ oxide sample and is seen in Figure 7.29. This highly crystalline region is shown to contain both niobium and bismuth ions, with d-spacings of 5.97 Å, 3.75 Å, 3.50 Å, 3.19 Å, 2.66 Å and 1.74 Å corresponding to the {020}, {101}, {111}, {121}, {220} and {161} lattice planes respectively for the low temperature orthorhombic form of $BiNbO_4$.

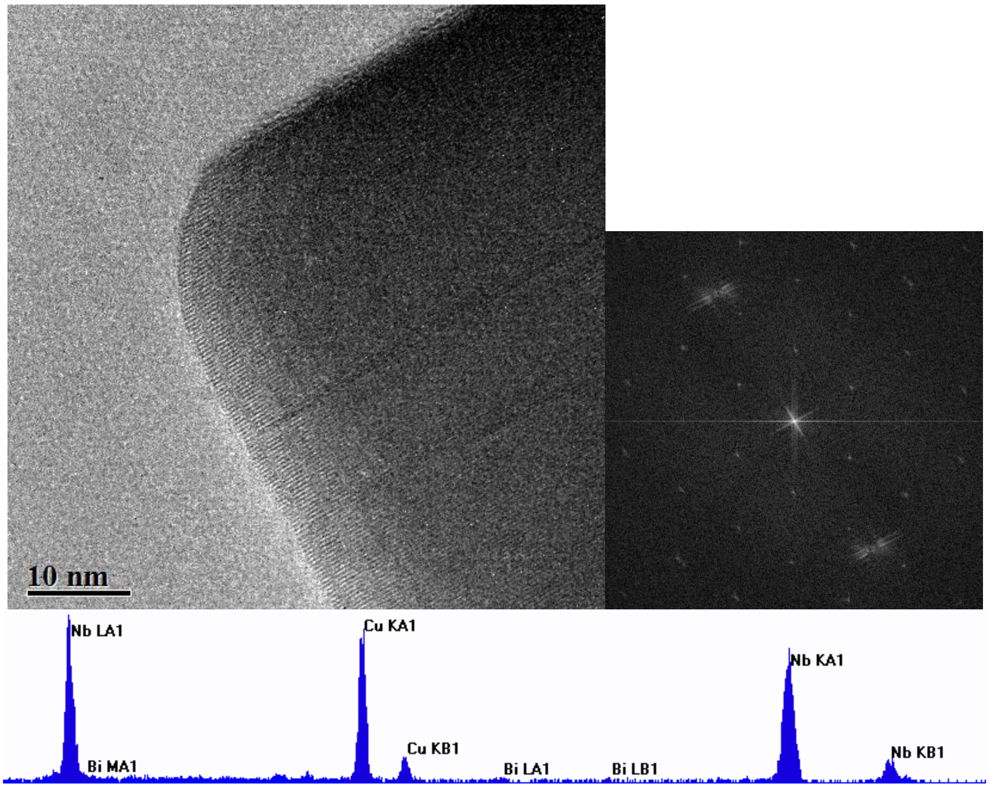

Figure 7.28. HRTEM micrograph of the $Bi_{0.2}Nb_{0.8}$ sample after calcination at 700 °C (l) with corresponding FFT (r). EDS spectra for the area shown below.

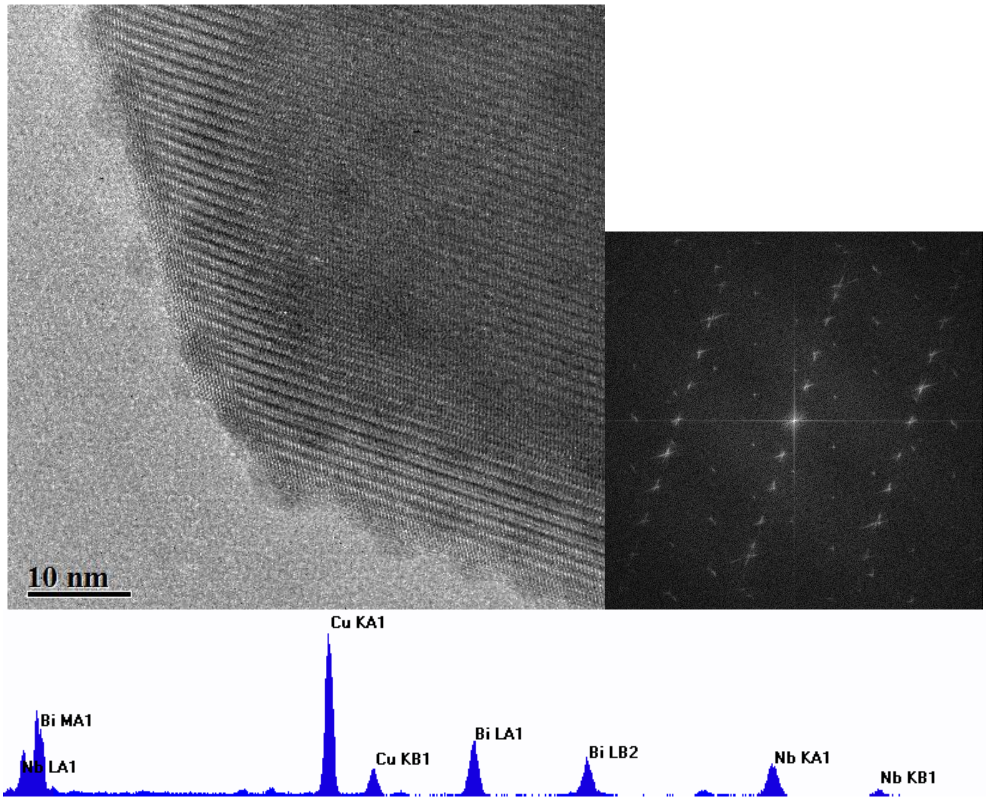

Figure 7.29. HRTEM micrograph of the $Bi_{0.4}Nb_{0.6}$ sample after calcination at 700 °C (l) with corresponding FFT (r). EDS spectra for the area shown below.

Further crystals of $BiNbO_4$ were found in the $Bi_{0.6}Nb_{0.4}$ oxide sample with an example seen in Figure 7.30. D-spacings calculated from the FFT of the micrographs were found to be 5.61 Å and 2.87 Å indicating the {020} and the {200} lattice planes of the orthorhombic phase.

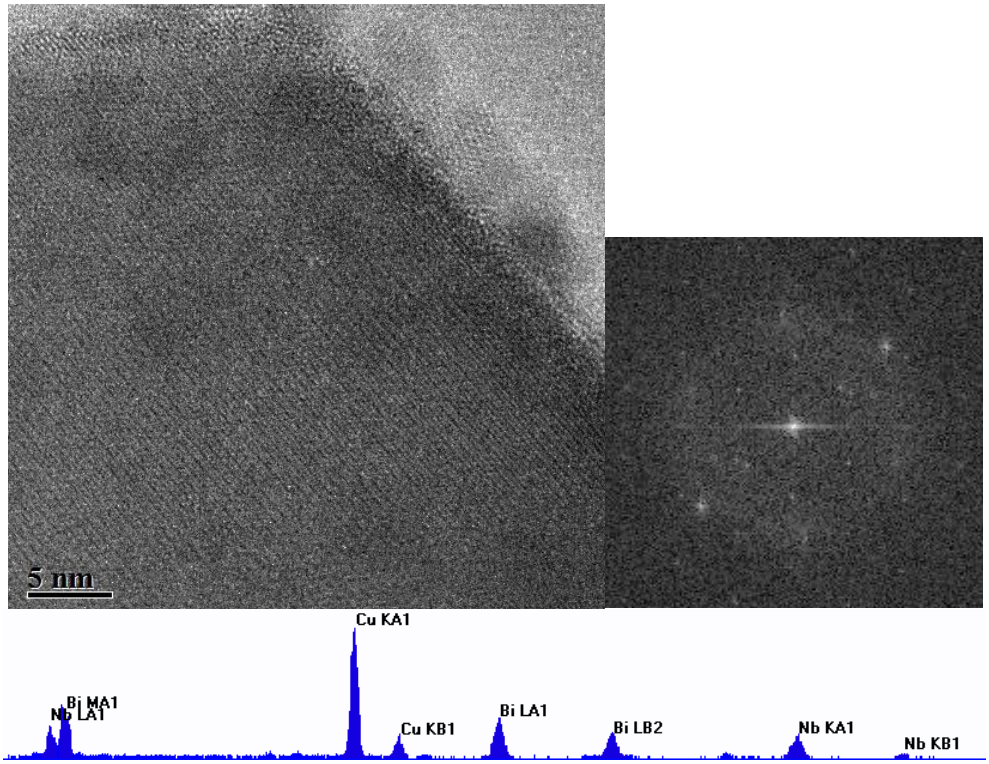

Figure 7.30. HRTEM micrograph of the $Bi_{0.6}Nb_{0.4}$ sample after calcination at 700 °C (l) with corresponding FFT (r). EDS spectra for the area shown below.

And finally, a group of fluorite particles are shown in Figure 7.31, found in the $Bi_{0.8}Nb_{0.2}$ oxide sample. These particles were found to contain both bismuth and niobium ions from the EDS spectrum.

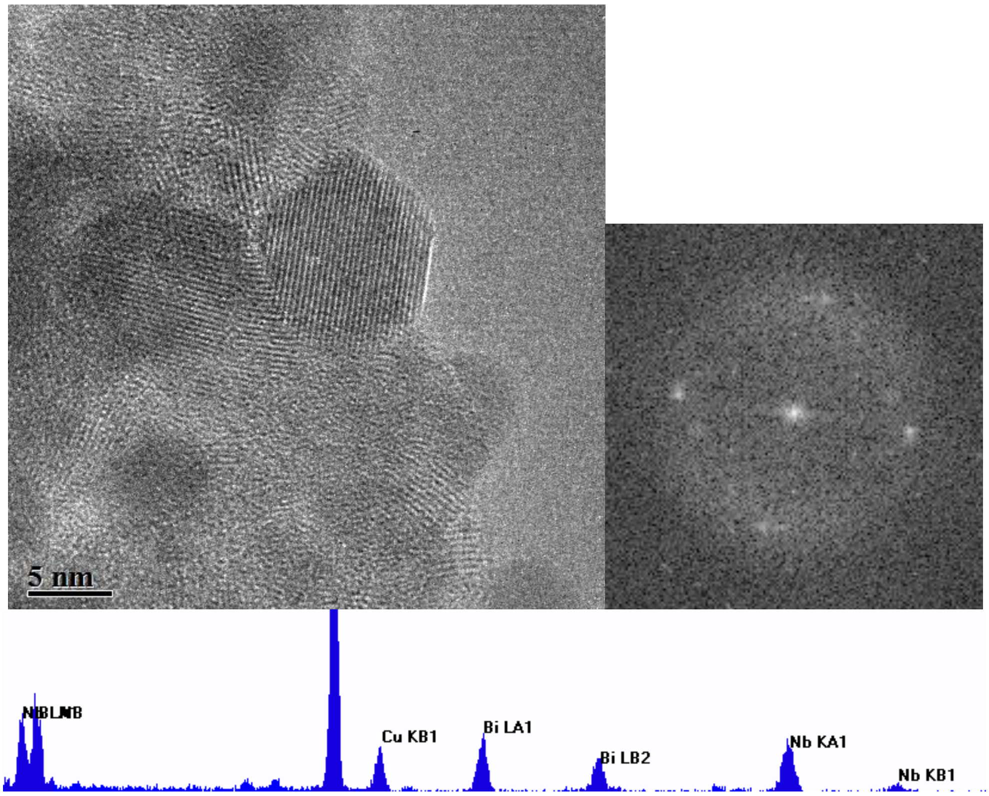

Figure 7.31. HRTEM micrograph of the $Bi_{0.8}Nb_{0.2}$ sample after calcination at 700 °C (l) with corresponding FFT (r). EDS spectra for the area shown below.

XPS analysis was carried out on the samples calcined at both 350 °C and 500 °C to see if the surface composition changed over this relatively small heating range. The results are seen below in Table 7.9. It can be seen that the surface composition does change with heating for the bismuth rich samples ($Bi_{0.6}Nb_{0.4}$ and $Bi_{0.8}Nb_{0.2}$), with the surface enrichment of bismuth increasing.

Table 7.9. Comparison of bismuth and niobium percentages from XPS data for the Bi-Nb oxide nanoparticles after calcination at 350 °C and 500 °C, excluding the oxygen signal.

Sample Bi_2O_3-Nb_2O_5	Atom & Orbital	Binding Energy/ eV	Atomic Concentration/ %
$Bi_{0.2}Nb_{0.8}$ at 350 °C	Bismuth 4f	159.08	32.71
	Niobium 3p	365.08	67.29
$Bi_{0.2}Nb_{0.8}$ at 500 °C	Bismuth 4f	156.00	39.72
	Niobium 3p	362.00	60.28
$Bi_{0.4}Nb_{0.6}$ at 350 °C	Bismuth 4f	159.08	69.61
	Niobium 3p	365.08	30.39
$Bi_{0.4}Nb_{0.6}$ at 500 °C	Bismuth 4f	155.00	69.01
	Niobium 3p	361.00	30.99
$Bi_{0.6}Nb_{0.4}$ at 350 °C	Bismuth 4f	159.08	59.01
	Niobium 3p	364.08	40.99
$Bi_{0.6}Nb_{0.4}$ at 500 °C	Bismuth 4f	156.00	83.52
	Niobium 3p	361.00	16.48
$Bi_{0.8}Nb_{0.2}$ at 350 °C	Bismuth 4f	159.08	80.55
	Niobium 3p	364.08	19.45
$Bi_{0.8}Nb_{0.2}$ at 500 °C	Bismuth 4f	156.00	93.18
	Niobium 3p	361.00	6.82

As the calcination temperatures used thus far were over a relatively small range, it was decided to calcine one of the Bi-Nb oxide samples at 900 °C to see if a larger temperature increase would produce a single phase homogenous sample, rather than a mixture of phases. The Rietveld refinement for the PXRD pattern of the $Bi_{0.6}Nb_{0.4}$ oxide sample is seen in Figure 7.32 after heating at 900 °C. It can be seen that the fit to the $BiNbO_4$ pattern is good, with a Chi squared value of 9.27. Scherrer analysis indicates that the sample is still nanoparticulate with the mean crystallite size calculated as 53 ± 4 nm. The stoichiometry of the $BiNbO_4$ phase and the nominal $Bi_{0.6}Nb_{0.4}$ oxide sample dictates that there should be some remaining pure Bi_2O_3 present. This was indeed found to be the case upon examination in the microscope where several particles of δ-Bi_2O_3 were found. Therefore, it can be concluded that at 900 °C there is sufficient energy for the $BiNbO_4$ phase to be formed preferentially to the type II or III phases seen at lower temperatures.

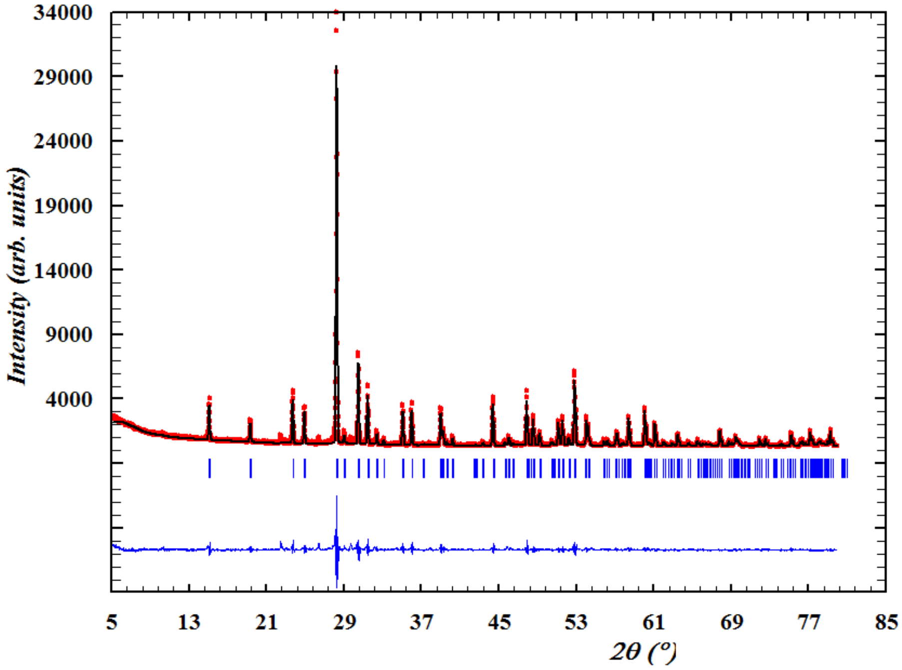

Figure 7.32. Rietveld refinement for the $Bi_{0.6}Nb_{0.4}$ oxide sample after heating at 900 °C

The EDS data shown in Figure 7.33 shows clearly the two different compositions and phases seen in the sample.

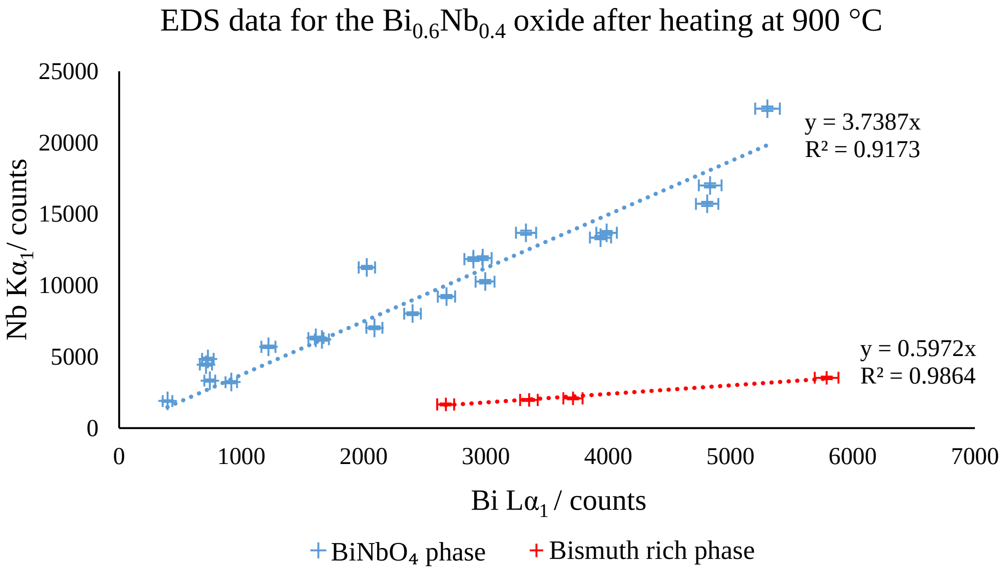

Figure 7.33. EDS data collected for the $Bi_{0.6}Nb_{0.4}$ oxide sample showing that two phases has been formed.

Unit cell parameters for the $BiNbO_4$ phase were calculated from the Rietveld refinement using FullProf. The results, Table 7.10, show the unit cell is slightly longer in the a and c direction in comparison with the literature probably due to the nanoparticulate nature of the sample.

Table 7.10. Comparison between the calculated cell parameters for the $Bi_{0.6}Nb_{0.4}$ oxide sample and literature parameters for $BiNbO_4$ [105].

					Unit Cell Parameter Length/ Å			*Unit Cell Parameter Literature Length/ Å*		
Oxide sample	Phase	θ/ rads	Index	d_{hkl}/ Å	a	b	c	a	B	c
$Bi_{0.6}Nb_{0.4}$	$BiNbO_4$	0.13	020	5.87	5.68119 (0.00007)	11.714 (0.00014)	4.984 (0.00006)	5.673	11.714	4.978
		0.17	011	4.60						
		0.21	101	3.75						
		0.22	111	3.58						
		0.25	121	3.16						
		0.27	200	2.84						
		0.28	210	2.76						
		0.31	220	2.56						

7.4 Ion exchange experiments

Whilst studying these mixed oxide nanoparticles compositions, it became clear that the particles had fluid like properties, in the sense that the composition and homogeneity of the particles could be varied with temperature. It was also reasoned, that due to the small size of the particles and the more relaxed lattice structure (as shown by the unit cell parameter calculations), ion-exchange within the particles should be possible. Therefore, a series of experiments were set up with the Bi-Nb oxide nanoparticles to see if ion exchange in solution was possible. The full experimental details are seen in Chapter 3.

The first set of experiments involved the suspension of the Bi-Nb oxide nanoparticles previously synthesised in a solution of excess bismuth nitrate. These solutions were heated at 50 °C for a week before filtration and drying. The particles were then analysed to see if there had been a change in composition. The EDS results of these particles show that there had indeed been a change in composition. Analysis in the microscope using EDS showed that there was still a range of compositions present within each sample across the 30 particles analysed, therefore the ion exchange had not made the particles any more homogeneous. The average composition for each sample is given in Table 7.11.

Table 7.11. Composition of Bi-Nb nanoparticles calculated from EDS after ion exchange in bismuth nitrate solution compared to the initial composition.

Sample Bi_2O_3-Nb_2O_5	Initial %Bi	Initial %Nb	%Bi after ion exchange	%Nb after ion exchange
$Bi_{0.2}Nb_{0.8}$	25.25	74.75	35.19	64.81
$Bi_{0.4}Nb_{0.6}$	63.17	36.83	60.89	39.11
$Bi_{0.6}Nb_{0.4}$	72.37	27.37	48.65	51.35
$Bi_{0.8}Nb_{0.2}$	63.14	36.86	81.41	18.49

A further set of experiments were carried out where PEG was added to the bismuth nitrate solution after addition of the previously synthesised Bi-Nb oxide nanoparticles. Results of all sample compositions after the PEG burn off stage and the calcination process are shown in Table 7.12.

Table 7.12. Composition of Bi-Nb nanoparticles calculated from EDS after ion exchange in bismuth nitrate solution and PEG compared to the initial composition.

Sample Bi_2O_3-Nb_2O_5	Initial %Bi	Initial %Nb	%Bi after ion exchange in PEG	%Nb after ion exchange in PEG
$Bi_{0.2}Nb_{0.8}$	25.25	74.75	52.50	47.50
$Bi_{0.4}Nb_{0.6}$	63.17	36.83	62.79	37.21
$Bi_{0.6}Nb_{0.4}$	72.37	27.37	66.03	33.97
$Bi_{0.8}Nb_{0.2}$	63.14	36.86	74.03	25.97

Two sets of experiments were devised in order to compare two sets of conditions and determine if one method was more effective in encouraging ion exchange than the other. It may be anticipated that the resin-gel method would be more effective than just diffusion alone in the solution method. The reason for this is the additional mixing of the ions in the molten gel and increased temperature used in the process providing more energy for the ions to move through the particles.

It was found, in fact, that this was not the case with both experiments showing similar results. The percentage of bismuth in the particles generally increased in both methods by a similar amount. The exception for this was the $Bi_{0.6}Nb_{0.4}$ sample where the average bismuth percentage seemed to decrease. PXRD showed that the phases in the samples had not changed, just the composition of the particles.

7.5 Summary of the Bi_2O_3-Nb_2O_5 system

The results presented in this chapter have shown that the Bi-Nb oxide system is highly complicated with a number of different mixed oxide phases being observed. For the samples calcined at 350 °C and 500 °C, many similarities were seen to the studies carried out by Zhou *et al*. [168], with solid solutions of fluorite, pyrochlore and perovskite structures being observed in the PXRD patterns and in the microscope. The reason for this combination of phases forming is due to the oxygen positioning in the different structures and how this impacts the metal ion environment. In the fluorite and pyrochlore structure the oxygen ions occupy the tetrahedral interstices, whereas in the perovskite structure they occupy the octahedral interstices. The niobium ions prefer the perovskite structure, where the structure is more contracted, as it is a small ion. It is therefore likely that the perovskite units are more niobium rich, whereas the fluorite and pyrochlore units are more bismuth rich. Evidence for T-Nb_2O_5 was also found in samples with a high proportion of niobium. XPS data showed that, as with the Bi-Ce oxide nanoparticles, the bismuth cations showed a strong preference for surface site occupation.

At 700 °C the low temperature orthorhombic $BiNbO_4$ phase formed across all compositions as the majority phase, however, due to the stoichiometry of $BiNbO_4$ other phases were found in the samples, depending on whether the sample had excess niobium or bismuth ions. It is interesting to note that 700 °C is substantially lower than the temperature at which $BiNbO_4$ is usually observed, highlighting the difference in nanoparticle structure and accessible phases in comparison with the bulk.

Ion exchange experiments indicated that the particle compositions could be altered when in solution with a vast excess of Bi^{3+} ions. This gives further evidence to the fluid-like nature of nanoparticles and how their properties can vary greatly to the bulk structure.

8. The Bi_2O_3-CeO_2-Nb_2O_5 quaternary system

8.1 Introduction

At present, although there has been some research into the ternary oxide systems of Bi_2O_3-CeO_2, Bi_2O_3-Nb_2O_5 and CeO_2-Nb_2O_5, there have been no investigations into the quaternary oxide system Bi_2O_3-CeO_2-Nb_2O_5. Therefore, it was not known what phases, if any, would be observed, although it was hoped that given the lattice relaxation possible in all nanoparticles, mixed oxide particles would be formed containing all three metal ions.

Four samples of varying compositions were therefore synthesised and analysed using: HRTEM, PXRD, EDS and XPS. The method of synthesis and the compositions synthesised are outlined in Chapter 3; the results for each sample are discussed below. After initial analysis of the samples, following calcination of samples in the tube furnace at 350 °C, various heat treatments were applied to the samples to see if the particles became more crystalline and homogenous with increased temperature.

8.2 Results for samples calcined at 350 °C

Initial results were gathered from particles calcined at 350 °C, to confirm if a quaternary oxide had been formed and what phases were present. The PXRD data for the samples calcined at 350 °C can be seen in Figure 8.1. These initial PXRD patterns showed that mixed metal oxide particles had indeed been formed, as none of the patterns correspond directly to the parent oxides. For all four of the mixed oxide samples there is strong evidence for a fluorite or fluorite-related phase being present. For the $CeNb_2Bi$ oxide, the Ce_2NbBi oxide and the CeNbBi oxide sample, the fluorite peaks are split, indicating the appearance of another phase with lower symmetry. Since the new split peaks do not correlate to either of the other parent structures (α-Bi_2O_3 or Nb_2O_5) we may conclude that there must be a new phase emerging. The fact that a fluorite-related structure prevails even if the proportion of cerium in the sample is not the majority component suggests the metal ions are forming some type of solid solution based on this structure.

For the $CeNbBi_2$ oxide PXRD suggests that only the fluorite structure is present, although a slight shoulder was observed on the {111} peak of the pattern for this sample, which could indicate the presence of a minority phase. This conclusion agrees with the evidence from the HRTEM discussed later in the chapter. Calculated d-spacings from the fast Fourier transforms of the micrographs suggest that in addition to the fluorite structure, perovskite and pyrochlore phases were also present. It can be said, however, that the majority of particle studied had the fluorite structure, therefore, any minority phases may not be seen by X-ray diffraction as those peaks will be overwhelmed by the intensity of the fluorite peaks.

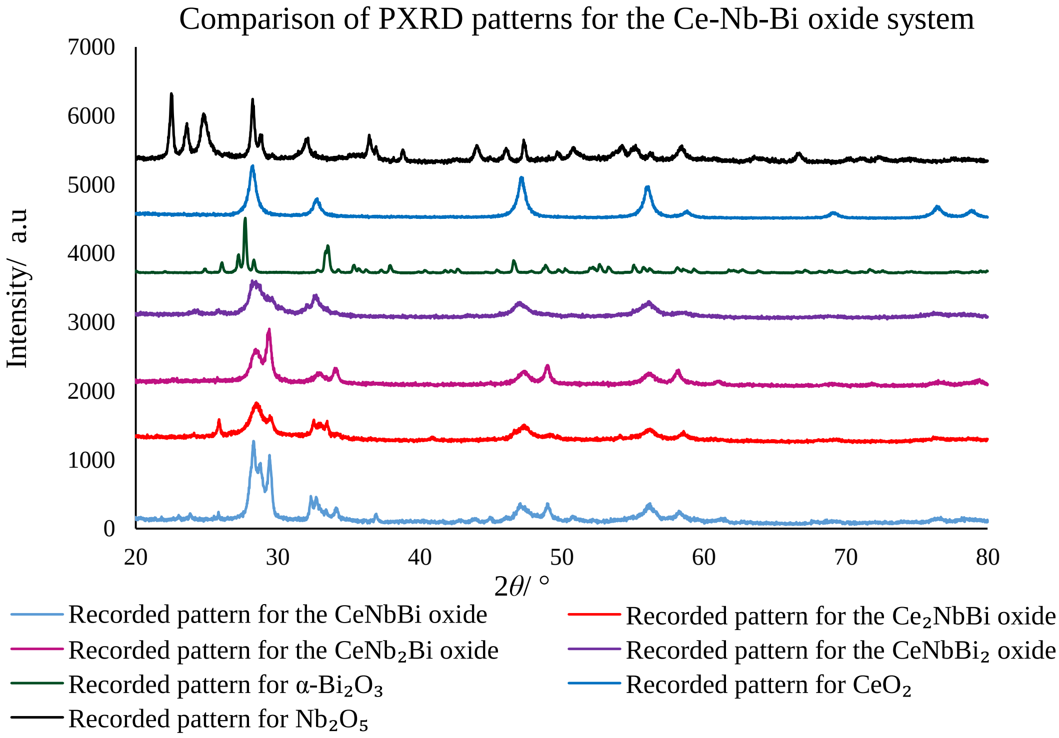

Figure 8.1. Recorded PXRD patterns for the four Ce-Nb-Bi mixed oxide samples along with the recorded patterns for the parent oxides.

The remaining three samples all show splitting of the peaks to a greater or lesser extent, with peaks emerging at a higher 2θ than the original peaks. This indicates that the new phase forming has a smaller basic unit. From previous studies on similar compounds, comparison with calculated PXRD patterns for perovskite, as well as evidence from the HRTEM, it can be deduced that this new phase is based on perovskite units. There was also some evidence from the HRTEM that a pyrochlore phase had also been formed. The fluorite, perovskite and pyrochlore structures can be difficult to distinguish by PXRD as they all have the same fcc cation arrangement (Figure 8.2), and hence share the same strong diffraction peaks.

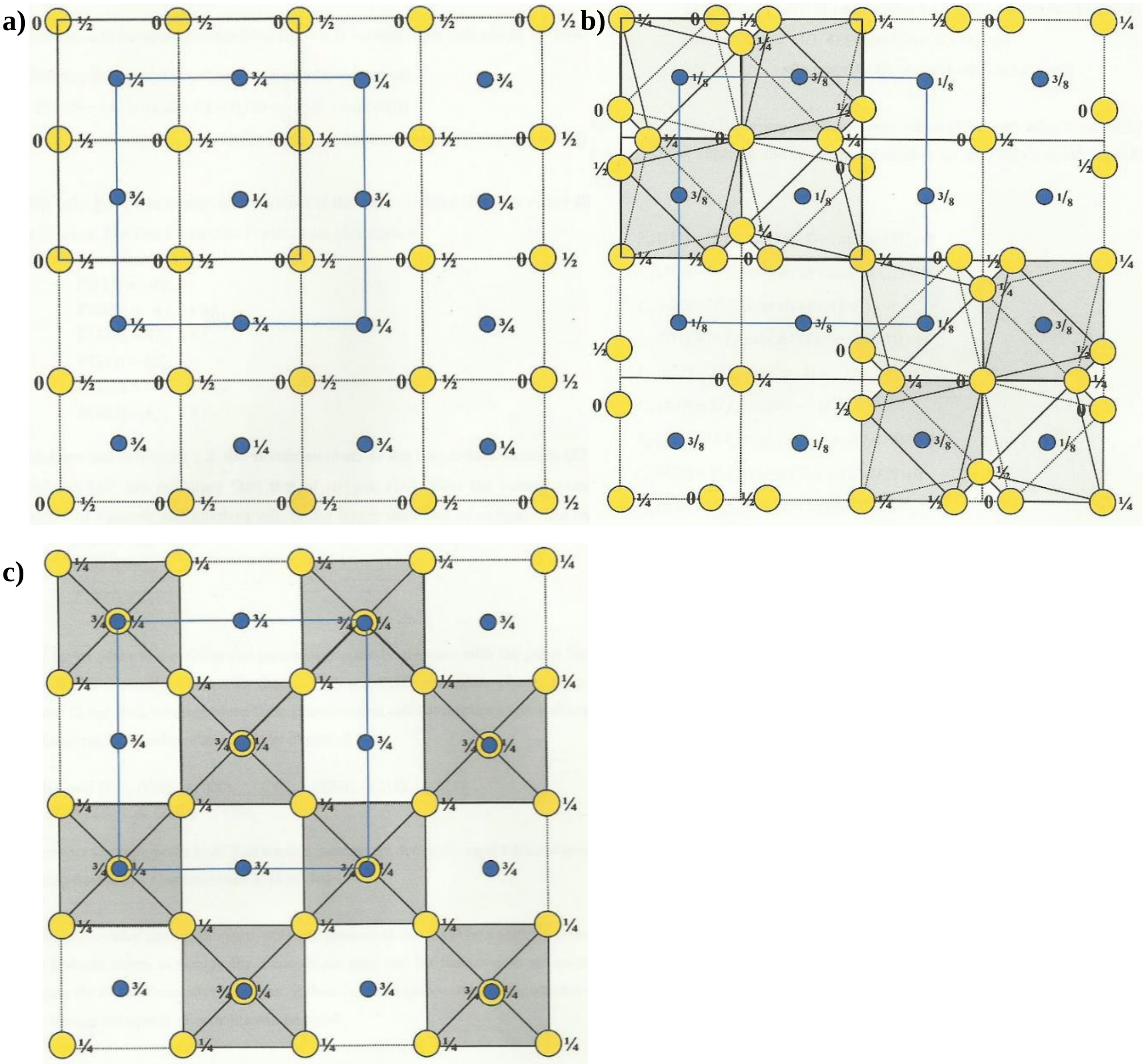

Figure 8.2. The relationship between the structures of (a) fluorite (b) pyrochlore and (c) perovskite. An area of 2 x 2 fluorite unit cells is shown in each case, and the fcc cation cell is shown as a blue square. Oxygen atoms are seen in yellow

In the $CeNb_2Bi$ oxide sample, there was substantially more of the perovskite phase present. This can be explained by the fact that when the lattice changes from a fluorite structure to a perovskite structure, the oxygen atoms occupy the octahedral interstices rather than the tetrahedral interstices in the cation sub-lattice, as in fluorite. This then permits the structure to contract which is energetically beneficial for the small Nb^{5+} ion. Consequently, as the level of niobium is increased, more of the perovskite phase will be formed. This was previously seen in the Bi-Nb oxide system.

The PXRD patterns for all the samples show significant peak broadening expected from nanoparticles. The mean particle sizes calculated for each sample using Scherrer analysis of various lattice planes identified in the PXRD pattern can be seen in Table 8.1. The particle size for α-Bi_2O_3 is much larger than the other structures; this may be due the monoclinic unit cell of α-Bi_2O_3 being larger than that of the fluorite unit cell. It should also be noted that peak broadening can also be due to strain and disorder within the lattice. Therefore, the values given for average particle size could be underestimating the size of the particle as trying to incorporate other metal ions into the fluorite structure such as Bi^{3+} which is larger than Ce^{4+} could induce some strain (despite the lattice relaxing due to the small size) and will almost certainly introduce disorder leading to a broadening of the reciprocal lattice points unless the substitution is completely random. However, taking all these factors into account, the values from the Scherrer analysis seem to give reasonable values which correlate well to the particle sizes seen in the HRTEM.

Table 8.1. Phases present in each sample as deduced from the PXRD patterns along with the mean particle size in the sample calculated using Scherrer analysis for various lattice planes.

Sample Ce:Nb:Bi	*Phase*	*Index*	*Crystallite size calculated from each peak index/ nm*	*Mean crystallite size from Scherrer analysis/ nm*
1:1:1	CeO_2	{111}	8.27	7 ± 0.8
		{220}	6.78	
		{311}	7.00	
1:1:2	CeO_2	{200}	6.23	6 ± 0.3
		{220}	6.02	
		{311}	6.63	
1:2:1	*Mixed fluorite, pyrochlore and perovskite phase*	*{111}*	*11.62*	8 ± 2
		{220}	*11.10*	
		{311}	*10.12*	
	CeO_2	{220}	6.58	
2:1:1	CeO_2	{111}	6.52	8 ± 2
		{200}	11.77	
		{220}	7.08	
Bi_2O_3	α-Bi_2O_3	{102}	46.58	34 ± 8
		{002}	36.76	
		{112}	36.84	
		{121}	39.95	
		{200}	21.13	
		{221}	28.89	
		{220}	27.78	
		{22-1}	32.44	
Nb_2O_5	T-Nb_2O_5 *M*-Nb_2O_5	{001}	24.78	17 ± 5
		{400}	*14.19*	
		{101}	*10.76*	
		{111}	22.91	
		{220}	16.06	
		{201}	15.75	
CeO_2	CeO_2	{111}	12.34	14 ± 1
		{200}	13.51	
		{220}	14.15	
		{311}	13.35	
		{222}	14.88	
		{331}	15.23	

Unit cell parameters were calculated for the fluorite phase, as identified in the PXRD patterns. These values were then compared to literature values, Table 8.2. It can be seen that the unit cell parameters for all the Bi_2O_3-CeO_2-Nb_2O_5 samples are similar to the literature values with the a, b and c parameters only slightly larger than in the bulk. This is what would be expected for nanoparticle samples of fluorite and compares well with the ternary oxide systems.

Table 8.2. Unit cell parameters calculated for all Ce-Nb-Bi oxide samples compared to literature values. [85]

					Unit Cell Parameter Length/ Å			*Unit Cell Parameter Literature Length/ Å*		
Ratio Ce:Nb:Bi	Phase	θ / rads	Index	d_{hkl}/ Å	a	b	c	a	b	c
1:1:1	CeO_2	0.247 0.410 0.491	111 220 311	3.15 1.934 1.635	5.46	5.46	5.46	5.41	5.41	5.41
2:1:1	CeO_2	0.249 0.292 0.413	111 200 220	3.13 2.68 1.92	5.42	5.42	5.42	5.41	5.41	5.41
1:2:1	*Pyrochlore* CeO_2	*0.297* 0.414 *0.428* *0.508*	*400* 220 *440* *622*	*2.63* 1.92 *1.86* *1.58*	5.43	5.43	5.43	5.41	5.41	5.41
1:1:2	CeO_2	0.284 0.411 0.490	200 220 311	2.75 1.93 1.64	5.46	5.46	5.46	5.41	5.41	5.41

All samples were analysed using the HRTEM, with results from this analysis generally confirming the conclusions formed from the PXRD data. It was seen from the calculated d-spacings of the lattice, using the FFT of the image that the majority of particles were of the CeO_2 fluorite structure type. The compositions of these particles, as shown by the EDS data, were not particularly consistent but did seem to suggest that all three metal ions were present in the structure, presumably in some type of solid solution. In addition to particles of the fluorite structure, some larger crystals were observed, with d-spacings consistent with the perovskite and pyrochlore structures. This also agrees well with data collected from X-ray diffraction, and is strong evidence for three distinct phases being present in the Bi_2O_3-CeO_2-Nb_2O_5 system.

Examples of crystals observed in the microscope with the fluorite structure are seen in Figures 8.3 and 8.4. Firstly, Figure 8.3 shows a micrograph from the $CeNb_2Bi$ oxide sample. The two crystalline particles in the image show d-spacings of 3.20 Å corresponding to the {111} lattice plane of the fluorite structure. EDS data shows the particles are rich in bismuth and niobium with some cerium also present.

It is therefore, likely that the material has a defect structure with the ions in solid solution. The mean composition for this sample, calculated from the crystals analysed, was $Ce_{0.26}Nb_{0.4}Bi_{0.34}O_y$. The reason that there is less niobium than expected in comparison with the nominal composition is perhaps because only very small particles were examined by EDS, therefore any large crystals of Nb_2O_5 could have been overlooked.

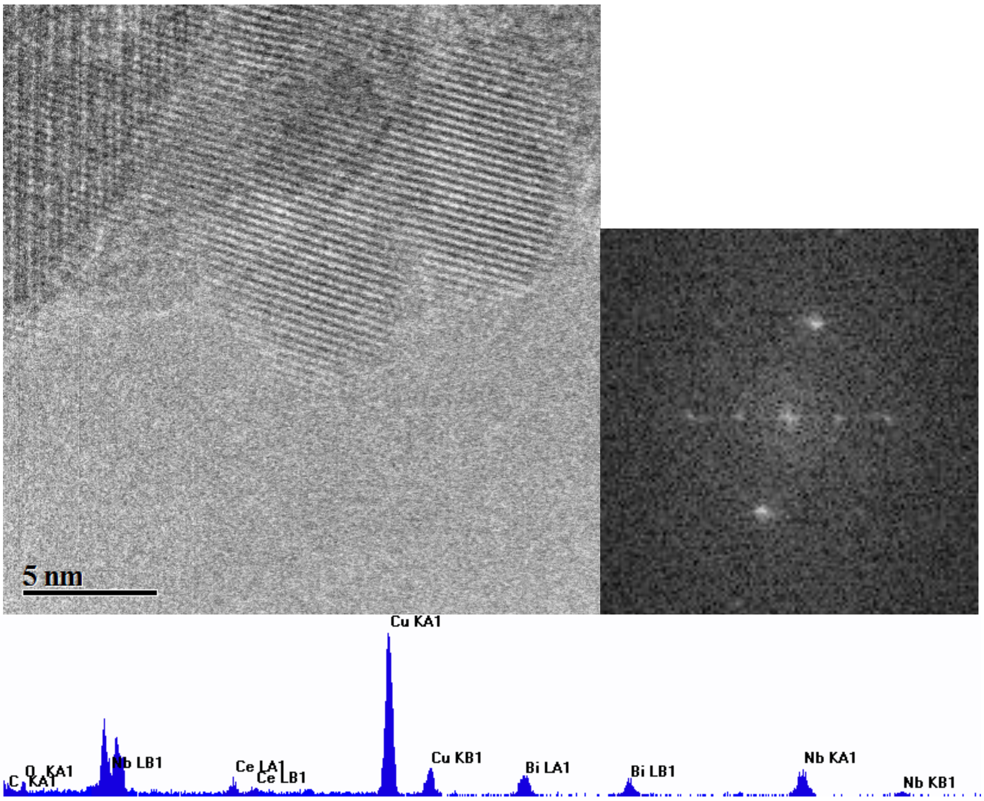

Figure 8.3. HRTEM micrograph of a highly crystalline region of the $CeNb_2Bi$ oxide sample (l) with corresponding FFT (r). EDS spectra for the area shown below showing the presence of three metal ions.

Figure 8.4 presents a micrograph of a crystalline region of the Ce_2NbBi oxide sample. From the FFT, d-spacings were calculated for the lattice planes as 3.30 Å, 2.94 Å, 2.19 Å and 1.67 Å indicative of the {111}, {200}, {220} and {311} planes respectively for the fluorite structure. The EDS spectrum shows the particles are rich in all three metals. Again, it is likely that the ions are in solid solution. The mean composition calculated for this sample was $Ce_{0.31}Nb_{0.39}Bi_{0.30}O_y$. The percentage of bismuth present in the sample seems correct, however, there is significantly less cerium and more niobium than expected. It could be that the mixed oxide nanoparticles analysed were more niobium rich and there were other particles of pure CeO_2 which were not analysed elsewhere in the sample. The main problem with EDS analysis is that only a very small fraction of particles can be analysed.

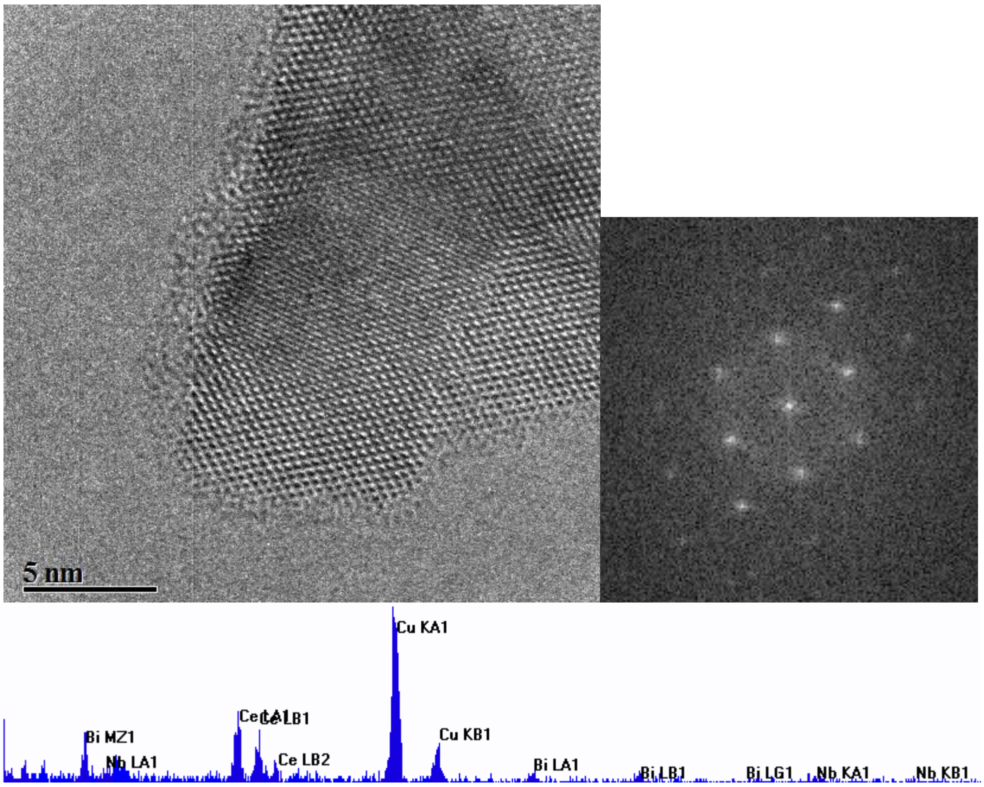

Figure 8.4. HRTEM micrograph of a highly crystalline region of the Ce_2NbBi oxide sample (l) with corresponding FFT (r). EDS spectra for the area shown below.

Evidence for the pyrochlore phase was seen in two of the four samples synthesised, namely those of CeNbBi oxide and $CeNb_2Bi$ oxide. It is possible that this phase was present in all samples, however, as such a small proportion of particles are viewed in the microscope and it is possible that any particles of pyrochlore in the two other samples were not seen using this technique. PXRD records the average diffraction for the whole sample and therefore, will give a fairer representation of which phases are present. It may also be that the small fluorite crystals tended to be located in small aggregates whereas the perovskite and pyrochlore phases may have formed larger particles in more dense aggregates which were not amenable to HRTEM imaging.

Figure 8.5 shows a highly crystalline region of CeNbBi oxide with d-spacings calculated from the FFT giving values of 6.16 Å, 3.21 Å, and 2.83 Å indicating the pyrochlore structure has been formed. The d-spacings correspond approximately to the {111}, {311} and {400} lattice planes respectively. It should also be noted that these calculated d-spacings are slightly larger than those expected from the literature which can be expected as it is known that the crystal lattice tends to relax slightly in the nano-form. This evidence along with the peaks in the PXRD pattern for the CeNbBi oxide confirm that a pyrochlore structure has been formed. The EDS data accompanying the micrograph shows the presence of bismuth, niobium and cerium in solid solution. The calculated mean composition for this sample was $Ce_{0.31}Nb_{0.34}Bi_{0.35}O_y$, which is very close to the starting composition and within error.

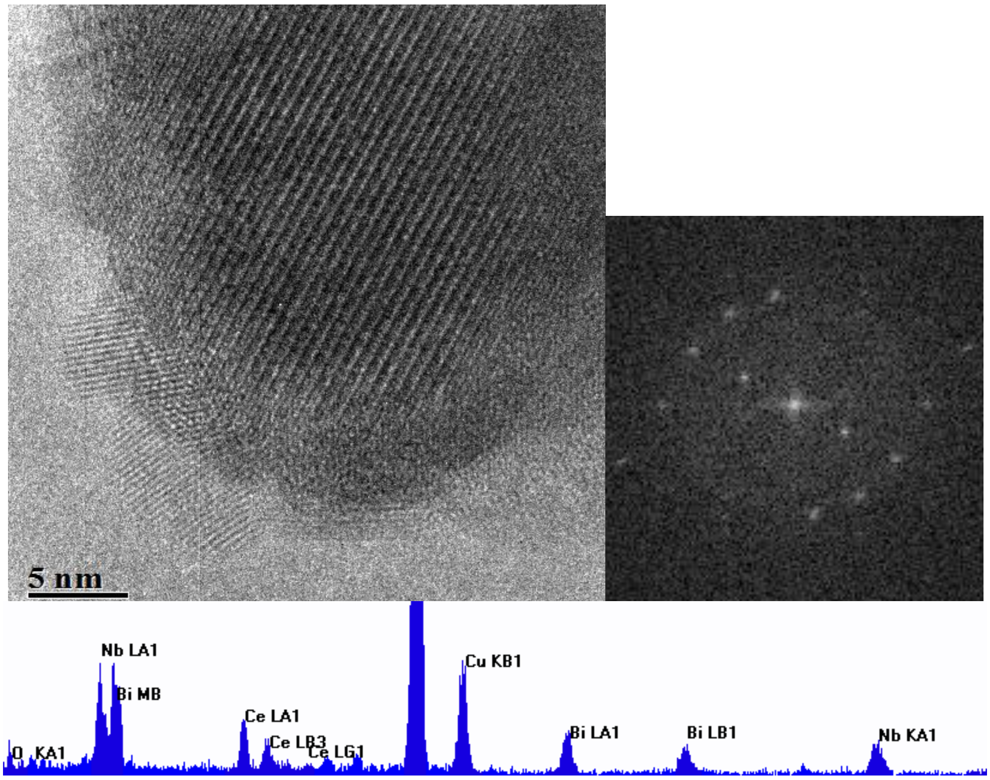

Figure 8.5. HRTEM micrograph of a highly crystalline region of the CeNbBi oxide sample (l) with corresponding FFT (r). EDS spectra for the area shown below confirming the presence of all three metal ions.

The crystalline particles of $CeNb_2Bi$ oxide seen in Figure 8.6 have been identified as being the pyrochlore phase with calculated d-spacings as 6.28 Å and 3.06 Å which again correspond to the {111} and {222} lattice planes. The EDS data shows all 3 metal ions present with a high proportion of Nb ions as expected from the composition of the sample.

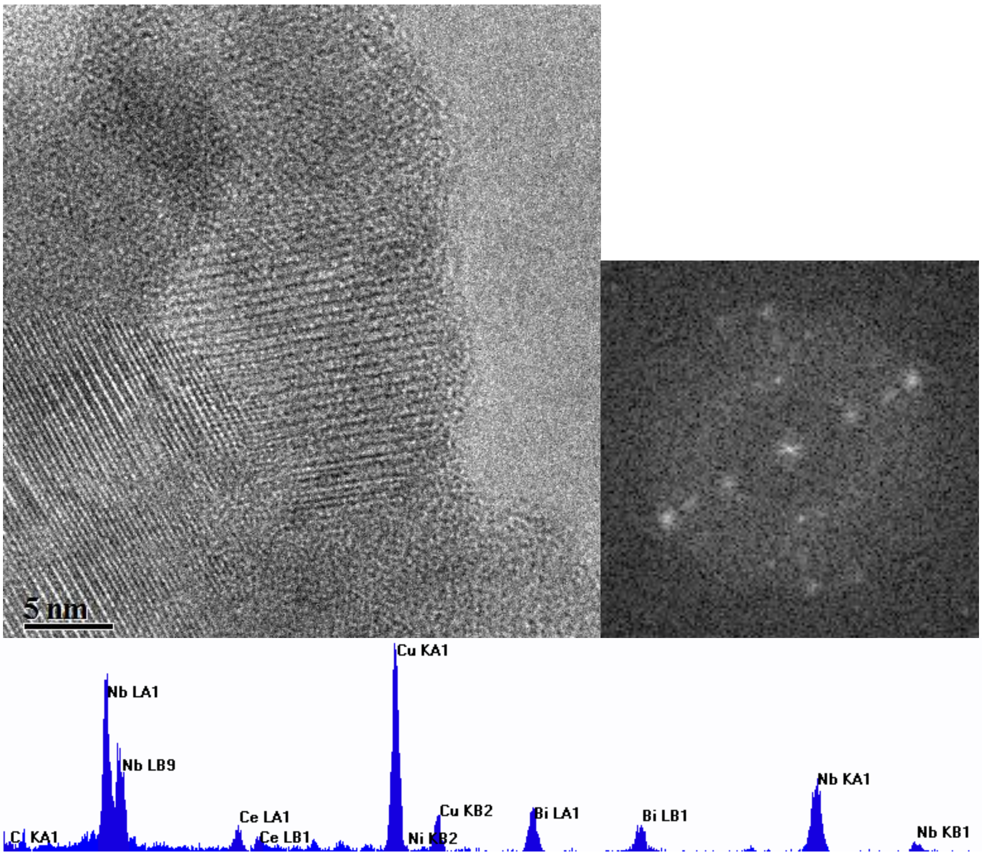

Figure 8.6. HRTEM micrograph of a highly crystalline region of the CeNb$_2$Bi oxide sample (l) with corresponding FFT (r). EDS spectra for the area shown below confirming the presence of all three metal ions.

Figure 8.7 presents a micrograph of crystalline CeNbBi$_2$ oxide. Calculated d-spacings for this nanoparticle were 3.86 Å, 3.11 Å, 2.00 Å and 1.56 Å corresponding to the {110}, {112}, {220} and {204} lattices planes of the perovskite structure respectively. EDS analyses were taken at several different positions on the particle with all indicting that cerium, bismuth and niobium were present, implying that the ions are in solid solution within the perovskite structure. The calculated mean composition for this sample was $Ce_{0.36}Nb_{0.30}Bi_{0.33}O_y$. There is significantly less bismuth present than was initially used. Again, the reason for this could be that the volatile nature of bismuth meant that a small proportion was lost during the annealing process. Alternatively, it could be that there were particles of pure Bi_2O_3 which were not analysed using EDS as they were seen to be unsuitable for single particle analysis due to the size and thickness of the particles.

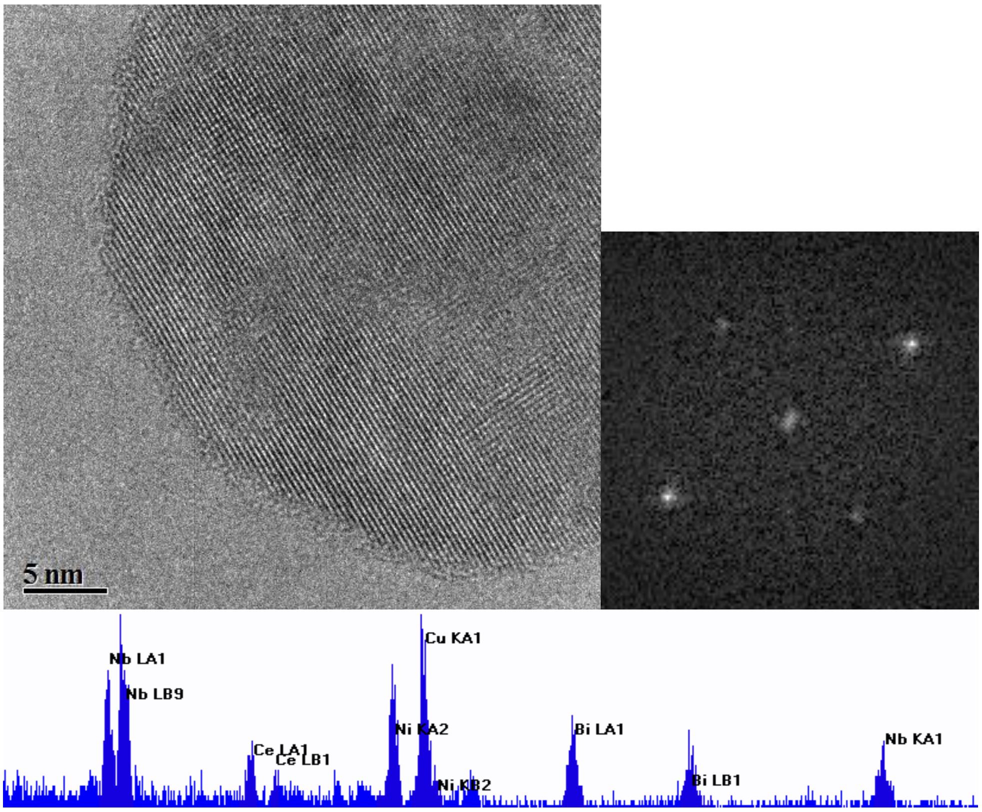

Figure 8.7. HRTEM micrograph of a crystalline region of the CeNbBi$_2$ oxide sample (l) with corresponding FFT (r). EDS spectra for the area shown below confirming the presence of all three metal ions (nickel signal from TEM grid).

As well as the three crystalline phases observed, which have already been discussed, there were some areas of quasi-crystalline material present in all samples, an example of which is seen in Figure 8.8. The most likely reason for this is that temperatures used in synthesis (350 °C) were insufficient to ensure that all the material was fully crystalline. An alternative explanation is that in some regions the long range ordering of the cations may be lost even if the oxygen ions are still ordered as the HRTEM resolution is limited to imaging the cation lattice only. This would give the appearance of an amorphous material.

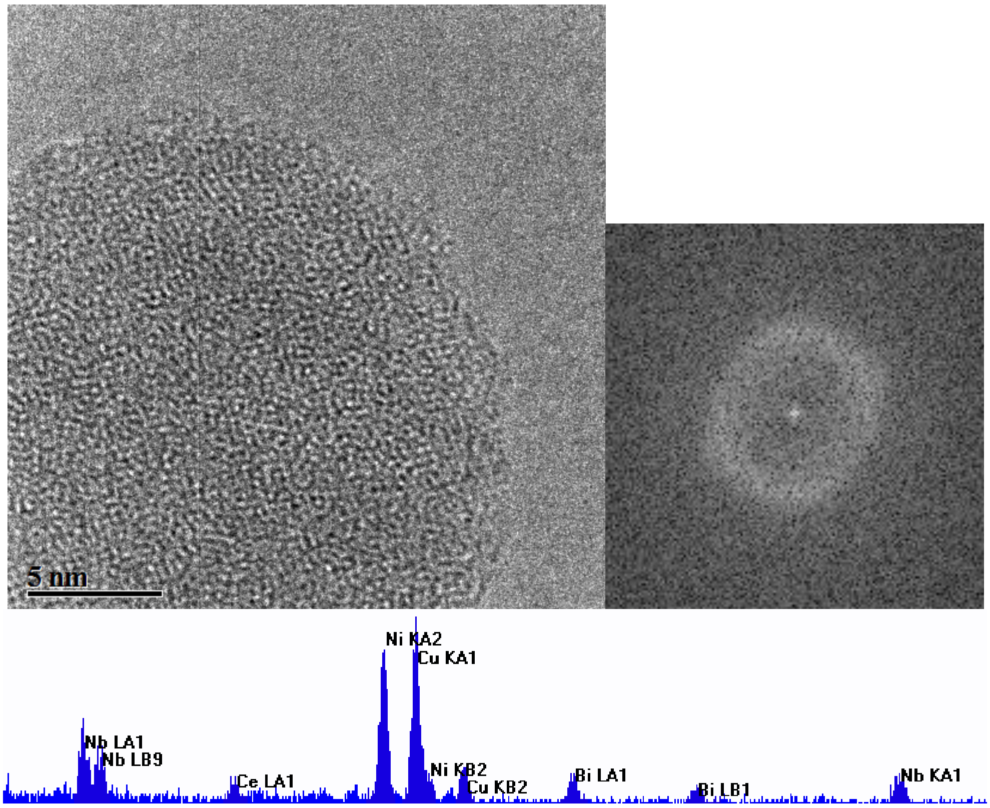

Figure 8.8. HRTEM micrograph of a quasi-crystalline region of the CeNbBi$_2$ oxide sample (l) with corresponding FFT (r). EDS spectra for the area shown below confirming the presence of all three metal ions (nickel signal from TEM grid).

The EDS data for each sample generally indicates that there is not one single composition being formed. This is not surprising as usually temperatures of approximately 1000 °C are required to form the mixed phases such as BiNbO$_4$ or CeNbO$_4$ in the bulk. However, synthesising metal oxides at these temperatures usually leads to sintering of particles and increased particle size. Due to the large range of compositions present in the particles, it is reasonable to infer the ions are in solid solution, which is entropically favourable. Most importantly, it can be seen from the PXRD and HRTEM data that mixed metal oxide particles have been formed, not just the parent oxides.

Tables 8.3 and 8.4 give the average d-spacings observed in the HRTEM for each lattice plane of each phase with a comparison to literature values. It can be seen that on the whole, d-spacings calculated from synthesised samples showed larger d-spacings than the literature values. This trend was expected due to lattice relaxation in nanoparticles.

The most prevalent phase seen for all samples in the microscope was the fluorite structure as expected from the PXRD patterns. Also seen for all samples apart from Ce$_2$NbBi oxide were the pyrochlore and perovskite structures, again as expected from the extra peaks in the PXRD patterns. For the Ce$_2$NbBi oxide sample there were also some particles of pure α-Bi$_2$O$_3$. It is likely there would also be some pure α-Bi$_2$O$_3$ particles across all samples due to the inhomogeneity in the samples. However, as the α-Bi$_2$O$_3$

particles tend to be larger, they may have been discriminated against and analyses not taken for these areas. If there was any α-Bi_2O_3 in the other samples it is likely to be a minority component as this phase was not seen using PXRD. To increase the homogeneity of the samples, they could be heated in order to encourage diffusion of ions and create a more consistent crystal composition.

Table 8.3. Average d-spacings for each mixed oxide sample as observed in the HRTEM for the fluorite structure compared to literature values. [85]

	Index of fluorite structure							
Sample Ce:Nb:Bi	Average d-spacing for {111} / Å	Literature value/ Å	Average d-spacing for {200} / Å	Literature value/ Å	Average d-spacing for {220} / Å	Literature value/ Å	Average d-spacing for {311} / Å	Literature value/ Å
1:1:1	3.24 ±0.11	3.12	2.80 ± 0.11	2.71	2.01 ± 0.06	1.91	1.75 ± 0.04	1.63
2:1:1	3.21 ± 0.08	3.12	2.87 ± 0.18	2.71	2.03 ± 0.13	1.91	1.67 ± 0.09	1.63
1:2:1	3.30 ± 0.18	3.12	2.66 ± 0.31	2.71	2.24 ± 0.27	1.91	1.86 ± 0.01	1.63
1:1:2	3.19 ± 0.07	3.12	2.93 ± 0.12	2.71	1.96 ± 0.05	1.91	1.56 ± 0.05	1.63

Table 8.4. Average d-spacings for each mixed oxide sample as observed in the HRTEM for the perovskite, pyrochlore and α-Bi_2O_3 structures compared to literature values. [172, 107, 35]

Sample Ce:Nb:Bi	{110} planes of perovskite/ Å	Literature value/ Å	{111} planes of pyrochlore/ Å	Literature value/ Å	{222} planes of pyrochlore/ Å	Literature value/ Å	{120} planes of α-Bi_2O_3 / Å	Literature value/ Å
1:1:1	3.69 ± 0.30	3.82	6.19 ± 0.30	6.03	3.06 ± 0.03	3.02	-	-
2:1:1	-	-	-	-	-	-	3.44 ± 0	3.24
1:2:1	3.83 ± 0.01	3.82	5.89 ± 0.32	6.03	3.03 ± 0.04	3.02	-	-
1:1:2	3.73 ± 0.23	3.82	6.48 ± 0.00	6.03	-	-	-	-

The EDS data provided an average composition for the nanoparticle samples but did not provide any information about the atomic arrangement of the particles. Although, due to the range of compositions observed in the HRTEM, it was concluded that the specimens were not homogenous. The large variation in elemental composition across all samples supports the idea that a solid solution of cations is formed. In order to get an idea of the arrangement of the metal ions in the particles XPS experiments were conducted to allow for comparison between the surface composition and the average sample composition, as calculated from EDS.

An example XPS survey scan recorded of the Ce_2NbBi oxide sample is seen in Figure 8.9. The survey scan and high resolution scans for all the samples indicated single oxidation states of bismuth and niobium being present (+3 and +5 respectively). As with the ternary oxide systems, many split peaks were seen for the Ce 3d signal, indicating cerium was present in the +3 and +4 state.

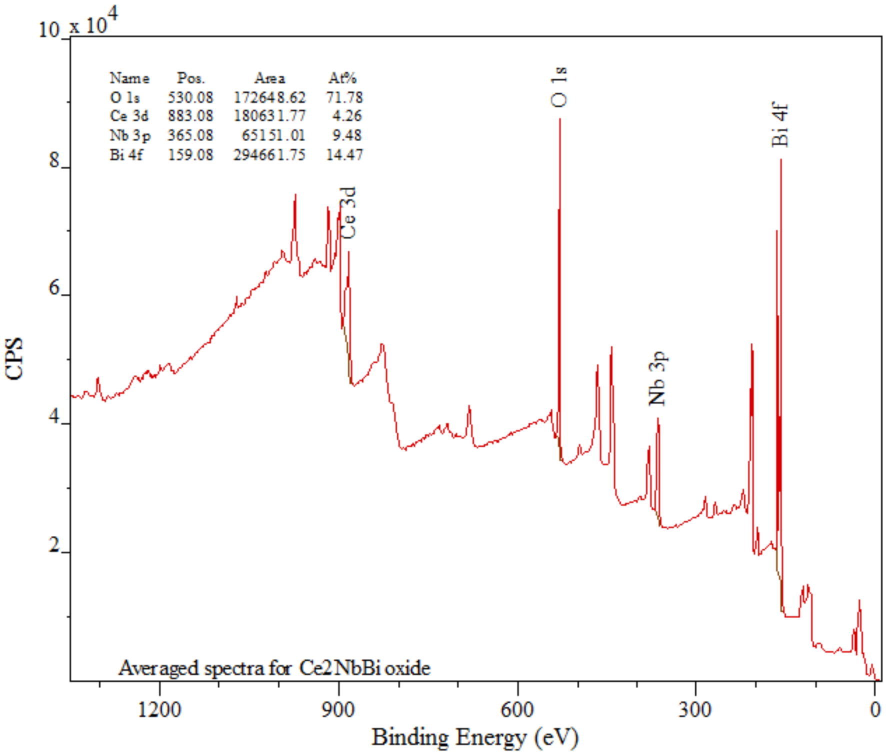

Name	Pos.	Area	At%
O 1s	530.08	172648.62	71.78
Ce 3d	883.08	180631.77	4.26
Nb 3p	365.08	65151.01	9.48
Bi 4f	159.08	294661.75	14.47

Figure 8.9. XPS survey scan for the Ce_2NbBi oxide sample.

The atomic concentrations calculated for each of the quaternary oxide samples are presented in Table 8.5. The XPS data indicates a strong preference for Bi^{3+} to occupy the surface sites across all sample compositions, with niobium being the next most abundant ion on the surface. The reason that bismuth prefers surface coordination is likely due to its preference for asymmetric coordination due its lone pair of electrons, as seen in the ternary oxide systems containing bismuth. [161] Cerium is the least abundant surface element due to its preference for a high coordination number which is found in the core of the nanoparticle. As discussed for the ternary oxides, niobium is able to bind with a lower coordination number, hence it being situated at the surface more readily than cerium. This was also seen by Stošić *et al*. in their studies on the CeO_2-Nb_2O_5 system. [121]

Table 8.5. Atomic concentration percentages for each element in the quaternary oxide samples, as calculated from XPS.

Sample	*Atom & Orbital*	*Binding Energy/ eV*	*Atomic Concentration /%*	*Std Dev*
CeNbBi at 350 °C	Bismuth 4f	160.08	67.37	0.34
	Niobium 3p	366.08	22.89	0.14
	Cerium 3d	884.08	9.76	0.29
Ce_2NbBi at 350 °C	Bismuth 4f	159.08	51.27	0.44
	Niobium 3p	365.08	33.60	0.16
	Cerium 3d	883.08	15.14	0.08
$CeNb_2Bi$ at 350 °C	Bismuth 4f	159.08	53.73	0.24
	Niobium 3p	365.08	38.96	0.03
	Cerium 3d	883.08	7.32	0.11
$CeNbBi_2$ at 350 °C	Bismuth 4f	159.08	75.90	0.03
	Niobium 3p	365.08	18.41	0.21
	Cerium 3d	883.08	5.70	0.09

The data is contrasting to the results gathered from EDS, (comparison seen in Table 8.6) where the composition was approximately equal to the stoichiometry of the expected material. Therefore, it can be confirmed that, as suspected from HRTEM analysis, the particles themselves are not homogeneous and the ions are not in an ideal solution. The bismuth lone pair and the coordination environment preferences of niobium and bismuth dictate the atomic arrangement heavily within the structure.

Table 8.6. Comparison of overall particle composition calculated from EDS analysis and surface composition from XPS.

Sample	*%Ce from EDS*	*%Ce from XPS*	*%Nb from EDS*	*%Nb from XPS*	*% Bi from EDS*	*% Bi from XPS*
CeNbBi	33.85	9.76	32.48	22.89	31.60	67.37
Ce_2NbBi	33.88	15.14	39.19	33.60	26.72	51.27
$CeNb_2Bi$	29.24	7.32	39.75	38.96	31.02	53.73
$CeNbBi_2$	40.33	5.70	29.39	18.41	30.28	75.90

8.3 Thermal treatments

As with the ternary oxide systems, the Bi_2O_3-CeO_2-Nb_2O_5 nanoparticles were heated at 500 °C and 700 °C for 7 days under flowing oxygen in the tube furnace in order to see how the particles changed with temperature. It was expected that any areas of quasi-crystalline material would have enough energy to crystallise and the homogeneity of the particles may improve.

After the initial investigations determined that the CeNbBi oxide nanoparticles were mainly based on the fluorite structure with some units of pyrochlore and perovskite also being observed, heating experiments were undertaken to see how stable the phases were and if they changed with temperature The PXRD pattern for the CeNbBi oxide particles after heating at different temperatures are shown in Figure 8.10. It can be seen that no phase changes occur with heating to 500 °C but at 700 °C the peak intensities change quite markedly indicating that some structural change has occurred in the particles. The pattern for the particles heated at 700 °C also has much sharper peaks indicating the crystallinity of the sample has improved. Similarly, the patterns for the Ce_2NbBi oxide samples show no change upon heating from 350 °C to 500 °C, but again, the peak intensities and peak sharpness alter considerably at 700 °C.

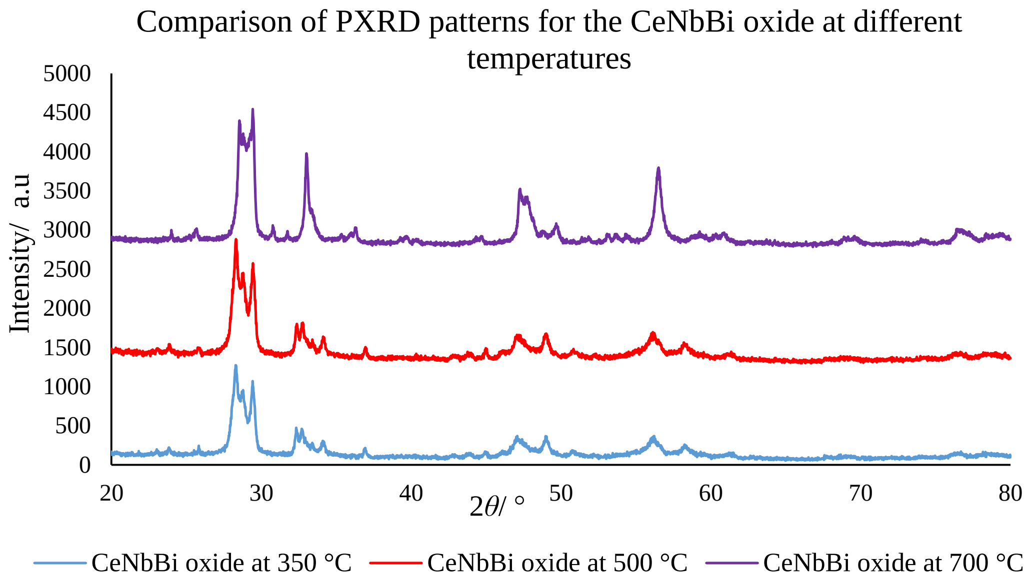

Figure 8.10. PXRD pattern for the CeNbBi oxide sample after heating at various temperatures.

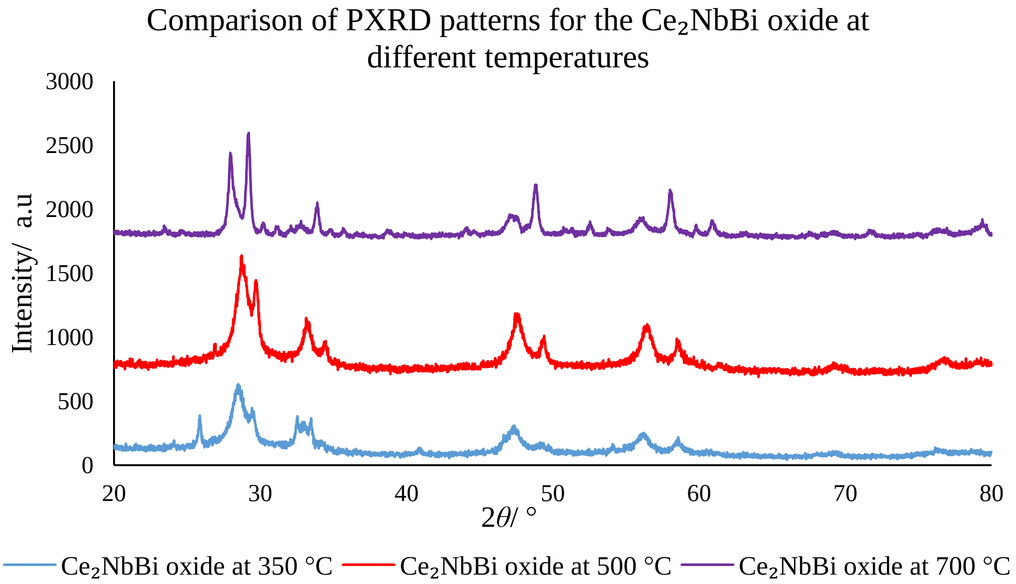

Figure 8.11. PXRD pattern for the Ce_2NbBi oxide sample after heating at various temperatures.

The PXRD patterns for the $CeNb_2Bi$ oxide sample, Figure 8.12, also follow the same pattern, with no phase change from 350 °C to 500 °C, but at 700 °C a clear phase change is seen. The fluorite and pyrochlore peaks remain, but new peaks corresponding to the low temperature $BiNbO_4$ phase are seen. These peaks are very sharp indicating a high degree of crystallinity and a larger crystallite size.

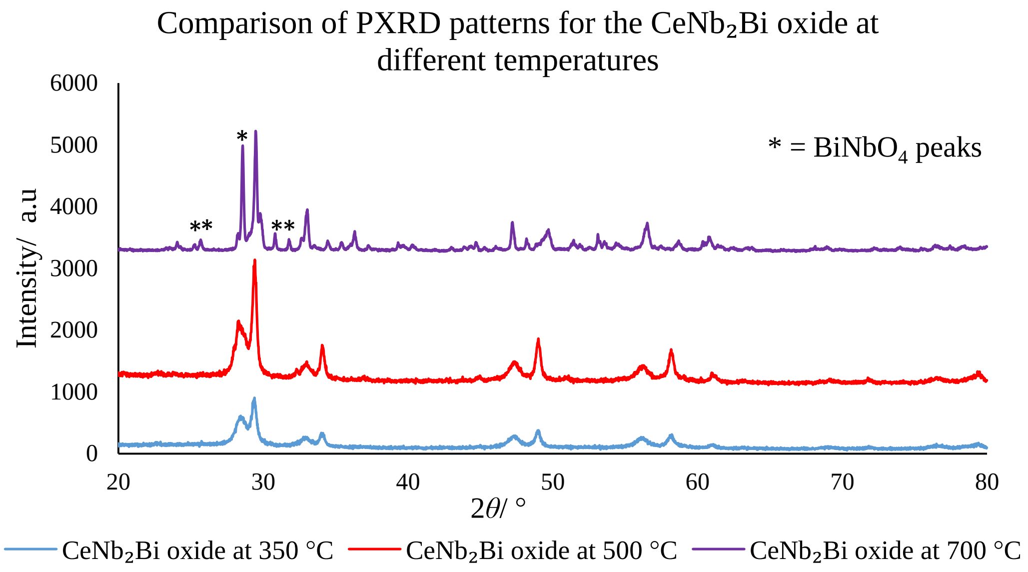

Figure 8.12. PXRD pattern for the CeNb$_2$Bi oxide sample after heating at various temperatures.

The CeNbBi$_2$ oxide sample sees a phase change after heating to just 500 °C with results seen in Figure 8.13. The fluorite related peaks remain, but a new phase seems to appear, with a strong peak being seen at 25.79°. It is unclear what phase this corresponds to but it is likely to represent a distorted bismuth oxide phase. In addition to this new peak, the fluorite peaks seem to split, representing the formation of pyrochlore and perovskite units. At 700 °C the same peaks are seen but are sharper and more resolved due to the larger size of the crystallites.

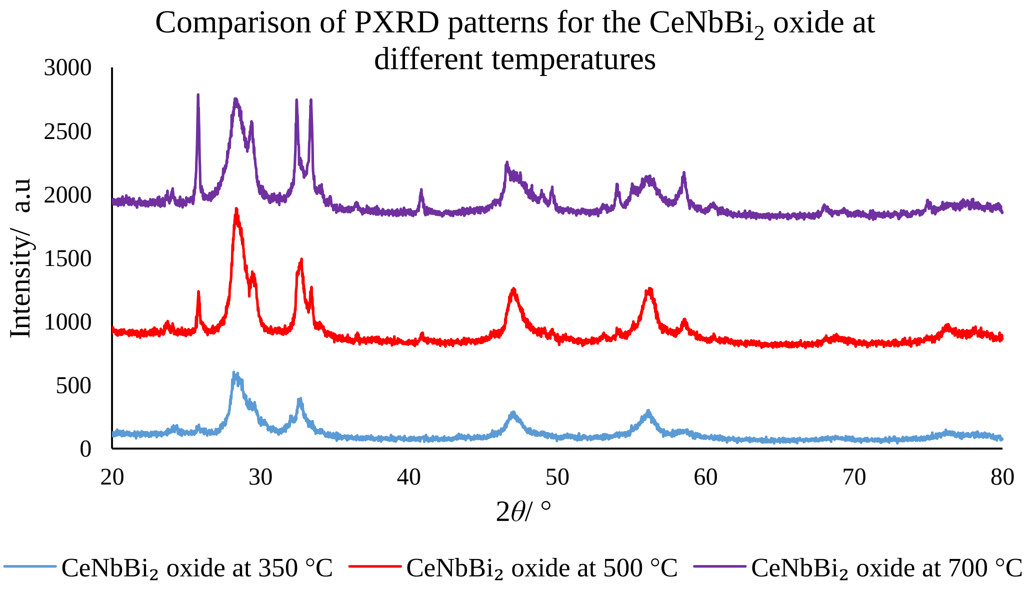

Figure 8.13. PXRD pattern for the CeNbBi$_2$ oxide sample after heating at various temperatures.

Scherrer analysis was carried out on the data for all samples, with results showing a steady increase in mean crystallite size after the temperature is increase from 500 °C to 700 °C, Figure 8.14. The mean crystallite size stays approximately the same after heating to 500 °C, which is not unexpected as no phase change occurs and sintering at this temperature will be minimal.

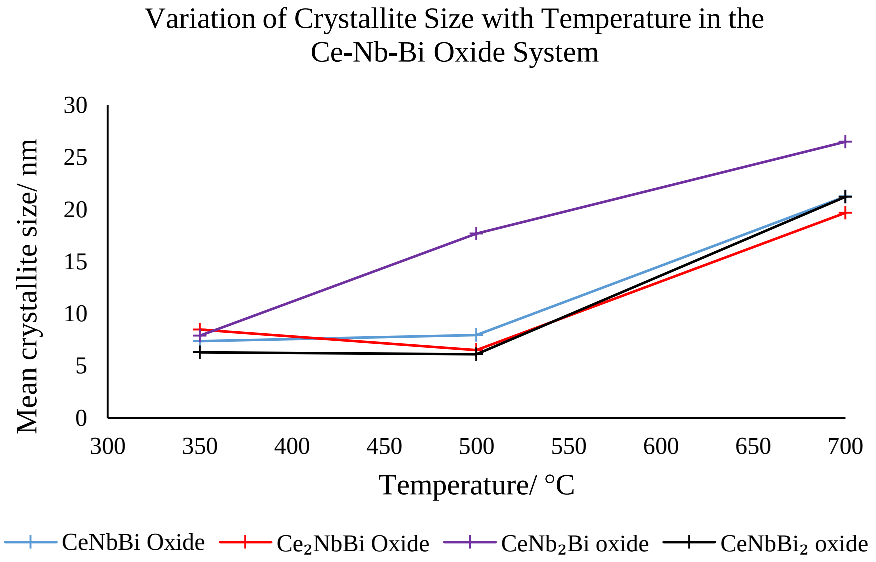

Figure 8.14. Plot showing the relationship between composition and mean crystallite size at various temperatures.

From the EDS analysis of the particles in the microscope, an average composition of the mixed particles for each sample could be calculated by adjusting the ratio of each of the three metals to the bulk samples. The results for this, Table 8.7, show that there is variation in the particle composition with temperature but this does not follow a consistent trend. This would support the theory that the ions are in a solid solution with a large degree of inhomogeneity, which changes with temperature to a slightly different composition.

Table 8.7. Composition of the mixed Ce-Nb-Bi oxide nanoparticles varying with temperature.

Sample Ce-Nb-Bi oxide	*Calcination temperature/ °C*	*Composition of mixed phase calculated from EDS*
CeNbBi	350	$Ce_{0.31}Nb_{0.34}Bi_{0.35}$
	500	$Ce_{0.27}Nb_{0.25}Bi_{0.48}$
	700	$Ce_{0.51}Nb_{0.11}Bi_{0.38}$
Ce_2NbBi	350	$Ce_{0.31}Nb_{0.39}Bi_{0.30}$
	500	$Ce_{0.33}Nb_{0.30}Bi_{0.37}$
	700	$Ce_{0.40}Nb_{0.35}Bi_{0.25}$
$CeNb_2Bi$	350	$Ce_{0.26}Nb_{0.40}Bi_{0.34}$
	500	$Ce_{0.42}Nb_{0.34}Bi_{0.24}$
	700	$Ce_{0.46}Nb_{0.15}Bi_{0.38}$
$CeNbBi_2$	350	$Ce_{0.36}Nb_{0.30}Bi_{0.33}$
	500	$Ce_{0.18}Nb_{0.25}Bi_{0.57}$
	700	$Ce_{0.35}Nb_{0.13}Bi_{0.52}$

Approximately 30 particles per sample were viewed in the microscope in order to establish if and how the particles had changed with temperature. It was found, on the whole, that the samples heated to 500 °C had changed very little to those viewed after calcination at 350 °C, with a combination of fluorite, pyrochlore and perovskite crystals identified. There were also several particles of the quasi-crystalline phase observed in addition to the crystalline phases.

The micrograph presented in Figure 8.15, depicts a large crystal of pyrochlore surrounded by several smaller particles of fluorite seen in the CeNbBi oxide sample after heating at 500 °C. The d-spacing from the FFT of 5.98 Å indicated the observed {111} plane of pyrochlore, while the d-spacings of 3.20 Å and 2.76 Å indicated the {111} and {200} planes of fluorite. Similarly, a large crystal of pyrochlore is seen in the Ce_2NbBi oxide sample at 500 °C, Figure 8.16, with d-spacings of 6.18 Å and 3.06 Å indicating the {111} and {222} planes of this phase. EDS spectra for both regions show that there are bismuth, cerium and niobium ions present. The phases seen in the microscope agree well with the phases identified in the PXRD pattern.

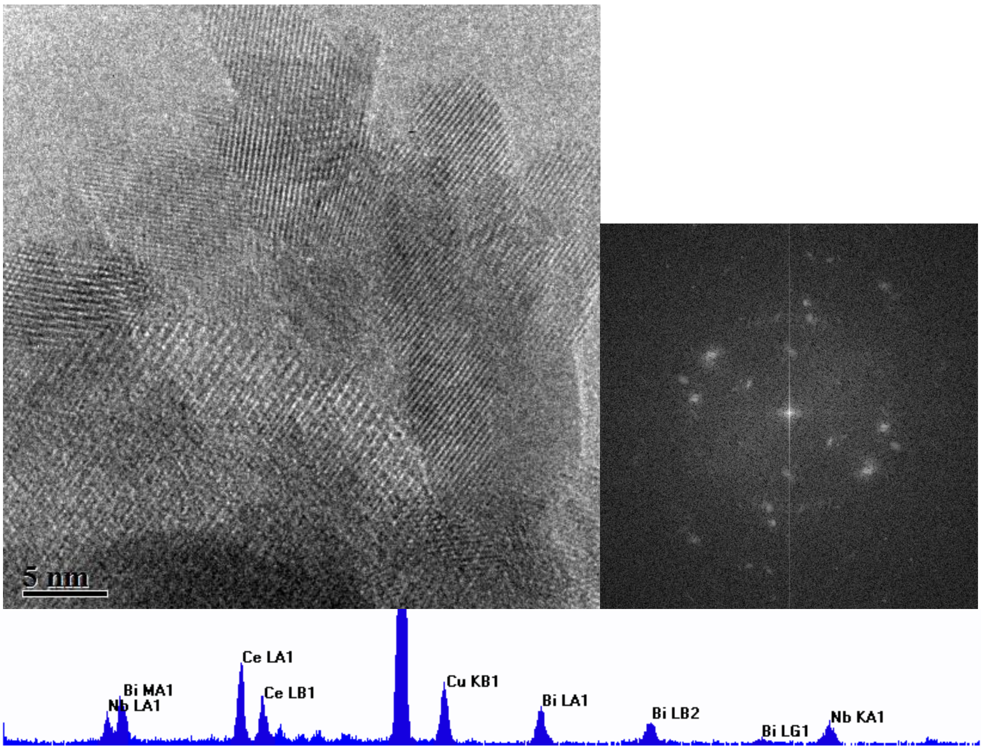

Figure 8.15. HRTEM micrograph of the CeNbBi oxide sample after calcination at 500 °C (l) with corresponding FFT (r). EDS spectra for the area shown below.

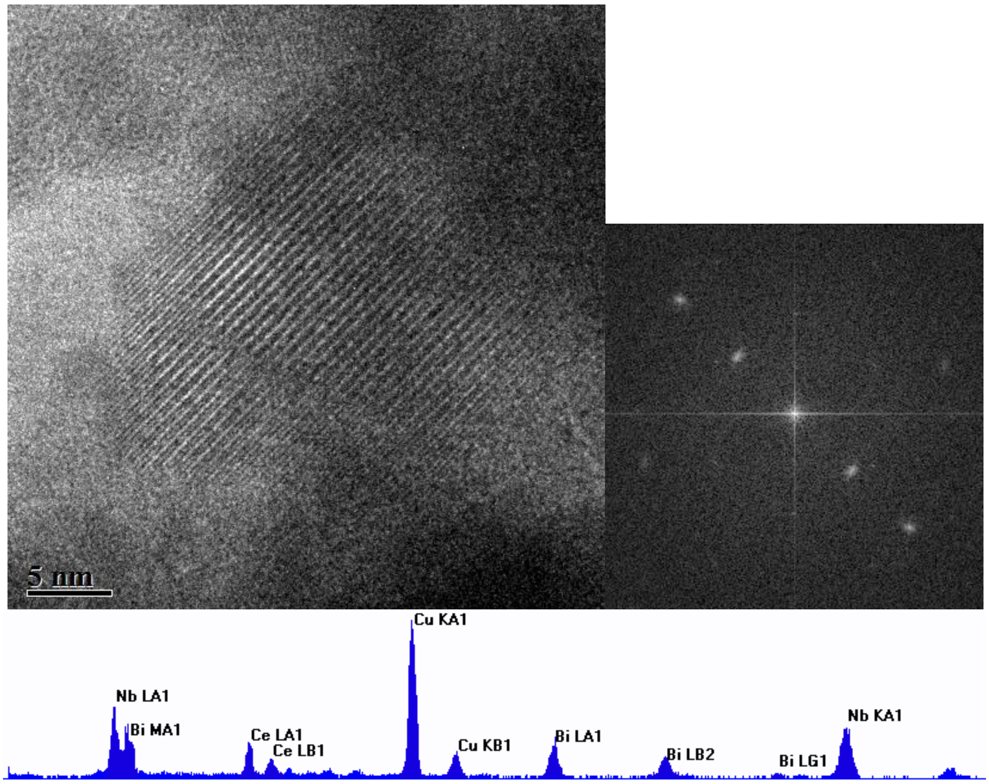

Figure 8.16. HRTEM micrograph of the Ce_2NbBi oxide sample after calcination at 500 °C (l) with corresponding FFT (r). EDS spectra for the area shown below.

A large area rich in bismuth and niobium is seen in the micrograph, Figure 8.17, taken of the $CeNb_2Bi$ oxide sample after heating at 500 °C. The d-spacing visible in the micrograph is 3.24 Å which correlates to the {111} plane of the δ-Bi_2O_3 fluorite structure. Cerium rich fluorite particles were also seen in this sample (with traces of bismuth and niobium) and it is not known why the particle shown did not contain cerium.

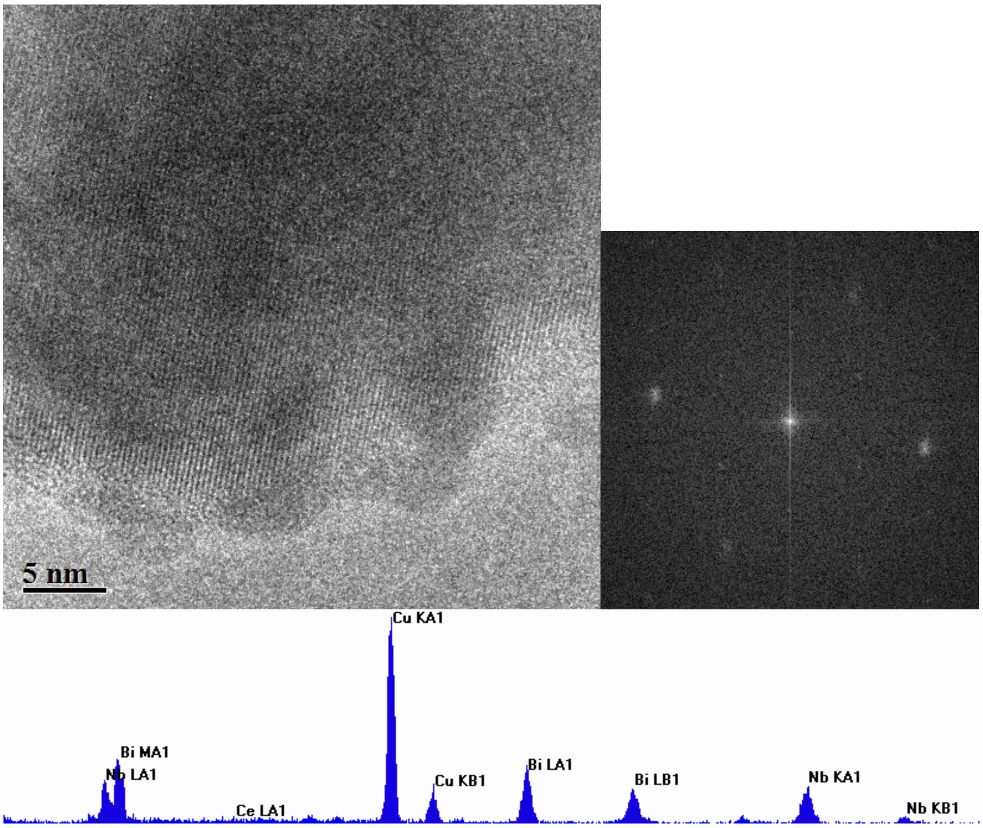

Figure 8.17. HRTEM micrograph of the $CeNb_2Bi$ oxide sample after calcination at 500 °C (l) with corresponding FFT (r). EDS spectra for the area shown below.

Further crystals of pyrochlore were seen in the $CeNbBi_2$ oxide sample after heating at 500 °C, with d-spacings of 6.08 Å and 3.07 Å being seen in the micrograph presented in Figure 8.18. These d-spacings correspond to the {111} and {222} lattice planes of pyrochlore. The region of pyrochlore particles seen in the micrographs were shown to contain all three metal ions by EDS. Crystals of perovskite and fluorite were also identified in this sample during examination in the microscope. Again, this data correlates well to the PXRD data.

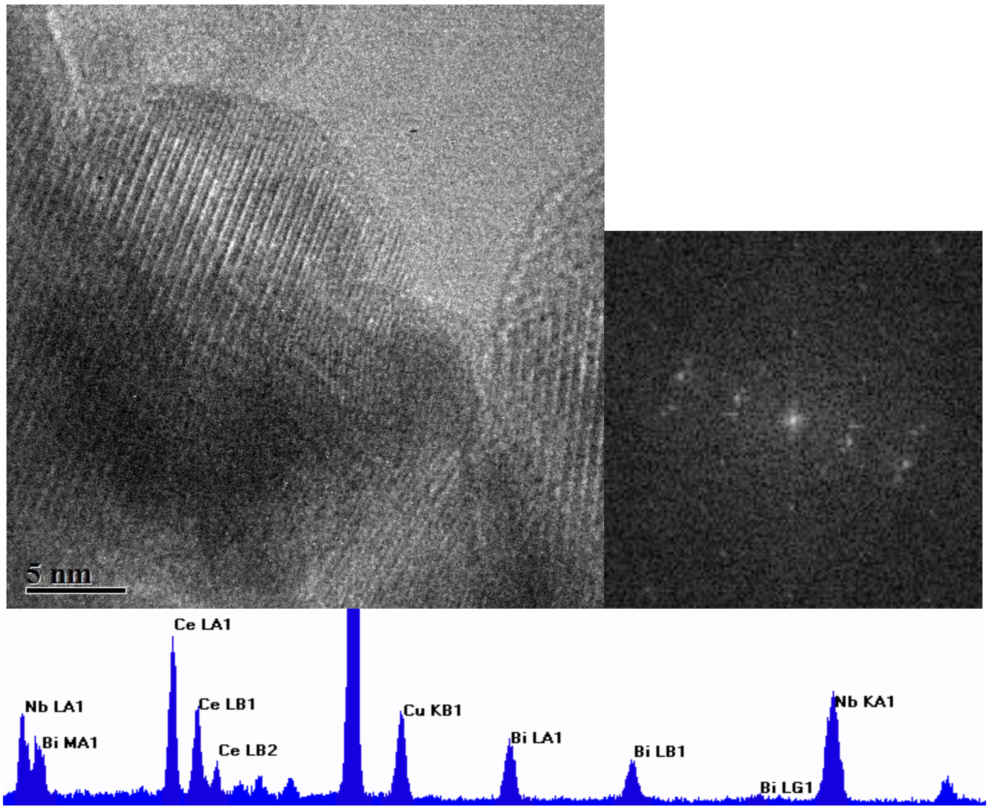

Figure 8.18. HRTEM micrograph of the CeNbBi$_2$ oxide sample after calcination at 500 °C (l) with corresponding FFT (r). EDS spectra for the area shown below.

Samples calcined at 700 °C showed evidence for fluorite, pyrochlore, BiNbO$_4$ and the quasi-crystalline phase in the microscope. This shows that at 700 °C, which is sufficient to form BiNbO$_4$, there is still not enough energy for the sample to fully crystallise. It can, therefore, be assumed that much higher temperatures are required to fully crystallise this sample.

An example of a fluorite particle observed in the CeNbBi oxide sample at 700 °C can be seen in Figure 8.19. The fluorite particle is larger than those seen at lower temperatures due to the sintering process. The d-spacing of 3.29 Å shows that the {111} plane is being observed. The EDS spectrum indicates that although the particle is clearly cerium rich, there are also peaks seen for niobium and bismuth, and the fluorite particle is therefore a quaternary oxide. A large region of pyrochlore was identified in the Ce$_2$NbBi oxide sample at 700 °C, Figure 8.20. Calculated d-spacings from the FFT of 5.95 Å and 3.06 Å corresponded to the {111} and {222} lattice planes. EDS determined that all three metal ions were also present in this large crystal.

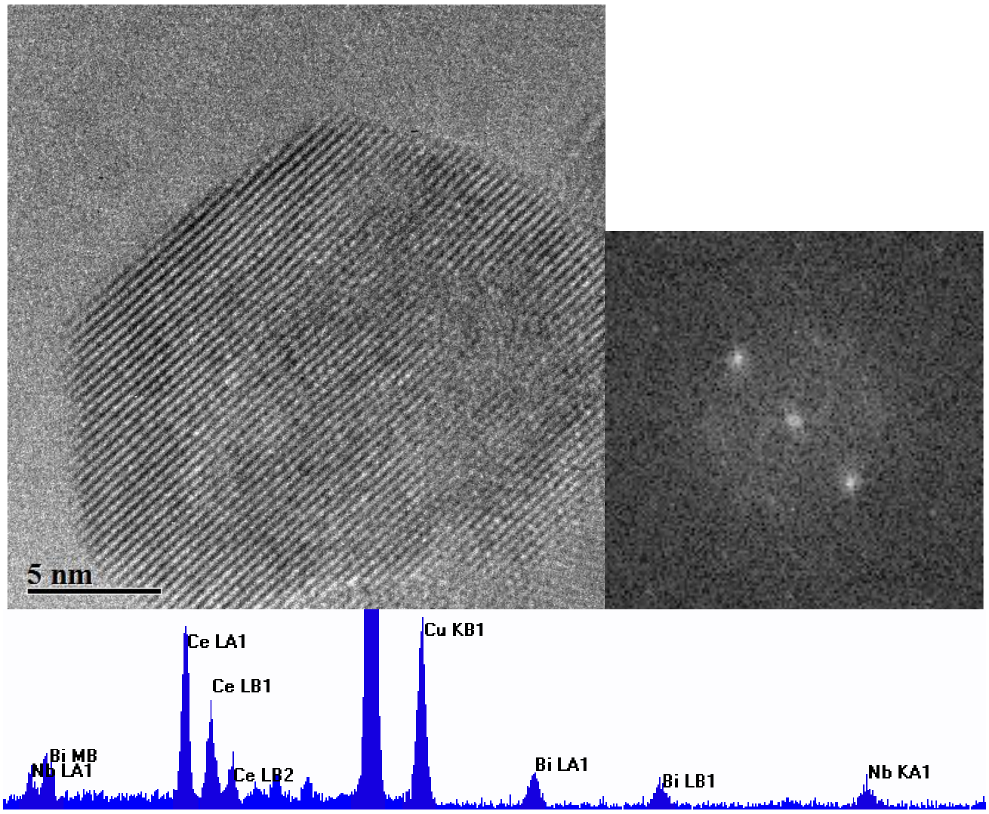

Figure 8.19. HRTEM micrograph of the CeNbBi oxide sample after calcination at 700 °C (l) with corresponding FFT (r). EDS spectra for the area shown below.

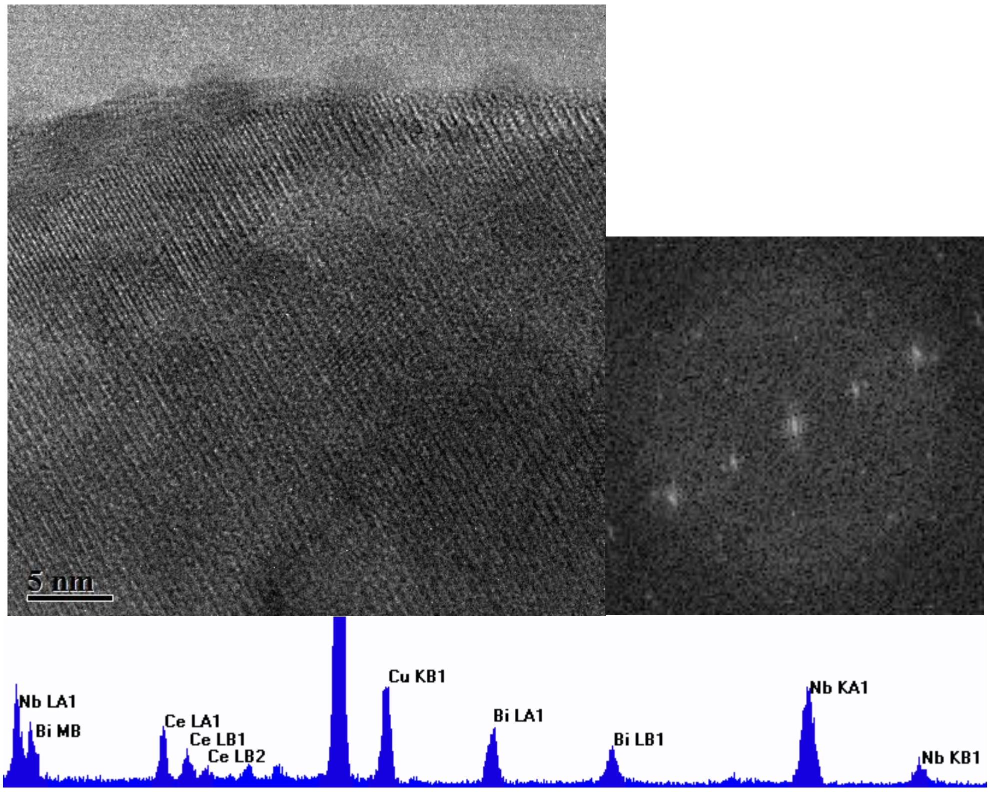

Figure 8.20. HRTEM micrograph of the Ce$_2$NbBi oxide sample after calcination at 700 °C (l) with corresponding FFT (r). EDS spectra for the area shown below.

Two examples of the phases seen in the CeNb$_2$Bi oxide sample heated at 700 °C can be seen in Figures 8.21 and 8.22. Firstly, the micrograph in Figure 8.21 shows a large fluorite particle with d-spacings of 3.14 Å and 2.87 Å observed, relating to the {111} and {200} lattice planes, with EDS confirming the presence of all three metal ions. The second phase observed in the microscope was BiNbO$_4$, of which there was evidence from the PXRD pattern. The EDS shows presence of only bismuth and niobium, therefore it is a pure phase with no cerium doping. The d-spacings calculated from the FFT are 5.91 Å and 3.05 Å indicating the {020} and {040} lattice planes of the low temperature BiNbO$_4$ phase.

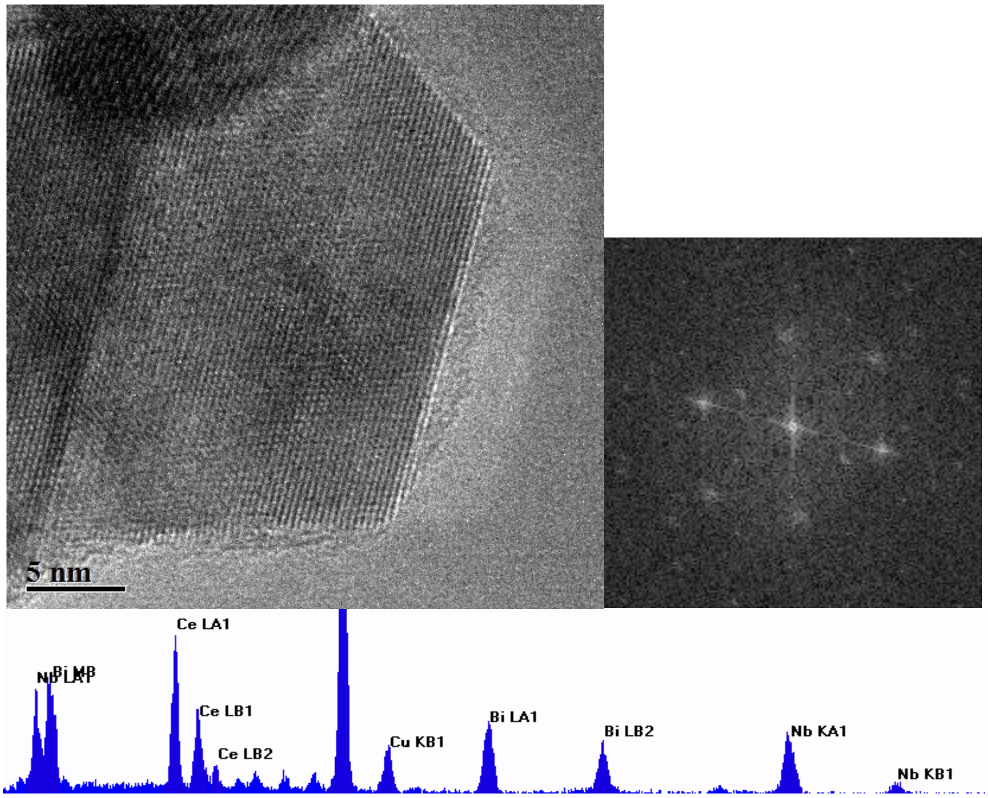

Figure 8.21. HRTEM micrograph of the CeNb$_2$Bi oxide sample after calcination at 700 °C (l) with corresponding FFT (r). EDS spectra for the area shown below.

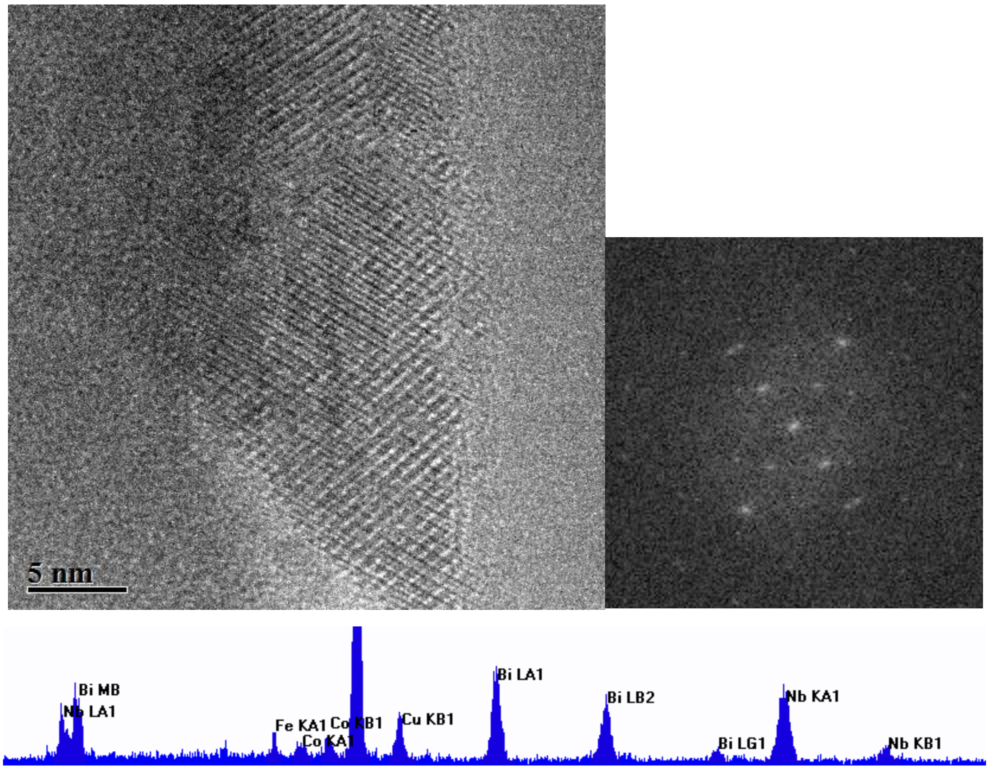

Figure 8.22. HRTEM micrograph of the CeNb$_2$Bi oxide sample after calcination at 700 °C (l) with corresponding FFT (r). EDS spectra for the area shown below.

A region of overlapping fluorite particles was seen in the CeNbBi$_2$ oxide sample, Figure 8.23, with d-spacings of 3.20 Å and 2.76 Å observed. These values correspond to the {111} and {200} lattice planes of fluorite.

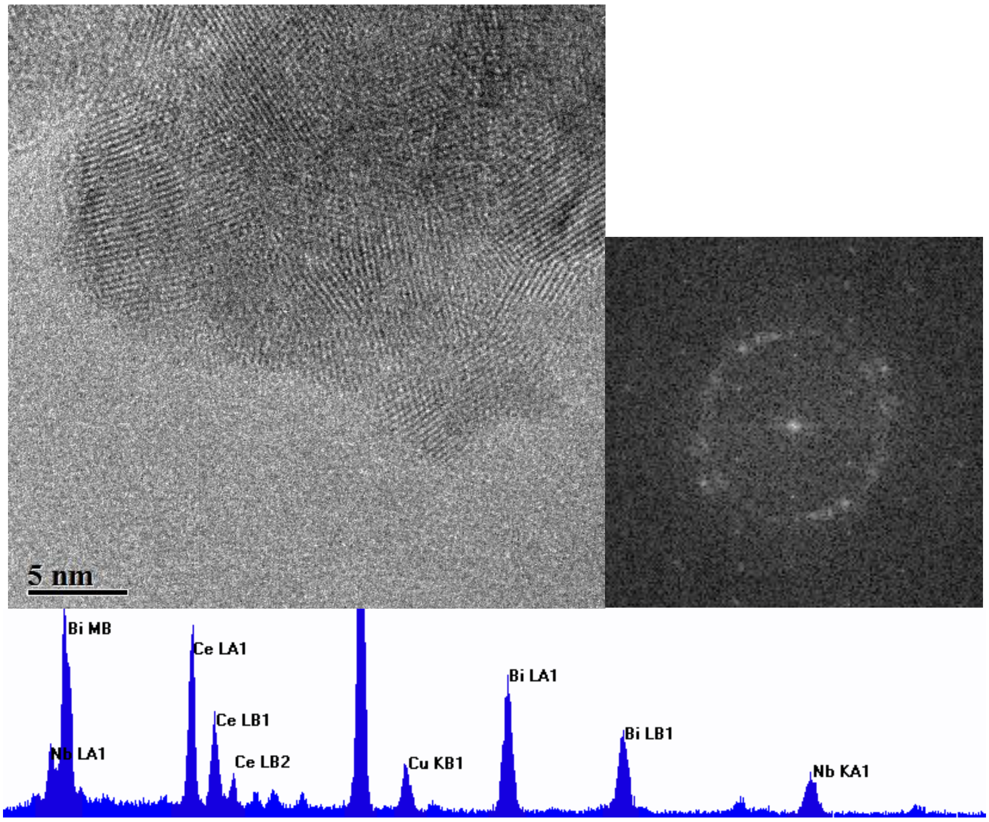

Figure 8.23. HRTEM micrograph of the CeNbBi$_2$ oxide sample after calcination at 700 °C (l) with corresponding FFT (r). EDS spectra for the area shown below.

The results of particles observed in the microscope correlate well to the phases seen in the PXRD patterns with the predominant phases in each sample being fluorite and pyrochlore, with evidence of BiNbO$_4$ in the CeNb$_2$Bi oxide sample heated at 700 °C.

8.4 XPS analysis

As with the ternary oxide samples, XPS analysis was carried out on the quaternary samples calcined at 350°C and 500 °C to see if the surface composition changed with heating. It can be seen from the results, Table 8.8, that the surface composition for each sample stays relatively constant with temperature; this is analogous to the ternary oxide systems. It has already been discussed that the overall composition determined by EDS varies markedly with temperature, therefore, it must be concluded that having a bismuth rich surface is very energetically favourable for these particles. It also follows that there is a strong degree of order in the surface structure of the particles. These results agree well with the findings of the ternary oxide systems where bismuth was also seen in excess at the surface. It is therefore shown that this remains true in the quaternary system. It must be the case that the dominant factor in determining the atomic arrangement of the particles is the lone pair of electrons on the bismuth ion, with the fact that niobium can accommodate a low coordination number being a secondary factor in the arrangement of ions.

Table 8.8. Comparison of cerium, bismuth and niobium percentages from XPS data for the Ce-Nb-Bi oxide nanoparticles after calcination at 350 °C and 500 °C, excluding the oxygen signal.

Sample Ce-Nb-Bi oxide	*Atom & Orbital*	*Binding Energy/ eV*	*Atomic Concentration /%*	*Std Dev*
CeNbBi at 350 °C	Bismuth 4f	160.08	67.37	0.34
	Niobium 3p	366.08	22.89	0.14
	Cerium 3d	884.08	9.76	0.29
CeNbBi at 500 °C	Bismuth 4f	160.08	69.24	0.17
	Niobium 3p	366.08	21.51	0.35
	Cerium 3d	883.08	9.24	0.32
Ce_2NbBi at 350 °C	Bismuth 4f	159.08	51.27	0.44
	Niobium 3p	365.08	33.60	0.16
	Cerium 3d	883.08	15.14	0.08
Ce_2NbBi at 500 °C	Bismuth 4f	160.08	64.41	0.43
	Niobium 3p	366.08	25.14	0.53
	Cerium 3d	883.08	10.44	0.45
$CeNb_2Bi$ at 350 °C	Bismuth 4f	159.08	53.73	0.24
	Niobium 3p	365.08	38.96	0.03
	Cerium 3d	883.08	7.32	0.11
$CeNb_2Bi$ at 500 °C	Bismuth 4f	160.08	53.48	0.24
	Niobium 3p	365.08	39.90	0.47
	Cerium 3d	883.08	6.58	0.29
$CeNbBi_2$ at 350 °C	Bismuth 4f	159.08	75.90	0.03
	Niobium 3p	365.08	18.41	0.21
	Cerium 3d	883.08	5.70	0.09
$CeNbBi_2$ at 500 °C	Bismuth 4f	160.08	81.51	0.67
	Niobium 3p	366.08	13.77	0.64
	Cerium 3d	883.08	4.72	0.27

Likewise, the Ce(III) and Ce(IV) percentages remain relatively constant at different temperatures, Table 8.9.

Table 8.9. Comparison of the Ce(III) and Ce(IV) percentages across the Ce-Nb-Bi oxide system.

Sample	*% Ce^{3+}*	*STDEV*	*%Ce^{4+}*	*STDEV*
CeNbBi at 350 °C	13.75	3.51	86.25	3.51
CeNbBi at 500 °C	19.21	6.33	80.79	6.33
Ce_2NbBi at 350 °C	21.94	4.05	78.06	4.05
Ce_2NbBi at 500 °C	11.74	0.35	88.26	0.35
$CeNb_2Bi$ at 350 °C	19.00	2.08	81.00	2.08
$CeNb_2Bi$ at 500 °C	11.72	1.58	88.28	1.58
$CeNbBi_2$ at 350 °C	18.84	3.40	81.16	3.40
$CeNbBi_2$ at 500 °C	13.99	5.40	86.01	5.40

8.5 Bulk synthesis of the quaternary system

A series of experiments were carried out in order to see if any quaternary oxide particles could be synthesised using a bulk solid state method. The same proportions of cerium, niobium and bismuth used in the resin-gel method were combined to form four samples of varying compositions. Oxides of the metals being investigated were ground and heated at 850 °C. Full experimental details can be seen in Chapter 3.

It was not expected that a quaternary oxide would form in this case, due to the high synthesis temperatures and the lack of lattice relaxation in bulk materials, and this was found to be the case. By examining the PXRD patterns of the four samples synthesised, Figure 8.24, it was found that a mixture of binary and ternary oxides were formed. The patterns for the CeNbBi oxide, Ce_2NbBi oxide and $CeNb_2Bi$ oxide all match well with only slightly differing peak intensities in some instances, to be expected as the proportions of the phases will vary depending on the quantity of each metal. The peaks for these three samples were identified by X'pert HighScore Plus and comparison with the literature as CeO_2, Bi_2O_3, T-Nb_2O_5, $BiNbO_4$ and $CeNbO_4$. The patterns show that the phases formed are highly crystalline with intense, sharp peaks being recorded. Unlike the nanoparticle samples, there was little background or peak broadening. The pattern for the $CeNbBi_2$ oxide sample showed the presence of different phases due to the increased proportion of bismuth. These were identified as $Bi_5Nb_3O_{15}$ and Bi_3NbO_7 as well as CeO_2, $CeNbO_4$ and $BiNbO_4$. From these results, it can be seen that reacting the oxides of bismuth, cerium and niobium at high temperature favours the formation of the ternary oxides.

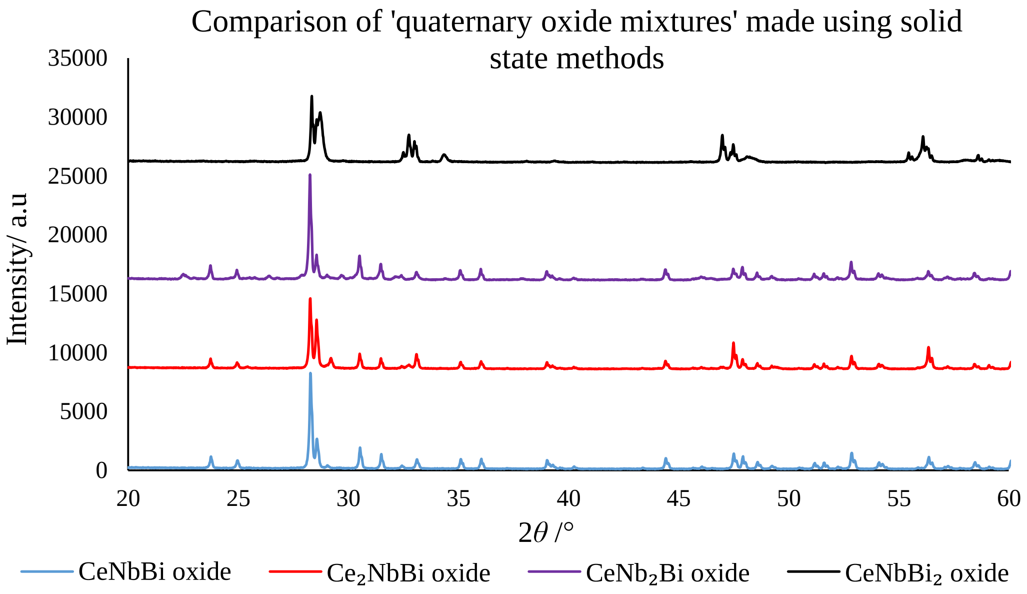

Figure 8.24. PXRD patterns for the bulk 'quaternary oxides' synthesised.

Imaging of the samples proved difficult due to the size and thickness of the particles meaning that fringes could not be seen, and therefore confirmation of phases seen in the PXRD could not be carried out.

8.5 EDS Mapping

In order to further verify that particles had been formed containing all three metals, EDS mapping was carried out on the FEG Tecnai Osiris 80-200 microscope in the Department of Materials Science & Metallurgy at the University of Cambridge. The machine is equipped with a FEG and was run in STEM mode. Four EDS detectors are spaced evenly around the column for high collection efficiency of X-rays.

The CeNbBi oxide sample heated at 700 °C was examined in the STEM. This sample was chosen as it was thought that as the particles were slightly larger than the samples calcined at 700 °C, it would be easier to collect more X-rays from these particles, thereby giving more meaningful data. The results showed good evidence for cerium, bismuth and niobium being present in a range of oxide particles examined. This further strengthens the model of a new quaternary oxide system being formed.

The first area scanned, Figure 8.25, showed a region of agglomerated nanoparticles resembling the fluorite particles seen previously in the JEOL HRTEM. A suitable particle was chosen to map and can be seen within the orange box. Another region was highlighted, shown in a yellow box, which was used to correct any sample drift. The EDS mapped particle can be seen in Figure 8.26. The EDS maps show clearly that atoms of cerium, bismuth and niobium are contained within the particle. It appears that the particle has a high concentration of cerium as the blue colour is the densest throughout the whole particle. The bismuth and niobium ions are dispersed reasonably well throughout the particle but the colour is not as dense as for cerium.

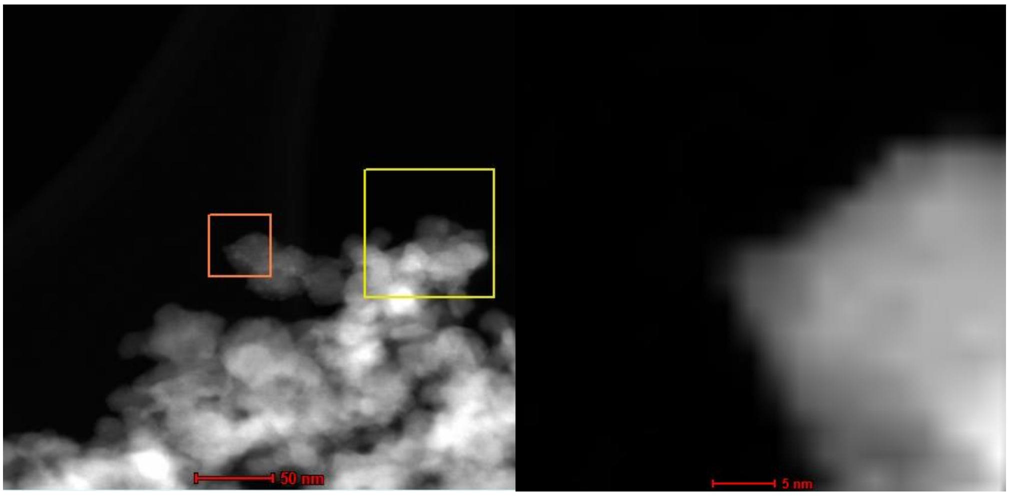

Figure 8.25. Low magnification survey scan of an area of nanoparticles in the CeNbBi oxide sample heated at 700 °C (l). The orange box shows the region to be mapped by EDS and the yellow box shows the area used for relative drift correction. The image on the right show the high magnification scan of the nanoparticle to be mapped by EDS.

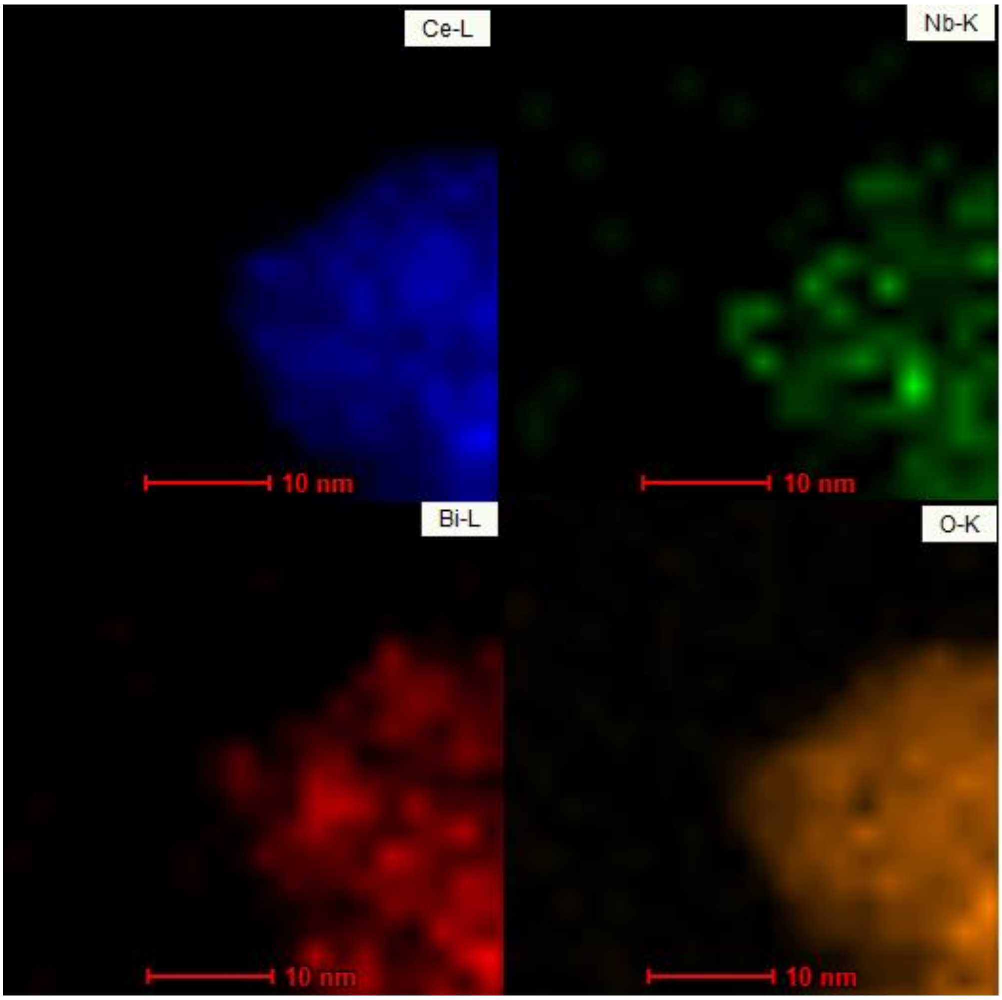

Figure 8.26. EDS maps for the nanoparticle in the CeNbBi oxide sample heated at 700 °C scanned in Figure 8.25. It can be seen that cerium, niobium and bismuth are present throughout the particle.

The second region scanned, along with the specific particle to be mapped, can be seen in Figure 8.27. The agglomerated region of particles and particle size is similar to the area seen in Figure 8.25. The mapped particle, Figure 8.28, shows very similar results to those seen above; the particle contains all three metals but is cerium rich. The same distribution of ions is also seen. The results give further evidence that an ideal solid solution has not been formed as there are regions where the concentration of one ion type dominates, but there is less elemental segregation than might be expected from the XPS data alone.

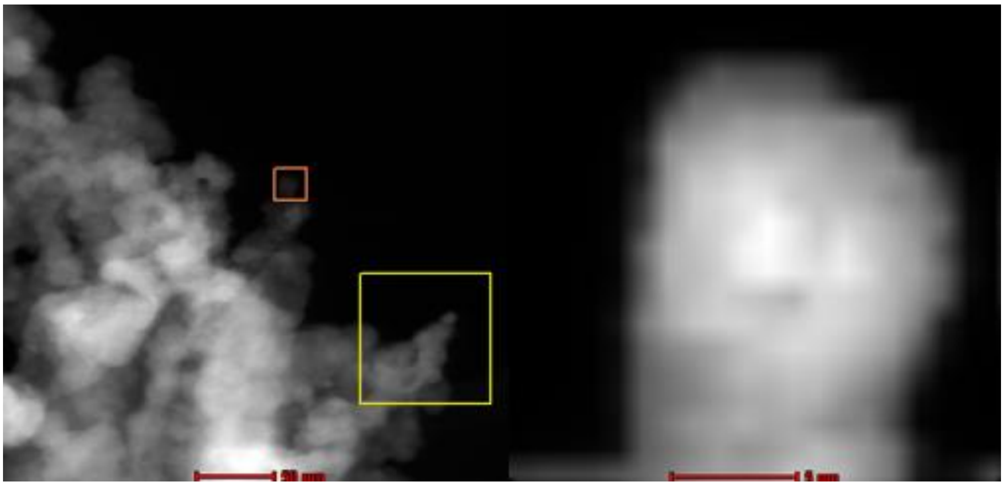

Figure 8.27. Low magnification survey scan of an area of nanoparticles in the CeNbBi oxide sample heated at 700 °C (l). The orange box shows the region to be mapped by EDS and the yellow box shows the area used for relative drift correction. The image on the right show the high magnification scan of the nanoparticle to be mapped by EDS.

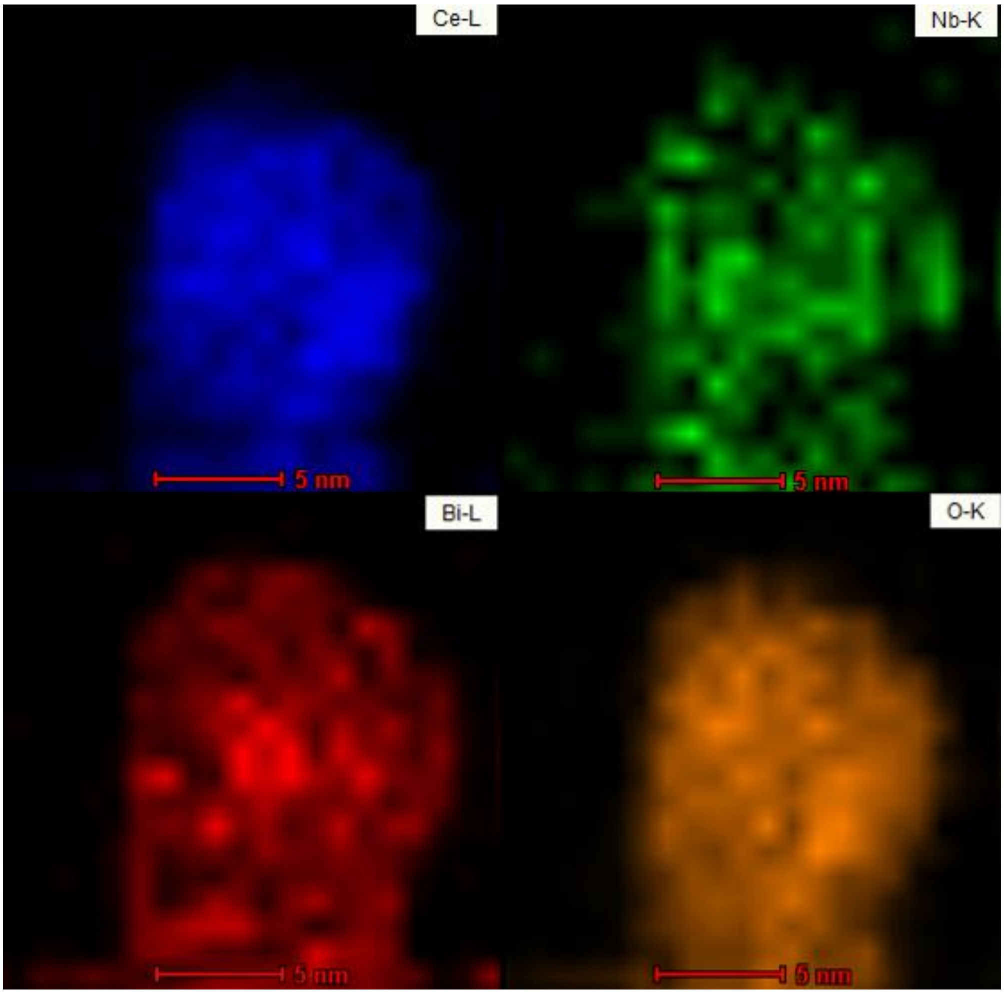

Figure 8.28. EDS maps for the nanoparticle in the CeNbBi oxide sample heated at 700 °C scanned in Figure 8.27. It can be seen that cerium, niobium and bismuth are present throughout the particle.

A further group of agglomerated particles in the CeNbBi oxide sample heated at 700 °C were scanned, and can be seen in Figure 8.29, with the chosen mapped particle from the area seen in Figure 8.30. Results compare well to the previous two particles. This implies that all the particles of this type are fairly uniform, being comprised of a higher proportion of cerium and less of niobium and bismuth.

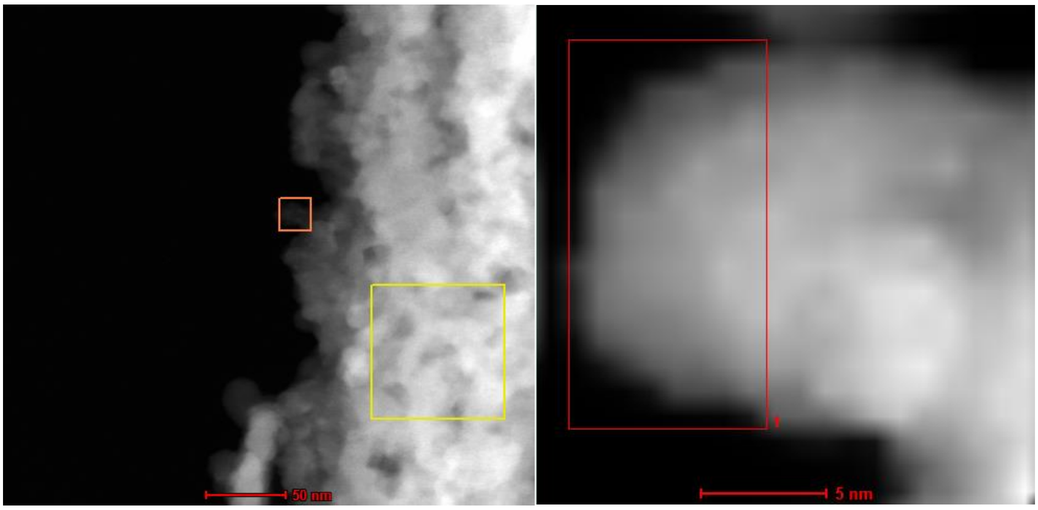

Figure 8.29. Low magnification survey scan of an area of nanoparticles in the CeNbBi oxide sample heated at 700 °C (l). The orange box shows the region to be mapped by EDS and the yellow box shows the area used for relative drift correction. The image on the right show the high magnification scan of the nanoparticle to be mapped by EDS.

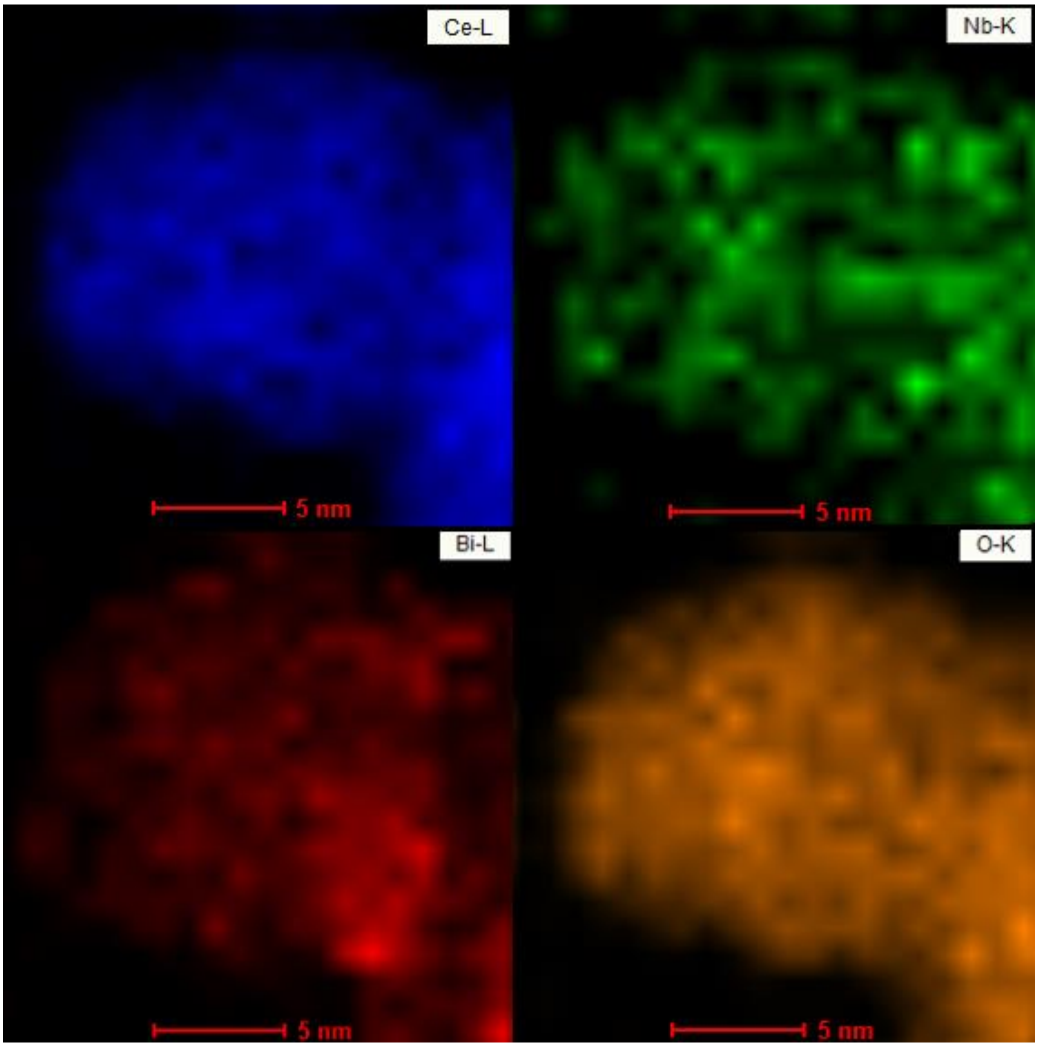

Figure 8.30. EDS maps for the nanoparticle in the CeNbBi oxide sample heated at 700 °C scanned in Figure 8.29. It can be seen that cerium, niobium and bismuth are present throughout the particle.

The final area analysed in this sample of the CeNbBi oxide sample heated at 700 °C is seen in Figure 8.31. It appears to be a different phase to the previous three areas, as a large (approx. 500 nm) crystal is seen rather than the small agglomerated particles seen earlier. The EDS maps of the area, Figure 8.32, show that in contrast to the previous maps, this particle is rich in bismuth and niobium, although cerium is still present throughout the particle. Although no electron diffraction was carried out on this crystal, it could be postulated that the area observed was a pyrochlore or perovskite crystal as seen in fringe spacings in the JEOL HRTEM.

It can be concluded from the EDS mapping results that the particles generally contain the three metal ions, regardless of what phase is formed, but in different proportions depending on the crystal structure. This is good evidence for the different behaviours observed in a nanoparticulate system in comparison with the bulk, in this case largely influenced by the more relaxed lattice.

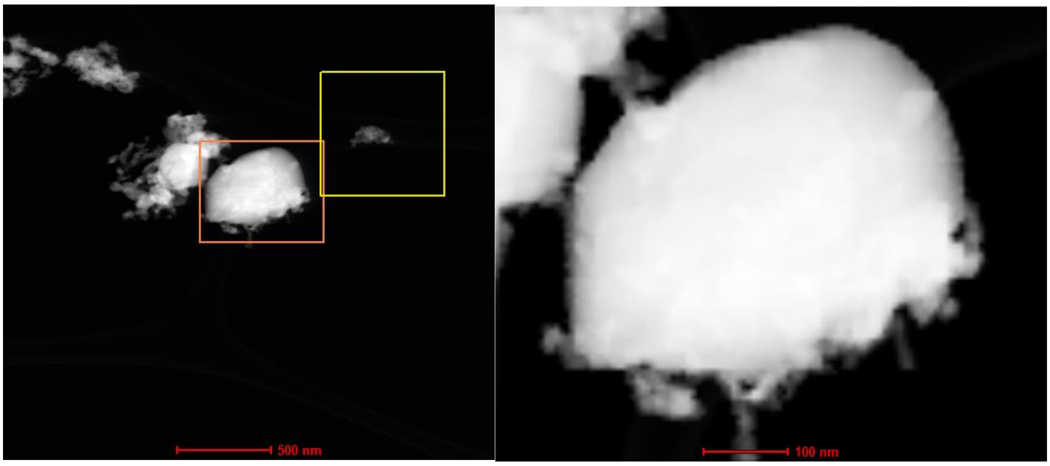

Figure 8.31. Low magnification survey scan of an area of nanoparticles in the CeNbBi oxide sample heated at 700 °C (l). The orange box shows the region to be mapped by EDS and the yellow box shows the area used for relative drift correction. The image on the right show the high magnification scan of the nanoparticle to be mapped by EDS.

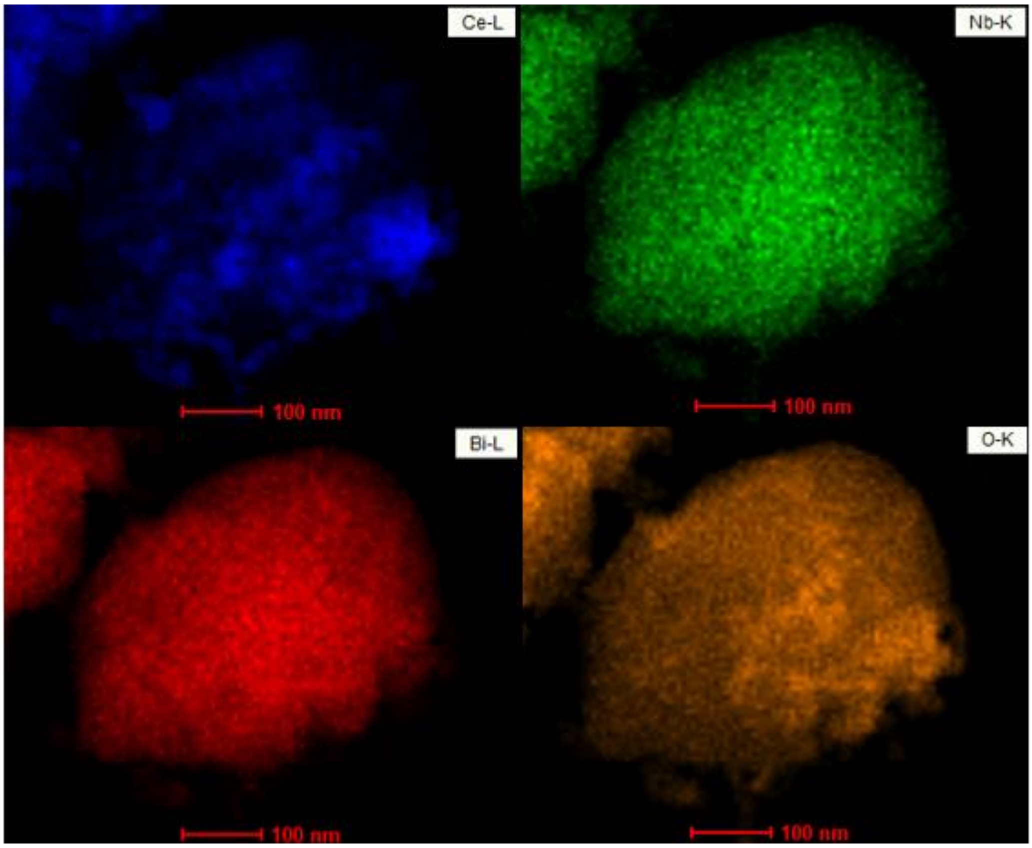

Figure 8.32. EDS maps for the nanoparticle in the CeNbBi oxide sample heated at 700 °C scanned in Figure 8.31. It can be seen that cerium, niobium and bismuth are present throughout the particle, but in a different ratio to that observed in the smaller particles of a different phase.

8.6 Conclusions

It can be seen from these results that it is possible to synthesise a quaternary mixed metal oxide in nanoparticle form, containing cerium, bismuth and niobium ions, using the resin-gel method. The PXRD data shows that when these three metal ions are combined, a fluorite structure is formed preferentially, with the ions in what appears to be a limited solid solution. It is perhaps not surprising that this crystal structure is adopted to accommodate the different metal ions particularly from an ionic size perspective. In the nanoparticle form the crystal lattice relaxes making it easier for the larger Bi^{3+} ion to be substituted into the CeO_2 lattice. As Nb^{5+} has a smaller ionic radius than Ce^{3+} it is easily able to fit into the lattice. In both cases the anion lattice appears to be capable of distorting to accommodate these changes. However, this capability must be limited as when the concentration of niobium is increased in the $CeNb_2Bi$ oxide sample, a large proportion of a second phase is formed. Previous studies suggested that these phases would be perovskite and pyrochlore units. It is energetically favourable for the perovskite units to form because the oxygen anions then occupy the octahedral interstices rather than the smaller tetrahedral interstices as in fluorite, contracting the structure and making it more favourable for the small Nb^{5+} ions. The preference for pyrochlore units forming is possibly due to its ability to accommodate several cation sizes and charges, as well as its structural relationship to the fluorite structure. The d-spacings calculated from the HRTEM micrographs support this theory as niobium rich particles were found to have d-spacings corresponding well to the pyrochlore and perovskite structures. However, it is not just when there is excess niobium that the perovskite and pyrochlore phases form, as these phases were seen across all compositions. This would suggest that even a small amount of niobium is enough to force the formation of these other phases in addition to the fluorite units. It is probable that the non-uniformity of the distribution of metal ions forces the formation of several different phases due to the size and charge of the different ions.

All samples showed some evidence of quasi-crystalline regions even at calcination temperatures of 700 °C. The most likely reason for this is that even higher temperatures are needed to ensure the sample is fully crystalline. A second theory, however, is that in some regions, the long range ordering of the cations may be lost even if the oxygen ions are still ordered. This is possible as the HRTEM micrographs only show the arrangement of the cations and not of the oxygen ions as the metal-oxygen separation is beyond the resolution limit of the microscope used.

On the whole, the particles remained stable over the temperature ranges 350 °C to 700 °C with the same fluorite, pyrochlore and perovskite phases being seen at all temperatures. As the temperature increased so did the size of the crystals in each sample due to sintering. This also affected the PXRD pattern, resulting in narrower and sharper peaks. EDS showed that the particle composition did change with heating but not in a systematic way, suggesting that the nanoparticles have more fluid like properties which allow ionic movement. However, the XPS data, in contrast, showed that the surface composition varied very little with the preference being for a bismuth enriched surface.

In contrast to the resin-gel method, when an attempt at synthesising quaternary particles using a solid state method was carried out, binary and ternary known oxide phases were formed with no evidence for a quaternary system. It should be discussed that it is highly plausible that the nanoparticles formed are not equilibrium assemblages. Given that they are produced by decomposition of a resin-gel, it is likely that initially they are far from the equilibrium state. This could be the reason why at lower temperature the fluorite-like phase tends to predominate as this structure seems to be the most ‘adaptable’ to cations of differing size and valency. As the annealing temperature is raised, however, movement of cations allows both crystal growth and the nucleation of more complex structures, such as pyrochlore, which are suitable for accommodating cations of differing size. Presumably, if heating at higher temperatures continued, the phase distribution would ultimately be identical to that found in the bulk preparations. What is therefore witnessed in these nanoparticle species if a succession of metastable states, where the particles adapt a ‘compromise’ structure which is forced on them by the low temperature synthesis.

Overall it can be seen that the Bi_2O_3-CeO_2-Nb_2O_5 nanoparticulate system is highly complicated, most likely due to small energy barriers between phases. Therefore, it was seen that a range of phases and arrangements of atoms is possible. However, it can also be said from XPS evidence, there is still a strong preference for certain atomic arrangements such as bismuth dominating the surface sites. This means that there are still energetic factors which make these ordered arrangements preferable and prevent an ideal solid solution being formed.

9. Computational modelling of particles

9.1 Introduction to modelling

In addition to the practical work completed in preparation of this thesis, preliminary computational calculations were attempted in order to substantiate the results already presented, and to help further explain the energetic interactions within the mixed metal oxide systems. The calculations performed were based on simple ionic interactions between the ions in the crystal lattice. The programme was written by Dr. D.A. Jefferson in Visual Basic, which enabled the total bond energy of a particle to be calculated by summing the ionic interactions between each ion in the lattice and its nearest neighbour. Models of the simulated particles could also be constructed.

9.2 Results from simulations of fluorite type structures

Initially, lattice energies were calculated for pure spherical CeO_2 and Bi_2O_3 particles of varying sizes to compare the relative values of each phase. The particles were neutralised, either by introducing random oxygen vacancies, or by reducing the appropriate number of Ce^{4+} ions to $Ce^{3+.}$ The results of these calculations can be seen in Figure 9.1. The data shows that, as expected, the lattice energy of the CeO_2 clusters was substantially lower than for the Bi_2O_3 clusters. This is due to the extra ionic attraction between Ce^{4+} and O^{2-} compared with Bi^{3+} and O^{2-}, making it a stronger attraction. It was also shown that the particle energy becomes much more favourable for larger particles of each phase than for smaller particles, before plateauing.

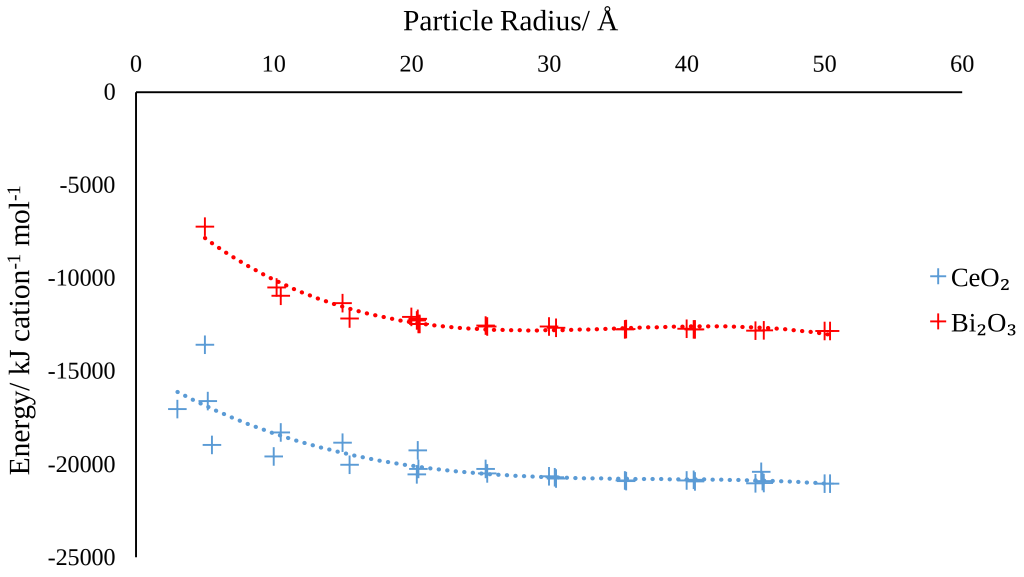

Figure 9.1. Plot showing the variation in total particle bond energy with particle size for CeO_2 *and* Bi_2O_3*.*

Calculations on mixed metal oxide nanoparticles were carried out next. This initially involved comparing the relative lattice energy of a cerium oxide particle coated in a shell of bismuth oxide with the reverse: having a bismuth oxide core covered in a shell of cerium oxide. It was expected that having a layer of bismuth oxide on the surface would be energetically favourable, as this was observed experimentally from XPS data. There are several reasons for why this should be the case. The first reason is that the charge gradient is more favourable if the 3+ ion is on the surface. The second argument is a steric one with respect to the bismuth lone pair; the most logical place for the bismuth to be situated is at the surface of the particle as this will disrupt the ionic arrangement the least, as the bismuth lone pair of electrons will interact less with the rest of the particle. In addition, the oxygen vacancies associated with bismuth ions should be more stable at the surface.

The results for the energy calculations of particles with a bismuth oxide shell and a cerium oxide core are seen in Table 9.1. Firstly it should be noted that all values are more negative than for the pure Bi_2O_3 particles showing these mixed oxide particles are more energetically favourable. This is due to the Ce^{4+} ions incorporated in the structure which increase the bond enthalpy. It should also be noted that all particles had a higher energy than pure CeO_2, due to the decreased ionic interaction of Bi^{3+}, with two exceptions, those particles of 35.5 Å radii and bismuth oxide shells of thickness 5 and 10 Å. In this case it would appear that the energetic gain from the lower field gradient and the relatively low ratio of bismuth:cerium ions makes these compositions and arrangements more favourable. In all the other particles, it seems that the purely ionic interactions outweigh any benefit from the lower field gradient.

Secondly, the energetic trends in particle size will be discussed. As the particle size increases from 10 Å to 50 Å the bond enthalpy generally seems to decrease implying that the larger particles are more energetically favourable. This is what would be expected as with increased particle growth, there are more ionic interactions.

Lastly, it can be seen that generally the total bond energy increases as the bismuth shell thickness increases. The only exception to this is the case of the 35 Å radius particles, where the example with a 10 Å Bi_2O_3 shell is marginally more stable than that with a 5 Å shell. This trend is probably because as the bismuth shell thickness increases, the ratio of 3+ ions: 4+ ions in the particle increases. This means that the average bond enthalpy will be less negative, making the particle higher in energy.

Table 9.1. Results of the energy calculations for particles with a bismuth oxide shell and a cerium oxide core. The results are shown for a variety of shell thicknesses and total particle sizes.

Bismuth oxide shell thickness/ Å	*Cerium oxide core radius/ Å*	*Particle radius/ Å*	*N (Bi)*	*N (Ce 4+)*	*N (Ce 3+)*	*N(Bi)/N(Ce)*	*N(O)*	*Charge*	*Total bond energy/ kJ cation^{-1} mol^{-1}*
5	15.0	20.0	484	336	0	1.44	1398	0	-14375
10	10.0	20.0	716	104	0	6.88	1282	0	-11464
5	30.5	35.5	1720	3004	0	0.57	8588	0	-21141
10	25.5	35.5	3000	1698	26	1.74	7935	0	-22346
15	20.5	35.5	3796	926	2	4.09	7549	0	-14380
20	15.5	35.5	4364	360	0	12.12	7266	0	-13376
5	45.0	50.0	3496	9604	0	0.36	24452	0	-18936
10	40.0	50.0	6392	6708	0	0.95	23004	0	-17075

A cross-sectional model of the $Bi_{3796}Ce^{4+}_{926}Ce^{3+}_{2}O_{7549}$ particle constructed from a CeO_2 core and Bi_2O_3 shell is shown in Figure 9.2.

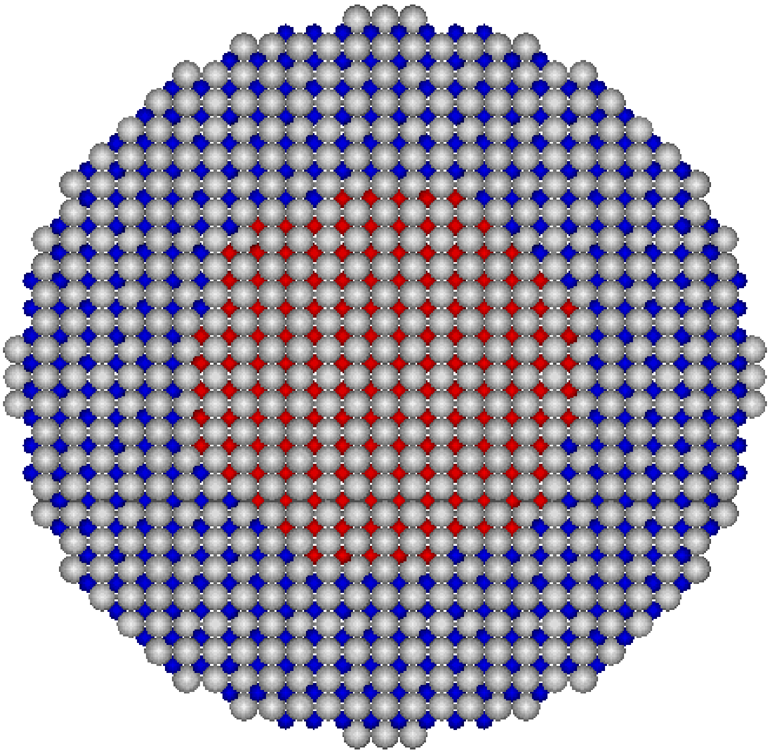

Figure 9.2. Cluster of composition $Bi_{3796}Ce^{4+}_{926}Ce^{3+}_{2}O_{7549}$ *with a* CeO_2 *core and* Bi_2O_3 *shell. Bismuth ions shown in blue, cerium in red and oxygen in grey.*

The results for the energy calculations of particles with a cerium oxide shell and a bismuth oxide core are seen in Table 9.2. This was expected to be the less favourable arrangement for reasons previously discussed. There does not seem to be a clear trend of bond enthalpy variation with particle size or CeO_2 shell thickness. It can be seen, however, that when the ratio of bismuth:cerium ions is particularly low, the bond enthalpy is noticeably lower. Therefore, it can be deduced that as the overall energy of the particles is controlled mainly by the ionic interactions of the +3 and +4 cations with the oxygen anions, the primary reason for the bismuth preferentially occupying surface sites is due to the oxygen vacancies having a lower energy near the surface. On average there does not seem to be a clear preference for a surface arrangement of bismuth or cerium ions from the data generated in these calculations. It appears as though a range of atomic orderings are possible with a variety of accessible energies between them. A possible reason for the bismuth rich surfaces seen experimentally in the Bi-Ce oxide nanoparticles is the relative growth rates of the two phases. It may well be that the kinetics of the crystal growth mechanism for the CeO_2 phases allows this ‘core’ to form first with a Bi_2O_3 ‘shell’ growing around this.

Table 9.2. Results of the energy calculations for particles with a cerium oxide shell and a bismuth oxide core. The results are shown for a variety of shell thicknesses and total particle sizes.

Cerium oxide shell thickness/ Å	*Bismuth oxide core radius/ Å*	*Particle radius/ Å*	*N (Bi)*	*N (Ce 4+)*	*N (Ce 3+)*	*N(Bi)/N(Ce)*	*N(O)*	*Charge*	*Total bond energy / kJ cation^{-1} mol^{-1}*
5	15.0	20.0	336	484	0	0.69	1472	0	-15204
10	10.0	20.0	104	716	0	0.15	1588	0	-14810
5	30.5	35.5	2981	1720	0	1.73	7911	1	-15502
10	25.5	35.5	1724	3000	0	0.57	8586	0	-17838
15	20.5	35.5	922	3796	0	0.24	8975	0	-19256
20	15.5	35.5	345	4364	0	0.08	9245	1	-20265
5	45.0	50.0	9601	3496	0	2.75	21393	1	-14873
10	40.0	50.0	6687	6392	0	1.05	22815	-1	-14693

A cross-sectional model of the $Ce_{6392}Bi_{6687}O_{22815}$ particle constructed from a Bi_2O_3 core and CeO_2 shell is shown in Figure 9.3. This model is made up of a 10 Å CeO_2 shell and a 40 Å radius Bi_2O_3 core making the total particle radius 50 Å.

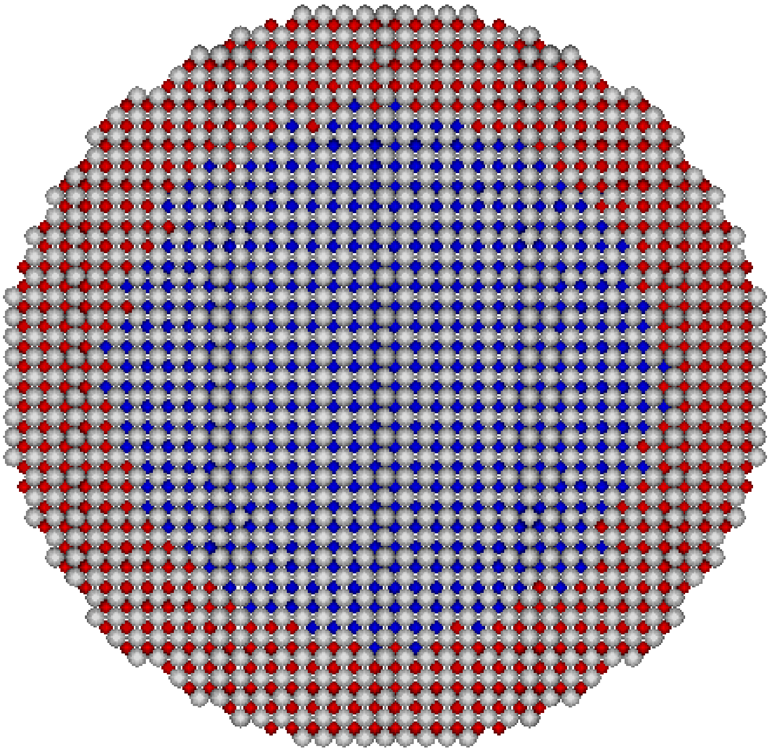

Figure 9.3. Cluster of composition $Ce_{6392}Bi_{6687}O_{22815}$ model with a Bi_2O_3 core and a CeO_2 shell. Bismuth ions shown in blue, cerium in red and oxygen in grey.

Lastly, calculations were performed for a random distribution of bismuth ions throughout the CeO_2 structure. The appropriate number of bismuth atoms were randomly generated throughout the structure with the particles then being neutralised through oxygen vacancy generation. It was expected that this arrangement would give a higher energy value in comparison to the previous two shell arrangements. For each particle radius, an average of 10 calculations were performed to account for any random arrangements which might give a particularly high or low energy depending on where the Bi^{3+} ions had been placed in the structure. The results for the random mixture of Bi^{3+} in the CeO_2 lattice are seen in Table 9.3. It can be seen that the same general trend of decreasing bond energy with particle size remains true in this model. In addition, if each particle radius in the random model is compared to the relative bismuth oxide 'shell' and cerium oxide 'core' models it is seen that the latter predicts a more negative total bond energy. This means that the 'core and shell' models provide the more favourable atomic arrangement. This helps provide an energetic explanation as to why the given arrangements were seen in the mixed oxide nanoparticle experimentally.

Table 9.3. Results of energy calculations for a random mixture of Bi^{3+} ions in the CeO_2 structure.

Particle radius/ Å	*N(Bi)*	*N(Ce)*	*N(O)*	*Charge*	*Mean bond energy / kJ cation^{-1} mol^{-1}*	*Std Dev*
20.0	484	336	1398	0	-14369.0	142.57
35.5	1720	3004	8588	0	-17328.6	31.48
50.0	3496	9604	24452	0	-18341.8	5.21

As has previously been discussed, it might be predicted that an ideal solid solution would be the most energetically favoured arrangement due to the maximised entropy of the system. In fact, if the entropy is calculated for a random mixture of Bi^{3+} ions in the CeO_2 structure, it is apparent that the entropic factor is negligible in comparison to the enthalpic contribution to the overall particle energy. Table 9.4 presents the calculated values for configurational entropy of the particles described using Boltzmann's famous equation:

$$S = K_b lnW$$

Table 9.4. Configurational entropy calculations for a random mixture of Bi^{3+} ions in the CeO_2 structure.

Particle radius/ Å	N(Bi)	N(Ce)	N(O)	Charge	Configurational entropy/ kJ K^{-1} mol^{-1}
20.0	484	336	1398	0	4.64
35.5	1720	3004	8588	0	25.28
50.0	3496	9604	24452	0	63.21

It can, therefore, be seen that the enthalpic contributions of the ions in the crystal lattice far outweigh any entropic gain from having a more random distribution of cations. A cross-sectional model of the $Bi_{1720}Ce_{3004}O_{8588}$ particle constructed from a random distribution of Bi^{3+} ions in a CeO_2 lattice is shown in Figure 9.4. This model has a particle radius of 35.5 Å.

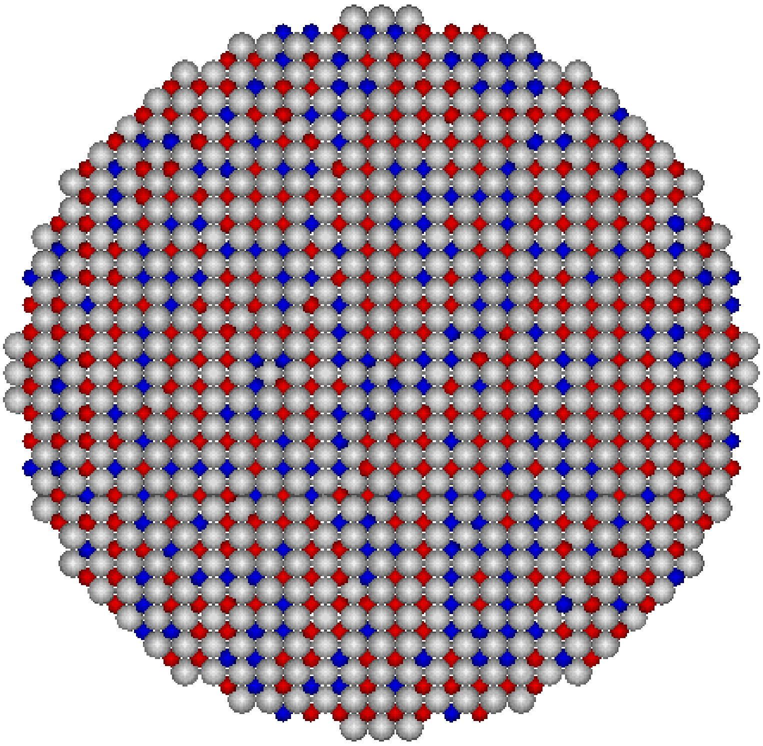

Figure 9.4. Cluster of composition $Bi_{1720}Ce_{3004}O_{8588}$ with bismuth ions distributed randomly through the CeO_2 lattice. Bismuth ions in blue, cerium in red and oxygen in grey.

9.3 Conclusions

The preliminary computational results for the mixed oxide particles in the Ce-Nb-Bi system show that there are significant energy differences between different arrangements of the cations, which must play a part in how they arrange themselves in the structure. It is clear that these mixed oxides are highly complicated systems with a range of variables which need to be taken into account to help explain the arrangement of the cations. In addition to the lattice energy arguments for any given arrangement, the electronics of the cations involved and the kinetics of formation must help dictate the actual structure observed. One theory for the segregation of the ions in the oxide structure is that the CeO_2 core forms first due to its very negative, and therefore favourable, lattice energy, then the Bi_2O_3 structure forms around this. Another point which should be noted is that the curvature of the sphere changes with radius, meaning that the interface of the ‘core’ and ‘shell’ may not be consistent across these calculations. This could account for some of the subtle differences in the calculated bond enthalpies.

These initial attempts to model the mixed oxide systems have shown that it is possible to draw some conclusions about the energetics of the particles which agree with experimental results. For example, segregation of the ions via a ‘core and shell’ model can significantly affect the overall bond enthalpy of the particle. This supports the experimental findings of having a more bismuth rich surface in the Bi-Ce mixed oxide particles. However, it is clear that there are many other variables which need to be systemically changed in order to fully understand how and why the cations seem to segregate experimentally, such as the thickness of the shell, the ratio of 3+:4+ ions and the number of oxygen vacancies. There are many further calculations which need to be performed not only on the fluorite type particles, but also on the pyrochlore type structures, in order to better understand the energetics of the Ce-Nb-Bi mixed oxide system.

10. Conclusions and further work

10.1 General overview

The work presented in this thesis has proved that mixed oxide nanoparticles containing bismuth, cerium and niobium can certainly be formed using the resin-gel method. These particles have been analysed and characterised via HRTEM, EDS, XPS and PXRD to confirm which phases were present in each sample and to calculate the elemental compositions. It has also been seen, through cell parameter calculations, that the crystal lattice structures in the nanoparticles are more relaxed than bulk materials, thereby confirming previous theories on nanoparticle structure relaxation. It is believed that this phenomenon aided the incorporation of cations of different sizes into the crystal lattice. The particles have also proved to be relatively stable with regard to heat treatments in terms of the phases observed and the calculated compositions. However, the more fluid nature of nanoparticle structure has also been observed in the ion exchange experiments, with compositions being varied relatively easily in solution despite only very low temperatures being applied. This suggests that, in fact, a series of meta-stable phases were formed, with ion exchange in solution allowing the compositions to change. Although it was predicted that within this quaternary system a series of solid solutions would be seen, this in fact, was not always the case. It was seen that a series of phases based on pyrochlore, perovskite and fluorite were preferred to an ideal solid solution. It has been demonstrated that the structural properties of mixed oxide nanoparticles do vary greatly in comparison with the bulk in terms of lattice parameters and ability to accommodate different cations, with examples of this behaviour documented in this thesis.

Although systems of solid solutions had previously been thought to be favourable due to entropic effects, in the Ce-Nb-Bi oxide system, the enthalpic gain of forming these various phases appears to be preferable. One would think that the resin-gel synthesis would promote the formation of solid solutions due to the extensive mixing of the ions prior to nanoparticle formation, however, this was not the case. It appears that the mixed oxide system is fairly ordered due to the surface site preference of the bismuth cations and the stability of the structures with heat treatment. This bismuth surface arrangement has been seen to be energetically preferable from the computational calculations, and potentially electronically preferable due to the bismuth lone pair.

There is still much work to be done in this system including further computational modelling work, further stability tests and catalytic studies.

10.2 Summary of materials synthesised and characterised

Preliminary results showed that it was possible to produce nanoparticles of binary oxides of cerium, niobium and bismuth using the resin-gel method and that these could be characterised using a combination of microscopy and X-ray diffraction. Following on from this work, a range ternary oxides composed of cerium, niobium and bismuth were synthesised using the resin-gel method, with the resulting particles on the nanoscale. The compositions of these particles were calculated by comparing EDS analyses to bulk standard samples of $CeNbO_4$ and $BiNbO_4$ synthesised by solid state methods.

Within the Bi_2O_3-CeO_2 system, it was found that a series of solid solutions were formed for a range of compositions, up to 60% doping of the CeO_2 structure with bismuth. This proves that the fluorite structure is highly tolerant to doping, confirming results from the literature. It was also found from XPS that the surface of the Bi-Ce oxide nanoparticles was highly bismuth rich and remained so even after several heat treatments, up to 700 °C. A structural change was found to occur in particles over 60% bismuth doping, with the α-Bi_2O_3 structure forming preferentially and a small proportion of fluorite particles found via HRTEM.

Within the CeO_2-Nb_2O_5 system it was found that the initial calcination temperature of 350 °C was not sufficient to form crystalline samples and that the niobium rich particles analysed in the HRTEM were amorphous. More cerium rich particles were found to have the fluorite structure. Both the amorphous and fluorite phases were found across all compositions, unlike the Bi-Ce oxide system where there was a clear phase change. Heating the samples encouraged the formation of crystalline T- and M-Nb_2O_5 in samples with a higher concentration of niobium, although they did contain some cerium according to EDS. Overall it was concluded that the Ce-Nb oxide system forms only a limited solid solution in fluorite with the amorphous phase crystallising to T-Nb_2O_5 at higher temperatures. These findings agreed well with previous literature which also found limited solubility of niobium ions in the fluorite structure and that the presence of cerium dramatically affected the crystallinity of the Nb_2O_5. The particles were found to be inhomogeneous with evidence from XPS showing niobium's preference for surface site occupation.

Within the Bi_2O_3-Nb_2O_5 system it was found that a range of mixed oxide phases could be formed, including fluorite, pyrochlore and perovskite. These three phases had previously been found in the Bi_2O_3-Nb_2O_5 system by several groups in the literature. T-Nb_2O_5 was also observed in samples with a higher proportion of niobium. All four of these phases were also observed upon heating the samples to 500 °C, however, at 700 °C temperatures were sufficient for the $BiNbO_4$ phase to form. This is particularly interesting as usually 700 °C is not sufficient for $BiNbO_4$ to form in the bulk, therefore, this result highlights the ability of nanoparticles to form phases not normally accessible at lower temperatures.

Within the quaternary oxide system it was found that particles could be made containing bismuth, cerium and niobium in a limited solid solution. The mixed oxide particles were found to adopt the fluorite and pyrochlore structures, with more niobium rich particles favouring the perovskite structure. As with the Ce-Nb oxide particles, some amorphous particles were observed across all compositions even after heating to 700 °C. EDS data showed that the particles were relatively stable with their composition changing little with heat. XPS experiments showed that, as found in the other systems, the surface of the particles were bismuth enriched.

Overall, the aims of the project were satisfied by successfully synthesising quaternary oxide nanoparticles, containing cerium, bismuth and niobium, via the resin-gel method for the first time.

10.3 Future work

Although this project produced many successful results in the synthesis and understanding of the Bi_2O_3-CeO_2-Nb_2O_5 mixed oxide system, there are still many questions left unanswered. Below are several suggestions which could help discover more about the structures within this system.

- Calculating the oxygen content of the mixed oxide nanoparticle samples using EDS or alternatively EELS to determine the stoichiometry of the various samples.

- Carrying out studies to understand the mechanism of the resin-gel and how the mixed nanoparticles are formed. Previous attempts by members of the group to determine the pair distribution function from X-ray data have not been successful due to the very dilute nature of the gel. Alternative methods to help understand the mechanism would have to be devised.

- Carrying out further heating experiments to study the transition from the metastable phases observed in the nanoparticles to the bulk equilibrium phases.

- Testing the ternary and quaternary oxide materials to see if catalytic properties improve in comparison to the catalytic properties observed in the binary oxides.

- Further modelling calculations of various particles sizes and arrangement of cations could be carried out to compare with experimental results.

Bibliography

1. G. Gregori, B. Rahmati, W. Sigle, P.A. van Aken and J. Maier, *Solid State Ionics*, (2011), **192**, 65–69.
2. H.J. Wang, P. Blennow, K. Thydén, Å.H. Persson, L. Mikkelsen and T. Klemensø, *J. Power Sources*, (2013), **228**, 75-82.
3. V. Petrykin, K. Macounova, M. Okube, S. Mukerjee and P. Krtil, *Catal. Today*, (2013), **202**, 63-69.
4. W. Hume-Rothery, G.W. Mabbott and K.M. Channel Evans, *Phil. Trans. R. Soc. A*, (1934), **233**, 1-97.
5. T.K. Bhattacharya, A. Ghosh, H.S. Tripathi and S.K. Das, *Bull. Mater. Sci*., (2003), **26**, 703-706.
6. P. Fornasiero, R. Dimonte, G.R. Rao, J. Kaspar, S. Meriani, A. Trovarelli and M. Graziani, *J. Catal*., (1995), **151**, 168–177.
7. M. Ozawa, M. Kimura and A. Isogai, *J. Alloys Compd*., (1993), **193**, 73–75.
8. H.T. Cahen, T.G.M. Van Den Belt, J.H.W. De Wit and G.H.J. Broers, *Solid State Ionics*, (1980), **1**, 411-423.
9. A.A. Yaremchenko, C.C. Kharton, E.N. Naumovich and A.A. Vecher, *J. Solid State Electrochem*., (1998), **2**, 146-149.
10. J.F. Marucco, B. Poumellec, J. Gautron and P. Lemasson, *J. Phys. Chem. Solids*, (1985), **46**, 709-717.
11. T.D. Manning, I.P. Parkin, C. Blackman and U. Qureshi, *J. Mater. Chem*., (2005), **15**, 4560-4566.
12. R. Feynman, There's plenty of room at the bottom, *American Physical Society meeting at CalTech*, (1959).
13. R. Feynman, *Eng. Sci*., (1960), **23**, 22-36.
14. M. Faraday, Phil. *Trans. R. Soc. Lond*., (1857), **147**, 145-181.
15. X.W. Lou, C.M. Li and L.A. Archer, *Adv. Mater*., (2009), **21**, 2536–2539.
16. C.J. Murphy, T.K. Sau, A.M. Gole, C. J. Orendorff, J. Gao, L. Gou, S.E. Hunyadi and T. Li, J. *Phys. Chem. B*, (2005), **109**, 13857-13870.
17. L.E. Greene, M. Law, D.H. Tan, M. Montano, J. Goldberger, G. Somorjai and P. Yang, *Nano Lett.*, (2005), **5**, 1231–1236.
18. Y. Sun and Y. Xia, *Science*, (2002), **298,** 2176-2179.
19. J. Kreuter, *Int. J. Pharm*., (2007), **331**, 1-10.

20. S. Gelperina, K. Kisich, M.D. Iseman, and L. Heifets, *Am. J. Respir. Crit. Care Med.*, (2005), **172**, 1487-1490.

21. B.R. Jarrett, M. Frendo, J. Vogan and A.Y. Louie, *Nanotechnology*, (2007), **18**, 35603.

22. W. Wu, Q. He and C. Jiang, *Nanoscale Res. Lett.*, (2008), **3**, 397-415.

23. C. Tassa, S.Y. Shaw and R. Weissleder, *Acc. Chem. Res.*, (2011), **44**, 842-852.

24. B. Kang, M.A. Mackey and M.A. El-Sayed, *J. Am. Chem. Soc.*, (2010), **132**, 1517–1519.

25. K. Wolff and U. Hilleringmann, Proceedings of the 39th Solid-State Device Research Conference (ESSDERC), (2009), 460-463.

26. A.J. Jacobson, *Chem. Mater.*, (2010), **22**, 660-674.

27. B. Schimmoeller, S.E. Pratsinis and A. Baiker, *ChemCatChem*, (2011), **3**, 1234-1256).

28. American Micro-System Incorporated, *Metal-Oxide Semiconductor Integrated Circuits* (Microelectronics series), Van Nost. Reinhold, New York, NY, USA, (1972).

29. J.G. Bednorz and K.A. Müller, *Z. Physik B*, (1986), **64**, 189-193.

30. A.R. West, *Solid State Chemistry and its Applications*, Wiley-Blackwell; New Ed edition, (1985).

31. S. Tsunekawa, K. Ishikawa, Z.-Q. Li, Y. Kawazoe and A. Kasuya, *Phys. Rev. Lett.*, (2000), **85**, 3440-3443.

32. X. Zhou and W. Huebner, *App. Phys. Lett.*, (2001), **3512**, 10-13.

33. E.M. Levin and R.S. Roth, *J. Res. Natl. Stand, Sec. A*, (1968), **68A**, 189-206.

34. L.G. Sillen, *Ark. Kemi. Mineral. Geol. A*, (1937), **12**, 1-15.

35. G. Malmros, *Acta Chem. Scand.*, (1970), **24**, 384-396.

36. A. Matsumoto, Y. Koyama and I. Tanaka, *Phys. Rev B.*, (2010), **81**, 094117.

37. H.A. Harwig and A.G. Gerards, *Thermochim. Acta*, (1979), **28**, 121-131.

38. L.G. Sillen, *Naturwissenschaften*, (1940), **28**, 206-207.

39. P.D. Battle, C.R.A. Catlow, J. Drennan and A.D. Murray, *J. Phys. C: Solid State Phys.*, (1983), **16**, 561-566.

40. G. Gattow and H. Schroder, *Z. Anorg. Allg. Chem.*, (1962), **318**, 176-189.

41. B.T.M Willis, *Acta Crystallogr.*, (1965), **18**, 75-76.

42. N. Sammes, G.A. Tompsett, H. Näfe and F. Aldinger, *J. Eur. Ceram. Soc.*, (1999), **19**, 1801-1826.

43. P.W.M. Jacobs and D.A. Mac Dónaill, *Solid State Ionics*, 1987, **23**, 279–293.

44. P.W.M. Jacobs and D.A. Mac Dónaill, *Solid State Ionics*, 1987, **23**, 295–305.

45. P.W.M. Jacobs and D.A. Mac Dónaill, *Solid State Ionics*, 1987, **23**, 307–318.

46. J.M. Carlsson, B. Hellsing, H.S. Domingos and P.D. Bristowe, *Phys. Rev. B*, (2002), **65**, 205122.

47. A. Walsh, G.W. Watson, D.J. Payne, R.G. Edgell, J.H. Guo, P.A. Glans, T. Learmonth and K.E. Smith, *Phys. Rev. B*, (2006), **73**, 235104-13.

48. S.F. Radaev, V.I. Simonov and F. Yu. Kargin, *Acta Cryst. Sec. B: Struct. Sci.*, (1992), **48,** 604-609.

49. H.A. Harwig and A.G. Gerards, *J. Solid State Chem*., (1978), **26**, 265-274.

50. P. Shuk and H.H. Mobius, *Z. Phys. Chem-Leipzig*., (1985), **226**, 9-16.

51. J.C. Boivin and G. Mairesse, *Chem. Mater*., (1998), **10**, 2870-2888.

52. T. Takahashi, H. Iwahara and Y. Nagai, *J. Appl. Electrochem*., (1972), **2**, 97-104.

53. G. Mairesse, *Fast Ion Transport in Solids*, ed. B. Scrosati, A. Magistris, C.M. Mari and G. Mariotto, Kluver, Amsterdam, (1993), 271-290.

54. Gulf Research & Development Company, Pittsburgh, Pa., (1971), US Patent, US3761536.

55. M.G. White and J.W. Hightower, *AIChE J*., (1981), **27**, 545-551.

56. N. Kapur, B. Shan, J. Hyun, L. Wang, S. Yang, J.B. Nicholas and K. Cho, *Mol. Simulat*., (2011), **37**, 648-658.

57. J.M. Peacock, A.J. Parker, P.G. Ashmore and J.A. Hockey, *J. Catal*., (1969), **15**, 373-378.

58. E.L. Sazonova, L.P. Olenkova, L.M. Plyasova and D.V. Tarasova, *React. Kinet. Catal*., (1977), **7**, 413-417.

59. G.W. Keulks, *J. Catal*., (1970), **19**, 232-235.

60. S. Pudar, J. Oxgaard, K. Chenowth, A.C.T. van Duin and W.A. Goddard, *J. Phys. Chem. C*, (2007), **111**, 16405-16415.

61. M. Azad, S. Larose and S.A. Akbar, *J. Mater. Sci*., (1994), **29**, 4135-4151.

62. A. Cabot, A. Marsal, J. Arbiol and J.R. Morante, *Sens. Actuators, B*, (2004), **99**, 74-89.

63. S. Murcia-López, M.C. Hidalgo and J.A. Navío, *Appl. Catal., A*, (2011), **404**, 59-67.

64. G. Brauer, *Z. Anorg. Allgem. Chem*., (1941), **248**, 1-31.

65. K. Kato and S. Tamura, *Acta Crystallogr. Sect. B: Struct. Sci.*, (1975), **31**, 673-677.

66. H. Kodama, T. Kikuchi and M. Goto, *J. Less-Common Met*., (1972), **29**, 415-421.

67. L.K. Frevel and H.N. Rinn, *Anal. Chem*., (1955), **27**, 1329-1330.

68. K. Kato, *Acta Crystallogr. Sect. B: Struct. Sci.*, (1976), **32**, 764-767.

69. I. Nowak and M. Ziolek, *Chem. Rev*., (1999), **99**, 3603-3624.

70. W. Mertin, S. Andersson and R. Gruehn, *J. Solid State Chem*., (1970), **1**, 419-424.

71. J.S. Anderson, J.M. Browne and J.L. Hutchison, *J. Solid State Chem*., (1972), **5**, 419-431.

72. H. Schäfer, F. Schulte and R. Gruehn, *Angew. Chem*., (1964), **3**, 634-635.

73. S. Andersson, Z. *Anorg. Allg. Chem*., (1967), **351**, 106-112.

74. R. Gruehn, *J. Less-Common Met*., (1966), **11**, 119-126.

75. V. Plies and R. Gruehn, *J. Less-Common Met*., (1975), **42**, 77-88.

76. Avx Corporation, (2006), US Patent, US7511943 B2.

77. C.K. Gupta and A.K. Suri, *Extractive Metallurgy of Niobium*, Boca Raton, Florida; CRC Press, (1994).

78. G. Deo and I.E. Wachs, *J. Catal*., (1994), **146**, 323-334.

79. N. Ichikuni and Y. Iwasawa, *New Frontiers in Catalysis*, ed. L. Guczi, Elsevier: Amsterdam, (1992), 477.

80. T. Iizuka, K. Ogasawara and K. Tanabe, *Bull. Chem. Soc. Jpn*., (1983), **56**, 2927-2931.

81. K. Tanabe and S. Okazaki, *Appl. Catal. A*., (1995), **133**, 191-218.

82. S. Hasegawa, H. Aritani and M. Kudo, *Catal. Today*, (1993), **16**, 371-377.

83. M.G. Cutrufello, I. Ferino, V. Solinas, A. Primavera, A. Trovarelli, A. Auroux and C. Picciau, *PCCP Phys C*., (1999), **1**, 3369-3375.

84. R. Kodama, Y. Terada, I. Nakai, S. Komaba and N. Kumagai, *J. Electrochem. Soc*., (2006), **153**, A583-A588.

85. V.M. Goldschmidt and L. Thomassen, *Skr. Nor. Vidensk. Akad. Oslo*., (1923), **5**, 1-48.

86. H.S. Gandhi, A.G. Piken, M. Shelef and R.G. Delosh, *SAE Paper*, (1976), 760201.

87. M.G. Cutrufello, I. Ferino, R. Monaci, E. Rombi and V. Solinas, *Top. Catal*., (2002), **19**, 225–240.

88. B.M. Reddy, P. Lakshmanan, P. Bharali and P. Saikia, *J. Mol. Catal. A: Chem*., (2006), **258**, 355–360.

89. S. Wei, S. Ruijuan, L. Junlong, Z. Ensheng, L. Zhanshuang, X. Yide and S. Wenjie, Chin. *J. Catal*., (2007), **28**, 106–108.

90. S. Lippert, W. Baumann and K. Thomke, *J. Mol. Catal*., (1991), **69**, 199–214.

91. R. Juárez, A. Corma and H. Garcia, *Green Chem*., (2009), **11**, 949–952.

92. S. Sato, K. Koizumi and F. Nozaki, *Appl. Catal. A: Gen*., (1995), **133**, L7L10.

93. E. Mamontov, W. Dmowski, T. Egami and C.C. Kao, *J. Phys. Chem. Solids*, (2000), **61,** 431–433.

94. H.P. Zhou, H.S. Wu, J. Shen, A.X. Yin, L.D. Sun and C.H. Yan, *J. Am. Chem. Soc*., (2010), **132**, 4998 – 4999.

95. N.A.S. Amin and C.M. Chong, *Focus on Catalysis Research*, ed. L.P. Bevy, Nova Science Publishers, Inc., New York (USA), (2006).

96. S. Abanades and G. Flamant, *Sol. Energy*, (2006), **80**, 1611-1623.

97. S. Abanades, A. Legal, A. Cordier, G. Peraudeau, G. Flamant and A. Julbe, *J. Mater. Sci*., (2010), **45**, 4163-4173.

98. W.H. Zachariasen, *Z. Phys. Chem*., (1926), **123**, 134-150.

99. R. Dziembaj, M. Molenda, L. Chmielarz, M.M. Zaitz, Z. Piwowarska and A. Rafalska-Łasocha, *Catal. Today*, (2011), **169**, 112-117.

100. C. Endler-Schuck, A. Weber, E. Ivers-Tiffée, U. Guntow, J. Ernst and J. Ruska, *J. Fuel Cell Sci. Tech*., (2011), **8**, 041001-5.

101. B. Aurivillius, *Arkiv. Kemi*, (1951), **3**, 153-161.

102. R.S. Roth and J.L. Waring, *J. Res. Natl. Bur. Stand. Sec. A*, (1962), **66A**, 451-463.

103. E.T. Keve and A.C. Skapski, *J. Solid State Chem*., (1973), **8**, 159-165.

104. B. Muktha, J. Darriet, G. Madras and T.N. Guru Row, *J. Solid State Chem*., (2006), **179**, 3919-3925.

105. M.A. Subramanian and J.C. Calabrese, *Mater. Res. Bull*., (1993), **28**, 523-529.

106. W. Zhou, D.A. Jefferson and J.M. Thomas, *Proc. R. Soc. Lond. A,* (1986), **406**, 173-182.

107. H.J. Deiseroth and H. Muller Buschbaum, *Z. Anorg. Allg. Chem*., (1970), **373**, 152-156.

108. T. Barth, *Nor. Geol. Tidsskr*., (1925), **8**, 201-219.

109. E. Aguado, R. Enjalbert, J.M. Rojo and A. Castro, *Bol. Soc. Esp. Ceram. Vidrio*., (1995), **34**, 417-420.

110. C.D. Ling, *J. Solid State Chem*., (1999), **148**, 380-405.

111. L. Wang, W. Wang, M. Shang, S. Sun, W. Yin, J. Ren and J. Zhou, *J. Mater. Chem*., (2010), **20**, 8405-8410.

112. J. Gopalakrishnan, A. Ramanan, C.N.R. Rao, D.A. Jefferson and D.J. Smith, *J. Solid State Chem*., (1984), **55**, 101-105.

113. K. Gurunathan and P. Maruthamuthu, *J. Solid State Electrochem*., (1998), **2**, 176-180.

114. S. Tahara, A. Shimade, N. Kumada and Y. Suguhara, J. Solid State Chem., (2007), **180**, 2517-2524.

115. T. Negas, R.S. Roth, C.L. McDaniel, H.S. Parker and C.D. Olson, *Mater. Res. Bull*., (1977), **12**, 1161-1172.

116. R.S. Roth, T. Negas, H.S. Parker, D.B. Minor and C. Jones, *Mater. Res. Bull*., (1977), **12**, 1173-1182.

117. R.J. Cava, T. Negas, R.S. Roth, H.S. Parker, D.B. Minor and C.D. Olson, *The Rare Earths in Modern Science and Technology*, ed. G.J. McCarthy and J.J. Rhyne, New York/London: Plenum Press, (1978), 181-187.

118. A. Santoro, M. Marezio, R.S. Roth and D. Minor, *J. Solid State Chem*., (1980), **35**, 167-175.

119. S.J. Skinner and Y. Kang, *Solid State Sci*., (2003), **5**, 1475-1479.

120. J.G. Thompson, R.L. Withers and F.J. Brink, *J. Solid State Chem*., (1999), **143**, 122–131.

121. D. Stošić, S. Bennici, V. Rakić and A. Auroux, *Catal. Today*, (2012), **192**, 160– 168.

122. R. Benz, *Acta Crystallogr. Sect. B: Struct. Sci*., (1971), **27**, 853-854.

123. J. Nuss and M. Jansen, *J. Alloys Compd*., (2009), **480**, 57-59.

124. J. Beckers, A.F. Lee and G. Rothenberg, *Adv. Synth. Catal*., (2009), **351**, 1557-1566.

125. X. Chen and W. Eysel, *J. Solid State Chem*., (1996), **127**, 128-130.

126. D.B. Williams and C.B. Carter, *Transmission Electron Microscopy: A Textbook for Materials Science*, Springer US, (2009).

127. V.D. Scott and G. Love, *Quantitative Electron-Probe Microanalysis*, Ellis Horwood, Chichester, (1983).

128. V. Pecharsky and P. Zavalij, *Fundamentals of Powder Diffraction and Structural Characterization of Materials*, Springer, (2004).

129. D. Briggs and M.P. Seah, *Practical Surface Analysis: Auger and X-ray photoelectron spectroscopy*, Wiley, (1990).

130. O. Scherzer, *J. Appl. Phys*., (1949), **20**, 20-29.

131. J.K. Reddy, V. Durgakumari, M. Subrahmanyam and B. Sreedhar, *Mater. Res. Bull*., (2009), **44**, 1540–1546.

132. G. Qi, R.T. Yang and R. Chang, *Appl. Catal. B*, (2004), **51**, 93–106.

133. S. Dunkle and K.S. Suslick, *J. Phys. Chem. C,* (2009), **113**, 10341-10345.

134. X. Li, H. Zhang, F. Chi, S. Li, B. Xu and M. Zhao, *Mater. Sci. Eng. B*, (1993), **18**, 209-213.

135. J.R. Osman, J.A. Crayston, A. Pratt and D.T. Richens, *J. Sol-Gel Sci. Technol*., (2008), **42**, 126-132.

136. D. Vitry, Y. Morikawa, J.L. Dubois and W. Ueda, *Appl. Catal. A*, (2003), **251**, 411–424.

137. P.K. Dutta and J.R. Gregg, *Chem. Mater*., (1992), **4**, 843-846.

138. S. Sakka and H. Kozuka, *Handbook of Sol-Gel Science and Technology; Volume 1*, Springer, (2005).

139. M.P. Pechini, (1967), US Patent 3, 3306, 97.

140. D. Sánchez-Martínez, A. Martínez-de la Cruz and E. López-Cuéllar, *Mater. Res. Bull*., (2013), **48**, 691–697.

141. A.B. Taxak, S.P. Khatkar, S.D. Han, R. Kumar and M. Kumar, *J. Alloy. Compd*., (2009), **469**, 224-228.

142. L. Bendor, *Heterogen Chem Rev*., (1995), **2**, 41-50.

143. C.N.R. Rao, *Mat. Sci. Eng. B*, (1993), **18**, 1-21.

144. M. Niederberger, *Acc. Chem. Res*., (2007), **40**, 793-800.

145. D. Xu, X.N. Cheng, X.H. Yan, H.X. Xu and L.Y. Shi, *Trans. Nonferrous Met. Soc. China*, (2009), **19**, 1526-1526

146. L. Choong-Young, R. Marquart, Z.Q. Di and B.J. Kennedy, *J. Solid State Chem*., (2003) **174**, 310-318.

147. S.J. Skinner, I.J.E. Brooks and C.N. Munnings, *Acta Crystallogr. Sect. C: Cryst. Struct. Commun*., (2004), **60**, 37-39.

148. A. Castro and D. Palem, *J. Mater. Chem*., (2002), **12**, 2774-2780.

149. S. Dikmen, P. Shuk and M. Greenblatt, *Solid State Ionics*, (1999), **126**, 89-95.

150. J.W. Pell, K.M. Delak and H.C. zur Loye, *Chem. Mater*., (1998), **10**, 1764-1770.

151. G. Zhang, W. Wan, P. Long, Q. Li, C. Deng and Z. Yi, *J. Alloy Compd*., (2014), **616**, 328-332.

152. S. Dikmen, P. Shuk and M. Greenblatt, *Solid State Ionics*, (1998), **112**, 229-307.

153. L. Bourja, B. Bakiz, A. Benlhachemi, M. Ezahri, S. Villain, O. Crosnier and J.R. Gavarri, *J. Solid State Chem*., (2011), **184**, 608–614.

154. H. Zhao, S. Feng and W. Xu, *Mater. Res. Bull*., (2000), **35**, 2379–2386.

155. F. Hund, *Z. Anorg. Allg. Chem*., (1964), **333**, 248-255.

156. M. Prekajski, Z. Dohčević -Mitrović, M. Radović, B. Babić, J. Pantić, A. Kremenović and B. Matović, *J. Eur. Ceram. Soc*., (2012), **32**, 1983–1987.

157. G. Li, Y. Mao, L. Li, S. Feng, M. Wang, and X. Yao, *Chem. Mater*., (1999), **11**, 1259-1266.

158. K. Sardar, H. Y. Playford, R.J. Darton, E.R. Barney, A.C. Hannon, D. Tompsett, J. Fisher, R.J. Kashtiban, J. Sloan, S. Ramos, G. Cibin, and R.I. Walton, *Chem. Mater*., (2010), **22**, 6191–6201.

159. R.D. Shannon and C.T. Prewitt, *Acta Crystallogr*. Sec. A, (1976), **32A**, 751-767.

160. M.G. Harwood, *Nature*, (1949), **164**, 787.

161. L.A. Olsen, J. López-Solano, A. García, T. Balić-Žunić and E. Makovickya, *J. Solid State Chem*., (2010), **183**, 2133–2143.

162. L.E. Orgel, *J. Chem. Soc*., (1959), **12**, 3815.

163. R.G. Teller, J.F. Brazdil and R.K. Grasselli, *Acta Crystallogr., Sect. C: Cryst. Struct. Commun*., (1984), **C40**, 2001-2005.

164. F.B. Noronha, E.C. Fendley, R.R. Soares, W.E. Alvarez and D.E. Resasco, *Chem. Eng. J*, (2001), **82**, 21-31.

165. J.Z. Shyu, K. Otto, W.L.H. Watkins, G.W. Graham, R.K. Belitz and H.S. Gandhi, *J. Catal*., (1988), **114**, 23-33.

166. E. Abi-aad, R. Bechara, J. Grimblot and A. Aboukais, *Chem. Mater*., (1993), **5**, 793-797.

167. Y.Q. Jia, *J. Solid State Chem*., (1991), **95**, 184-187.

168. W. Zhou, D.A. Jefferson and J.M. Thomas, *J. Solid State Chem*., (1987), **70**, 129-136.

169. C.D. Ling, R. L. Withers, S. Schmid and J.G. Thompson, *J. Solid State Chem*., (1998), **137**, 42-61.

170. I.V. Piir, D.A. Prikhodko, S.V. Ignatchenko and A.V. Schukariov, *Solid State Ionics*, (1997), **101-103**, 1141-1146.

171. S.K. Blower and C. Greaves, *Acta Crystallogr. Sect. C: Cryst. Struct. Commun*., (1998), **44**, 587-589.

172. R. Ali and M. Yashima, *J. Solid State Chem*., (2005), **178**, 2867-2872.

173. R. Radhaa, H. Muthurajanb, N.K. Raoc, S. Pradhanc, U.N. Guptac, R.K. Jhac, S.A. Mirjia and V. Ravia, *Mater. Charac*., (2008), **59**, 1083-1087.